CHAPTER 1:

BACKGROUND

Since World War II, Ni–based superalloys have been developed to become highly successful, operating at high temperatures in the severe aggressive environmental conditions in turbine engines, while maintaining their strength. Superalloys are alloys developed for elevated temperature service, usually based on Group VIA elements where relatively severe mechanical stressing and surface stability are frequently required [1987Sim].

Approximately 70% of the weight in a modern jet turbine comprises nickel–based superalloys (NBSAs), and their success is due to their high yield stresses and excellent resistance to environmental attack at high temperatures [1987Sim]. The high yield stresses are possible because the microstructure is composed of fine, coherent, ordered precipitates in a compatible matrix. The precipitates are coherent with the matrix since they have a similar structure, so that the misfit between the lattice parameters of the matrix and precipitate phases is very low. The precipitates are ordered (specific atom types, e.g. Ni or Al, prefer specific sites), whereas the matrix is random or disordered (the atoms have no site preference). In NBSAs, the precipitates have the $L1_2$ structure: they are ordered fcc and are thus very closely related to the fcc matrix phases [1987Sim].

Although the NBSAs have excellent properties, they have reached their temperature capability limit for operation in turbine engines, despite advanced processing technologies like single crystal technology, air cooling and thermal barrier coatings [1987Sim]. Currently, the maximum temperature at which NBSAs operate is ~1100^{o}C, which is 85% of their melting temperature [1987Sim]. If the operating temperature could be increased to higher temperatures, this would improve the efficiency of turbine engines and enable greater thrust, improved fuel efficiency and reduced pollution. Therefore, there is interest in developing similar structured alloys based on an alloy with a higher melting point which can be used at temperatures of ~1300^{o}C and above. Platinum has been selected as the base material for these alloys because of its similarity to Ni in fcc structure and similar chemistry [2000Wol]. Thus, a Pt–based superalloy analogous to NBSAs was considered possible, but with a higher melting point (the respective melting points are 1769^{o}C for platinum, compared with 1455^{o}C for nickel) and improved oxidation resistance [2000Wol].

Platinum–based alloys have already been successfully applied in the aerospace and glass industries [1988Wha, 1990Lup]. For these applications, exceptional chemical stability, oxidation resistance, high melting points, ductility, thermal–shock resistance and electrical or thermal conductivity counter–balance the exceptionally high price of platinum [2003Cor]. Platinum–based alloys have been studied at Mintek and have microstructures that are analogous to the γ/γ′ microstructure of the NBSAs [2000Wol, 2001Hil1, 2002Cor, 2003Cor, 2003Süs1]. These platinum–based alloys have the potential to substitute NBSAs in extreme applications, because of their higher melting points and good corrosion resistance. Although platinum–based alloys are unlikely to replace all NBSAs on account of both higher price and higher density, it is likely that they can be used for the highest application temperature components. There is one important difference between the NBSAs and the platinum-based alloys. There is only one form of Ni_3Al, whereas the phase Pt_3Al has at least two forms [1990Mas], and the more desirable high temperature $L1_2$ form needs to be stabilised. There are one, if not two, lower temperature forms. One is the distorted $L1_2$ structure DO′c, which originates from a martensitic-type transformation at ~400^{o}C [1986Mis]. A low temperature modified DO′c structure has also been identified [2007Dou].

In the studies at Mintek, it was found that successful NBSAs analogues could be manufactured with alloys of the approximately composition Pt_{82}:Al_{14}:X_4 where X was Cr, Ti and Ru [2001Hil2, 2001Hil3]. The best properties were exhibited by the Pt–Al–Cr and Pt–Al–Ru alloys, although the precipitate volume fraction (~30%) was not as high as in the Ni–based Superalloys (~70%). Although much heavier, these platinum–based alloys have the advantages of good mechanical properties and high temperature oxidation resistance [2001Hil2, 2001Süs1]. The ternary alloys had mechanical properties which are better than those of the Ni– and Co–based superalloys, higher than conventional solid–solution strengthened Pt–based alloys, and comparable with mechanically alloyed ferritic oxide–dispersion–strengthened (ODS) alloys [2002Süs2]. Hill *et al.* [2001Hil4] showed that it was possible to obtain the (Pt) + ~Pt_3Al microstructure (which is a two–phase γ/γ′ structure) in a Pt–Al–Cr–Ru quaternary alloy. The best alloy composition so far is Pt_{84}:Al_{11}:Ru_2:Cr_3, and its oxidation resistance is better than the original ternary alloys [2001Süs2]. It has been shown that the quaternary and ternary alloys have room temperature tensile properties similar to that of other high temperature alloys [2004Süs2]. However, the quaternary alloy needs further optimisation in terms of heat treatments and additional alloying to obtain the best properties and this is ongoing [2008Sho]. In order to decrease both the density and the cost of the alloys,

other additions are being considered. Niobium is potentially useful because its high melting point should help to increase the melting point of the alloys.

As well as developing the alloys, the other part of the Mintek project is building a thermodynamic database to facilitate the further development of these Pt–based alloys. This work needs phase diagrams of all the component systems, as well as thermodynamic data. Currently, the database comprises Pt-Al-Cr-Ru, and it is being extended to contain niobium [2008Ukp]. This work will build on the information already gleaned from prior work, and will also extend the information to platinum–based alloys of higher order (i.e. alloys with more components, such as Ni and Co). The Thermo-Calc^{TM} program was chosen for the assessment of the phase diagrams to derive the database because it contains the Parrot module which is the accepted optimization process for fitting experimental data to thermodynamic expressions. The database comprises information on the different phases, which is stored as coefficients.

The Thermo–Calc^{TM} program needs data, and although the binary systems have been published [1990Mas], there were no published ternary systems for the Pt–Al–Cr–Ru system at the beginning of the programme. Experimental phase diagram work has been done on the ternary systems: Al–Cr–Ru [2000Com1, 2000Com2, and 2001Com], Pt–Al–Ru [2003Pri], Pt–Cr–Ru [2002Süs1, 2003Süs1, 2003Süs2, and 2004Süs], Pt–Al–Cr [2003Süs3, 2008Süs], Pt–Al–Co [2003Cho], Pt–Al–Ni [2003Gla] and Pt–Al–Nb [2006Ndl, 2007Ndl].

In the investigations by workers in Germany [2005Wen, 2004Vor], alloys with 10–13 at.% Al, 3–6 at.% Cr, 6 at.% Ni and balance Pt, showed similar two–phase microstructures to the Pt–Al–Cr–Ru alloy and lattice misfits similar to conventional NBSAs. The microstructures could be optimised by heat treating. A two–phase structure with cuboidal and $L1_2$–ordered γ' precipitates of about 300nm size could be generated by controlled cooling after a homogenization heat treatment. Vorberg ***et al.*** [2004Vor] reported a γ' volume fraction of about 50% in an alloy with 12 at.% Al, 6 at.% Cr, 6 at.% Ni and balance Pt after homogenization at 1500^{o}C for 12hrs and air cooling. The γ' morphology was between spherical and cuboid. In some related investigations, nickel was added in various amounts as a potential solid–solution strengthener and also to lower the density and price of the platinum–based alloys. The aluminum and nickel contents in the Pt–Al–Cr–Ni quaternary system were optimized to ensure a high γ' volume fraction and cuboid γ' morphology. In these investigations, it was found that chromium additions increased the γ' volume fraction

and decreased the absolute value of the lattice misfit between γ and γ′. Preferable partitioning of chromium to the γ matrix phase in Pt–Al based alloys was found by several researchers [2001Hil2, 2002Hil1, 2005Wen]. The Goldsmith radius of chromium (1.25Å) is smaller than that of platinum (1.38Å) and aluminum (1.44 Å) [1964Sch]. Therefore, increasing chromium content should more strongly decrease the lattice parameter of the matrix rather than that of the γ′ phase, and hence decrease the absolute value of the lattice misfit. A similar influence on the misfit by adding nickel (atomic radius 1.24Å) to Pt–Al–Cr–Ni alloys was also found previously by Hüller *et al.* [2005Hül].

The quaternary Ir–Nb–Pt–Al system has been studied by Huang *et al.* [2003Hua, 2004Hua1, 2004Hua2, 2005Hua], and an fcc/$L1_2$ two–phase structure exists in both Pt–Al and Ir–Nb binary systems, with the lattice parameters of $L1_2$ phases (Ir_3Nb and Pt_3Al) being similar. The solubility of Nb in the $L1_2$–Pt_3Al phase could not be obtained directly in the ternary alloy 86Pt–10Al–4Nb because of the small size of the phases. However, a composition of Nb and Ta indicates that Nb and Ta have similar atomic radius as Al and a similar electronic structure (they are in the same group in the periodic table of elements). These similarities would cause them to show similar solubility characteristics. The solubility of Ta in the $L1_2$–Pt_3Al phase was reported to be 5 at.%; accordingly, a similar solubility is expected for Nb in $L1_2$–Pt_3Al. Huang *et al.* [2004Hua2, 2005Hua], found that no phase transformation was detected, which indicated that the $L1_2$–Pt_3Al structure was stabilised at room temperature in the Ir–Nb–Pt–Al system, which was attributed to the Nb addition, according to the investigation on Pt–Al–Nb ternary system.

In the Pt-Al binary, the cubic $L1_2$–Pt_3Al is stable at room temperature only when the composition of this phase lies on the Al–rich side of stoichiometry, which is out of the fcc/Pt_3Al two–phase region. According to the binary phase diagram of Pt–Al, the cubic $L1_2$–Pt_3Al phase with 70–73 at.% Pt can be stable down to room temperature [1990Mas]. Mishima *et al.* [1986Mis] determined the phase transformation temperature to be around 400^{o}C and also revealed that the fcc to fct phase transformation is martensitic in nature. Hill *et al.* [2002Hil2] suggested that, in the Pt_3Al stoichiometric composition, when all Al atoms occupied all their corner positions in the $L1_2$–Pt_3Al crystal, the fcc structure could not convert to fct because fully occupied Al atoms around the Pt atoms limited the movement of Pt atoms. It seems conceivable that, in the hypo–stoichiometric composition, when a third element with high solubility in $L1_2$–Pt_3Al filled the empty sites of Al, these elements being

(Ti, Cr, Ta) [2002Hil2], could also have had the same effect as Al on the movement limitation of Pt atoms. The atomic percent of total Al and X (the value of (Al + X)/100) in the $L1_2$–Pt_3Al phase was 22.4, 22.7 and 23.1% for samples 86Pt–10Al–4Ti, 86Pt–10Al–4Cr and 86Pt–10Al–4Ta respectively, which was close to the stoichiometric composition of Pt_3Al. This indicated that high solubility of a third element substitute for Al in the Pt_3Al phase might be the main factor for the stabilisation of the $L1_2$–structure.

Thus, Nb has been identified as stabilising the beneficial $L1_2$ Pt_3Al phase, as well as for increasing the melting point, and reducing the cost and density by the substitution of some of the platinum. For the Pt-Al-Cr-Ru alloys, four ternary systems had to be studied: Al–Cr–Ru [2000Com1, 2000Com2 and 2001Com], Pt–Al–Ru [2003Pri], Pt–Cr–Ru [2002Süs1, 2003Süs1, 2003Süs2, and 2004Süs1] and Pt–Al–Cr [2003Süs3, 2008Süs]. Considering the addition of Nb to these alloys, the system becomes more complex and there are more ternaries. Pt–Al–Nb [2006Ndl, 2007Ndl] has already been studied. The next system chosen was Pt-Cr-Ru, and this work was to derive the Pt-Cr-Nb phase diagram, since no data were available in the literature.

CHAPTER 2:

LITERATURE REVIEW

2.1 The Elements: Pt, Cr and Nb

Physical properties of platinum, chromium and niobium are presented in Table 2.1 [1972Ros].

***Table 2.1. Physical properties of Pt, Cr and Nb* [1972Ros].**

	Platinum	**Chromium**	**Niobium**
Chemical symbol	Pt	Cr	Nb
Atomic number	78	24	41
Atomic weight	195.09	52.01	92.91
Crystal structure	fcc	rhombohedral	bcc
Lattice parameter (nm)	0.392	0.249	0.295
Colour	White	Greyish white	Steel grey
Melting point (^{o}C)	1769	1860	2468
Boiling points (^{o}C)	3800	2200	4927
Specific gravity	21.45	7.19	8.6
Density (Kg/m^{3})	21450	7190	8600

2.1.1 Platinum (Pt)

Platinum belongs to the "platinum group metals" (PGMs), the six metal group of platinum, palladium, rhodium, iridium, ruthenium and osmium. Platinum and its fellow group members occur in the native state generally alloyed with each other, and are all resistant to chemical attack and have high melting points. Platinum is soft, ductile and has good resistance to oxidation and high temperature corrosion, and excellent workability. It is one of the densest known metals [1972Ros]. Alloys of the PGMs are used for their exceptional catalytic properties. Platinum also has good weldability [1972Ros].

2.1.2 Chromium (Cr)

Chromium has high temperature wear resistant properties and a high melting point (1860^{o}C). It has two attributes when alloyed in steel [1972Ros]:

- First, it combines with carbon to form very hard chromium carbides. This considerably increases the hardness of the steel,
- The second virtue of chromium is that it enhances corrosion resistance and resistance to oxidation at higher temperatures.

2.1.3 Niobium (Nb)

Niobium metal is ductile and resists attack from almost all chemicals. It has been reported to have the ability to withstand oxidation [1972Ros], especially at elevated temperatures, which makes it potentially useful for gas turbine and rocket motor applications. However, work by Ndlovu on Pt-Al-Nb alloys showed that oxidation resistance was limited [2006Ndl, 2007Ndl]. In the nickel-based alloys, niobium is up to 4 at.% when it enhances the creep strength and hot oxidation resistance [1972Ros].

2.2 Binary Phase Diagrams

2.2.1 Binary Cr–Pt phase diagram

The assessed Cr–Pt phase diagram (Figure 2.1) given in Massalski [1990Mas] is drawn from Venkatraman *et al.* [1990Ven] who assessed the earlier work of Müller [1930Mül] and Waterstrat [1973Wat]. The phase diagram is characterized by a broad homogeneity range of the (Pt) terminal solid solution from ~29 to 100% at.% Pt at 1530^{o}C [1973Wat] and by the presence of two ordered intermediate phases CrPt and $CrPt_3$, although the existence of CrPt requires clarification. An ordered Cr_3Pt intermediate phase is found at a range from ~18 to ~23 at.% Pt. Both investigations by Müller [1930Mül] and Waterstrat [1973Wat] clearly indicated a maximum melting point of the (Pt) phase at ~80 at.% Pt. The composition and temperature of the two eutectics have been determined by Waterstrat [1973Wat]. He also reported a syntetic decomposition of Cr_3Pt, i.e. the presence of a liquid miscibility gap, which Venkatraman *et al.* [1990Ven] believed to be unlikely, although Süss *et al.* [2005Süs] found evidence of this. The liquidus and solidus of the (Pt) phase from ~30–100 at. % Pt is from Müller [1930Mül] and Waterstrat [1973Wat]. The solubility of Pt in Cr was reported by Raub *et al.* [1955Rau] as ~2.5 at.% Pt at 900^{o}C and is in good agreement with the selected solvus curve [1990Ven]. Reactions of the Cr-Pt binary system are shown Table 2.2 [1990Mas].

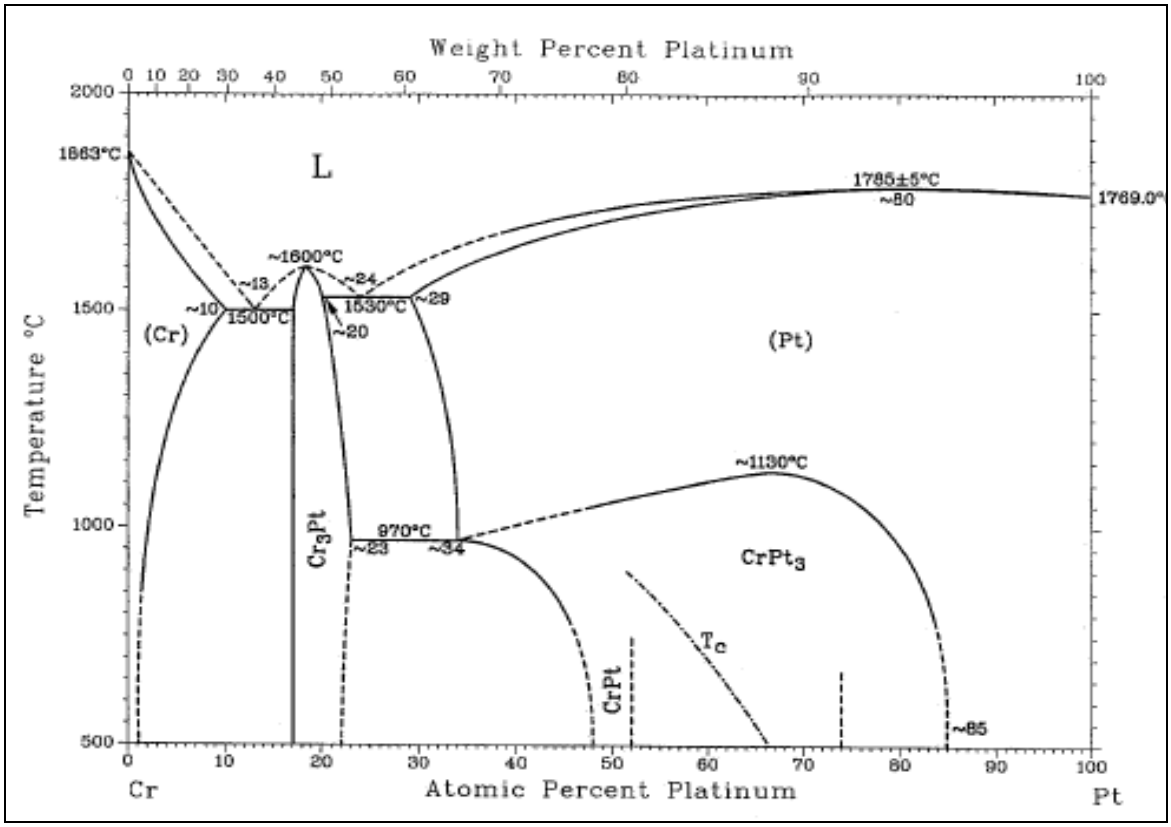

Figure 2.1. Binary Cr–Pt equilibrium phase diagram **[1990Mas].**

Table 2.2. Reactions of the Cr–Pt binary system **[1990Mas].**

Reaction	**Compositions of the respective phases (at.% Pt)**			**Temperature (^{o}C)**	**Reaction type**
L ↔ Cr	0			1863	Melting
L ↔ Cr_3Pt	~18			~1600	Congruent
L ↔ Cr_3Pt + (Pt)	~24	~20	~29	1530	Eutectic
L ↔ (Cr) + Cr_3Pt	~13	~10	~17	1500	Eutectic
(Pt) ↔ $CrPt_3$	~67			~1130	Ordering
(Pt) ↔ Cr_3Pt + $CrPt_3$	~34	~23	unknown	970	Eutectoid (?)
L ↔ (Pt)	~80			1785	Maximum
L ↔ Pt	100			1769	Melting

The ~Cr_3Pt phase has the ordered cubic A15–type structure, and occurs at a slightly off–stoichiometric composition at ~20 at.% Pt. The phase ~$CrPt_3$ has the $L1_2$–type ($AuCu_3$) structure occurring over a wide composition range, from ~34 to ~85 at.% Pt. The ordering reaction is very fast, and the disordered high–temperature phase can be retained only partially

by quenching [1973Wat]. The maximum of the order–disorder transformation occurs at ~1130°C and ~67 at.% Pt. According to Waterstrat [1973Wat], the ordered fcc $L1_2$–type structure of ~$CrPt_3$ changes continuously with increasing Cr content to the ordered pseudo–cubic $L1_0$–type structure at the composition CrPt. Although CrPt apparently shows the ordered layer arrangement of the $L1_0$ structure, the tetragonal distortion, which is typical of this structure, could not be observed [1973Wat]. However, thin film studies of the Cr–Pt system below 600°C indicated a small tetragonal distortion of the CrPt phase, as well as the presence of a two–phase region between CrPt and $CrPt_3$ [1978Bag1]. The results for the thin film studies are tentatively indicated by dashed lines in the assessed diagram.

Oikawa *et al.* [2001Oik] recently calculated the Cr–Pt diagram using Thermo-Calc^{TM}, and this was in good agreement with the data by Müller [1930Mül] and Waterstrat [1973Wat] but with the eutectic temperatures reversed. Massalski [1990Mas] had the higher eutectic temperature for the L → Cr_3Pt + (Pt) rather than L → Cr_3Pt + (Cr). Oikawa *et al.* [2001Oik] had the L → Cr_3Pt + (Cr) having the higher temperature, which agreed with the experiments of Süss *et al.* [2005Süs].

Figures 2.2–2.6 from Zhao *et al.* [2005Zha] show an application of thermal conductivity mapping in studying order–disorder transformations. An SEM backscattered electron image of Cr-Pt-Ru tri-junction, showing formation of A15 ($Cr_3(Pt,Ru)$ and σ ($Cr_y(Ru,Pt)_X$) phases resulting from interdiffusion of Pt, Ru, and Cr, as well as electron microprobe scan locations is shown in Figure 2.2 [2005Zha]. The increase in thermal conductivity above that of the disordered Pt–based fcc phase indicates the formation of the ordered phases. On the basis of the Cr–Pt binary phase diagram shown in Figure 2.6 [1973Wat, 1978Bag2, 1990Mas], it was deduced that the two peaks at ~100μm and 125 μm correspond to formation of fcc superlattice structures $L1_0$ (CrPt) and $L1_2$ ($CrPt_3$) respectively. The Cr_3Pt phase did not show an increase in thermal conductivity above that of the disordered fcc phase, probably because Cr_3Pt has a completely different crystal structure, Cr_3Si–type (*cP*4). It is clear from Figures 2.4 and 2.5 that a region of disordered fcc exists between the two ordered phases. The phase diagram was redrawn to show the ordered phases, as shown in Figure 2.6 by red dashed lines. This version is more rational, since the CrPt and $CrPt_3$ phases have related, but different, crystal structures compared to the parent fcc phase. So, there should be two–phase regions around them, similar to the Cu–Au binary system. The diffusion multiple was annealed at ~1200°C, which is above the order–disorder transition temperatures of both the CrPt and

$CrPt_3$ phases. Hence, the ordered phases were formed during cooling from ~1200°C to room temperature. Table 2.3 shows the Cr-Pt crystal structure data [1990Mas].

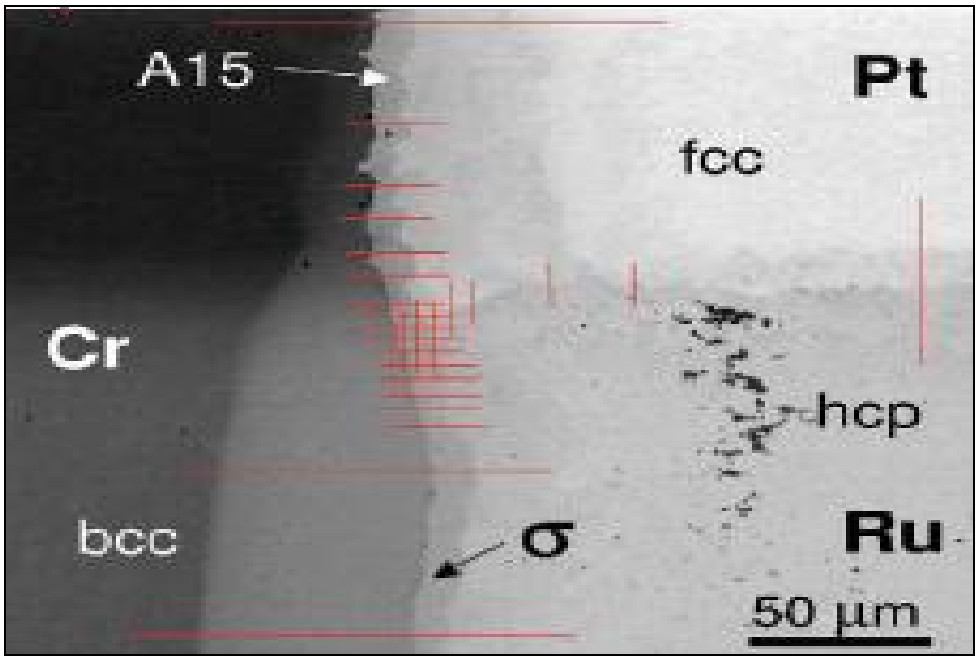

Figure 2.2. SEM-Backscattered electron image of Cr–Pt–Ru tri-junction, showing formation of A15 ($Cr_3(Pt,Ru)$) and σ ($Cr_y(Ru,Pt)_X$) phases resulting from interdiffusion of Pt, Ru, and Cr, as well as electron microprobe scan locations **[2005Zha].**

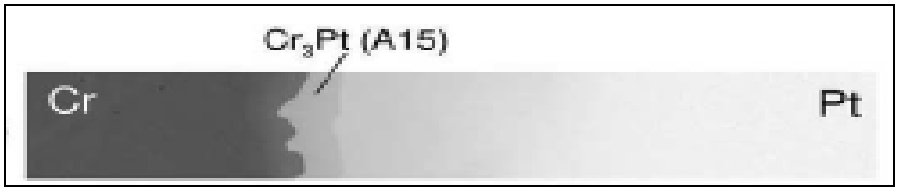

Figure 2.3. SEM–BSE image of upper region of Figure 2.2, showing the Cr–Pt binary diffusion couple **[2005Zha].**

Figure 2.4. Thermal conductivity map of upper region of Figure 2.2 **[2005Zha].**

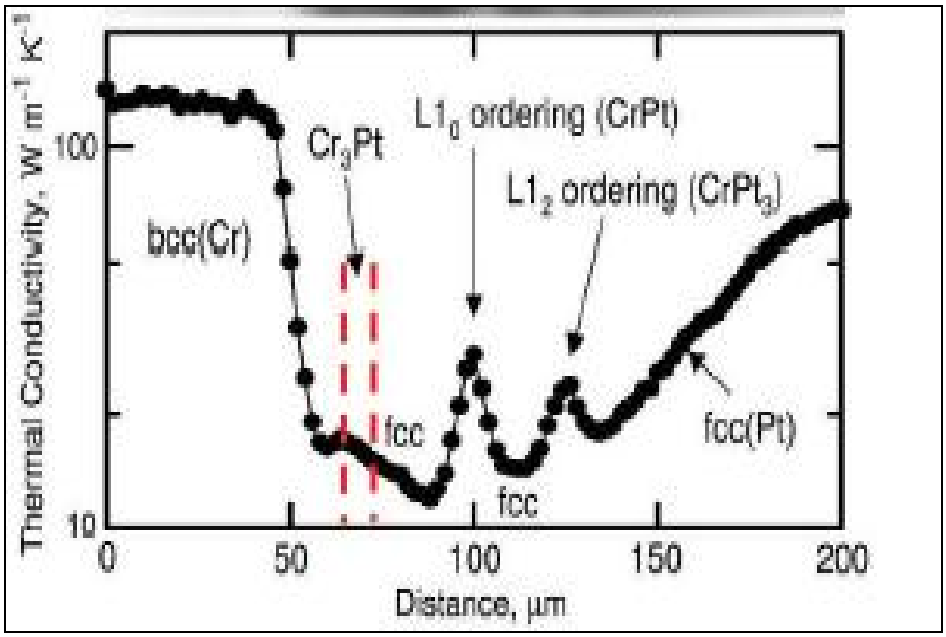

Figure 2.5. Thermal conductivity values along the dashed line in Figure 2.4, showing the increased thermal conductivity in regions where ordering occurs **[2005Zha].**

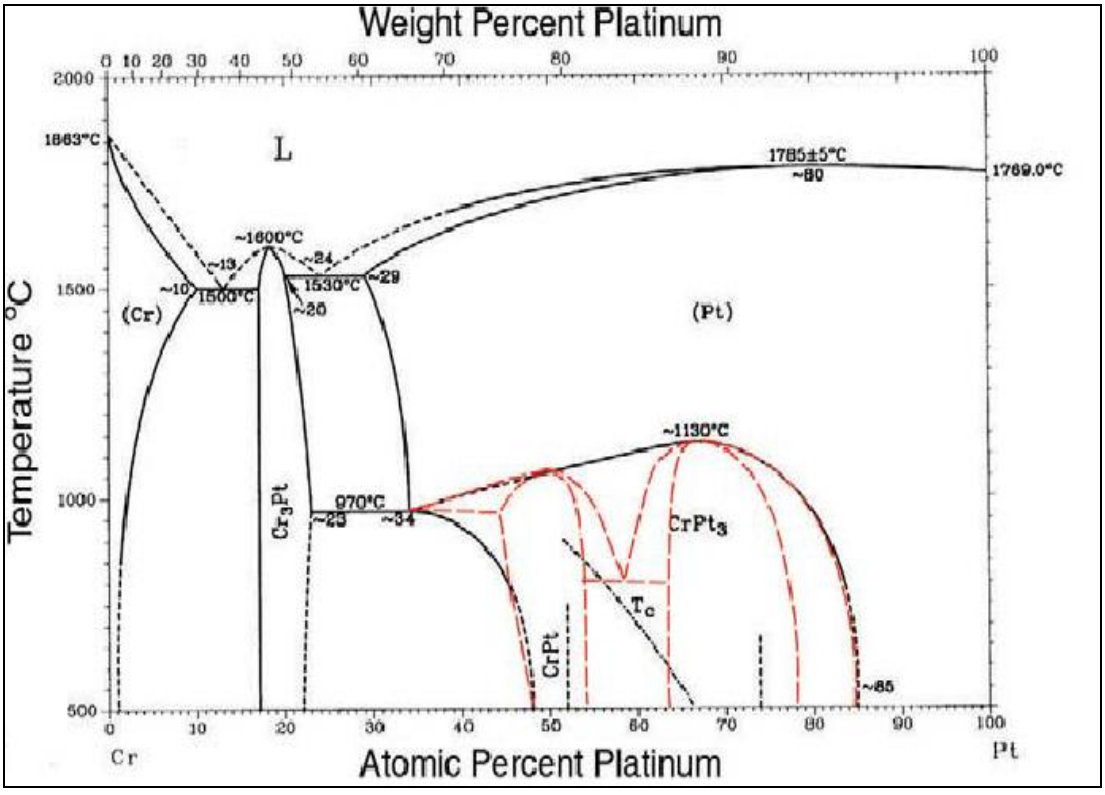

Figure 2.6. Proposed refinement (dashed lines) of the Cr–Pt phase diagram showing the two ordered phases in separate phase regions and the disordered region between them **[2005Zha].**

Table 2.3. Cr–Pt crystal structure data **[1990Mas].**

Phase	Composition (at. %Pt)	Pearson symbol	Space group	Strukturbericht designation	Prototype
(Cr)	0 to 10	*cI*2	$Im\bar{3}m$	A2	W
Cr_3Pt	17 to ~23	*cP*8	$Pm\bar{3}n$	A15	Cr_3Si
CrPt	~48 to ~52	*tP*2	*P*4/*mmm*	$L1_0$	AuCu
$CrPt_3$	~34 to 85	*cP*4	$Pm\bar{3}m$	$L1_2$	$AuCu_3$
(Pt)	~29 to 100	*cF*4	$Fm\bar{3}m$	A1	Cu

The Néel temperature, T_N, is the temperature at which an antiferromagnetic material becomes paramagnetic, which means that the thermal energy becomes large enough to destroy the macroscopic magnetic ordering within the material [2008Née]. Small additions of Pt increased the Néel temperature of pure Cr (38.5°C) rapidly to ~167°C (~0.6 at.% Pt) [1980But], ~310°C (~2 at.% Pt) [1968Kus] and ~187°C (~5 at.% Pt) [1979Ole]. In contrast to the disordered (Pt) solid solution, which is paramagnetic, the ordered $CrPt_3$ ($L1_2$) phase exhibits strong spontaneous magnetization [1977Got]. According to Pickart *et al.* [1963Pic], the $CrPt_3$ phase is ferrimagnetic and not ferromagnetic, as was concluded by other investigators [1990Ven]. The Curie temperature of the $CrPt_3$ phase increases with increasing Cr concentration from – 273°C (0K) at ~83 at.% Pt to ~900°C at ~52 at.% Pt [1968Kus]. The saturation magnetization has a maximum near the stoichiometric composition $CrPt_3$ [1977Got]. The spontaneous magnetization decreases with increasing Cr concentration and the ferromagnetic behaviour changes at ~52 at.% Pt [1935Fri, 1968Kus] to the antiferromagnetic behaviour of the Cr–Pt ($L1_0$) phase [1973Bes]. Table 2.4 shows the Cr-Pt lattice parameter data at room temperature [1990Ven].

Table 2.4. Cr–Pt lattice parameter data at room temperature **[1990Ven].**

Phase	Composition (at.% Pt)	Lattice parameter (nm)	Comment	Reference
(Cr)	0	0.2885	----	[1955Rau]
	~2	0.2891	----	[1955Rau]
Cr_3Pt	16	0.466	Two–phase region	[1935Fri]
	~17	0.4684	----	[1973Wat]
	~20	0.4712	Thin film	[1978Bag2]
	20.1	0.4711	----	[1955Rau]
	21	0.4706	----	[1968Reu]
	~23	0.4708	----	[1973Wat]

Table 2.4. Cr–Pt lattice parameter data at room temperature (continued).

Phase	**Composition (at.% Pt)**	**Lattice parameter (nm)**	**Comment**	**Reference**
Cr_3Pt Continued.	25	0.4706	Two–phase region	[1956Gre]
(Pt) or $CrPt_3$	29	0.384	Two–phase region, $L1_2$ superlattice.	[1935Fri]
	----	----		
	----	0.374	Two–phase region	[1940Geb]
	35	0.3800	$L1_2$ superlattice	[1973Wat]
	37	0.3775	$L1_2$ superlattice	[1956Gre]
	38	0.377	$L1_2$ superlattice	[1940Geb]
	39.5	0.3800	$L1_2$ superlattice	[1955Rau]
	40	0.385	$L1_2$ superlattice	[1935Fri]
		0.3796	$L1_2$ superlattice	[1973Bes]
	40.5	0.3804	$L1_2$ superlattice	[1973Wat]
	45	0.380	$L1_2$ superlattice	[1940Geb]
	50	0.3802	----	[1956Gre]
	---	0.3817	$L1_2$ superlattice	[1973Bes]
	50.1	0.3824	$L1_2$ superlattice	[1955Rau]
	50.2	0.3822	$L1_2$ superlattice	[1973Wat]
	51.5	0.389	$L1_2$ superlattice	[1935Fri]
CrPt	51.5	0.3822	Thin film, c = 0.3811 nm	[1978Bag2]
(Pt) or $CrPt_3$	52	0.382	$L1_2$ superlattice	[1940Geb]
	52.2	0.3831	$L1_2$ superlattice	[1955Rau]
	53	0.389	$L1_2$ superlattice	[1935Fri]
	55	0.3828	$L1_2$ superlattice	[1973Bes]
	56	0.383	$L1_2$ superlattice	[1940Geb]
	56.9	0.3833	$L1_2$ superlattice	[1973Bes]
	57	0.388	$L1_2$ superlattice	[1935Fri]
	58.6	0.3835	$L1_2$ superlattice	[1973Bes]
	60	0.388	----	[1935Fri]
	----	0.3842	$L1_2$ superlattice	[1973Bes]
	----	0.3845	$L1_2$ superlattice	[1977Got]
	60.4	0.3841	$L1_2$ superlattice	[1973Wat]
	65	0.3850	$L1_2$ superlattice	[1973Bes]
	----	0.3857	$L1_2$ superlattice	[1977Got]
	66	0.389	----	[1935Fri]
	70	0.386	----	[1940Geb]
	----	0.3873	$L1_2$ superlattice	[1973Bes]
	----	0.3866	$L1_2$ superlattice	[1977Got]
	70.4	0.392	$L1_2$ superlattice	[1935Fri]
	----	0.3866	$L1_2$ superlattice	[1973Wat]
	75	0.3874	$L1_2$ superlattice	[1962Bro]
	----	0.3871	$L1_2$ superlattice	[1973Bes]
	----	0.3875	$L1_2$ superlattice	[1977Got]
	76.7	0.3879	$L1_2$ superlattice	[1955Rau]
	77	0.388	----	[1940Geb]
	----	0.3862	$L1_2$ superlattice	[1973Bes]

Table 2.4. Cr–Pt lattice parameter data at room temperature (continued).

Phase	Composition (at.% Pt)	Lattice parameter (nm)	Comment	Reference
(Pt) or $CrPt_3$	~77	0.3877	Thin film,	[1978Bag2]
	----	----	$L1_2$ superlattice	
	77.5	0.3870	$L1_2$ superlattice	[1973Bes]
	78	0.393	----	[1935Fri]
	78	0.3885	$L1_2$ superlattice	[1977Got]
	80	0.3879	$L1_2$ superlattice	[1962Bro]
	----	0.3872	$L1_2$ superlattice	[1973Bes]
	----	0.3884	$L1_2$ superlattice	[1973Wat]
	81.7	0.3875	----	[1973Bes]
	82	0.3892	----	[1977Got]
	83.1	0.3875	----	[1973Bes]
	85.9	0.3881	----	[1973Bes]
	86	0.3882	----	[1962Bro]
	86.5	0.3894	----	[1955Rau]
	90	0.3895	----	[1962Bro]
	90.2	0.3902	----	[1973Wat]
	100	0.3919	----	[1955Rau]
	----	0.3918	----	[1962Bro]

2.2.2 Binary Cr–Nb phase diagram

The Cr–Nb binary phase diagram given in Massalski [1990Mas] is drawn from Venkatraman *et al.* [1990Ven] who assessed the earlier work on the Cr–Nb system. The assessed phase diagram is based primarily on the work of Goldschmidt *et al.* [1961Gol] and Rudy [1969Rud]. The Cr–Nb system is characterized by a congruently melting intermediate phase, Cr_2Nb, which forms a eutectic with each of the terminal solid solutions (Cr) and (Nb). There is a higher temperature (HT) and lower temperature (LT) Cr_2Nb between ~ 30 and 39 at.% Nb. Figure 2.7 shows the Cr-Nb phase diagram revised by Thoma *et al.* [1992Tho] by means of XRD and chemical analyses of equilibrated samples. Invariant reaction temperatures and solid solution ranges have been determined more quantitatively. The (Nb) liquidus was drawn with a steep slope (>10 000 ^{o}C/100 at.%), which is very unlikely [1991Oka]. Table 2.5 shows the reactions of the Cr-Nb system [1990Mas], whereas Table 2.6 shows the eutectic compositions and temperatures in the Cr-Nb binary system [1967Sul].

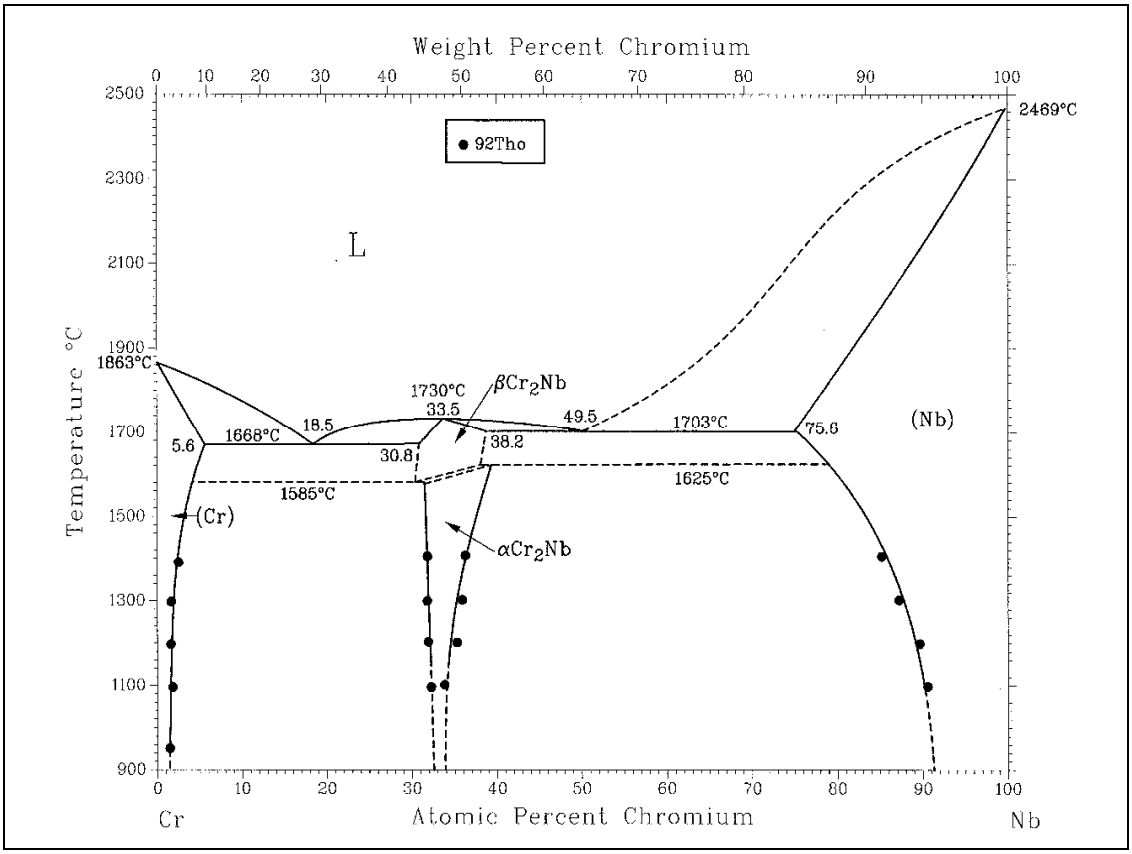

Figure 2.7. Binary Cr–Nb equilibrium phase diagram **[1992Tho, 1993Oka].**

Table 2.5. Reactions of the Cr–Nb system **[1990Mas].**

Reaction	**Compositions of the respective phases (at.% Nb)**	**Temperature (^{o}C)**	**Reaction type**
L ↔ Cr	0	1863	Melting
L ↔ Cr_2Nb (HT)	~35	~1625	Congruent
L ↔ Cr_2Nb (LT)	~35	~1400	Congruent
L ↔ (Cr) + Cr_2Nb	~12 ~6 ~30	1620	Eutectic
L ↔ Cr_2Nb + (Nb)	~50 ~39 ~85	1650	Eutectic
L ↔ Nb	100	2469	Melting

Table 2.6. Eutectic compositions and temperatures in Cr–Nb binary system **[1967Sul].**

Author	**Melting point $NbCr_2$, (^oC)**	**$NbCr_2$+(Nb) eutectic**		**$NbCr_2$+(Cr) eutectic**	
		(^oC)	**(at.% Cr)**	**(^oC)**	**(at.% Cr)**
[1956Ely]	----	1660	39.0	1600	78 – 79
[1958Ere]	----	1710	48.9	1660	79.9
[1959Sve]	----	----	----	1625	80.7
[1960Mis]	1740	1717	48.4	1660	81.4
[1961Gol]	~1750	1600	53.0	1610	88.0
[1961Pan]	1720±5	1660	49.0	1640	80.7

The Cr-Nb crystal structure data are presented in Table 2.7 [1990Mas]. The existence of a Laves–type phase that occurs at the stoichiometric composition Cr_2Nb has been firmly established which has the cubic $MgCu_2$–type structure at low temperatures. However, a modified structure at high temperatures has the hexagonal $MgZn_2$–type structure. It transforms at ~1585 to ~1625^{o}C [1961Pan] to the low–temperature cubic form. Since the exact transformation temperatures are not known, Cr_2Nb (HT) is indicated in the present diagram by a dashed line. Elliot [1954Ell] confirmed the $MgCu_2$–type structure for $NbCr_2$ (a = 698.5pm) and determined the incipient melting temperature (probably the βCr_2Nb + (Nb) eutectic) of the alloy as ~1710^{o}C.

Table 2.7. Cr–Nb crystal structure data **[1990Mas].**

Phase	**Composition (at.% Nb)**	**Pearson symbol**	**Space group**	**Strukturbericht designation**	**Prototype**
(Cr)	0 to 6	*cI*2	$Im\bar{3}m$	A2	W
Cr_2Nb (HT)	30 to 39	*LP*12	$P6_2/mmc$	C14	$MgZn_2$
Cr_2Nb (LT)	30 to 39	*cF*24	$Fd\bar{3}m$	C15	Cu_2Mg
(Nb)	85 to 100	*cI*2	$Im\bar{3}m$	A2	W

2.2.3 Binary Nb–Pt phase diagram

The Nb–Pt phase diagram (Figure 2.8) given in Massalski [1990Mas] is redrawn from Waterstrat *et al.* [1985Wat]. Six intermediate phases have been discovered in the Pt–Nb system [1970Shu]. The $NbPt_3$ compound is formed at ~2040°C by congruent solidification. The compound $NbPt_3$ exists in two structures: $\alpha NbPt_3$ and $\beta NbPt_3$ by ordering. The compounds Nb_3Pt and Nb_2Pt (which is Nb_5Pt_2 according to Shunk [1970Shu]) result from peritectic reactions at temperatures of ~2040±10°C and ~1800±10°C. Both compounds have homogeneity ranges over 3 at.%. The compound Nb_2Pt (Nb_5Pt_2) σ–phase is a type β–U crystalline structure, and the compound Nb_3Pt is of Cr_3Si type. The original diagram showed a phase called σ (Pt_2Nb_3) with its melting point just touching the liquidus curve. This phase is actually $PtNb_2$. The PtNb (B19) was formed at ~ 50 at.% Nb, $PtNb_2$ ($MoPt_2$) at ~ 67 at.% Nb, and $PtNb_3$ (A15) between ~ 74 and 78 at.% Nb. An increase in niobium content gives an increase in the lattice parameter of the Nb_3Pt compound from 514.7 to 516.6pm [1978Sav]. Reactions of the assessed Nb-Pt binary phase diagram are shown in Table 2.8 [1995Tri].

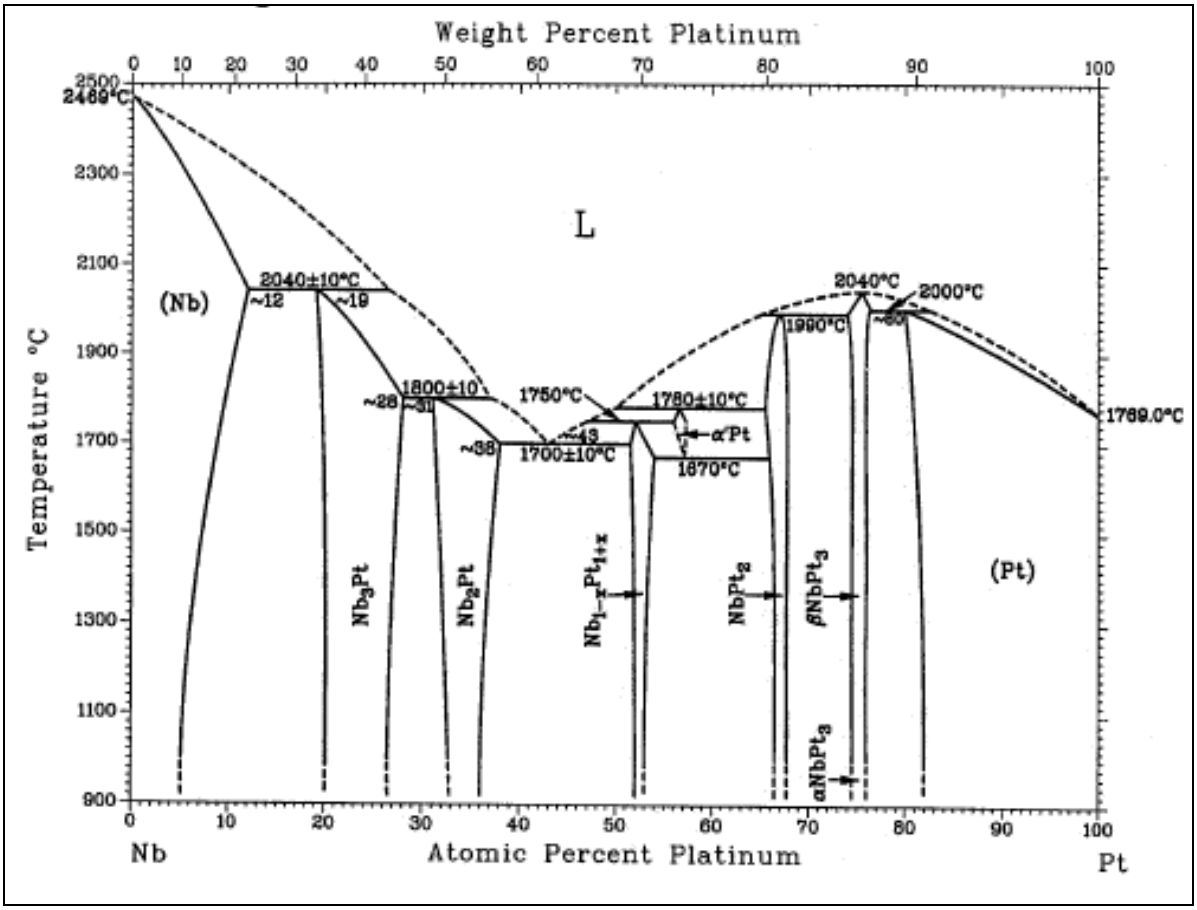

Figure 2.8. Binary Nb–Pt equilibrium phase diagram **[1990Mas].**

Table 2.8. Reactions of the assessed Nb–Pt phase diagram **[1995Tri].**

Reaction	**Compositions of the respective phases (at.% Pt)**			**Temperature (^{o}C)**	**Reaction type**
L ↔ Nb	0			2469	Melting
L + (Nb) ↔ Nb_3Pt	~26	~12	~19	2040	Peritectic
L + Nb_3Pt ↔ Nb_2Pt (σ)	36.4	28	31	1800	Peritectic
L ↔ Nb_2Pt (σ) + $Nb_{1-X}Pt_{1+X}$	43	51.2	38	1700	Eutectic
L + α'Pt ↔ $Nb_{1-X}Pt_{1+X}$	47	57	52	1750	Peritectic
L + $NbPt_2$ ↔ α'Pt	49	65	57	1780	Peritectic
α'Pt ↔ $Nb_{1-X}Pt_{1+X}$ + $NbPt_2$	57.5	54	66	1670	Eutectoid
L + $NbPt_3$ ↔ $NbPt_2$	66	74	67	1990	Peritectic
L ↔ $NbPt_3$	75			2040	Congruent
L + $NbPt_3$ ↔ (Pt)	82.5	76	80	2000	Peritectic
L ↔ Pt	100			1769	Melting

The crystal structure data in Massalski [1990Mas] are from Wallbamm [1943Wal] (Nb_3Pt); Matthias *et al.* [1961Mat] (Nb_2Pt); and Giessen *et al.* [1964Gie] ($Nb_{1-X}Pt_{1+X}$, $NbPt_2$, α$NbPt_3$). Waterstrat *et al.* [1985Wat] could not determine the relative stability of β and α$NbPt_3$. According to Maldonado *et al.* [1964Mal], α$NbPt_3$ is stable below 1000^{o}C. The Nb-Pt crystal structure data are shown in Table 2.9 [1990Mas], and Table 2.10 shows Nb-Pt lattice parameter data [1995Tri].

Table 2.9. Nb–Pt crystal structure data **[1990Mas].**

Phase	**Composition (at.% Pt)**	**Pearson symbol**	**Space group**	**Structurbericht designation**	**Prototype**
(Nb)	0 to 12	*cI*2	$Im\bar{3}m$	A2	W
Nb_3Pt	19 to 28	*cP*8	$Pm\bar{3}n$	A15	Cr_3Si
Nb_2Pt	31 to 38	*tP*30	$P4_2/mnm$	$D8_b$	σCrFe
$Nb_{1-X}Pt_{1+X}$	51 to 53	*oP*4	*Pmm*a	B19	AuCd
α'Pt	~57	- - --	- - --	- - --	- - --
$NbPt_2$	~67	*oI*6	*Immm*	- - --	- - --
β$NbPt_3$	~76	*mP*48	$P2_1/m$	- - --	- - --
α$NbPt_3$	~76	*oP*8	*Pmmm*	DOα	βCu_3Ti
(Pt)	80 to 100	*cF*4	$Fm\bar{3}m$	A1	Cu

Table 2.10. Nb–Pt lattice parameter data **[1995Tri].**

Phase	**Composition, (at.% Pt)**	**Lattice Parameter (nm)** a	b	c	**References**
Nb	0	0.33004	----	----	[1990Mas]
	5	0.3277	----	----	[1985Wat]
	10	0.3260	----	----	[1985Wat]
Nb_3Pt	----	0.511	----	----	[1956Gre]
	----	0.5153	----	----	[1955Gel]
	20	0.5182	----	----	[1985Wat]
	25	0.5152	----	----	[1968Reu]
	28	0.5139	----	----	[1985Wat]
	19 to 28	0.5147 to	----	----	[1961Kim]
	----	0.5166	----	----	
σ(Nb_2Pt)	32	0.9940	----	0.5145	[1983Wat,1985Wat]
	38	0.9902	----	0.5132	[1983Wat,1985Wat]
	----	0.991	----	0.512	[1961Kim]
($Nb_{1-X}Pt_{1+X}$)?	50	0.2780	0.4983	0.4611	[1983Wat,1964Gie]
	50	0.278	0.498	0.462	[1965Dwi]
α$NbPt_3$	75	0.5534	0.4873	0.4564	[1964Gie]
βNbPt3	75	0.5537	0.4870	0.2733 ($\alpha=90^o32'$)	[1964Gie]
(Pt)	82	0.3940	----	----	[1985Wat]
	85	0.3935	----	----	[1985Wat]
	90	0.3927	----	----	[1985Wat]
	95	0.3924	----	----	[1985Wat]
Pt	100	0.39236	----	----	[1990Mas]

Nb–Cr–Pt

The Nb–Cr–Pt ternary phase diagram was not published in the available literature, and no ternary data were found of this system.

CHAPTER 3:

EXPERIMENTAL PROCEDURE

3.1 Sample manufacture

An initial set of six alloy compositions was selected to be as far away from each other and the binary systems. After they were characterised, subsequent samples were chosen to fill in the gaps in the information. The samples were made by mixing weighed elements of at least 99.95% purity in the required proportions, and ~2g samples were produced by arc–melting in an argon atmosphere at Mintek, using Ti as an oxygen–getter in batches of six. The samples were turned and remelted several times to improve homogeneity. Table 3.1 shows the selected compositions of the samples, and these selected compositions are plotted in Figure 3.1.

Table 3.1. Selected compositions of the ternary Nb-Cr-Pt samples.

Sample name	**Alloy**	**Intended composition (at.%)**		
		Niobium	**Chromium**	**Platinum**
1	$Nb_{15}:Cr_{15}:Pt_{70}$	15	15	70
2	$Nb_{15}:Cr_{40}:Pt_{45}$	15	40	45
3	$Nb_{40}:Cr_{15}:Pt_{45}$	40	15	45
4	$Nb_{15}:Cr_{70}:Pt_{15}$	15	70	15
5	$Nb_{40}:Cr_{45}:Pt_{15}$	40	45	15
6	$Nb_{70}:Cr_{15}:Pt_{15}$	70	15	15
7	$Nb_{30}:Cr_{10}:Pt_{60}$	30	10	60
8	$Nb_{60}:Cr_{10}:Pt_{30}$	60	10	30
9	$Nb_{24}:Cr_{23}:Pt_{53}$	24	23	53
10	$Nb_{50}:Cr_{30}:Pt_{20}$	50	30	20
11	$Nb_{35}:Cr_{30}:Pt_{35}$	35	30	35
12	$Nb_{20}:Cr_{50}:Pt_{30}$	20	50	30
13	$Nb_{30}:Cr_{20}:Pt_{50}$	30	20	50
14	$Nb_{25}:Cr_{45}:Pt_{30}$	25	45	30
15	$Nb_{20}:Cr_{60}:Pt_{20}$	20	60	20
16	$Nb_{35}:Cr_{40}:Pt_{25}$	35	40	25
17	$Nb_{40}:Cr_{25}:Pt_{35}$	40	25	35
18	$Nb_{57}:Cr_{18}:Pt_{25}$	57	18	25

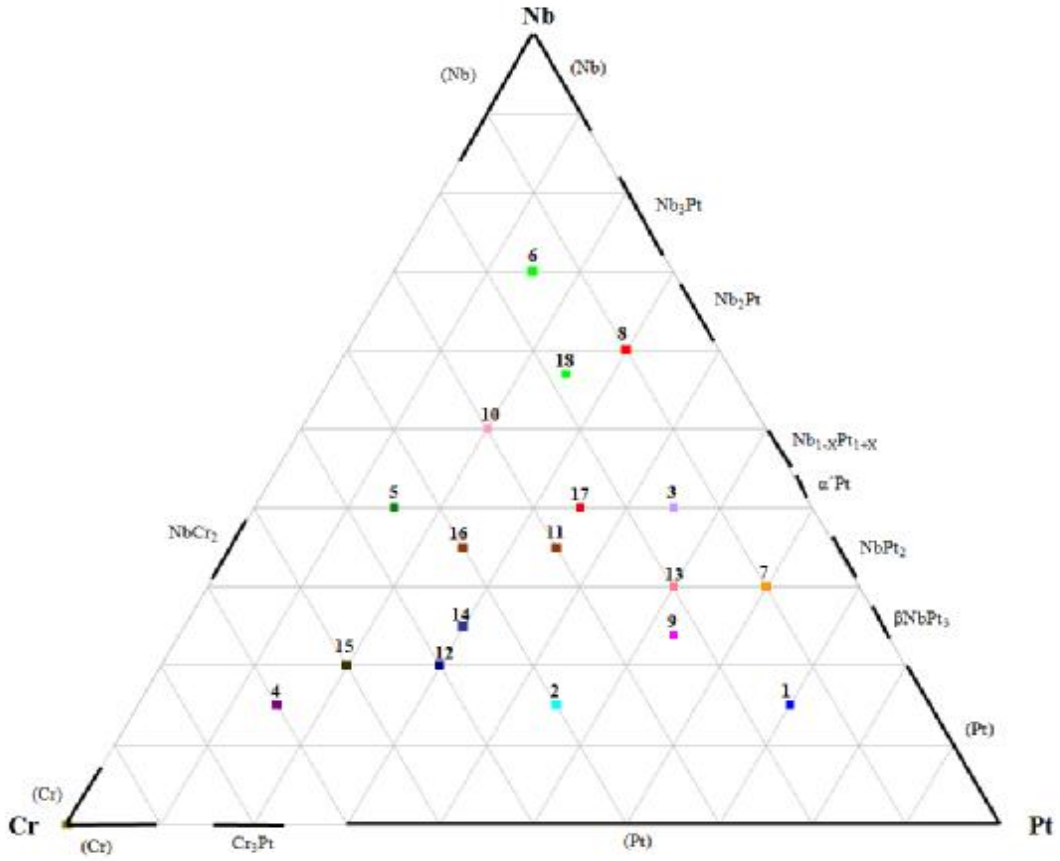

Figure 3.1. Selected compositions of the ternary Nb-Cr-Pt samples.

3.2 Metallography

The samples were sectioned in half and prepared for metallography in the as–cast condition. One half of each sample was mounted in a conductive resin and ground to 1200 grit on SiC paper, then polished on 6µm, 3µm and 1µm diamond cloths. The samples were then polished using an oxide polishing (OP–S) system, by which polishing is achieved through a combination of chemical treatment and gentle abrasive action.

3.3 Sample characterization

3.3.1 Scanning electron microscopy (SEM)

The microstructures were examined using JEOL JSM–840 and LEO-1525 scanning electron microscopes with energy-dispersive X-ray spectroscopy (SEM-EDX). All imaging was conducted in the backscattered electron (BSE) mode for phase contrast. BSE mode is suitable for phase differentiation because the intensity of the backscattered electrons is a function of the average atomic number of the phase, so different phases have a different amount of backscattered electrons collected which shows as different contrasts. The higher the average atomic number of the phase, the more electrons are collected and the brighter the phase appears. The average atomic number of the binary phases is shown in Table 3.2. During EDX analysis, at least five spot analyses were taken from each phase, but where there was a small size phase area, the best analysis was taken, taking into account the other measurements and the size of the area.

Table 3.2. Average atomic numbers for binary phases in the Nb–Cr–Pt ternary.

Phase	**Average atomic number**	**Contrast**
(Cr)	24.00	Dark ↕ Light
$NbCr_2$	29.67	
Cr_3Pt	37.50	
(Nb)	41.00	
α′Pt	45.24	
Nb_3Pt	50.25	
CrPt	51.00	
Nb_2Pt	53.33	
$Nb_{1-X}\ Pt_{1+X}$	60.61	
$CrPt_3$	64.50	
$NbPt_2$	65.67	
$NbPt_3$	68.75	
(Pt)	78.00	

In the text, phases are referred to by their contrast i.e. a phase with a light contrast is called a light phase.

3.3.2 X–ray diffraction (XRD)

X-ray diffraction (XRD) is a suitable technique for phase analyses incorporating lattice parameter and lattice type determinations on crystalline materials. It can also be used to determine and evaluate the effect of a solute on the lattice parameter of a phase.

XRD was undertaken on a Phillips (PW1830) X–ray diffractometer. A Cu–Kα source was used and the samples were rotated through a 2θ angular range from 10^o to 100^o. A step scan was used, with 0.02^o step size and 1.0s scan step time. The generator settings were 40KV and 20mA. Phases were identified by comparison with the ICDD database [2003Xpe] except for α´Pt, ~$Nb_{1-X}Pt_{1+X}$ and ~Nb_2Pt where there were no data.

XRD is based on Bragg diffraction. When a crystalline material is irradiated by a monochromatic source of X–rays, reflections will occur from the various lattice planes in the crystal. Each reflecting plane will diffract a portion of the X–ray beam as governed by the relationship:

$$n\lambda = 2d\sin\theta \qquad 3.1$$

where:

λ = Wavelength of the incident radiation
d = Interplanar spacing for plane (hkl)
θ = Incident angle of radiation with the plane
n = A small integer.

The reflections are characteristic for a specific crystal structure and give the d–values for a phase, from which the lattice parameter can be calculated through the relationship (for a cubic phase):

$$d^2_{hkl} = \frac{a^2}{\left(h^2 + k^2 + l^2\right)} \qquad 3.2$$

where:

d = Interplanar spacing for plane (hkl)
a = Lattice parameter
h, k and l = Miller indices, referring to the plane from which reflection originates.
The positions of the atoms in the unit cell are then determined by the space group.

3.3.3 Differential thermal analysis (DTA)

It was planned to do differential thermal analysis (DTA) on the alloys at Mintek in order to determine the reaction temperatures and enthalpies of formation for the different phases, but the equipment was not ready.

3.4 Mechanical testing

3.4.1 Hardness tests

After characterisation was completed, Vickers macrohardness measurements of the alloys were conducted on all the samples using a Vickers Ltd. Vicker's hardness indenting machine. The samples were all thermally mounted in Bakelite and had been surface ground and polished. A 5 kg load was used, with at least five measurements taken on random areas on the surface of the samples to obtain an average hardness value of the alloys. Care was taken to ensure that each individual indentation was more than two diameters away another indentation to avoid work hardening effects. In all cases, the load was applied for ~15 seconds.

The diamond-pyramid hardness number (DPH), or Vickers hardness number (VHN or VPH) can be determined according to the following equations [1988Die]:

$$DPH = \frac{2P\sin\left(\frac{\theta}{2}\right)}{(L^2)} \qquad 3.3$$

$$DPH = \frac{1.854P}{(L^2)} \qquad 3.4$$

where:

P = Applied load (Kg)
L = Average length of diagonals (mm)
θ = Angle between opposite faces of diamond (136^o).

This is equivalent to measuring the average diagonal and obtaining values from the correct tables.

3.4.2 Toughness

Macrohardness indentations were photographed using a Nikon FX-35A digital camera connected to a Nikon optical microscope, with Motic Images Plus 2.0 ML software. The alloys were categorized by slip modes, with planar slip having reasonable toughness or plastic deformation and wavy slip having high toughness. The alloys which had cracks were categorized under alloys with cracking.

3.4.2 Palmqvist fracture toughness (K_{IC})

The Palmqvist fracture toughness values were derived using the Shetty's equation [1985She, 1990Spi].

$$K_{IC} = 0.0889\sqrt{\frac{HVP}{\sum a}} \qquad 3.5$$

where:

K_{IC} = Fracture toughness (MPa√m)
HV = Hardness of the sample (N/m^2)
P = Applied load (N)
$\sum a$ = Crack length at each corner (m)
$P/\sum a$ = Applied load over sum of crack length (N/m).

CHAPTER 4:

RESULTS

4.1 Microstructural characterization of as–cast Nb–Cr–Pt alloys

4.1.1 Nominal Nb_{15}:Cr_{15}:Pt_{70}, Sample 1

The nominal Nb_{15}:Cr_{15}:Pt_{70} alloy possessed a mainly single phase microstructure of (Pt) grains of different orientations, as shown in Figure 4.1. Table 4.1 gives the energy dispersive spectroscope (EDX) analyses. These EDX data were plotted in Figure 4.2. The existence of a single (Pt) phase was confirmed by X-ray diffraction (XRD), as shown in Figure 4.4. The XRD spectrum shown in Figures 4.3 to 4.4 is reasonable in terms of the signal: background ratio. Most of the peaks, especially at high angles, were broad, signifying coring. There were good matches for the (Pt) phase, with the ICDD lines, with some very slight peak shifts to the left. There were also some much smaller unidentified peaks, but these did not match with CrPt, nor did the larger peaks.

The structure formed by the solidification reaction:

$$L \rightarrow (Pt)$$

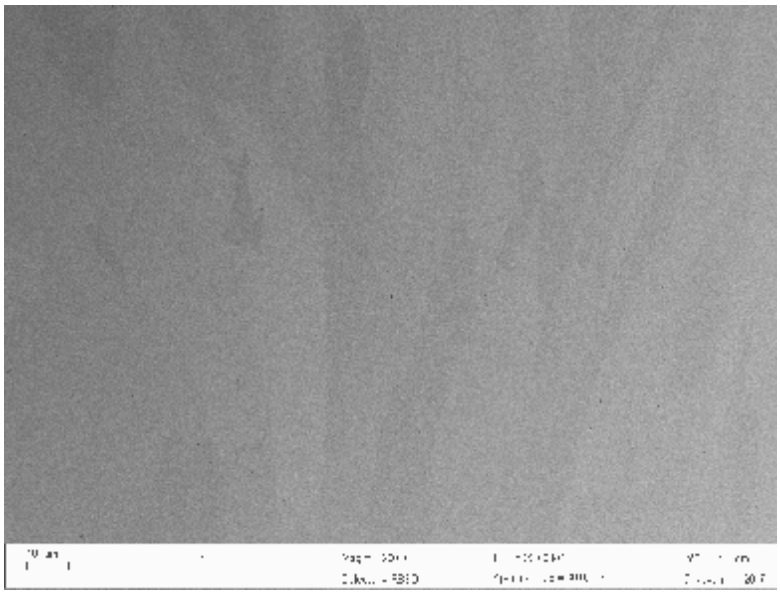

Figure 4.1. SEM-BSE image of the nominal Nb_{15}:Cr_{15}:Pt_{70} alloy in the as–cast condition, showing (Pt) grains of different orientations.

Table 4.1. EDX phase analyses for nominal $Nb_{15}:Cr_{15}:Pt_{70}$ (at.%) in the as–cast condition.

Phase contrast	Nb	Cr	Pt	Phase
Overall	14.6±2.1	16.0±1.0	69.5±1.1	(Pt)

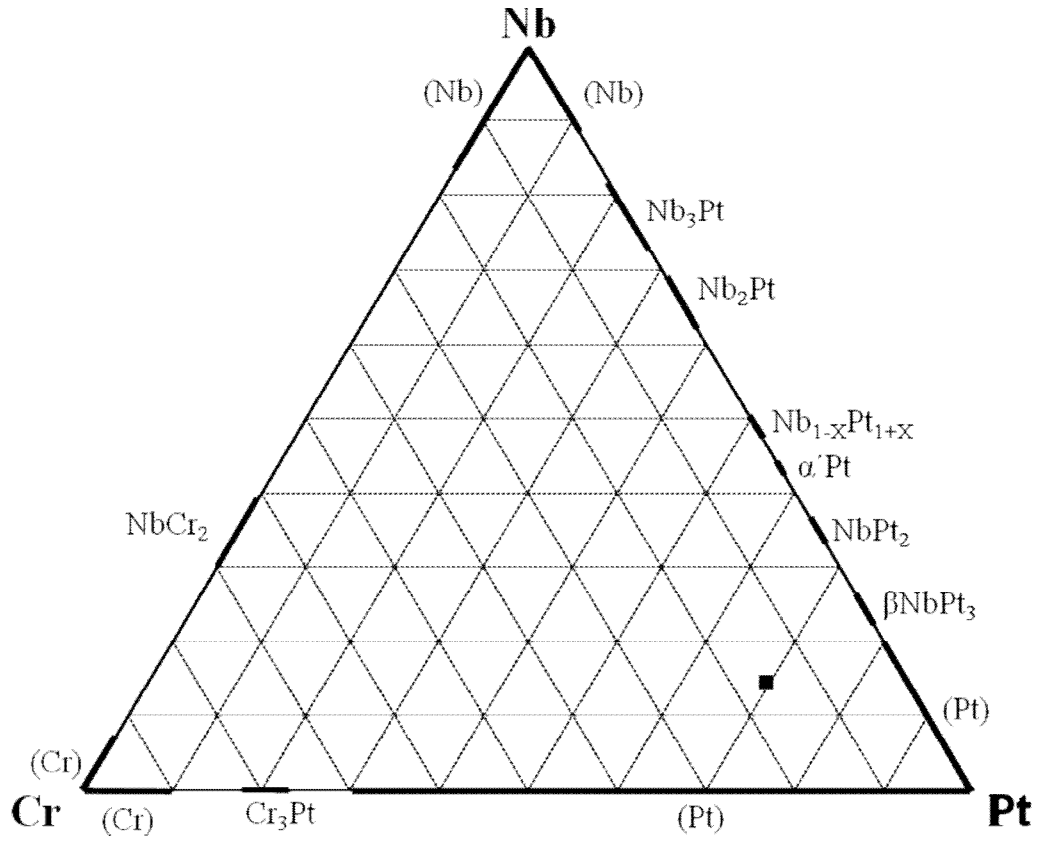

Figure 4.2. EDX phase compositions for the nominal $Nb_{15}:Cr_{15}:Pt_{70}$ (at.%) alloy in the as–cast condition; ■ overall composition.

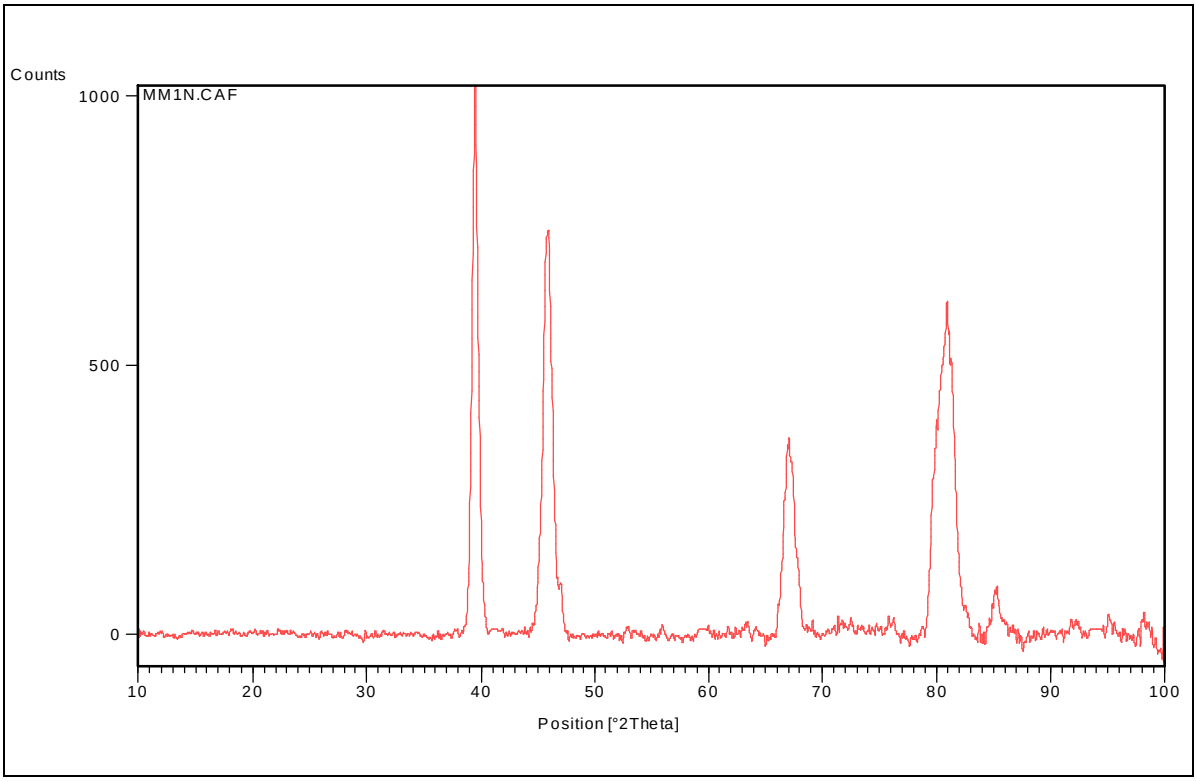

Figure 4.3. Raw XRD spectrum of nominal Nb_{15}:Cr_{15}:Pt_{70} in the as-cast condition.

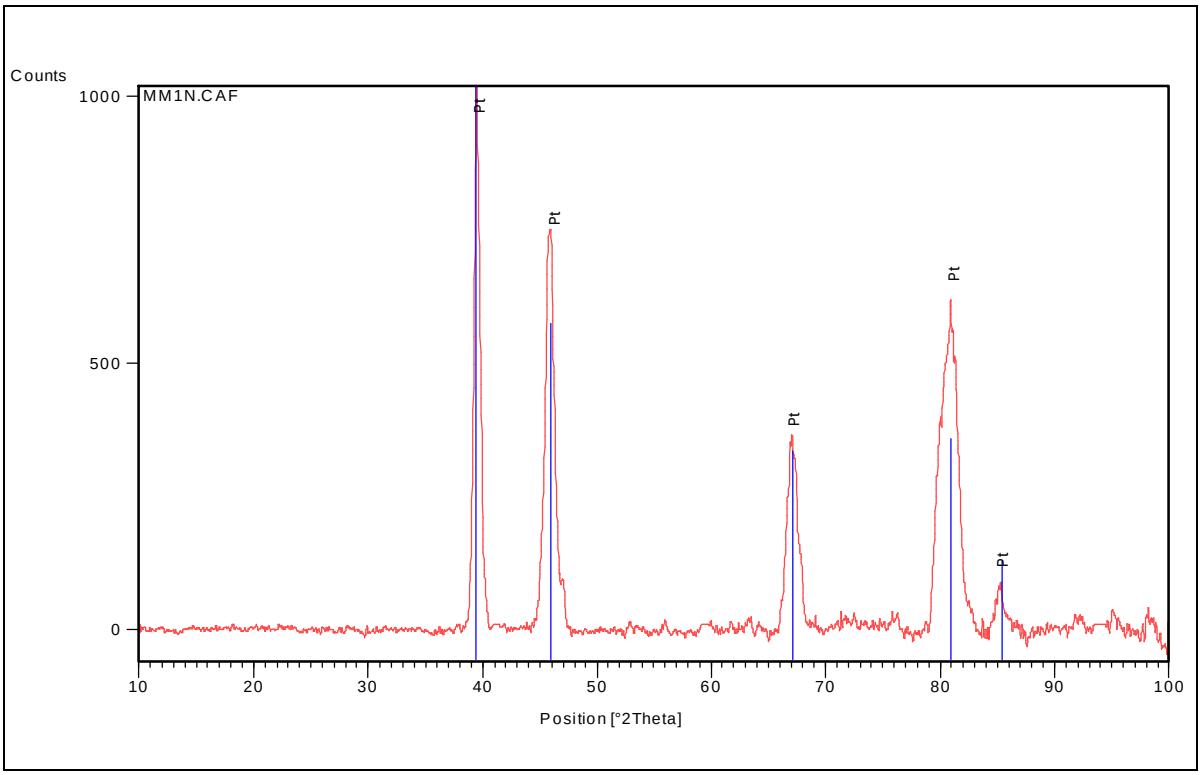

Figure 4.4. XRD spectrum of nominal Nb_{15}:Cr_{15}:Pt_{70} in the as-cast condition, showing blue Pt peaks.

4.1.2 Nominal Nb_{15}:Cr_{40}:Pt_{45}, Sample 2

The nominal Nb_{15}:Cr_{40}:Pt_{45} alloy comprised cored (Pt) dendrites, as shown in Figures 4.5 a and b. Table 4.2 gives the EDX analyses, which are plotted in Figure 4.6, showing the overall composition lying on the tie-line, which is a good indication that the alloy was in equilibrium. The XRD spectrum was quite good, with a high signal: background ratio (Figures 4.7-4.8 a-d). The presence of (Pt) was confirmed, with some slight peak shifts to the right. All the peaks were broad, signifying coring. There were some minor unidentified peaks. As a check, the spectrum was compared against the peaks of the CrPt, $CrPt_3$ and Cr_3Pt phases. The first two phases would not have been seen metallographically, and would only be discernable on ordering. The last phase was not seen by either SEM or XRD. Neither of the ordered phases were seen.

The solidification sequence deduced from the microstructure is as follows:

$$L \rightarrow \text{Cored (Pt)}$$

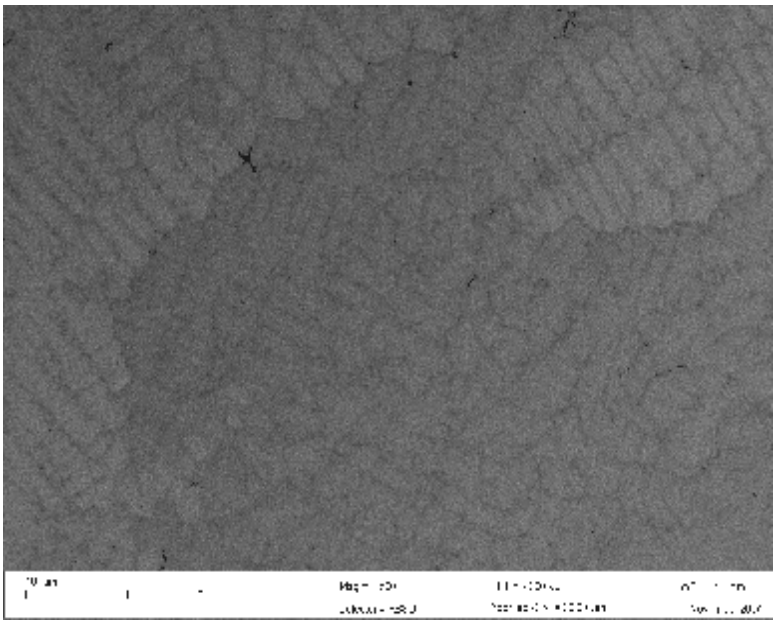

(a)

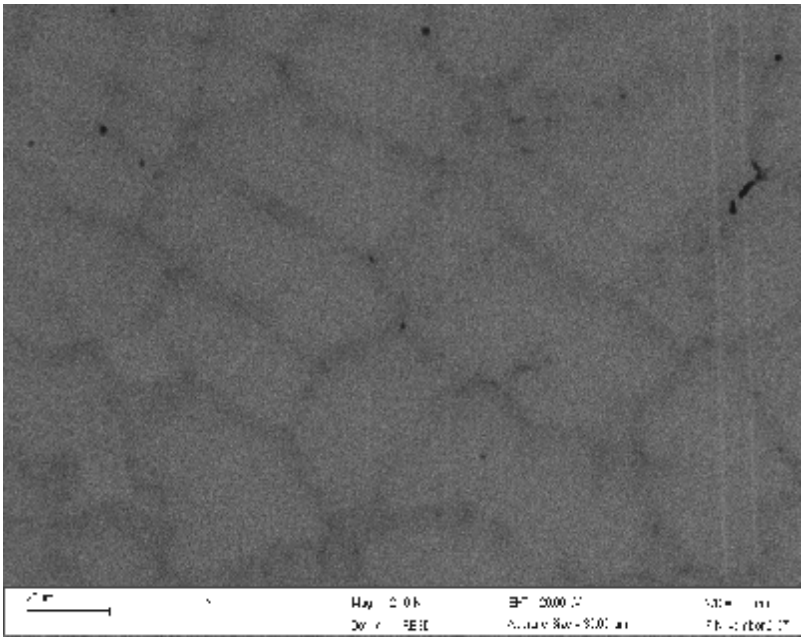

(b)

Figure 4.5 a-b. SEM-BSE images of the nominal Nb_{15}:Cr_{40}:Pt_{45} alloy in the as–cast condition, showing cored (Pt) dendrites.

Table 4.2. EDX phase analyses for the nominal Nb_{15}:Cr_{40}:Pt_{45} (at.%) alloy in the as–cast condition.

Phase contrast	**Nb**	**Cr**	**Pt**	**Phase**
Overall	15.0±0.0	40.2±0.1	44.8±0.1	-
Light (dendrites)	15.5±0.5	36.7±0.7	47.7±0.4	Cored (Pt)
Dark (interdendritic)	14.7±0.4	43.0±1.7	42.3±1.5	Cored (Pt)

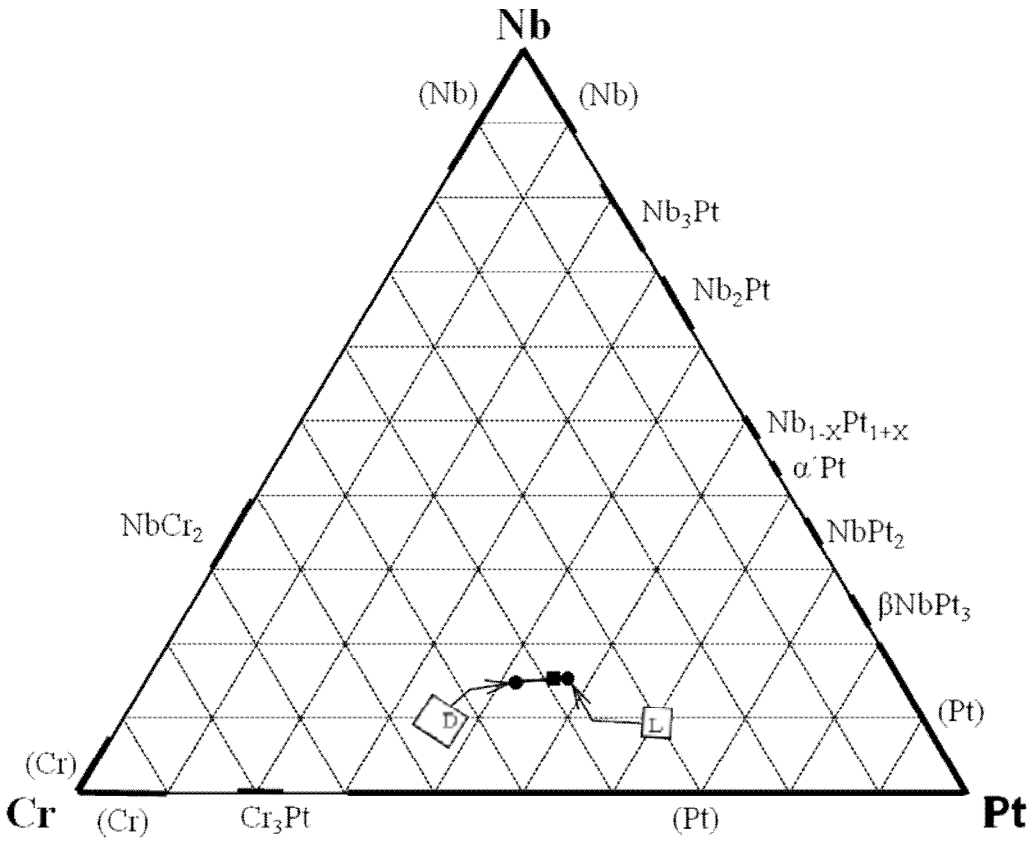

Figure 4.6. EDX phase compositions for the nominal $Nb_{15}:Cr_{40}:Pt_{45}$ (at.%) alloy in the as–cast condition: (L) light contrast; (D) dark contrast phase; ■ overall composition; ● phase composition.

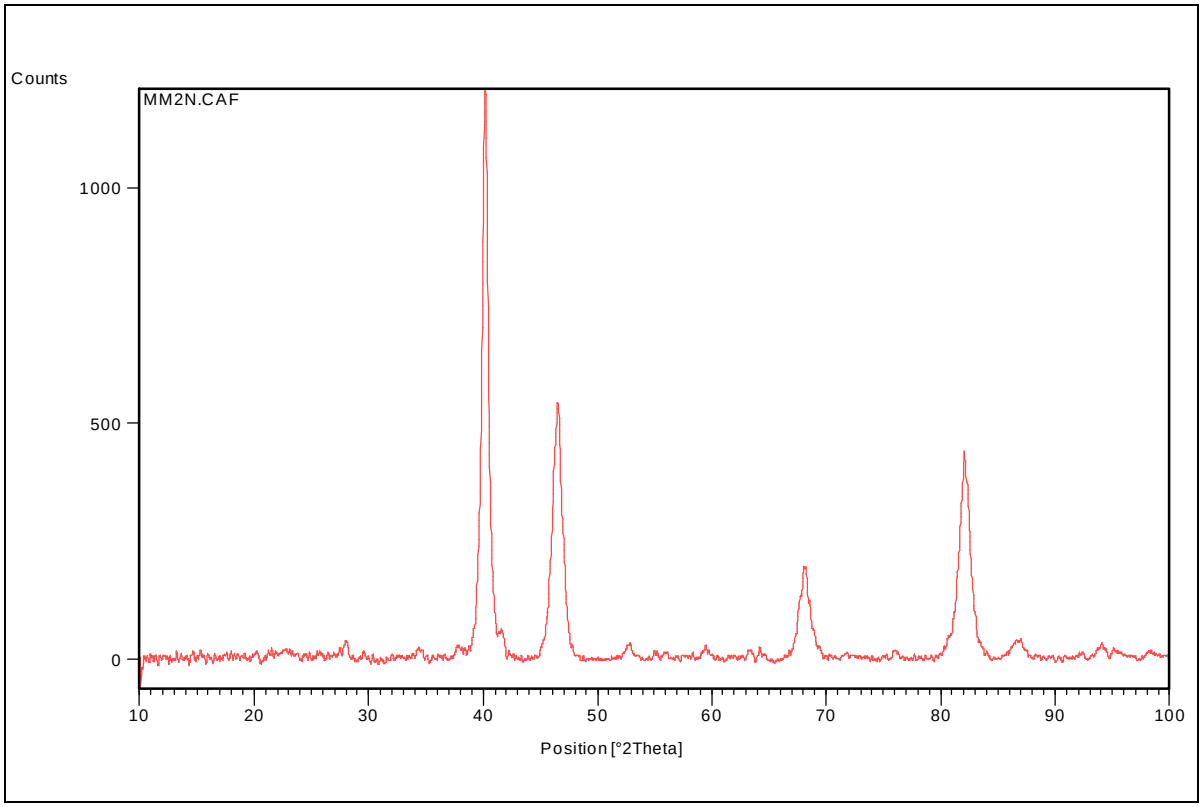

Figure 4.7. Raw XRD spectrum of nominal Nb_{15}:Cr_{40}:Pt_{45} in the as-cast condition.

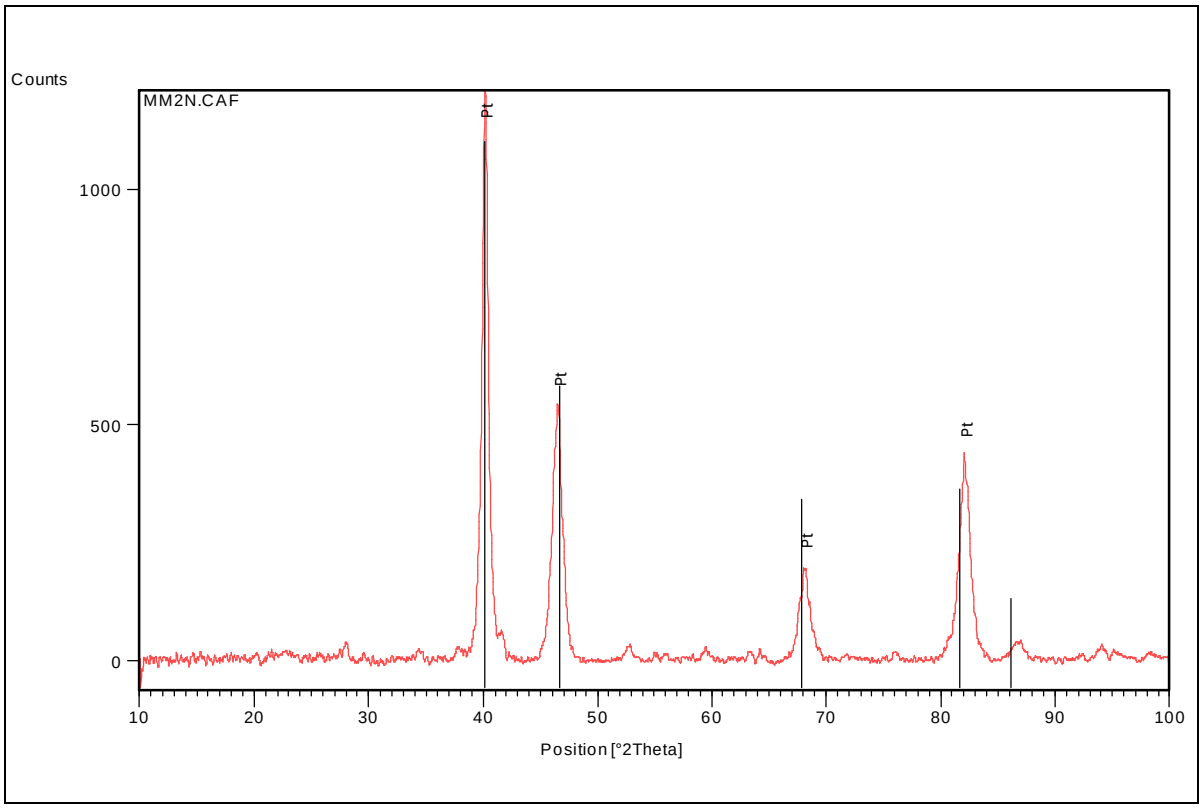

Figure 4.8 a. XRD spectrum of nominal Nb_{15}:Cr_{40}:Pt_{45} in the as-cast condition, showing black Pt peaks.

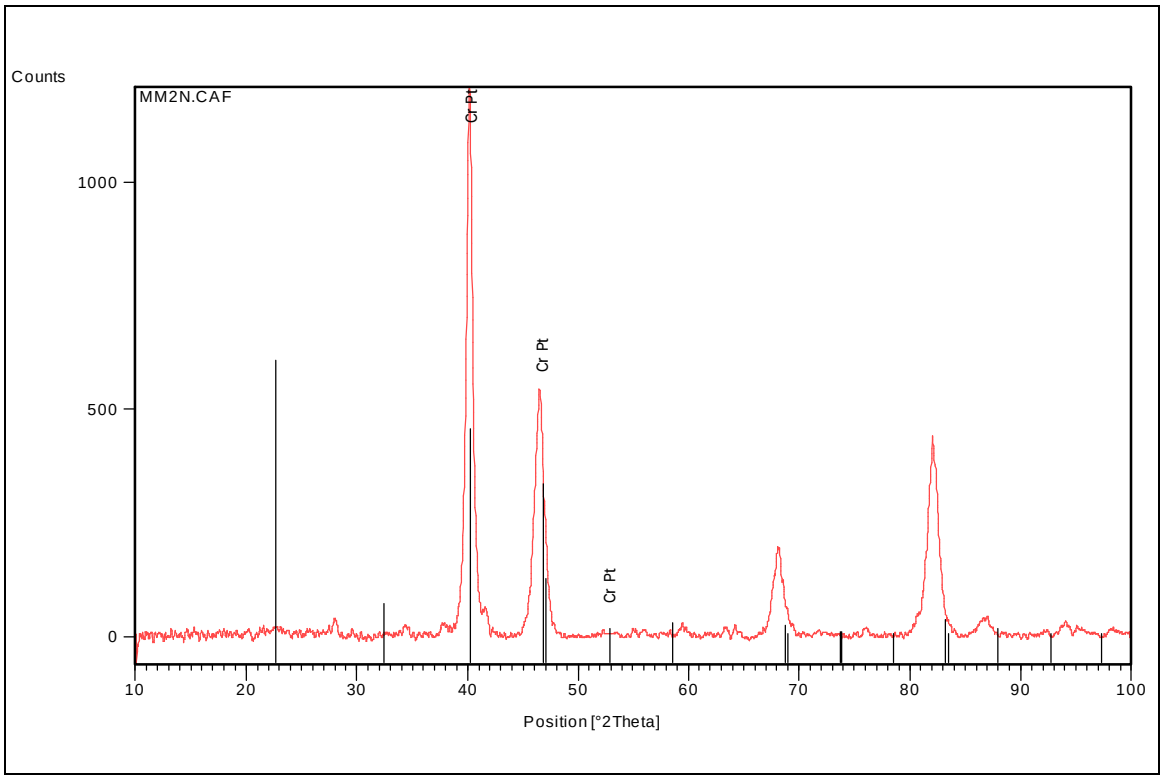

Figure 4.8 b. XRD spectrum of nominal Nb_{15}:Cr_{40}:Pt_{45} in the as-cast condition, showing black CrPt peaks.

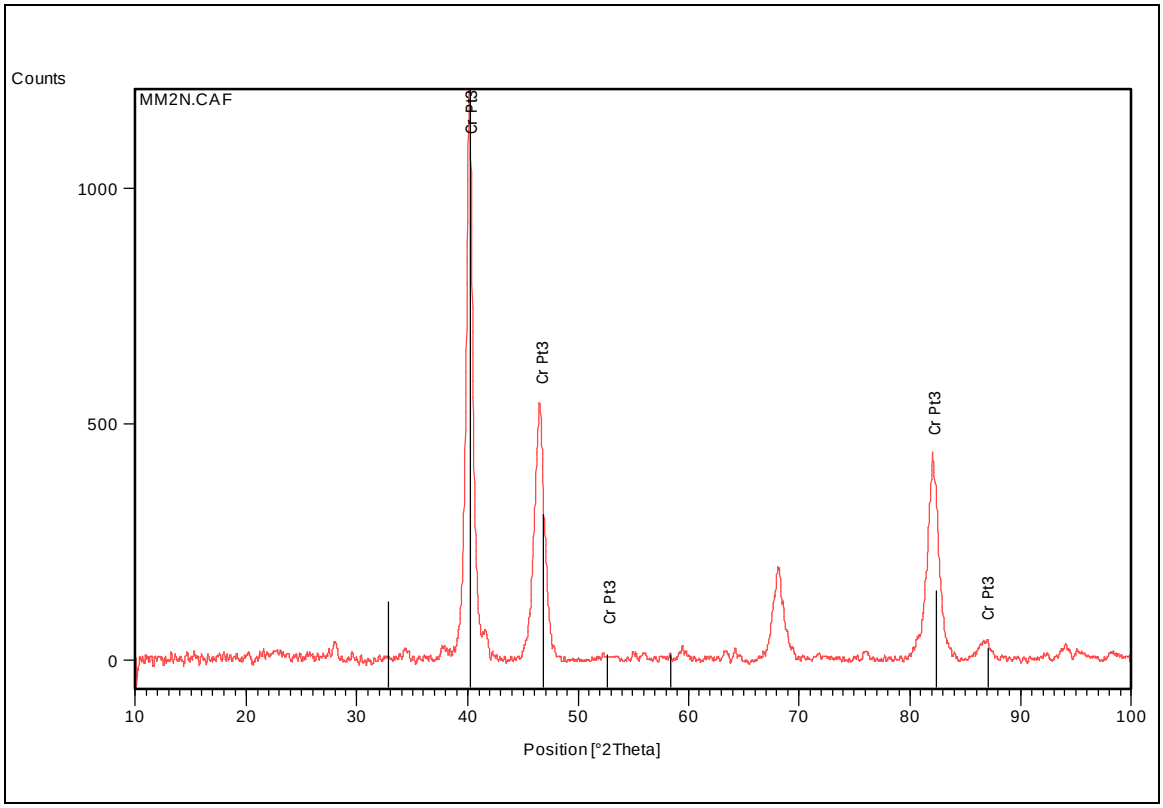

Figure 4.8 c. XRD spectrum of nominal Nb_{15}:Cr_{40}:Pt_{45} in the as-cast condition, showing black $CrPt_3$ peaks.

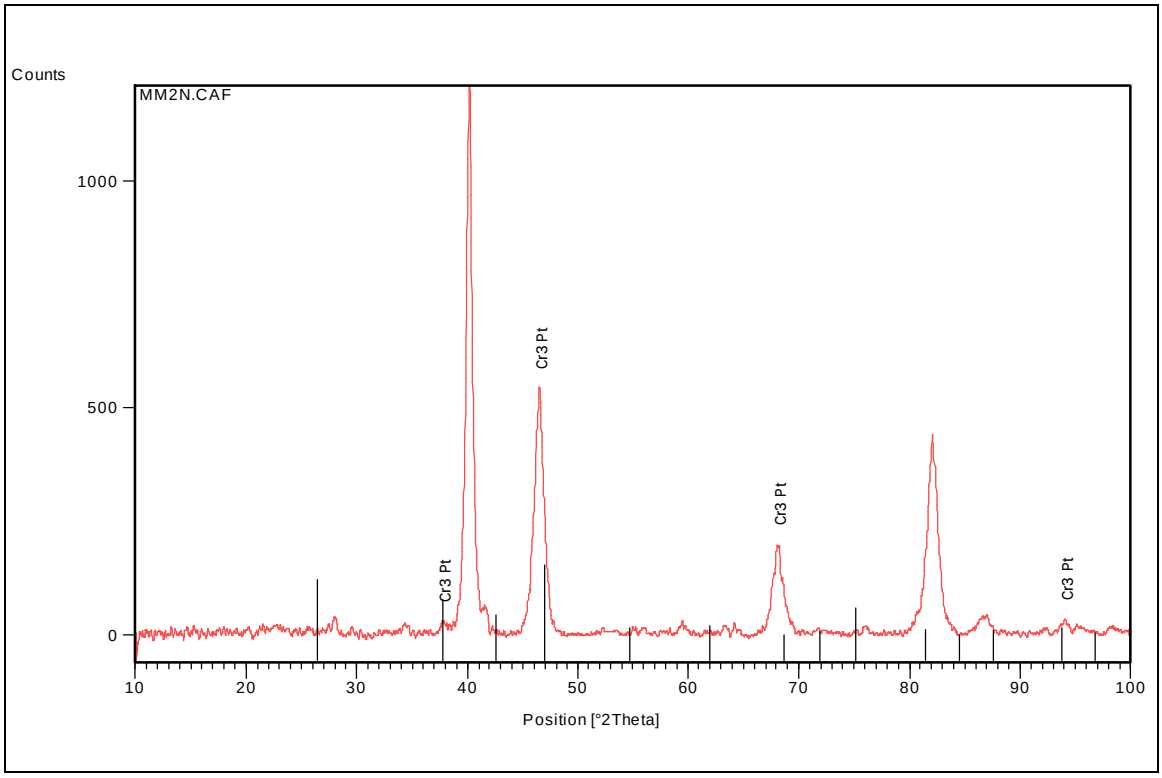

Figure 4.8 d. XRD spectrum of nominal Nb_{15}:Cr_{40}:Pt_{45} in the as-cast condition, showing black Cr_3Pt peaks.

4.1.3 Nominal Nb_{40}:Cr_{15}:Pt_{45}, Sample 3

The nominal Nb_{40}:Cr_{15}:Pt_{45} alloy possessed a three-phase microstructure of mainly cored ~$Nb_{1-X}Pt_{1+X}$ dendrites, with ternary phases 5 (τ5) and 4 (τ4), as shown in Figures 4.9 a and b. The dark phase was found to be a mixture of τ5 and τ4, because there was much scatter between two main values. This sample was inhomogeneous with a minor region near the edge. Table 4.3 gives the EDX analyses and these are plotted in Figure 4.10. The light and dark phase compositions had slightly high experimental errors. The EDX data showed the overall composition to be slightly off the tie-line, signifying the alloy to be slightly non-equilibrium. The X–ray diffraction (XRD) spectrum shown in Figure 4.13 was a reasonably good spectrum, with a high signal: background ratio and wide peaks expected from coring. However, it was not possible to check for the presence of ~$Nb_{1-X}Pt_{1+X}$, τ4 and τ5 phases, because there were no data for them in the database (ICDD). The unidentified peaks are assumed to be from the ~$Nb_{1-X}Pt_{1+X}$, τ4 and τ5 phases.

(a) The solidification sequence deduced from the microstructure is:

$$L \rightarrow \sim Nb_{1-X}Pt_{1+X} \text{ (dendrites)}$$

followed by the weak peritectic reaction

$$L + \sim Nb_{1-X}Pt_{1+X} \rightarrow \tau 5$$

and another weak peritectic reaction

$$L + \tau 5 \rightarrow \tau 4 \text{ (Chapter 5: Discussion)}$$

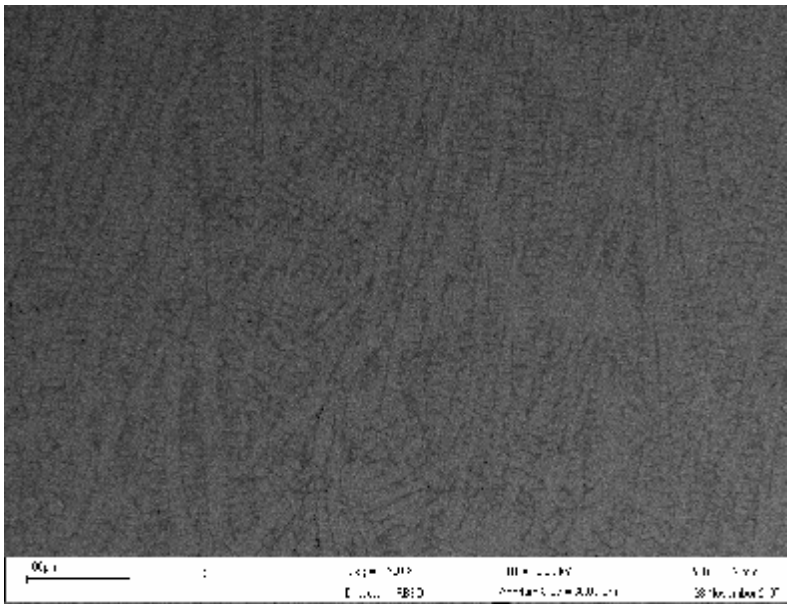

(a)

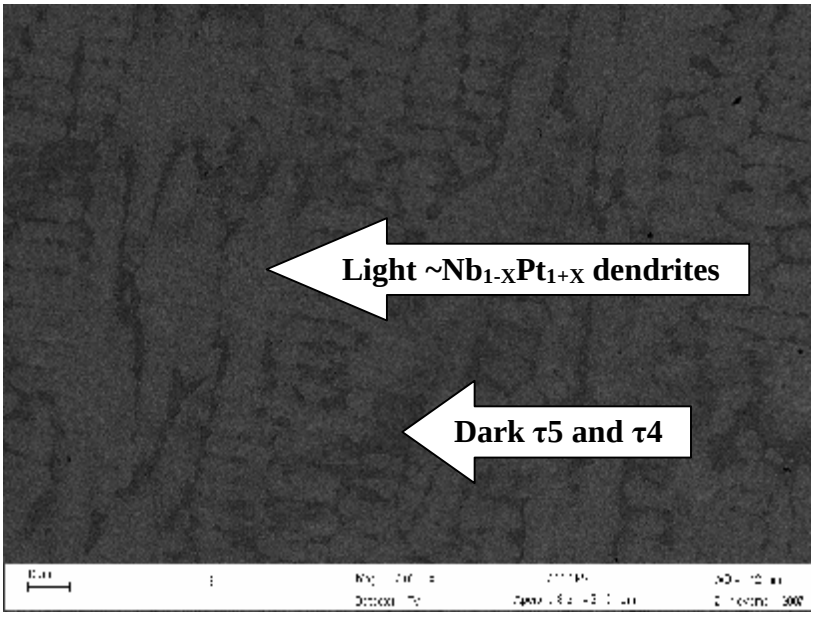

(b)

Figure 4.9 a-b. SEM-BSE images for the major part of nominal $Nb_{40}:Cr_{15}:Pt_{45}$ alloy in the as–cast condition, showing light $\sim Nb_{1-X}Pt_{1+X}$ dendrites, with dark mixture of τ5 and τ4 interdendritic phases.

Table 4.3. EDX phase analyses for the major part of nominal $Nb_{40}:Cr_{15}:Pt_{45}$ (at.%) in the as–cast condition.

Phase contrast	Nb	Cr	Pt	Phase
Overall	40.8±0.4	13.5±0.2	45.7±0.2	-
Light (dendrites)	40.3±0.8	10.4±0.8	49.3±0.3	~$Nb_{1-X}Pt_{1+X}$
Dark (interdendritic)	43.0±0.0	17.8±0.8	39.2±0.8	Mixture of τ5 and τ4

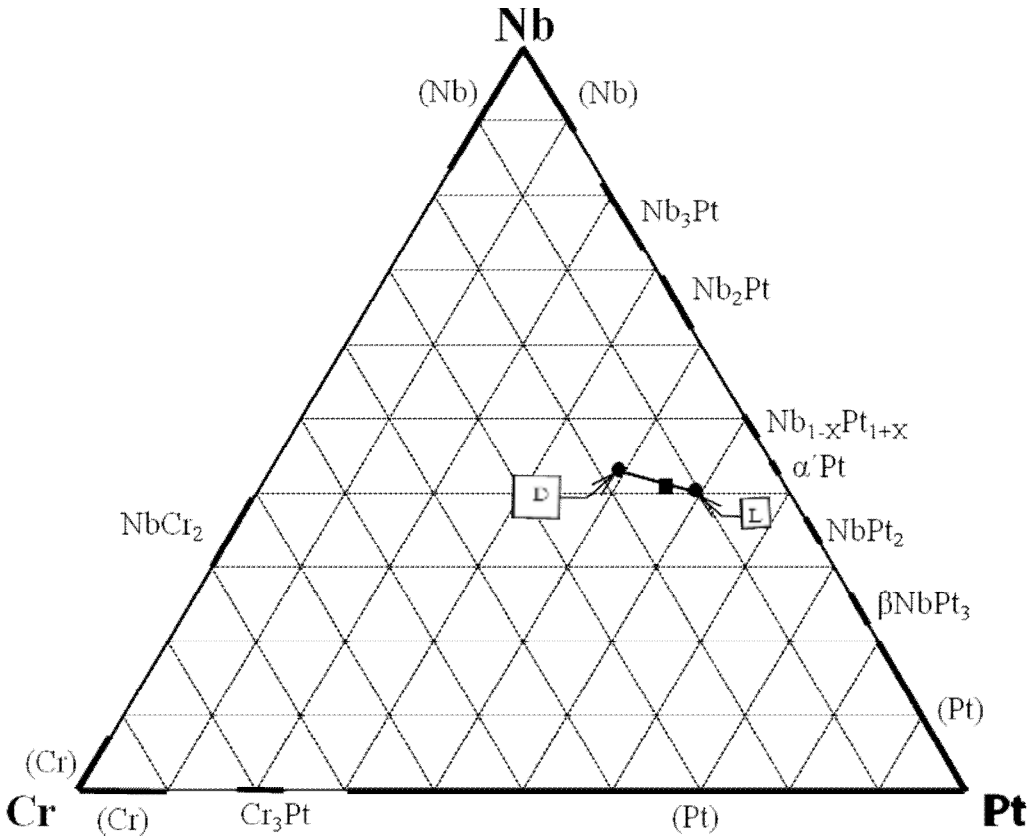

Figure 4.10. EDX phase compositions for the major part of nominal $Nb_{40}:Cr_{15}:Pt_{45}$ (at.%) alloy in the as–cast condition: (L) light contrast; (D) dark contrast phase; ■ overall composition; ● phase composition.

(b) In a small part near the edge, the sample was different although the overall composition was very similar. There were needles and dendrites (Figures 4.11 a and b) which are assumed to be the same phase, although they show different morphologies at different compositions. The ~$Nb_{1-X}Pt_{1+X}$ cored needles structure formed first and dendrites next, with a medium-grey τ5 phase on the needles and a dark ternary phase 4 (τ4) between the needles, as shown in Figures 4.11 a and b. The composition of the needles was closer to the Nb-Pt binary, but the phase analyses of both appeared to be contiguous, which is why they are interpretted as the same phase. The last phases formed were by peritectic reactions, and the phases were very small, making accurate analysis difficult. The ternary phase 5 (τ5) was checked by plotting out individual readings which showed a continuum and same morphology. Table 4.4 and Figure 4.12 give EDX analyses. The overall composition was on the tie-line between the light needle and medium-grey phase compositions, which were the major phases. The XRD spectrum shown in Figure 4.13 was a reasonably good spectrum, with a high signal: background ratio and wide peaks expected from coring. However, it was not possible to check for the presence of ~$Nb_{1-X}Pt_{1+X}$, τ4 and τ5 phases, because there were no data in the ICDD database. The peaks were assumed to be from ~$Nb_{1-X}Pt_{1+X}$, τ4 and τ5 phases.

The solidification sequence deduced from the minor microstructure is:

$$L \rightarrow {\sim}Nb_{1-X}Pt_{1+X}$$

$$L + {\sim}Nb_{1-X}Pt_{1+X} \rightarrow \tau5$$

$$L + \tau5 \rightarrow \tau4 \text{ (Chapter 5: Discussion)}$$

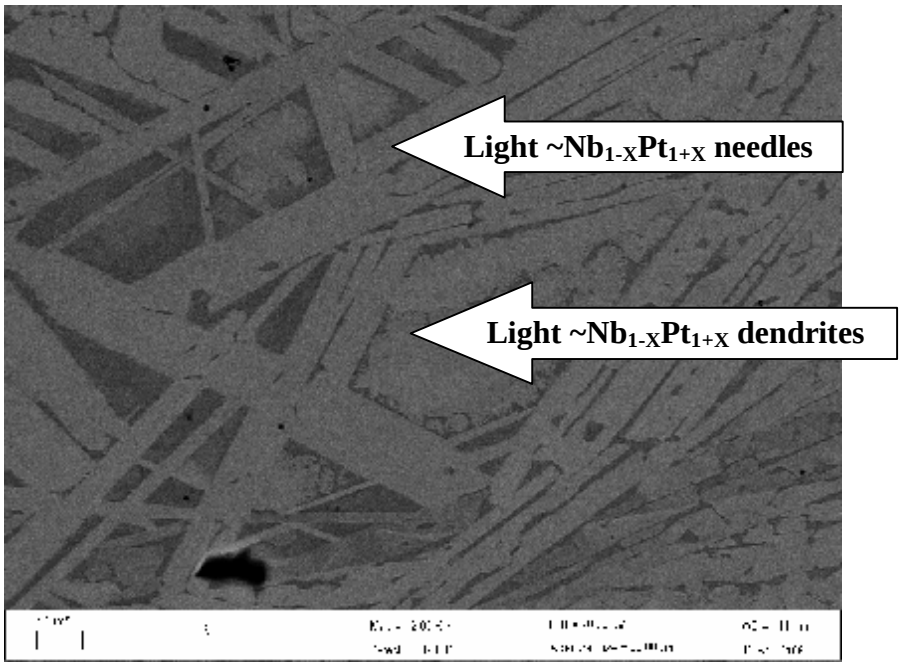

(a)

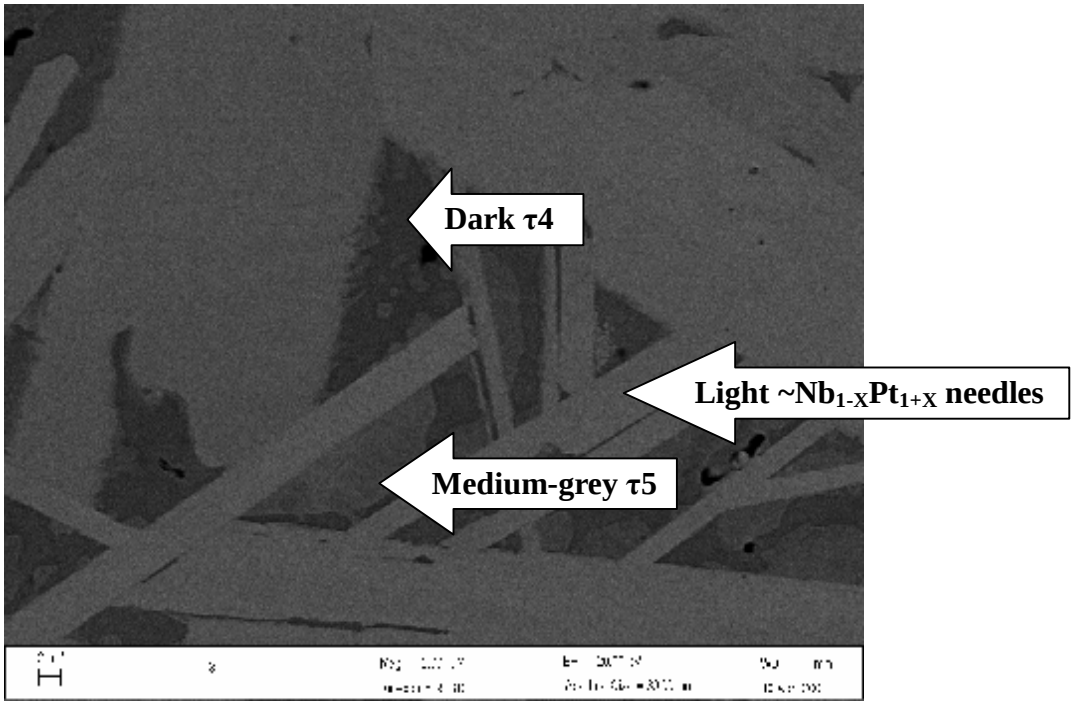

(b)

Figure 4.11 a-b. SEM-BSE images for the minor region, near the edge of nominal Nb_{40}:Cr_{15}:Pt_{45} alloy in the as–cast condition, showing light ~$Nb_{1-X}Pt_{1+X}$ needles and dendrites, medium-grey τ5 and dark τ4 phases between the needles.

Table 4.4. EDX phase analyses for the minor region, near the edge of nominal $Nb_{40}:Cr_{15}:Pt_{45}$ (at.%) in the as–cast condition.

Phase contrast	Nb	Cr	Pt	Phase
Overall	40.6±0.9	13.1±0.3	46.3±1.0	-
Light needles	41.4±0.9	10.5±1.4	48.1±1.2	~$Nb_{1-X}Pt_{1+X}$
Light dendrites	40.7±0.6	10.5±0.7	48.9±0.9	~$Nb_{1-X}Pt_{1+X}$
Medium-grey	40.4±1.3	13.2±2.3	46.4±1.3	τ5
Dark	39.7±0.4	28.7±0.6	31.6±0.3	τ4

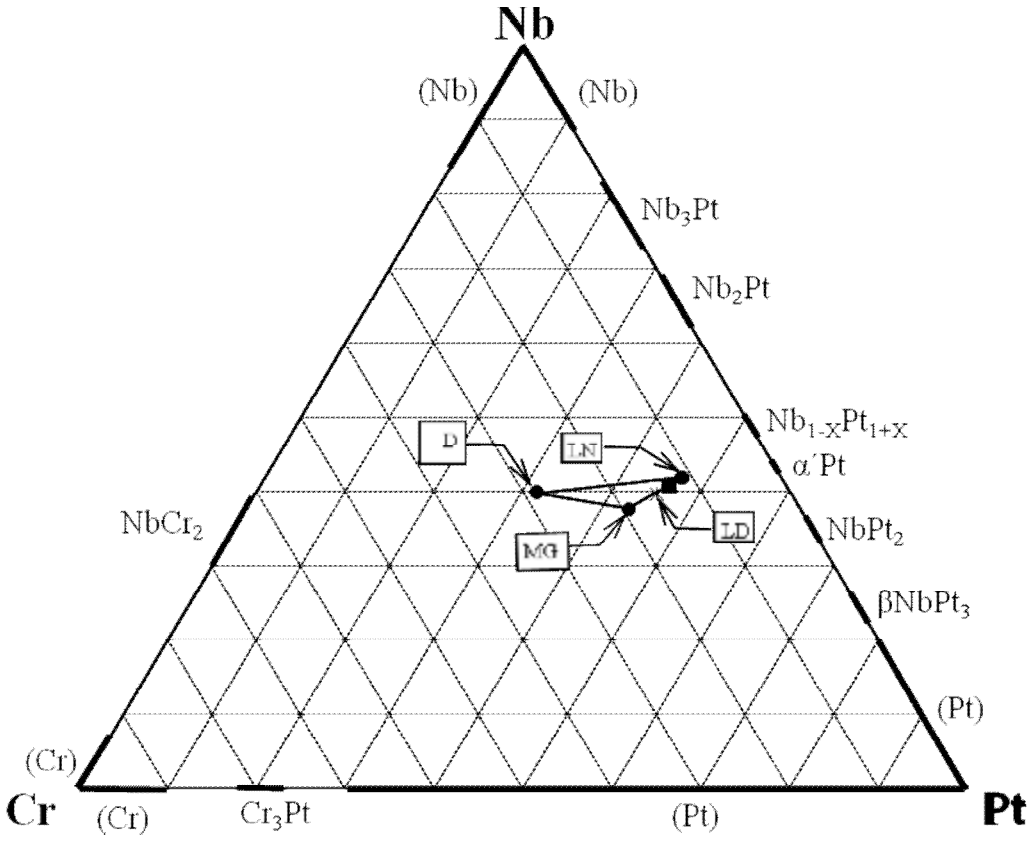

Figure 4.12. EDX phase compositions for the minor region, near the edge of nominal $Nb_{40}:Cr_{15}:Pt_{45}$ (at.%) alloy in the as–cast condition: (LN) light needle contrast; (LD) light dendrite contrast; (MG) medium-grey contrast; (D) dark contrast phase; ■ overall composition; ● phase composition; light dendrites (LD) are shown as ✸.

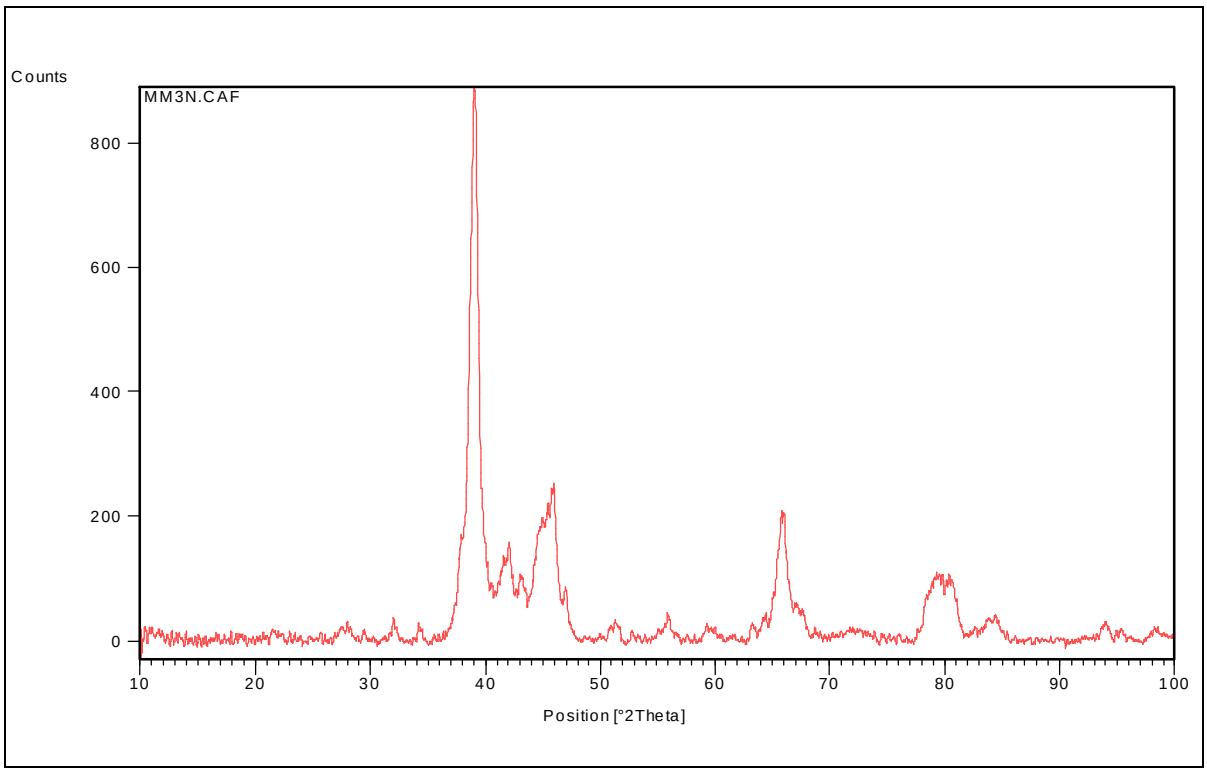

Figure 4.13. Raw XRD spectrum of nominal Nb_{40}:Cr_{15}:Pt_{45} in the as–cast condition.

4.1.4 Nominal Nb_{15}:Cr_{70}:Pt_{15}, Sample 4

The nominal Nb_{15}:Cr_{70}:Pt_{15} alloy had two bits (a) and (b). The microstructure of (a), comprised mainly dark (Cr) dendrites, with a medium-grey ~$NbCr_2$ phase and then a light ternary phase 1 (τ1), as shown in Figures 4.14 a and b. Table 4.5 gives the EDX analyses and these were plotted in Figure 4.15. The overall composition was within the triangle of the three phase compositions, signifying the alloy to be in equilibrium. The XRD spectrum shown in Figures 4.19 to 4.24 was poor, with a low signal: background ratio. The existence of (Cr) and ~$NbCr_2$ phases was confirmed by X-ray diffraction (XRD), as shown in Figures 4.20 to 4.22. There were some peak shifts for both of these phases: for (Cr) phase was found to be to the left, and for ~$NbCr_2$ phase varying in both ways. There were some unidentified peaks which are assumed to be τ1.

(a) The solidification sequence deduced from the microstructure is as follows:

$$L \rightarrow (Cr)$$

followed by peritectic reaction

$$L + (Cr) \rightarrow \sim NbCr_2$$

and then another peritectic reaction

$$L + \sim NbCr_2 \rightarrow \tau 1 \text{ (Chapter 5: Discussion)}$$

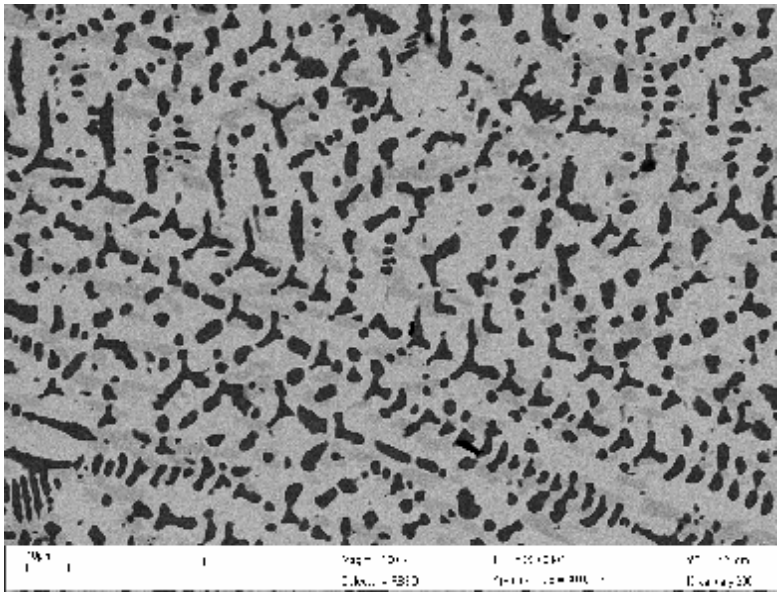

(a)

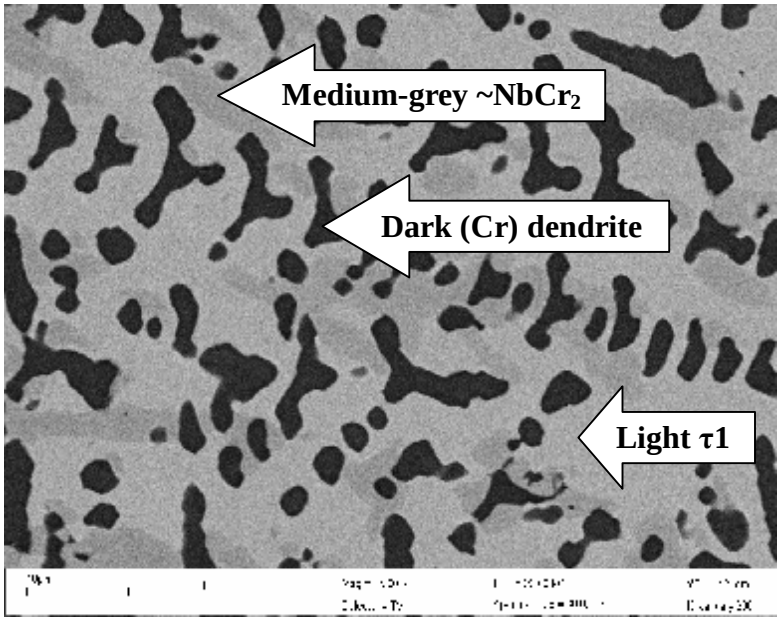

(b)

Figure 4.14 a-b. SEM-BSE images of the nominal $Nb_{15}:Cr_{70}:Pt_{15}$ alloy in the as–cast condition, showing dark (Cr) dendrites, medium-grey ~$NbCr_2$ and light τ1 phases.

Table 4.5. EDX phase analyses for nominal $Nb_{15}:Cr_{70}:Pt_{15}$ (at.%) in the as–cast condition, as shown in Figure 4.14 (a) and (b).

Phase contrast	Nb	Cr	Pt	Phase
Overall	13.6±0.4	73.1±0.3	13.3±0.2	-
Light	15.7±0.4	65.6±0.2	18.7±0.2	τ1
Medium-grey	28.1±0.4	58.2±0.6	13.6±0.3	~$NbCr_2$
Dark (dendrites)	1.7±0.2	93.5±0.3	4.8±0.1	(Cr)

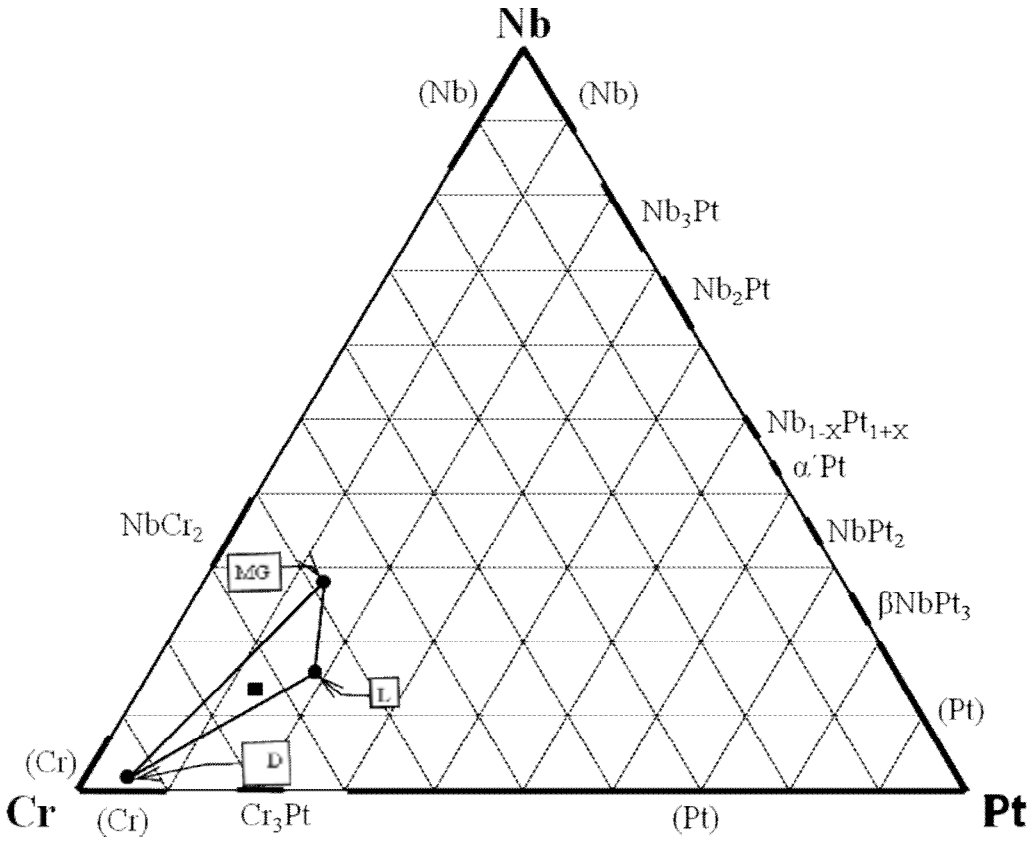

Figure 4.15. EDX phase compositions for the nominal $Nb_{15}:Cr_{70}:Pt_{15}$ (at.%) in the as–cast condition: (L) light contrast; (MG) medium-grey contrast; (D) dark contrast phase; ■ overall composition; ● phase composition.

(b) In a minor region along the edge, there was an unmelted Nb particle on one side of the sample, with a region of different microstructure. Adjacent to this region, there was an arc-like microstructure, which comprised a large outer medium-grey (Nb), outer light ~Nb_3Pt, inner medium-grey ~$NbCr_2$, inner light ternary phase 1 (τ1) and dark (Cr) dendrites, as can be seen in Figure 4.17. There is a eutectic-like mixture between outer light ~Nb_3Pt and inner medium-grey ~$NbCr_2$ phases. The presence of (Nb), (Cr), ~Nb_3Pt and ~$NbCr_2$ phases was confirmed by X-ray diffraction (XRD), as shown in Figures 4.19 to 4.24. Tables 4.6 and 4.7 give the EDX phases' analyses of nominal Nb_{15}:Cr_{70}:Pt_{15} alloy at this part of the sample.

The solidification sequence presumed is as follows:

$$L \rightarrow \sim NbCr_2$$

followed by a eutectic reaction

$$L \rightarrow \sim NbCr_2 + \sim Nb_3Pt$$

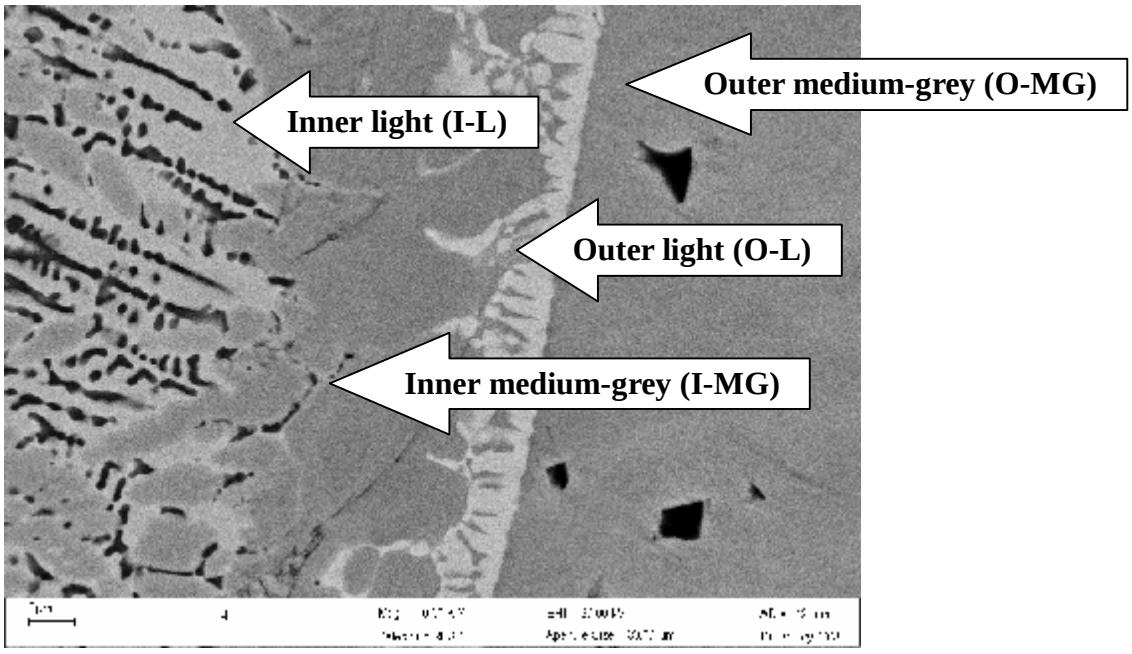

← INNER → ← REGION 1 → ← REGION 2 (OUTER) →

Figure 4.16. SEM-BSE image for the minor region of nominal Nb_{15}:Cr_{70}:Pt_{15} alloy in the as–cast condition, showing dark (Cr) dendrites, inner ~$NbCr_2$ (medium), outer (Nb) (medium), inner τ1 (light) and outer ~Nb_3Pt (light) phases.

Table 4.6. EDX phase analyses for the minor region at Region 1 of nominal $Nb_{15}:Cr_{70}:Pt_{15}$ (at.%) in the as–cast condition, as shown in Figure 4.16.

Phase contrast	**Nb**	**Cr**	**Pt**	**Phase**
Inner light (I-L)	16.4±1.2	64.5±0.6	19.0±0.9	τ1
Outer light (O-L)	54.2±1.6	29.1±1.9	16.7±0.4	~Nb_3Pt
Inner medium-grey (I-MG)	31.7±2.9	58.1±1.6	10.2±1.4	~$NbCr_2$

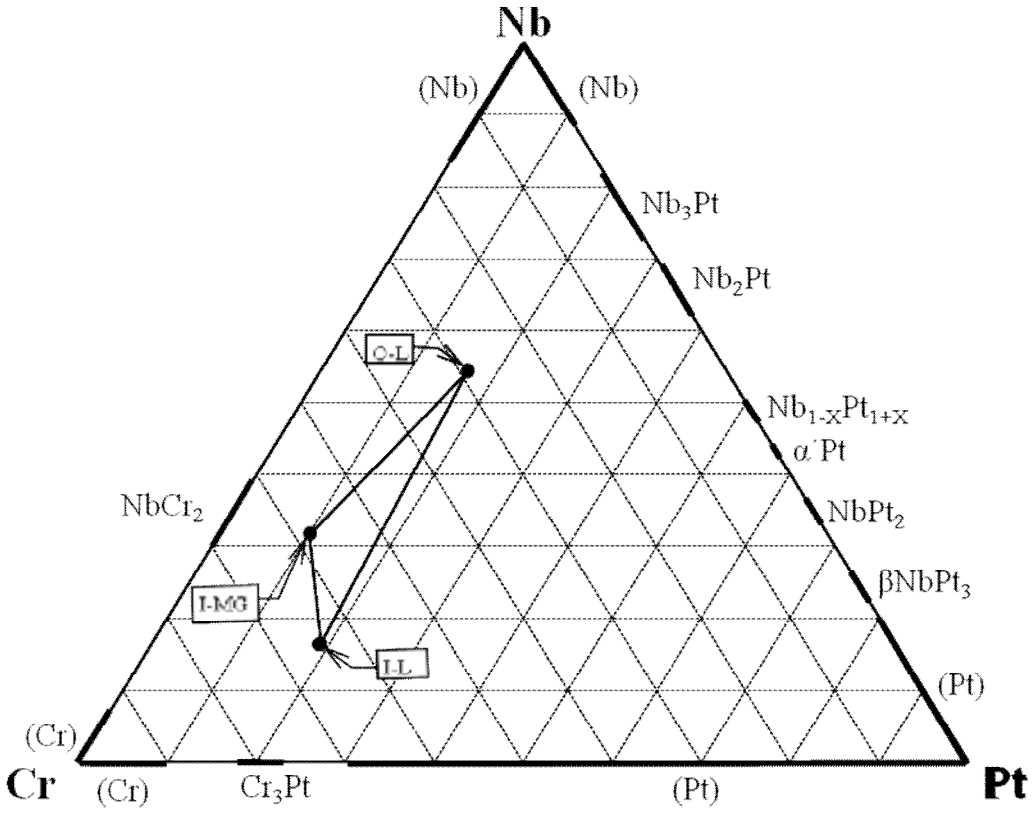

Figure 4.17. EDX phase compositions for the minor region at Region 1 of nominal $Nb_{15}:Cr_{70}:Pt_{15}$ (at.%) in the as–cast condition: (I-L) inner light contrast; (O-L) outer light contrast; (I-MG) inner medium-grey contrast phase; ● phase composition.

Table 4.7. EDX phase analyses for the minor region at Region 2 of nominal $Nb_{15}:Cr_{70}:Pt_{15}$ (at.%) in the as–cast condition, as shown in Figure 4.16.

Phase contrast	Nb	Cr	Pt	Phase
Outer medium-grey (O-MG)	97.6±0.6	1.0±0.1	1.4±0.5	(Nb)

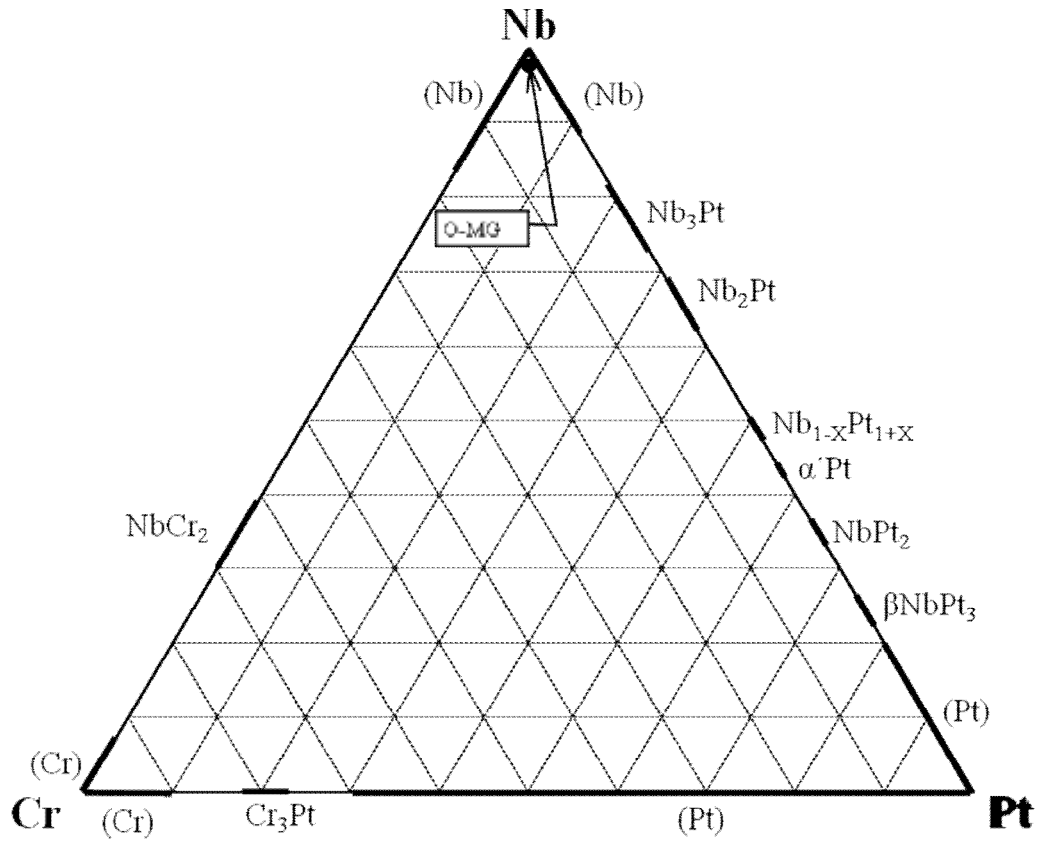

Figure 4.18. EDX phase compositions for the minor region at Region 2 of nominal $Nb_{15}:Cr_{70}:Pt_{15}$ (at.%) in the as–cast condition: (O-MG) outer medium-grey contrast phase; ● phase composition.

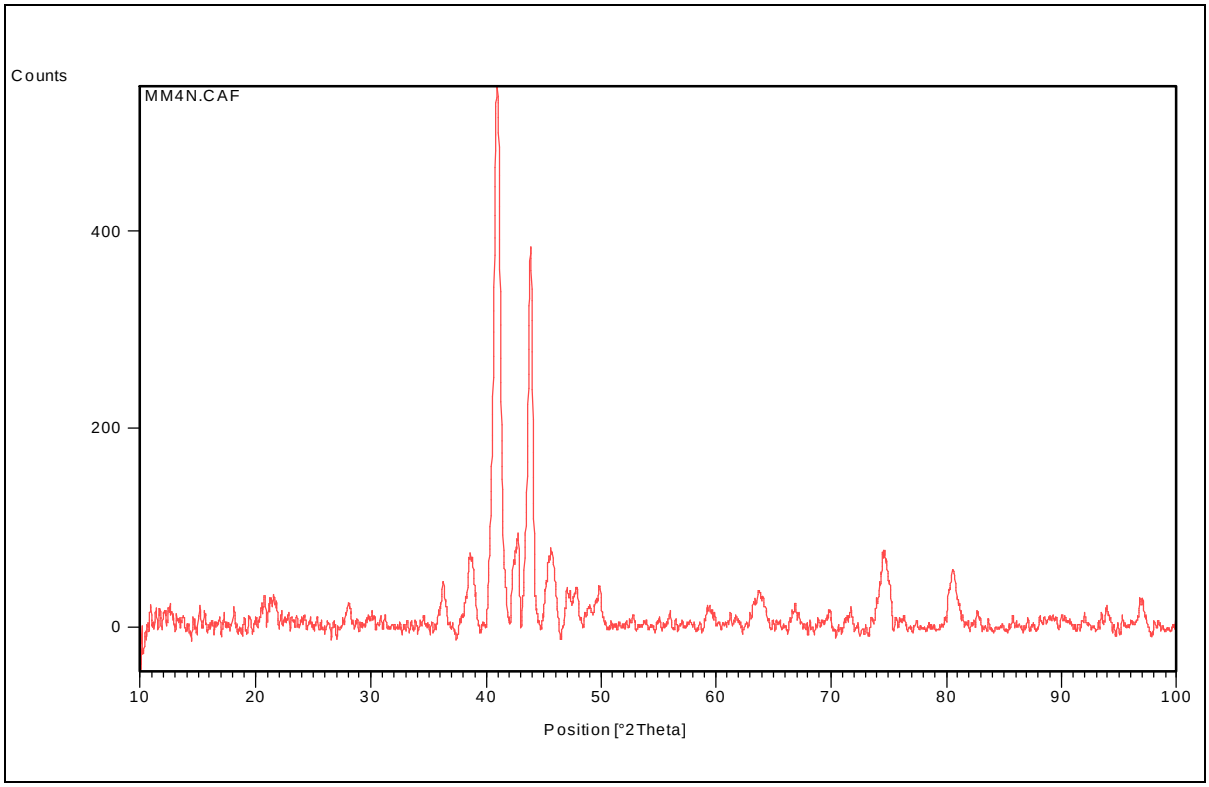

Figure 4.19. Raw XRD spectrum of nominal Nb_{15}:Cr_{70}:Pt_{15} in the as-cast condition.

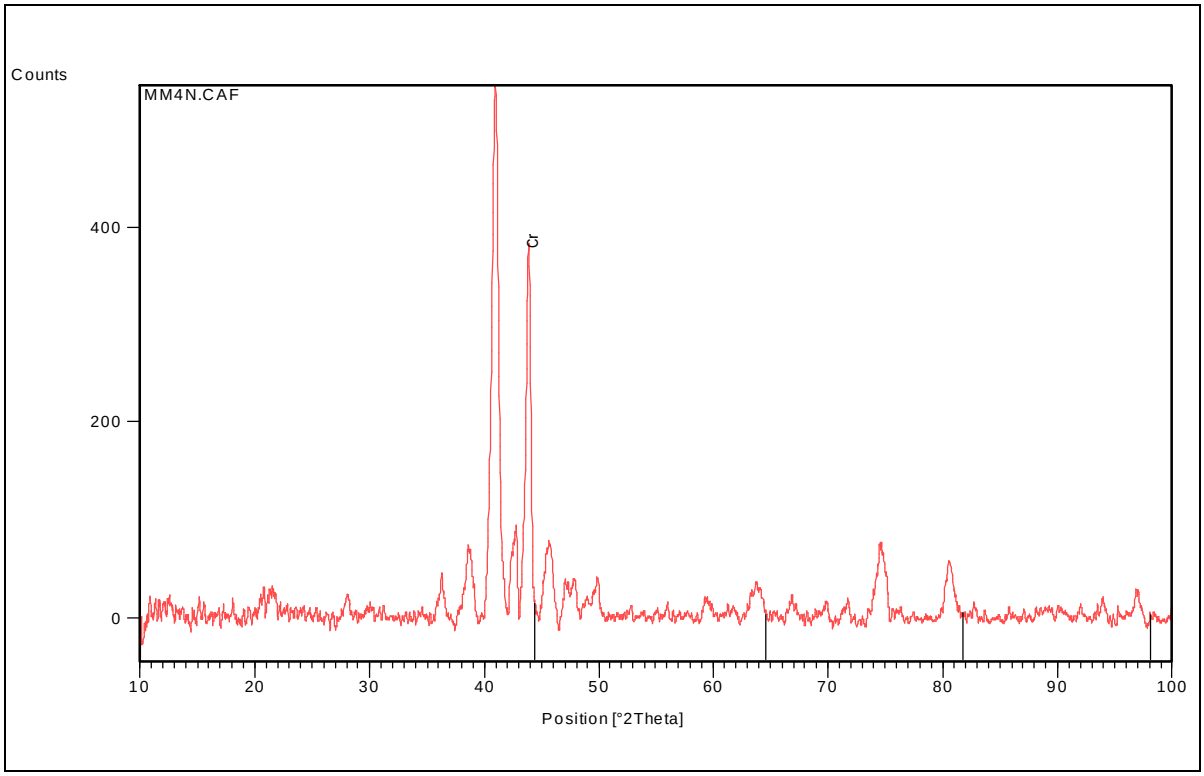

Figure 4.20. XRD spectrum of nominal Nb_{15}:Cr_{70}:Pt_{15} in the as-cast condition, showing black Cr peaks.

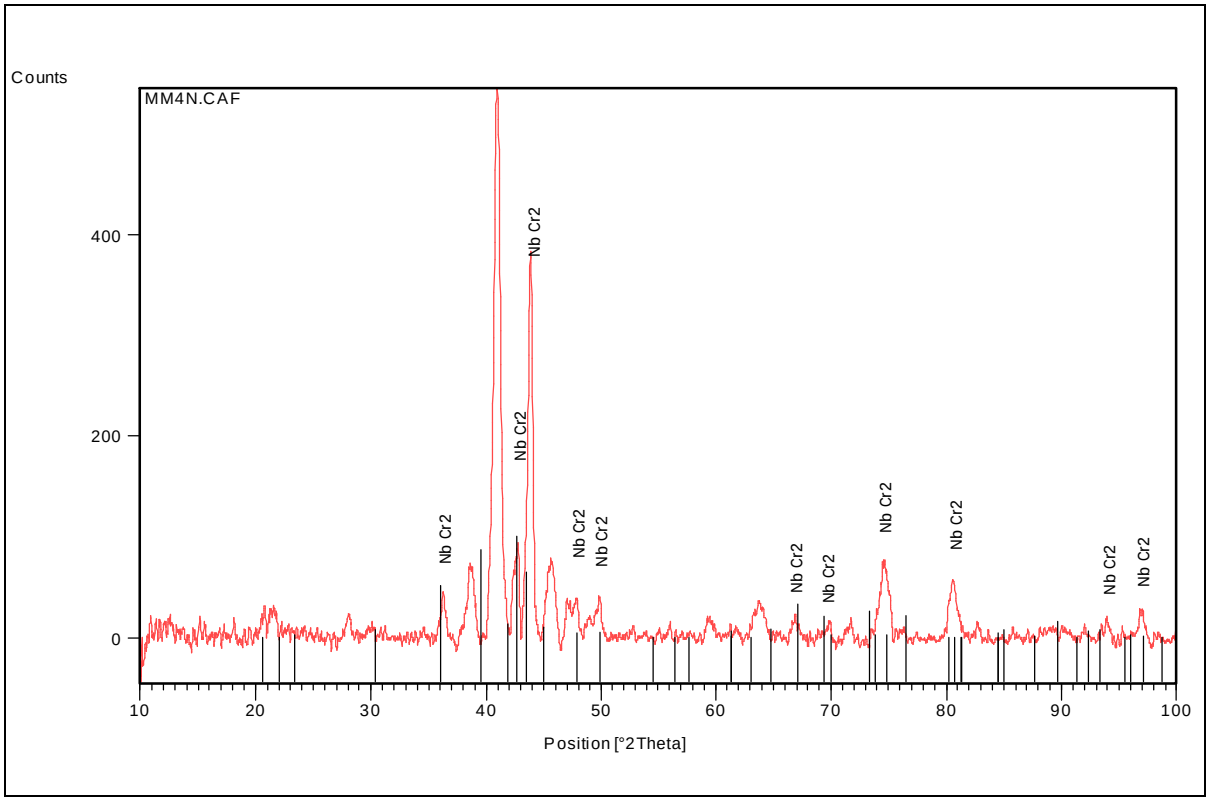

Figure 4.21. XRD spectrum of nominal Nb_{15}:Cr_{70}:Pt_{15} in the as-cast condition, showing black ~$NbCr_2$ peaks.

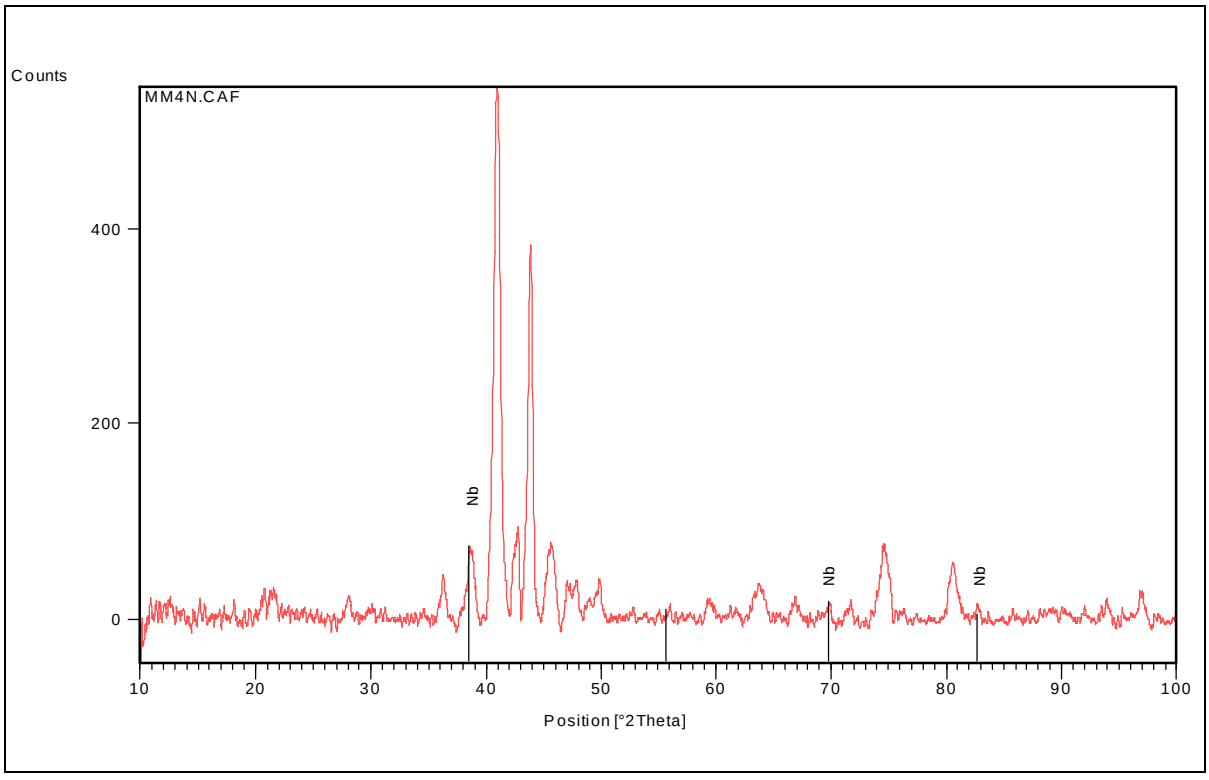

Figure 4.22. XRD spectrum of nominal Nb_{15}:Cr_{70}:Pt_{15} in the as-cast condition, showing black Nb peaks.

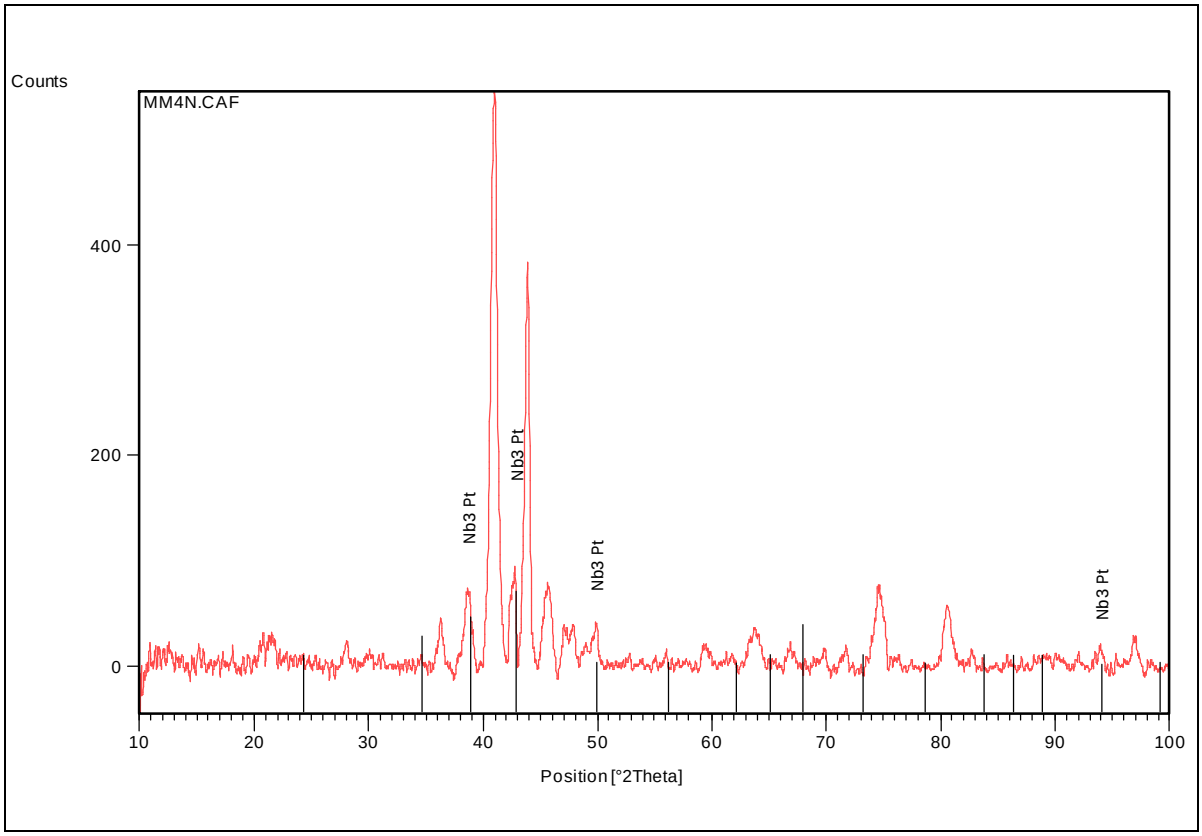

Figure 4.23. XRD spectrum of nominal Nb_{15}:Cr_{70}:Pt_{15} in the as-cast condition, showing black ~Nb_3Pt peaks.

4.1.5 Nominal Nb_{40}:Cr_{45}:Pt_{15}, Sample 5

The nominal Nb_{40}:Cr_{45}:Pt_{15} alloy was quite brittle with cracks. This alloy comprised dark ~$NbCr_2$ dendrites and a light ~Nb_2Pt interdendritic phase, with a sparse eutectic of ~$NbCr_2$ + ~Nb_2Pt, as shown in Figures 4.24 a and b. Table 4.8 gives the EDX analyses, which are plotted in Figure 4.25, showing the overall composition and eutectic overall to be on the tie-line between two phase compositions, signifying the alloy to be in equilibrium. The analyses had high experimental errors. The sparse eutectic analysis had small areas with no reported experimental error, as the best analysis was chosen. The XRD spectrum shown in Figures 4.26 and 4.27 was quite a poor spectrum, with a low signal: background ratio, although there were sharp peaks. There were matches for ~$NbCr_2$ phase with the X-ray diffraction database lines (ICDD), but with some peak shifts varying in both ways, as shown in Figure 4.27. However, it was not possible to check for the presence of ~Nb_2Pt, because there were no data for it in the X-ray diffraction database (ICDD). The unidentified peaks are likely to be from ~Nb_2Pt.

The solidification sequence deduced from the microstructure is as follows:

$$L \rightarrow \sim NbCr_2$$

followed by a sparse eutectic

$$L \rightarrow \sim NbCr_2 + \sim Nb_2Pt$$

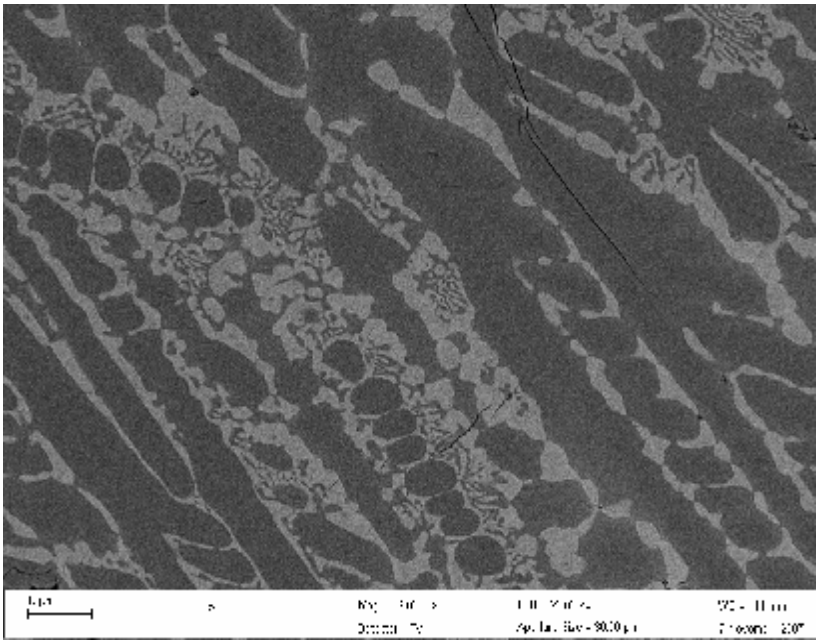

(a)

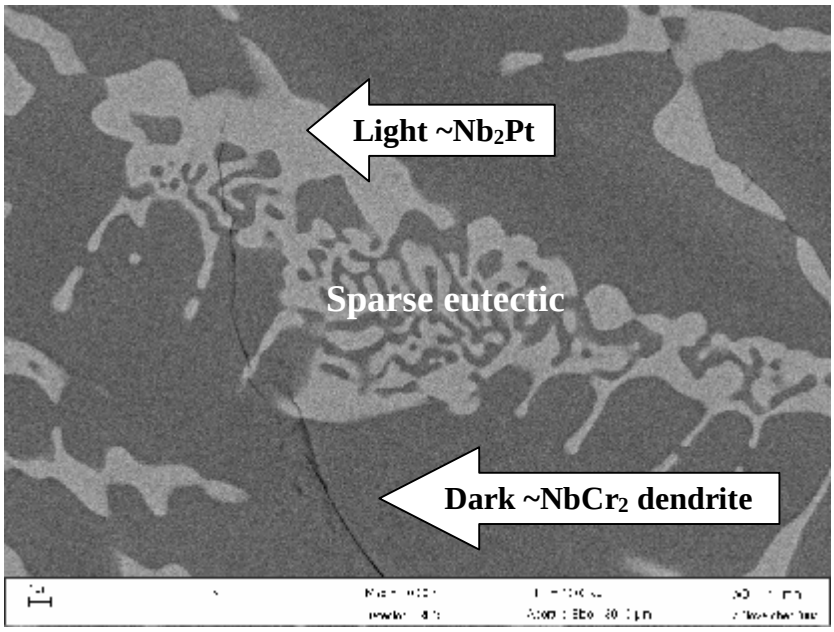

(b)

Figure 4.24 a-b. SEM-BSE images of the nominal $Nb_{40}:Cr_{45}:Pt_{15}$ alloy in the as–cast condition, showing dark $\sim NbCr_2$ dendrites, with a sparse eutectic of $\sim NbCr_2$ + $\sim Nb_2Pt$ (light).

Table 4.8. EDX phase analyses for nominal $Nb_{40}:Cr_{45}:Pt_{15}$ (at.%) in the as–cast condition.

Phase contrast	**Nb**	**Cr**	**Pt**	**Phase**
Overall	43.2±2.2	41.6±2.8	15.1±0.6	-
Dark (dendrites)	35.3±0.5	54.2±1.2	10.5±0.8	~$NbCr_2$
Light	53.0±1.2	26.1±0.8	21.0±0.6	~Nb_2Pt
Sparse eutectic	44.4	39.4	16.3	~$NbCr_2$ + ~Nb_2Pt

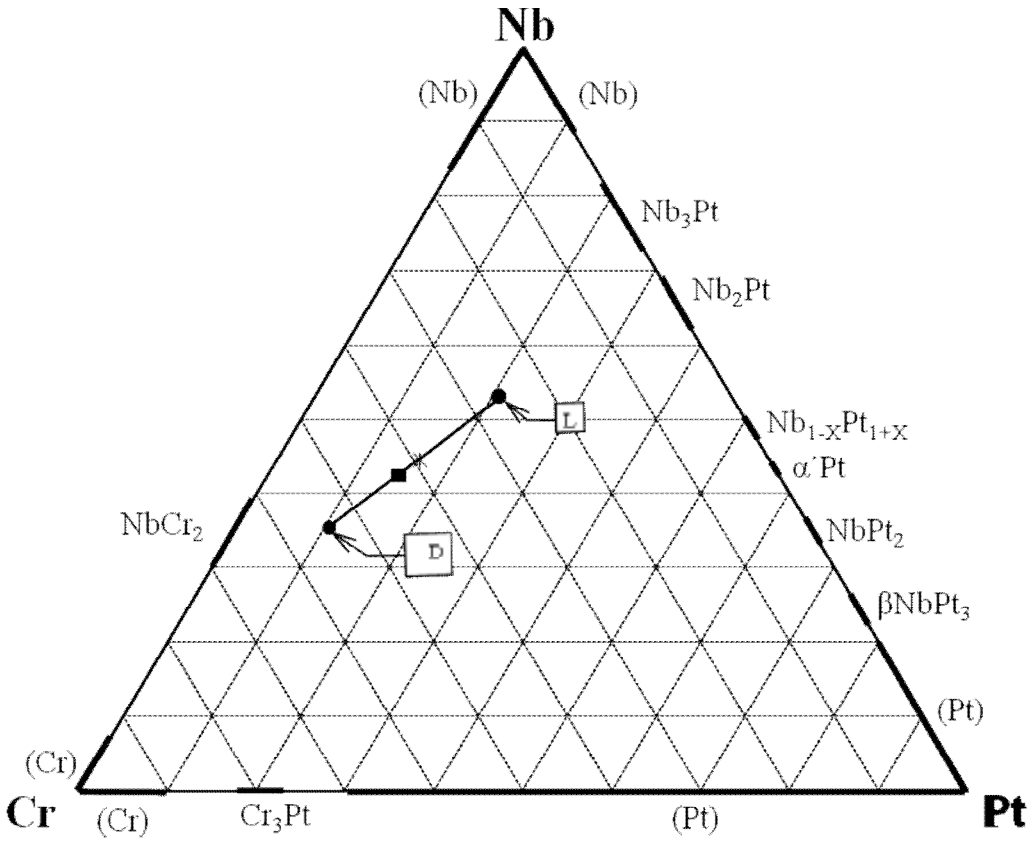

Figure 4.25. EDX phase compositions for the nominal $Nb_{40}:Cr_{45}:Pt_{15}$ (at.%) alloy in the as–cast condition: (L) light contrast; (D) dark contrast phase; ■ overall composition; ● phase composition; ✸ eutectic composition.

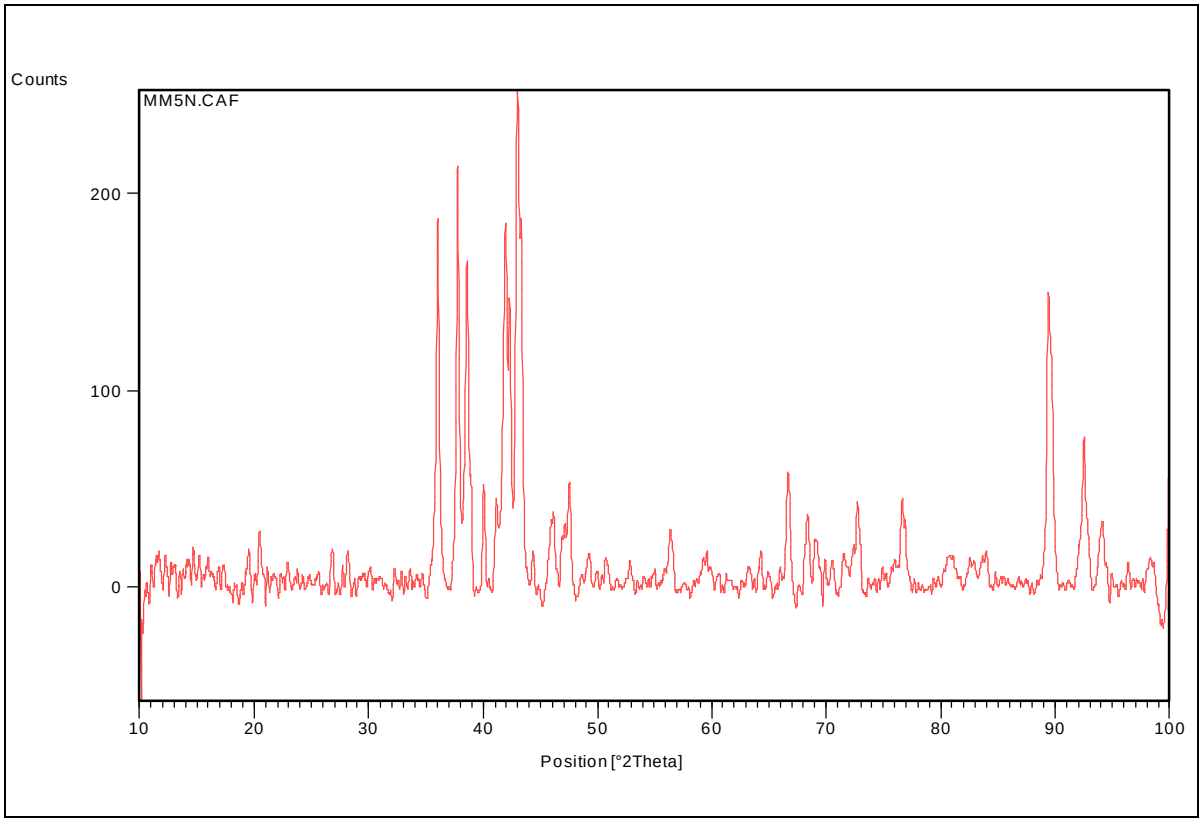

Figure 4.26. Raw XRD spectrum of nominal $Nb_{40}:Cr_{45}:Pt_{15}$ in the as-cast condition.

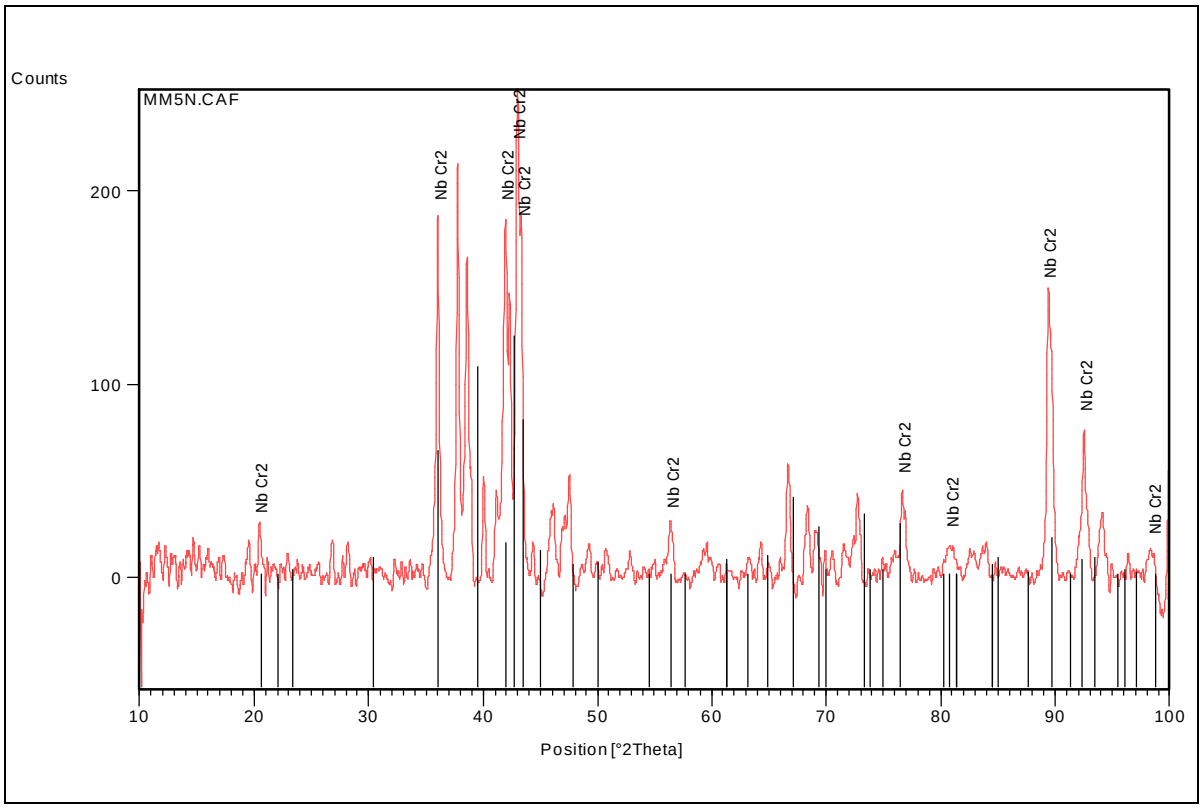

Figure 4.27. XRD spectrum of nominal $Nb_{40}:Cr_{45}:Pt_{15}$ in the as-cast condition, showing black ~$NbCr_2$ peaks.

4.1.6 Nominal Nb_{70}:Cr_{15}:Pt_{15}, Sample 6

The nominal Nb_{70}:Cr_{15}:Pt_{15} alloy possessed mainly medium-grey (Nb) dendrites, with a light cored ~Nb_3Pt matrix and small regions of a ~Nb_3Pt + ~$NbCr_2$ eutectic, as shown in Figures 4.28 a and b. The dendrites had ragged edges showing a peritectic reaction. Table 4.9 gives the EDX analyses, and these are plotted in Figure 4.29. The overall composition was off the tie-line between two phase compositions, because the eutectic overall incorporated another phase. Extrapolating through the eutectic overall composition from ~Nb_3Pt, which was one of the components, showed that the second component was ~$NbCr_2$. There were high experimental errors for eutectic overall because of its small size areas. There were also high errors for the light matrix because of coring, and for medium-grey dendrites because of their small size. The XRD spectrum shown in Figures 4.30-4.33 was poor, with a low signal: background ratio and having several sharp peaks. The presence of (Nb), ~Nb_3Pt and ~$NbCr_2$ phases was confirmed by X-ray diffraction, as shown in Figures 4.31 to 4.33. There were excellent matches for the ~Nb_3Pt phase with the ICDD lines, although with some slight peak shifts varying in both ways. There were also good fits for two (Nb) peaks, with the other two not fitting so well, but the shift increased with increasing angle, which is acceptable. Some ~$NbCr_2$ phase peaks matched to the specimen, with some peak shifts varying in both ways, but other peaks were not identified.

The solidification sequence deduced from the microstructure is as follows:

$$L \rightarrow (Nb)$$

followed by a peritectic reaction

$$L + (Nb) \rightarrow \sim Nb_3Pt$$

and then a eutectic reaction

$$L \rightarrow \sim Nb_3Pt + \sim NbCr_2$$

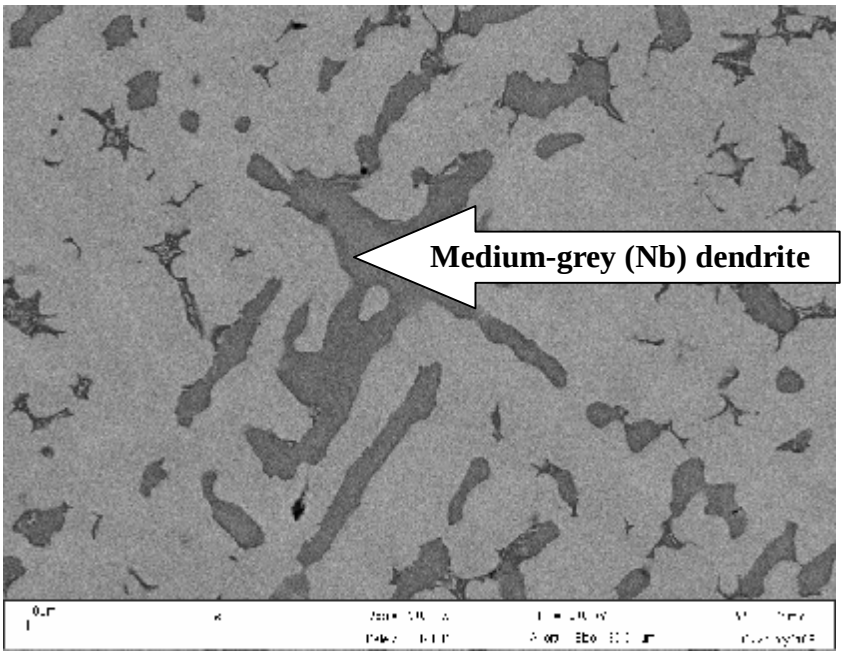

(a)

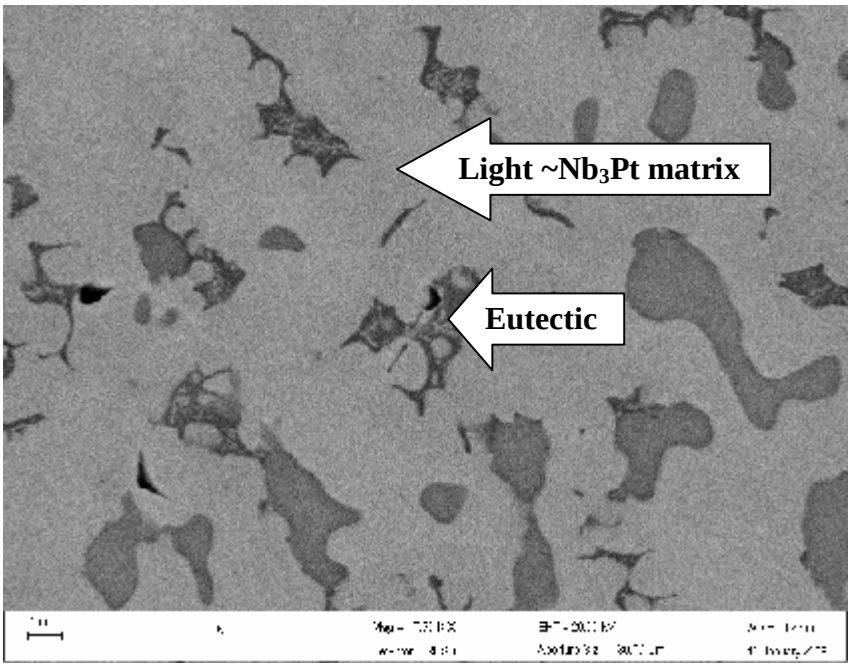

(b)

Figure 4.28 a-b. SEM-BSE images of the nominal Nb_{70}:Cr_{15}:Pt_{15} alloy in the as–cast condition, showing medium (Nb) dendrites, light ~Nb_3Pt matrix and a ~Nb_3Pt + ~$NbCr_2$ eutectic reaction.

Table 4.9. EDX phase analyses for nominal $Nb_{70}:Cr_{15}:Pt_{15}$ (at.%) in the as–cast condition.

Phase contrast	**Nb**	**Cr**	**Pt**	**Phase**
Overall	69.9±0.4	16.2±0.4	14.0±0.1	-
Medium-grey (dendrites)	76.2±1.0	17.5±1.1	6.4±0.2	(Nb)
Light matrix	73.6±0.5	9.4±0.4	17.0±0.2	~Nb_3Pt
Eutectic overall	48.3±3.3	45.0±4.2	6.7±1.1	~Nb_3Pt + ~$NbCr_2$

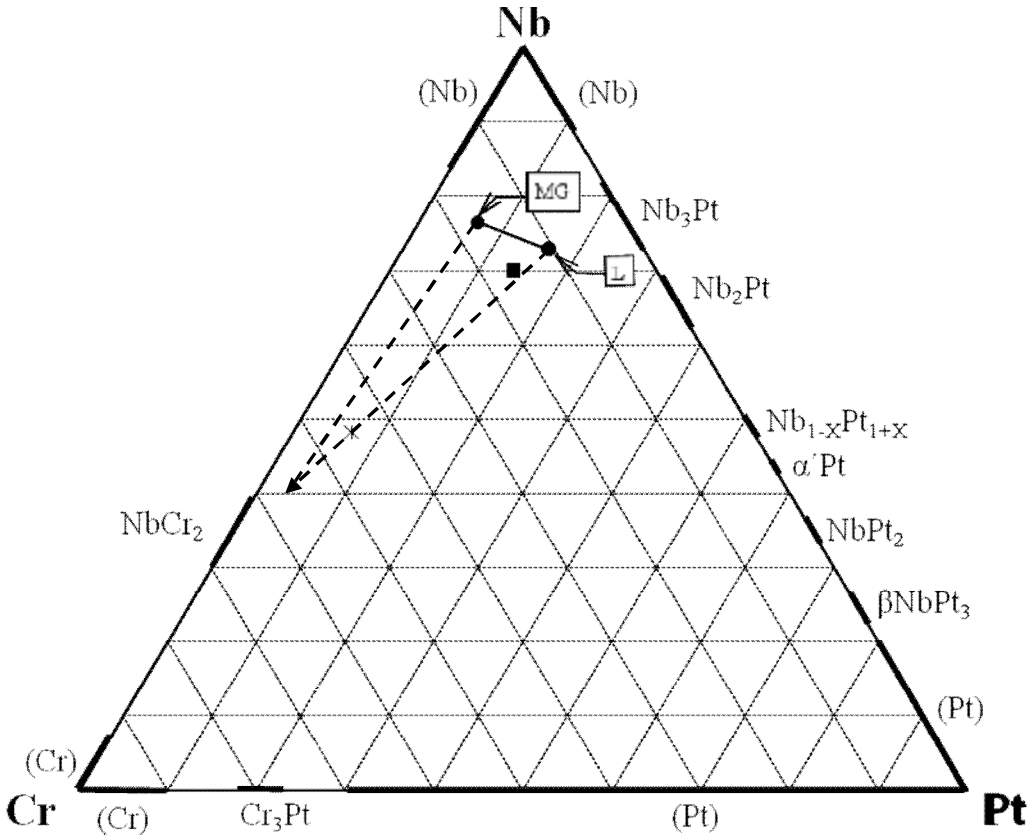

Figure 4.29. EDX phase compositions for the nominal $Nb_{15}:Cr_{70}:Pt_{15}$ (at.%) alloy in the as–cast condition: (L) light contrast; (MG) medium-grey contrast phase; ■ overall composition; ● phase composition; ✸ eutectic composition.

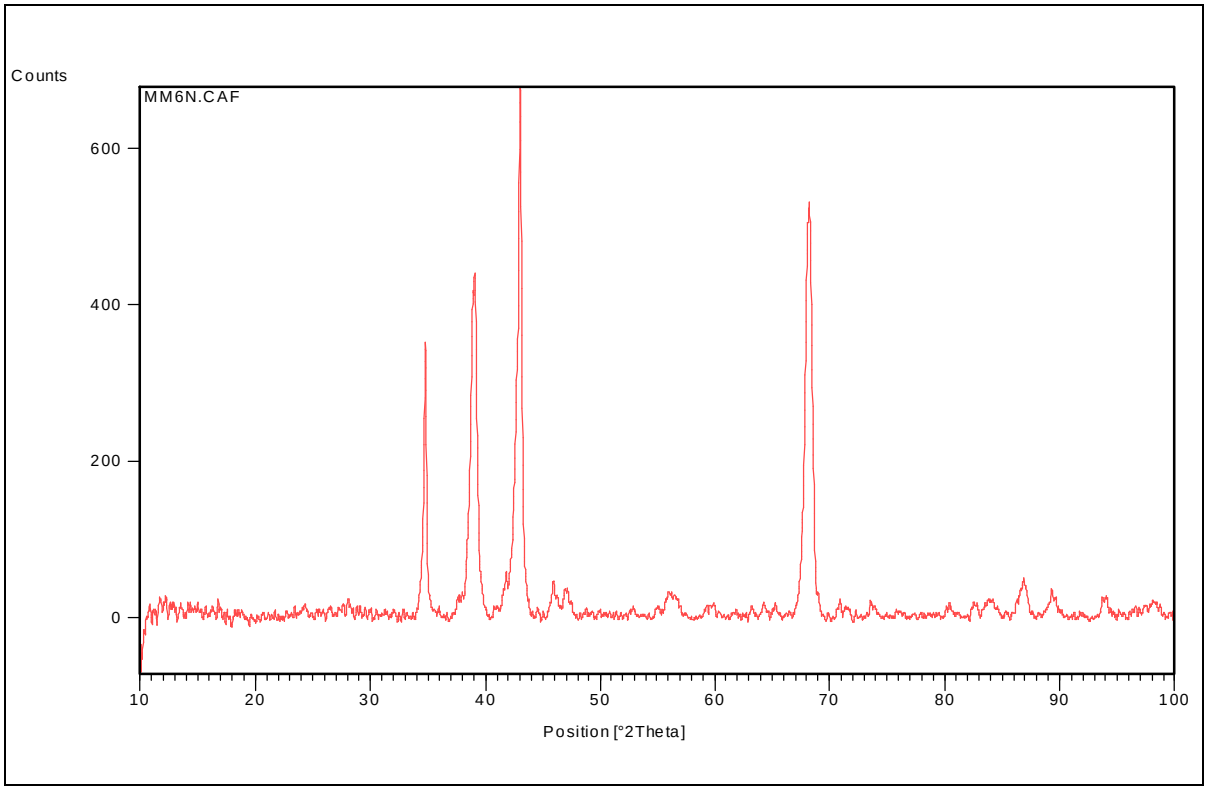

Figure 4.30. Raw XRD spectrum of nominal Nb_{70}:Cr_{15}:Pt_{15} in the as-cast condition.

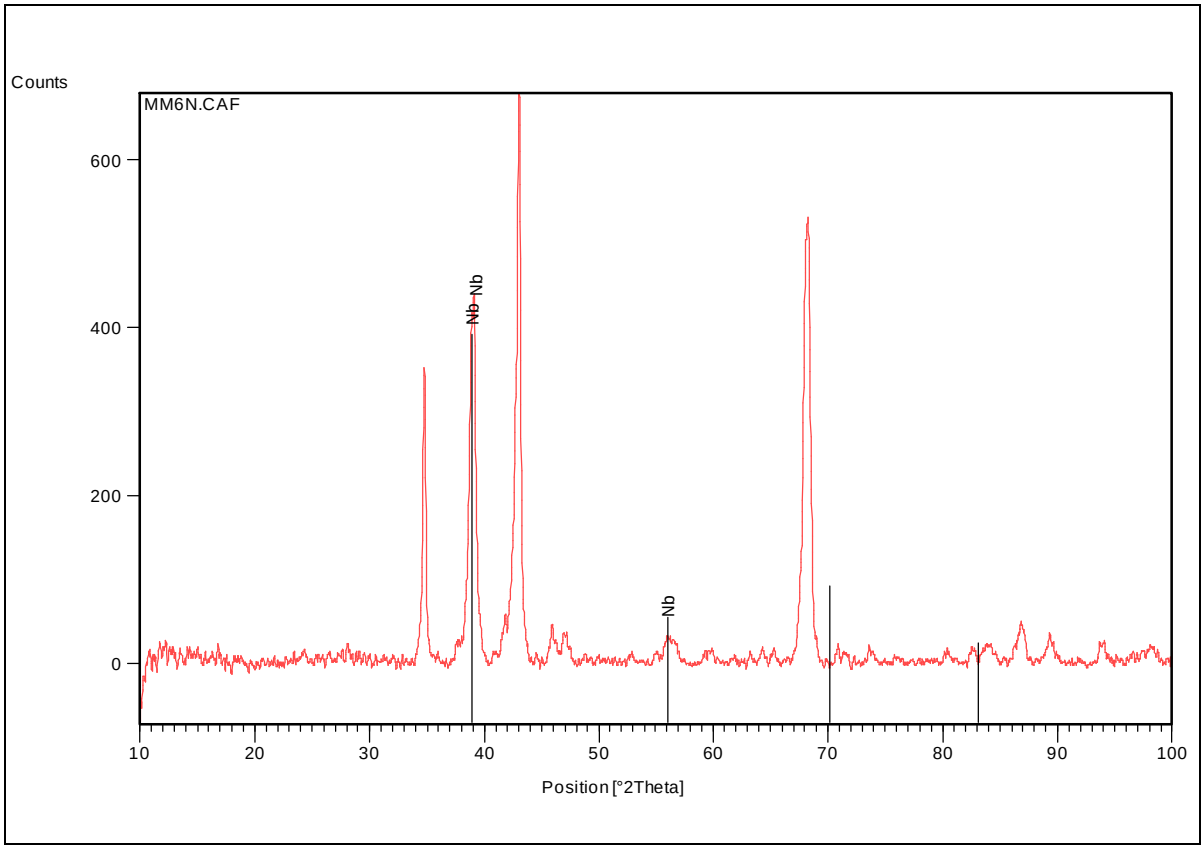

Figure 4.31. XRD spectrum of nominal Nb_{70}:Cr_{15}:Pt_{15} in the as-cast condition, showing black Nb peaks.

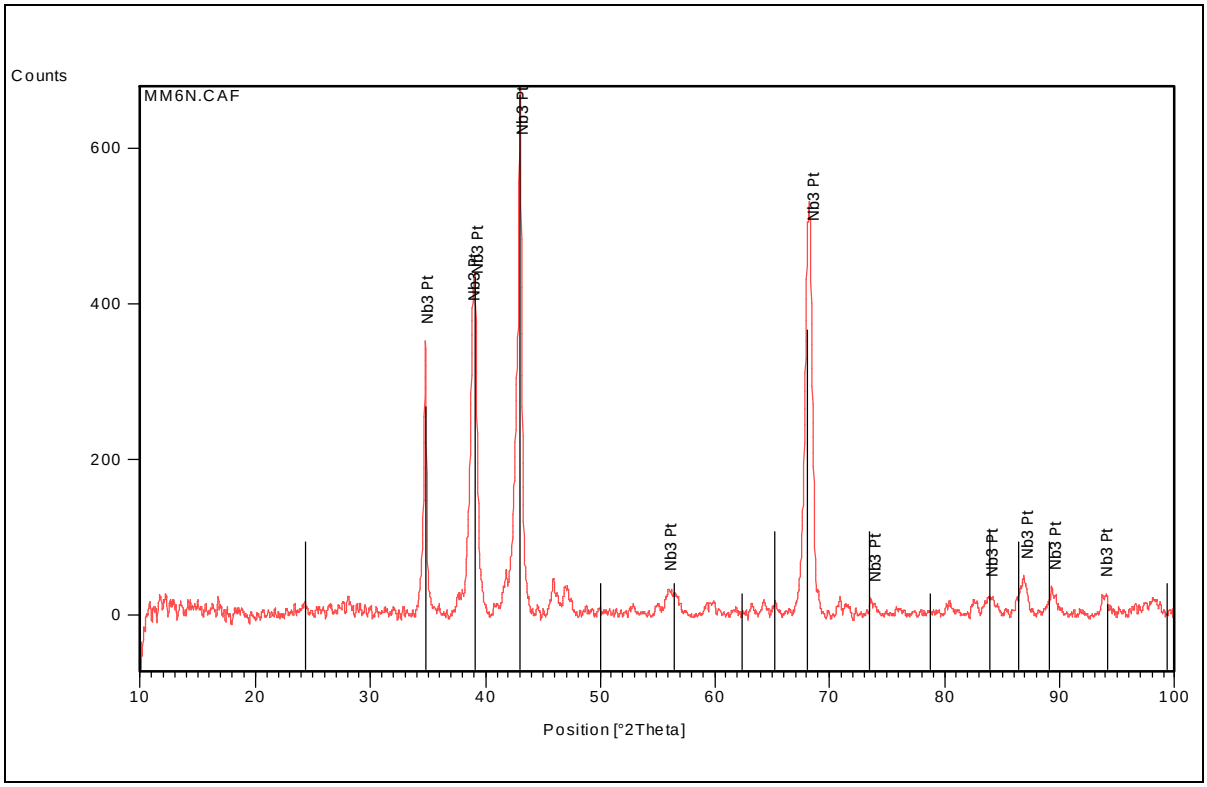

Figure 4.32. XRD spectrum of nominal Nb_{70}:Cr_{15}:Pt_{15} in the as-cast condition, showing black ~Nb_3Pt peaks.

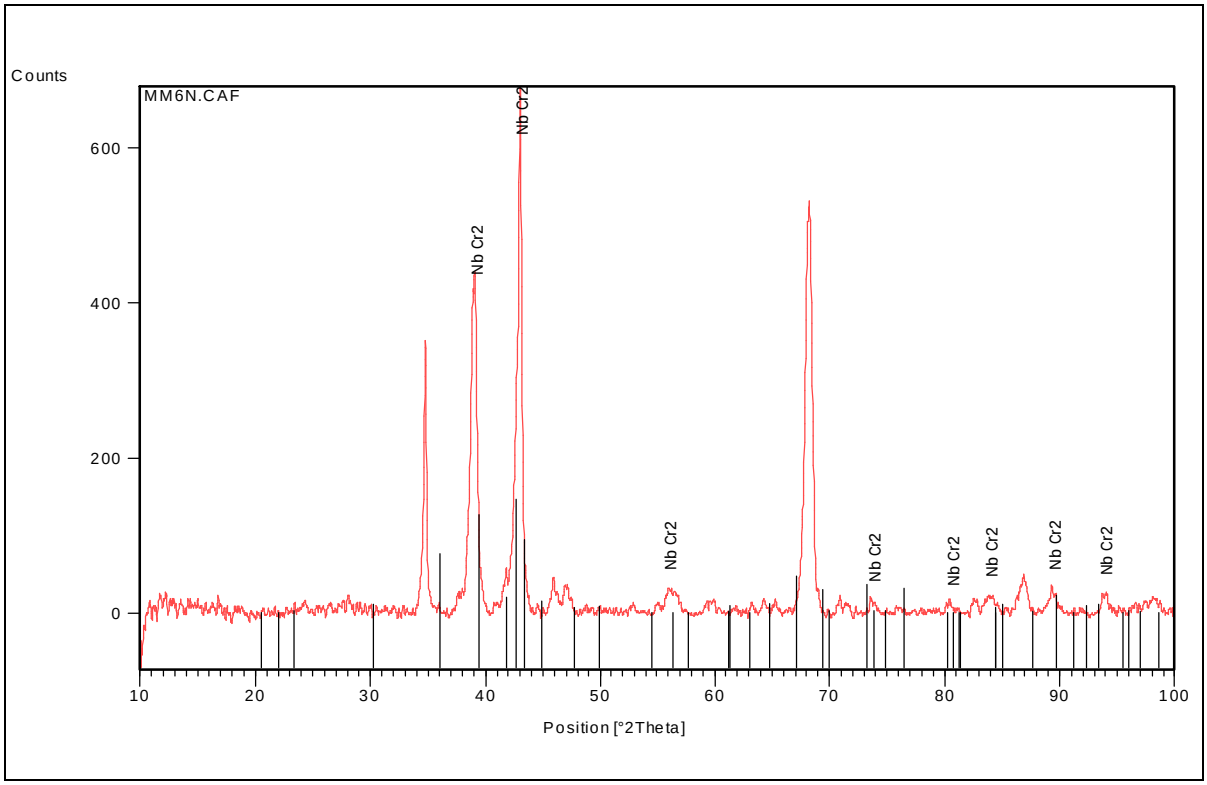

Figure 4.33. XRD spectrum of nominal Nb_{70}:Cr_{15}:Pt_{15} in the as-cast condition, showing black ~$NbCr_2$ peaks.

4.1.7 Nominal $Nb_{30}:Cr_{10}:Pt_{60}$, Sample 7

The nominal $Nb_{30}:Cr_{10}:Pt_{60}$ alloy possessed a microstructure of mainly light ~$\beta NbPt_3$ needles, with cored medium-grey to dark (Pt) phase, as shown in Figures 4.34 a and b. Table 4.10 gives the EDX analyses, and these are plotted in Figure 4.35, showing the overall composition to be on the tie-line joining the phase compositions. There were higher experimental errors for (Pt) due to coring. The XRD spectrum shown in Figures 4.36–4.38 was poor, with a low signal: background ratio. The existence of ~$\beta NbPt_3$ and (Pt) was confirmed by X-ray diffraction, as shown in Figures 4.37 to 4.38, with varying shifts for ~$\beta NbPt_3$. The (Pt) phase showed an excellent fit with some minor shifts to the left from the X-ray diffraction database lines (ICDD). A major peak was found at position $^{o}2\theta$ = 39.379, which matched ~$\beta NbPt_3$ and (Pt).

The solidification sequence deduced from the microstructure is as follows:

$$L \rightarrow \sim\beta NbPt_3$$

followed by the formation of a peritectic

$$L + \sim\beta NbPt_3 \rightarrow (Pt)$$

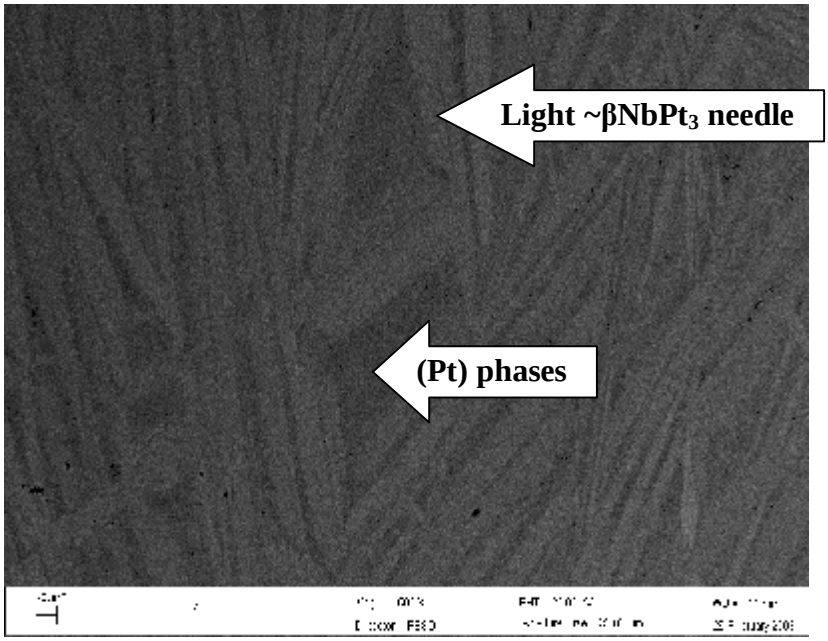

(a)

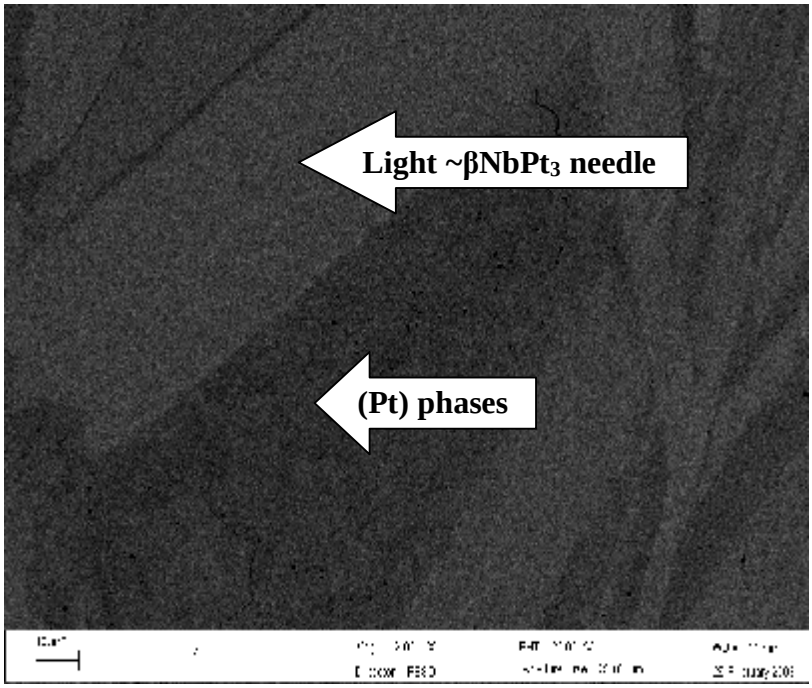

(b)

Figure 4.34 a-b. SEM-BSE images of the nominal $Nb_{30}:Cr_{10}:Pt_{60}$ alloy in the as–cast condition, showing light needles of ~β$NbPt_3$, medium-grey (Pt) and dark (Pt) phase.

Table 4.10. EDX phase analyses for nominal $Nb_{30}:Cr_{10}:Pt_{60}$ (at.%) in the as–cast condition.

Phase contrast	**Nb**	**Cr**	**Pt**	**Phase**
Overall	20.9±1.0	8.6±0.4	70.4±0.8	-
Light (needles)	22.5±0.7	3.2±0.6	74.3±0.6	~β$NbPt_3$
Medium-grey	20.2±0.6	12.8±0.8	67.0±0.8	(Pt)
Dark	17.8±0.9	19.2±1.7	63.0±1.1	(Pt)

The (Pt) phase had less Pt than the ~β$NbPt_3$ needles, but this would be expected since the phase extends to ~71 at.% Cr in the Cr-Pt binary. Thus, the phase would be expected to have a wide extent in the ternary. Elsewhere, (Pt) solidified as dendrites, and it is unlikely to solidify as needles. This confirms the phase indentification.

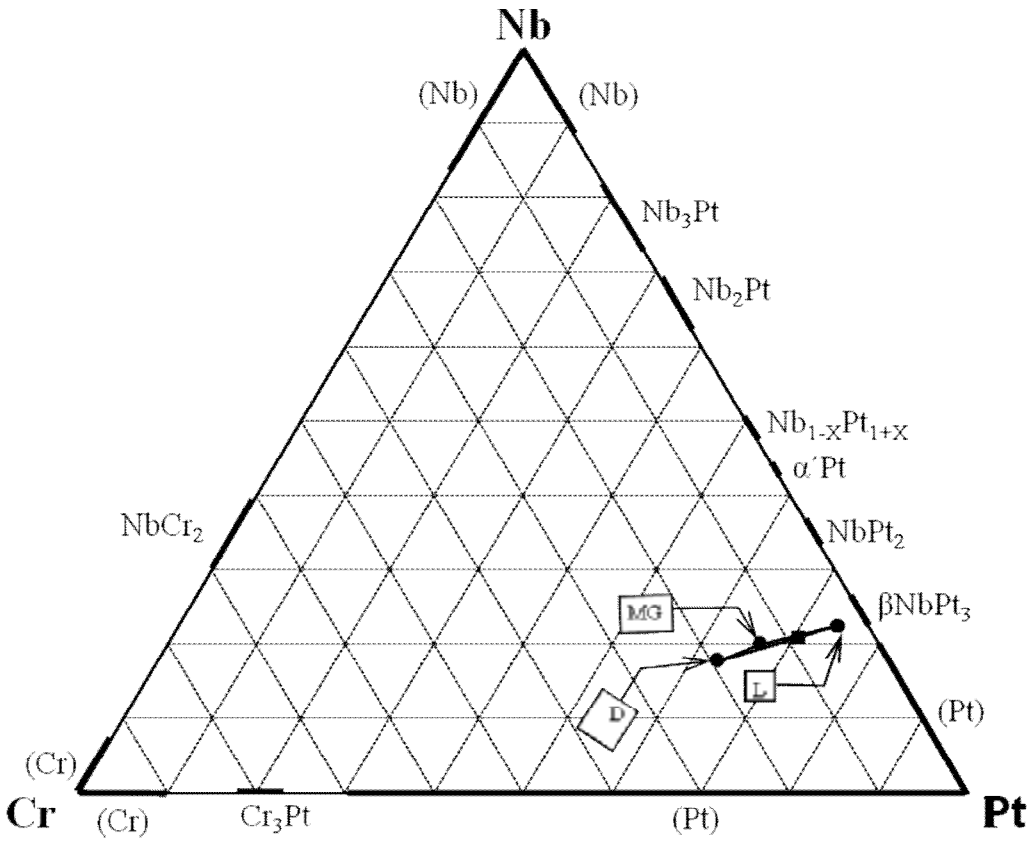

Figure 4.35. EDX phase compositions for the nominal $Nb_{30}:Cr_{10}:Pt_{60}$ (at.%) alloy in the as-cast condition: (L) light contrast; (MG) medium-grey contrast; (D) dark contrast phase; ■ overall composition; ● phase composition.

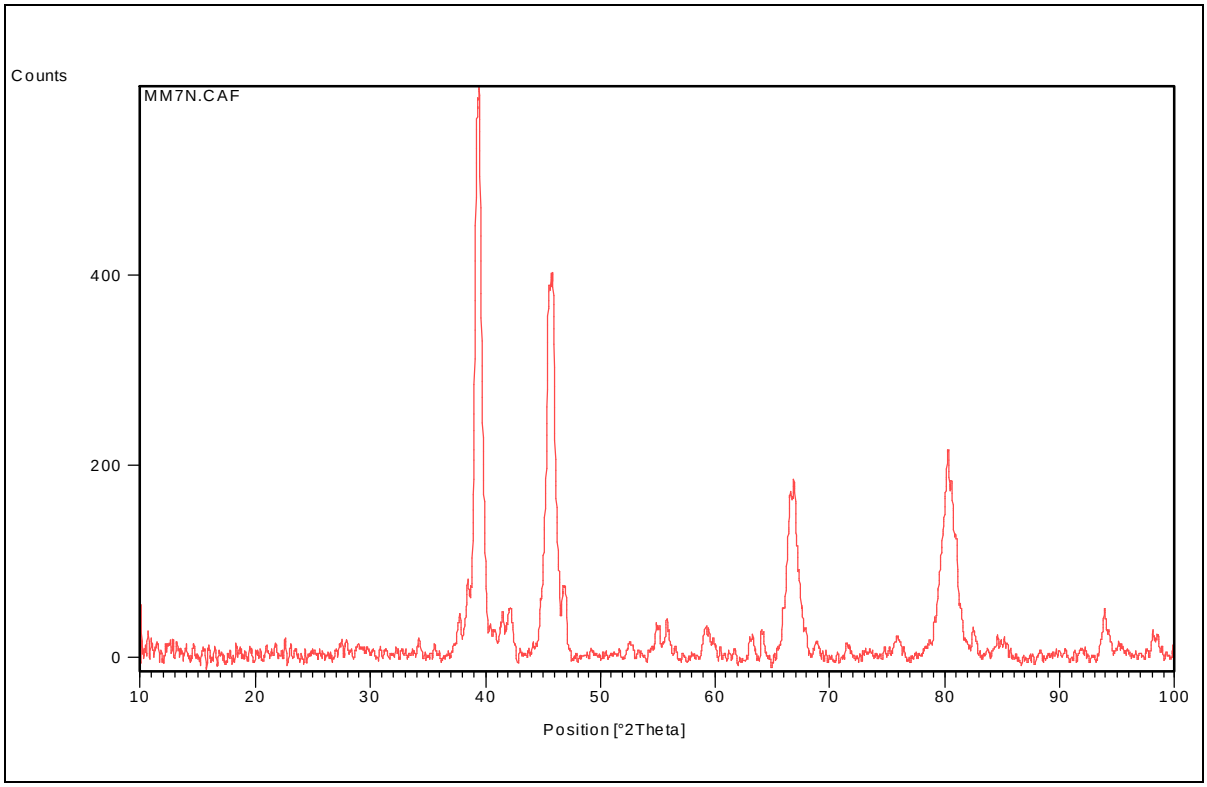

Figure 4.36. Raw XRD spectrum of nominal $Nb_{30}:Cr_{10}:Pt_{60}$ in the cast condition.

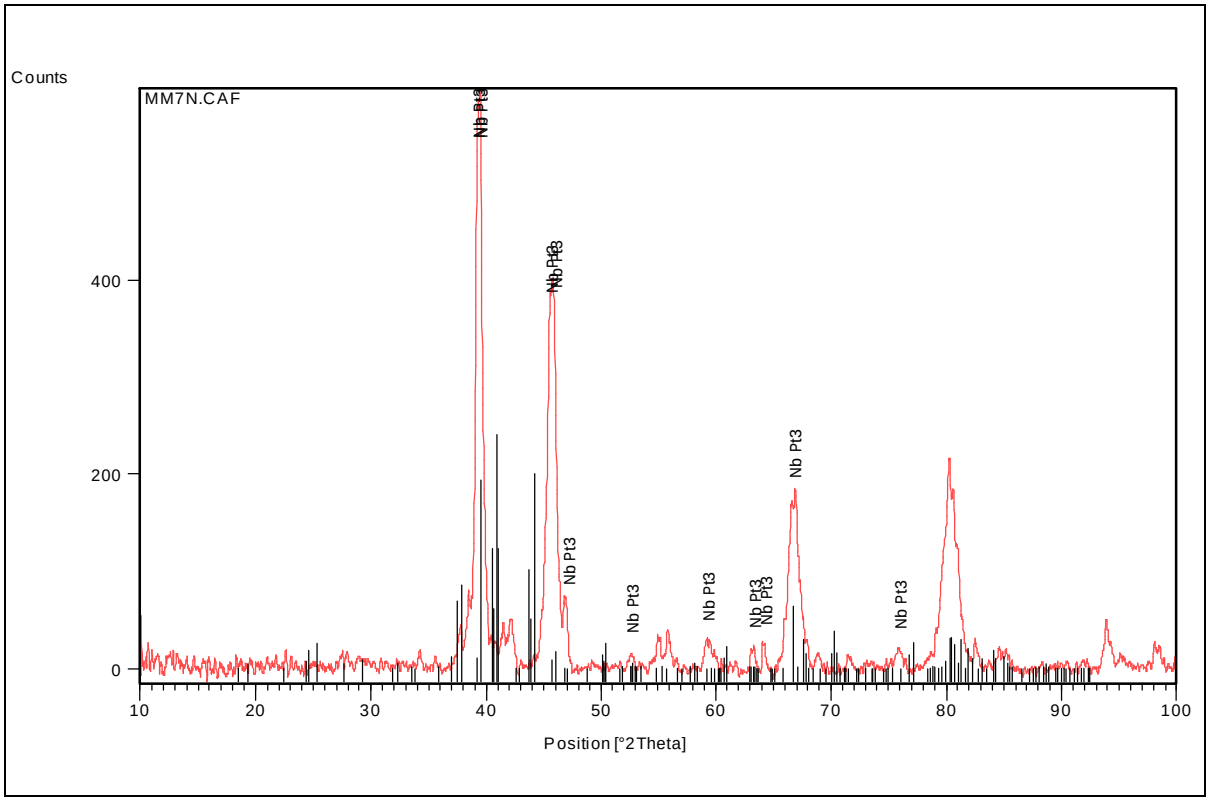

Figure 4.37. XRD spectrum of nominal $Nb_{30}:Cr_{10}:Pt_{60}$ in the cast condition, showing black ~$\beta NbPt_3$ peaks.

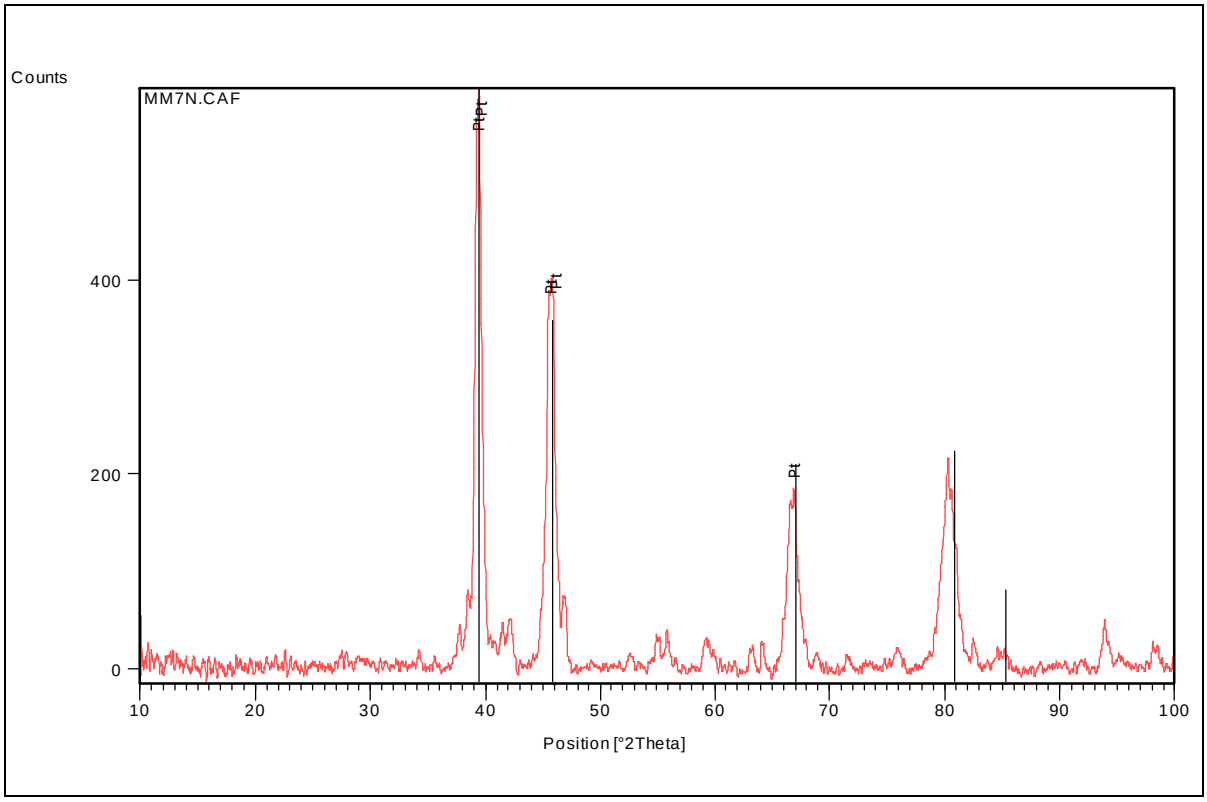

Figure 4.38. XRD spectrum of nominal Nb_{30}:Cr_{10}:Pt_{60} in the cast condition, showing black Pt peaks.

4.1.8 Nominal Nb_{60}:Cr_{10}:Pt_{30}, Sample 8

(a) Figure 4.39a shows the microstructure of nominal Nb_{60}:Cr_{10}:Pt_{30}, which comprised dark ~Nb_3Pt dendrites, cored medium-grey ~Nb_2Pt and light ternary phase 5 (τ5) phases. Table 4.11 gives the EDX analyses for this alloy, which were plotted in Figure 4.39 b, showing the overall composition to be on the tie-lines joining the phase compositions. There were slightly high experimental errors for the light and medium-grey phase compositions. The high errors for medium-grey phase composition were due to coring, and for light phase composition, due to its small size areas. The XRD spectrum shown in Figures 4.41–4.42 was quite good, with a high signal: background ratio and several sharp peaks. There were matches with ICDD for the ~Nb_3Pt phase peaks, with some slight peak shifts to the left, although not all peaks for ~Nb_3Pt were found in the spectrum. However, it was not possible to check for the presence of ~Nb_2Pt and τ5 phases, because of lack of data in the database (ICDD). Thus, the unidentified peaks are assumed to be from ~Nb_2Pt and τ5.

The solidification sequence interpretted from the microstructure is:

$$L \rightarrow \sim Nb_3Pt$$

followed by peritectic reaction

$$L + \sim Nb_3Pt \rightarrow \sim Nb_2Pt$$

and another peritectic reaction

$$L + \sim Nb_2Pt \rightarrow \tau 5 \text{ (Chapter 5: Discussion)}$$

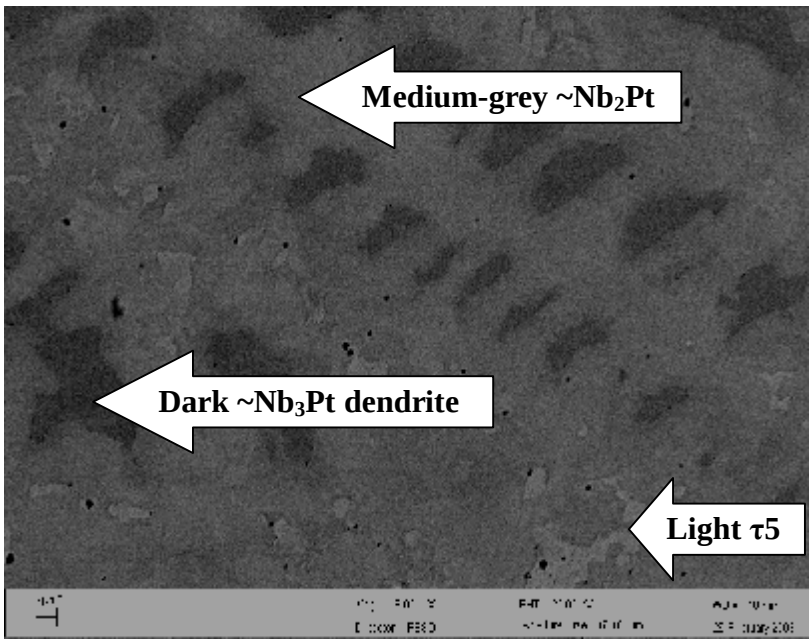

Figure 4.39 a. SEM-BSE image of the nominal $Nb_{60}:Cr_{10}:Pt_{30}$ alloy in the as–cast condition, showing dark ~Nb_3Pt dendrites, medium-grey ~Nb_2Pt and light τ5.

Table 4.11. EDX phase analyses for nominal $Nb_{60}:Cr_{10}:Pt_{30}$ (at.%) in the as–cast condition, as shown in Figure 4.39 a.

Phase contrast	Nb	Cr	Pt	Phase
Overall	56.1±0.3	9.0±0.6	34.9±0.3	-
Dark (dendrites)	66.3±0.4	5.1±0.2	28.6±0.3	~Nb_3Pt
Medium-grey	55.9±1.9	9.5±1.1	34.6±0.8	~Nb_2Pt
Light	40.9±1.1	14.8±0.5	44.3±0.6	τ5

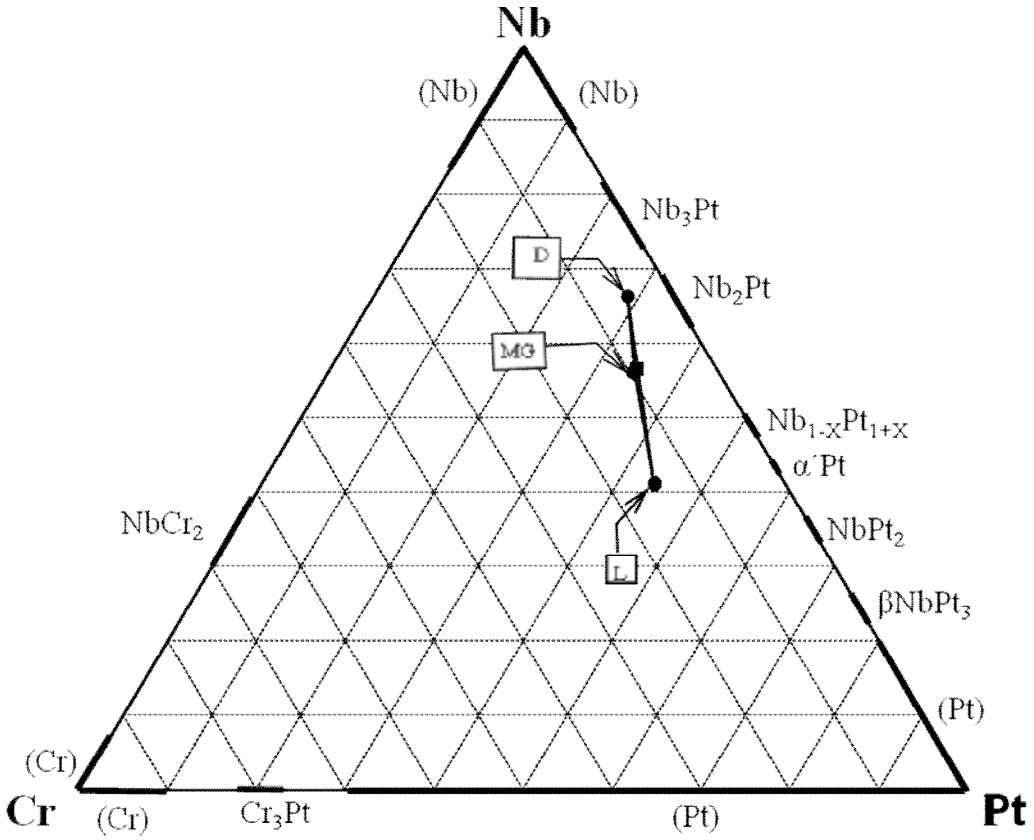

Figure 4.39 b. EDX phase compositions for the nominal $Nb_{60}:Cr_{10}:Pt_{30}$ (at.%) alloy in the as-cast condition: (L) light contrast; (MG) medium-grey contrast; (D) dark contrast phase; ■ overall composition; ● phase composition.

(b) From another part of nominal Nb_{60}:Cr_{10}:Pt_{30} alloy along the edge, the was a two-phase region, as shown in Figure 4.40 a. The two phases are light τ5 dendrites and medium-grey ~Nb_2Pt. Table 4.11a gives the EDX analyses and these are plotted in Figure 4.40 b. The overall composition was found to be slightly off the tie-line. There were slightly higher experimental errors for the medium-grey phase compositions.

The solidification sequence deduced from the microstructure is as follows:

$$L \rightarrow \tau5$$

followed by peritectic reaction

$$L + \tau5 \rightarrow \sim Nb_2Pt$$

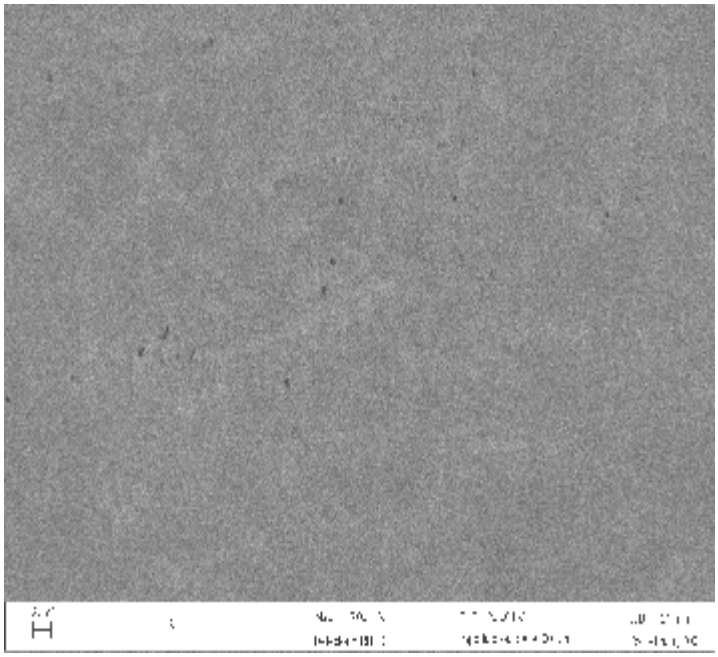

Figure 4.40 a. SEM-BSE image for the region near the edge in nominal Nb_{60}:Cr_{10}:Pt_{30} alloy in the as–cast condition, showing light τ5 dendrites and medium-grey ~Nb_2Pt.

Table 4.11a. EDX phase analyses for the region near the edge in nominal Nb_{60}:Cr_{10}:Pt_{30} (at.%) alloy in the as–cast condition, corresponding to Figure 4.40 a.

Phase contrast	**Nb**	**Cr**	**Pt**	**Phase**
Overall	56.7±0.5	9.0±0.2	34.3±0.3	-
Light	41.6±0.3	13.4±0.3	45.0±0.2	τ5
Medium-grey	62.1±0.9	6.2±0.5	31.7±0.6	~Nb_2Pt

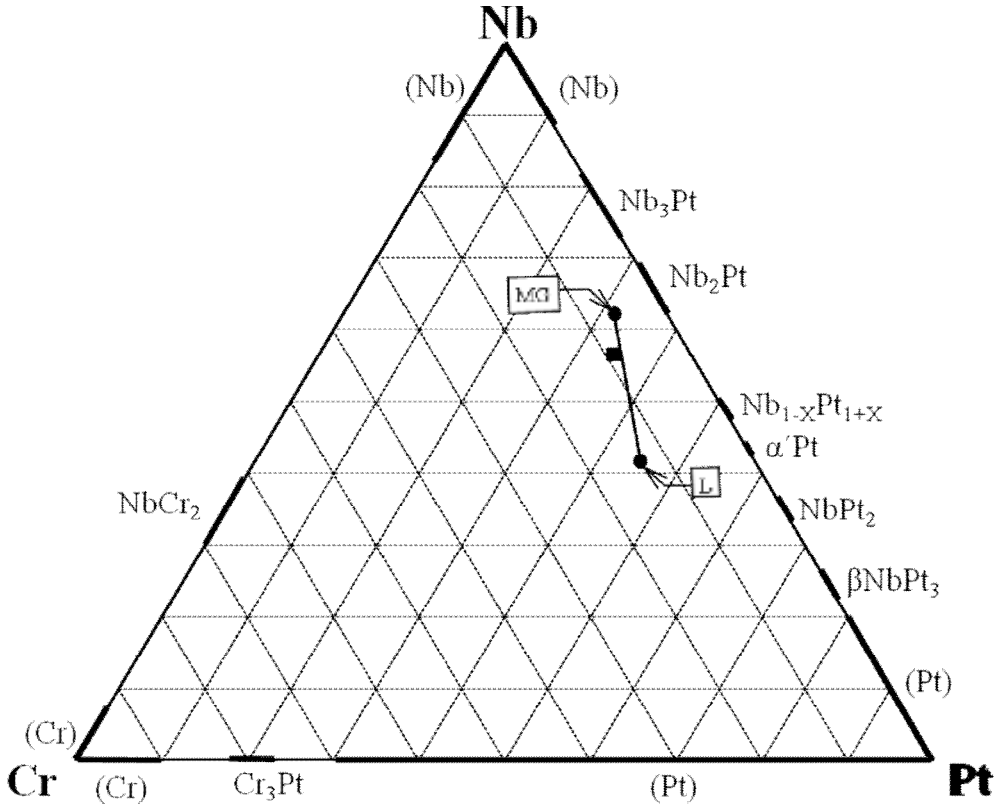

Figure 4.40 b. EDX phase compositions for the region near the edge in the nominal $Nb_{60}:Cr_{10}:Pt_{30}$ (at.%) alloy in the as-cast condition: (L) light contrast; (MG) medium-grey contrast; ■ overall composition; ● phase composition.

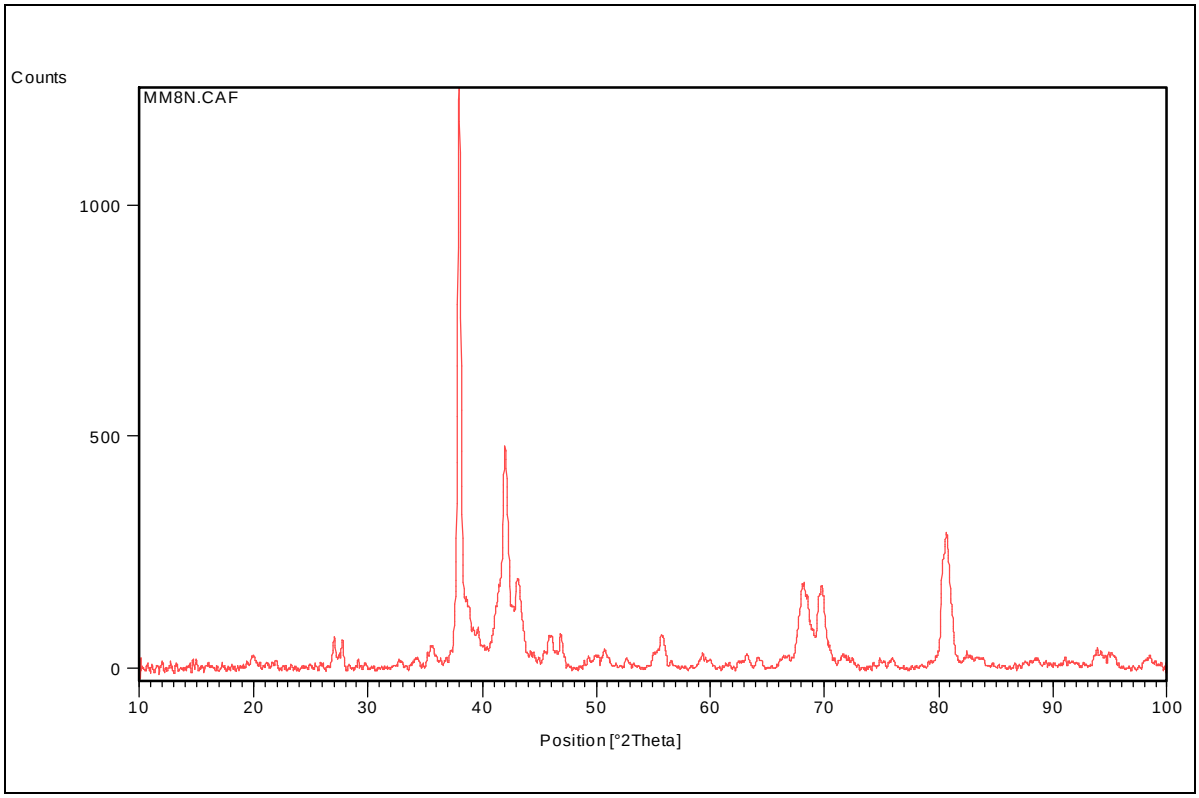

Figure 4.41. Raw XRD spectrum of nominal $Nb_{60}:Cr_{10}:Pt_{30}$ in the as-cast condition.

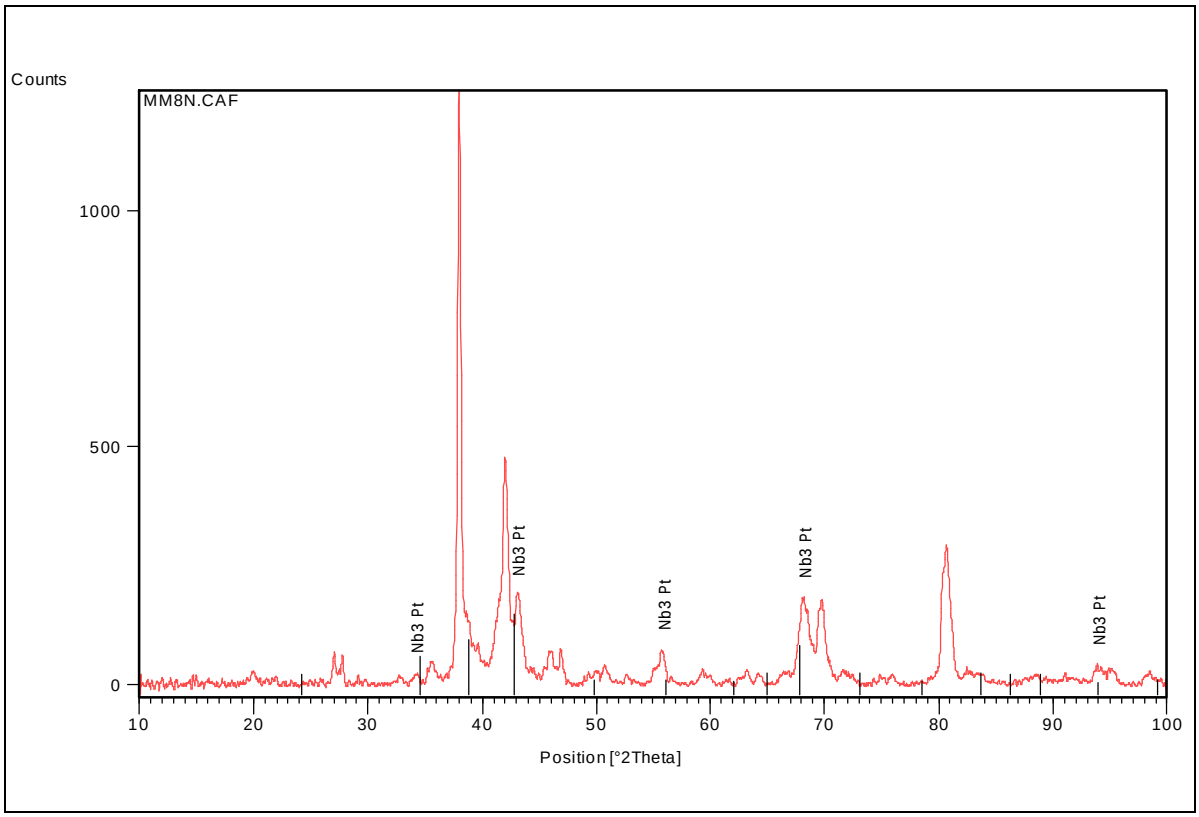

Figure 4.42. XRD spectrum of nominal $Nb_{60}:Cr_{10}:Pt_{30}$ in the as-cast condition, showing black ~Nb_3Pt peaks.

4.1.9 Nominal Nb_{24}:Cr_{23}:Pt_{53}, Sample 9

The nominal Nb_{24}:Cr_{23}:Pt_{53} alloy possessed a microstructure of mainly light cored ~$NbPt_2$ dendrites, and darker cored (Pt) phase, with some porosity, as can be seen in Figures 4.43 a and b. Table 4.12 gives the EDX analyses. These data were plotted in Figure 4.44, showing the overall composition to be on the tie-line between the phase compositions, but much closer to the dark (Pt) phase composition. There were fairly large experimental errors for some Cr and Pt analyses. The XRD spectrum shown in Figures 4.45–4.47 was good, with a high signal: background ratio. The existence of ~$NbPt_2$ and (Pt) was confirmed by XRD, as shown in Figures 4.46 to 4.47. The matches for the (Pt) phase were excellent with the ICDD, with very minor peak shifts to the right. There were also matches for ~$NbPt_2$, but with some peaks missing and shifts not been consistent. Very minor peak shifts to the right were also found for the ~$NbPt_2$ phase. A major peak was found at position $^{o}2\theta$ = 39.672, which matched ~$NbPt_2$ and (Pt).

The solidification sequence figured out is as follows:

$$L \rightarrow \sim NbPt_2$$

followed by peritectic reaction

$$L + \sim NbPt_2 \rightarrow (Pt)$$

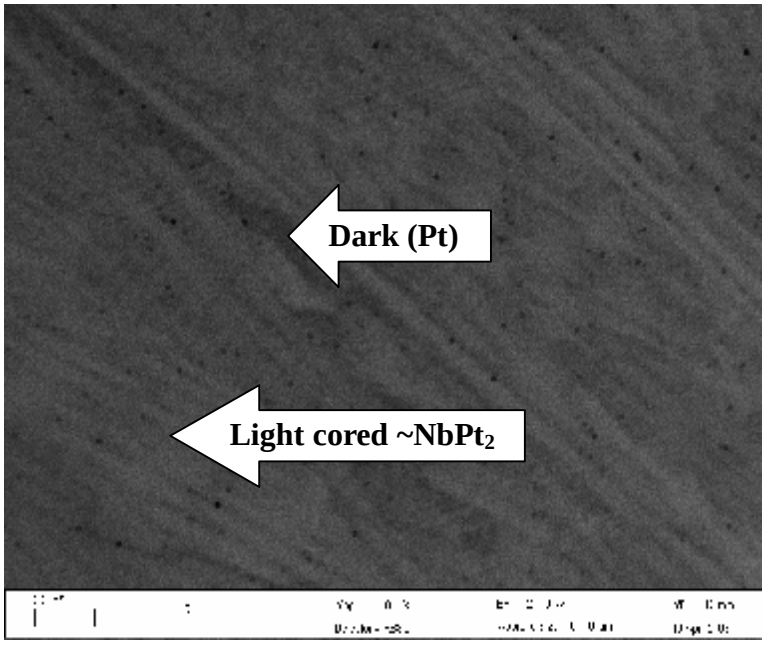

(a)

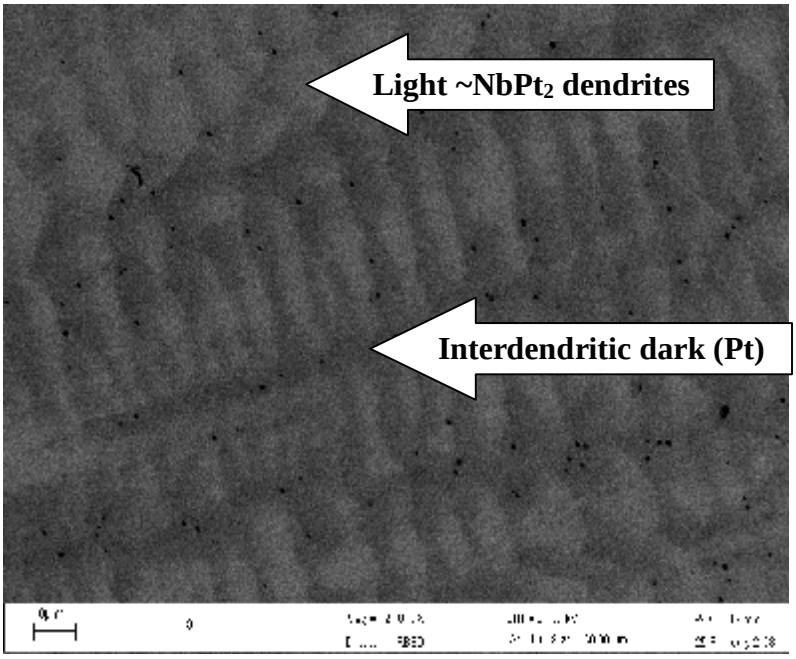

(b)

Figure 4.43 a-b. SEM-BSE images of the nominal $Nb_{24}:Cr_{23}:Pt_{53}$ alloy in the as–cast condition, showing light cored ~$NbPt_2$ dendrites, with darker cored (Pt) phase.

Table 4.12. EDX phase analyses for nominal $Nb_{24}:Cr_{23}:Pt_{53}$ (at.%) in the as–cast condition.

Phase contrast	**Nb**	**Cr**	**Pt**	**Phase**
Overall	21.7±0.1	23.6±0.4	54.7±0.4	-
Light inner dendrites	22.4±0.4	19.9±0.4	57.7±0.4	Cored ~$NbPt_2$
Light outer dendrites	24.2±0.2	23.5±1.1	52.3±1.0	Cored ~$NbPt_2$
Dark interdendritic	21.3±0.4	24.8±1.1	54.0±1.1	(Pt)

As for sample 7, there was also a wide extent for (Pt), which is expected from the binary Cr-Pt phase diagram.

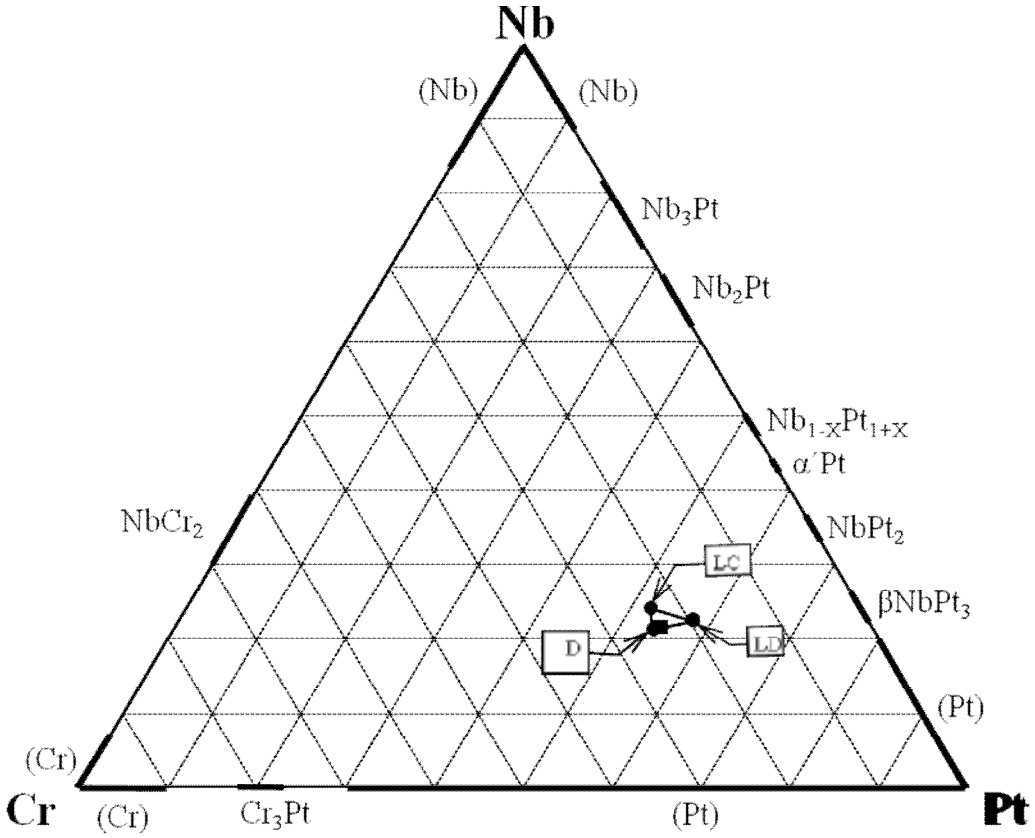

Figure 4.44. EDX phase compositions for the nominal $Nb_{24}:Cr_{23}:Pt_{53}$ (at. %) alloy in the as-cast condition: (LD) light dendrites contrast; (LC) light cored contrast; (D) dark contrast phase; ■ overall composition; ● phase composition.

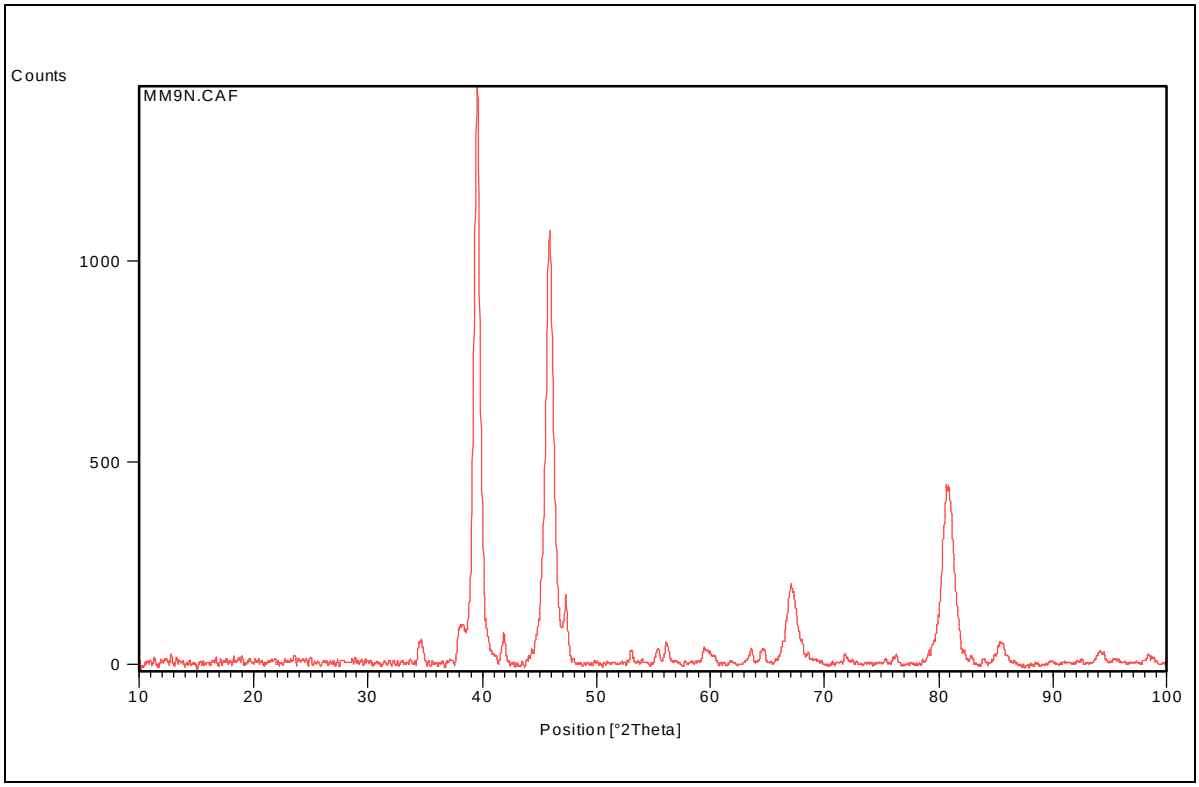

Figure 4.45. Raw XRD spectrum of nominal $Nb_{24}:Cr_{23}:Pt_{53}$ in the as-cast condition.

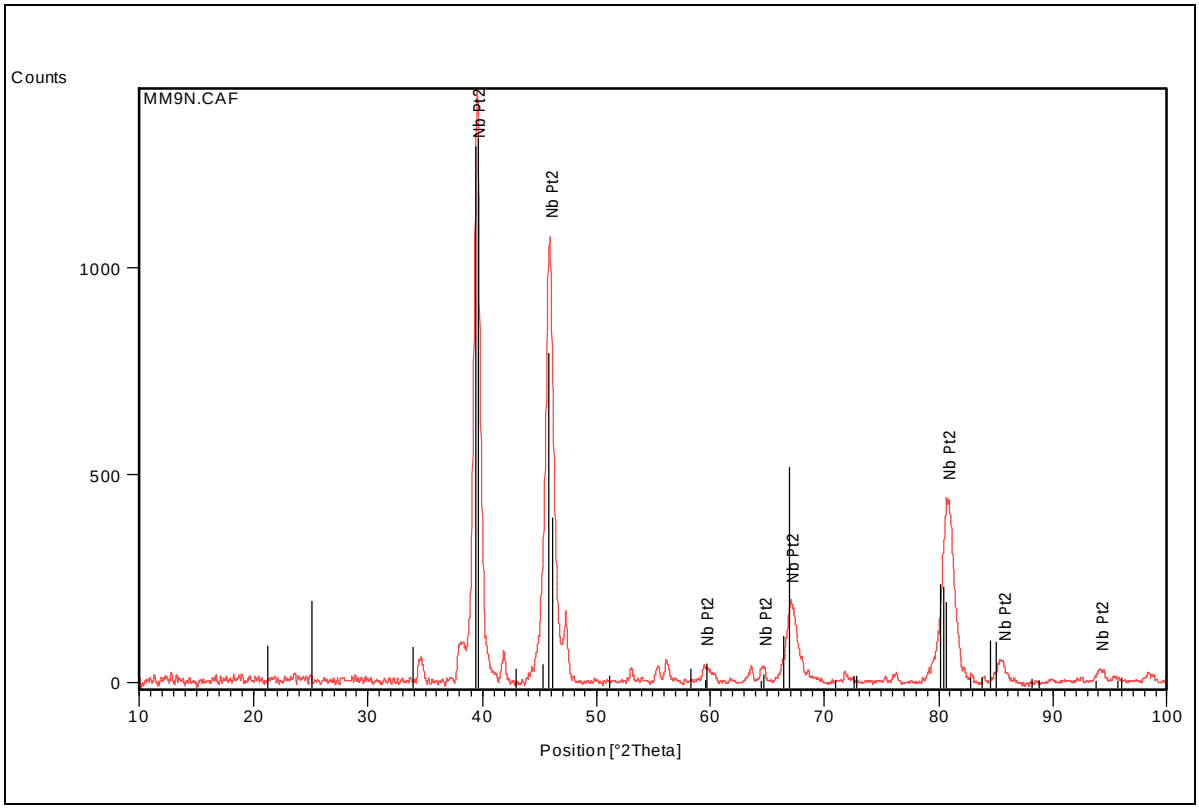

Figure 4.46. XRD spectrum of nominal $Nb_{24}:Cr_{23}:Pt_{53}$ in the as-cast condition, showing black ~$NbPt_2$ peaks.

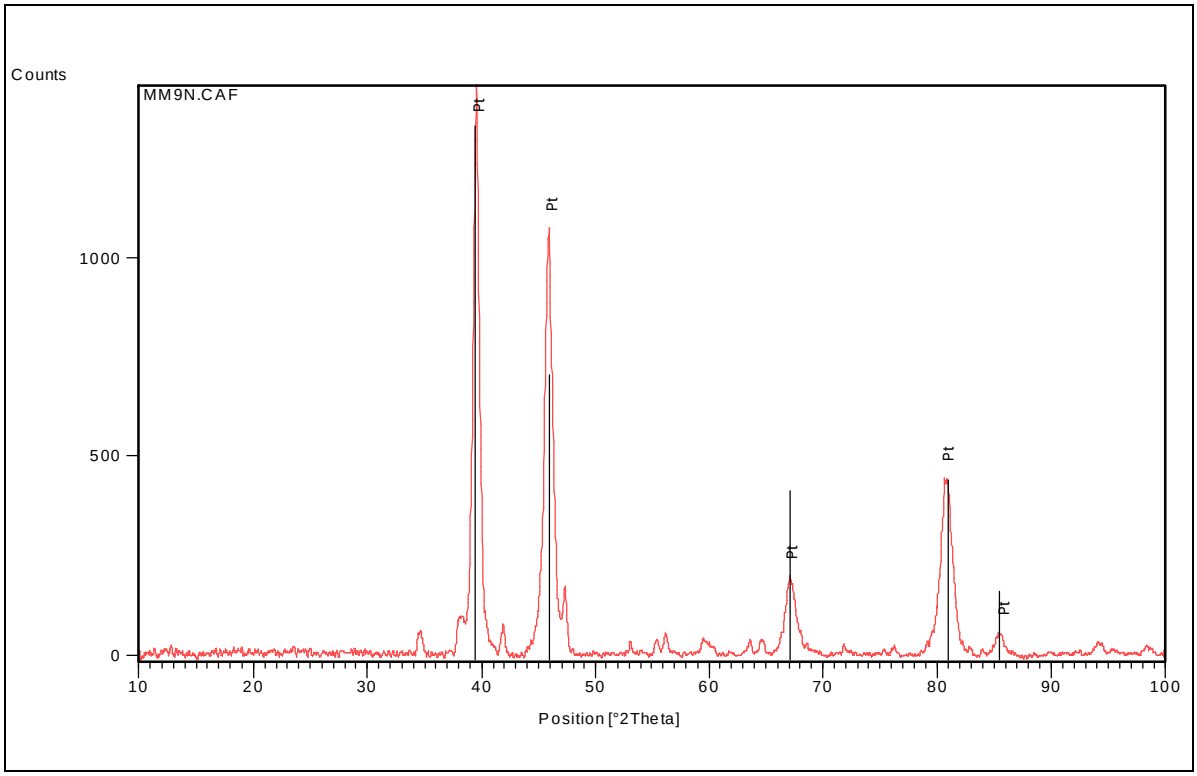

Figure 4.47. XRD spectrum of nominal Nb_{24}:Cr_{23}:Pt_{53} in the as-cast condition, showing black Pt peaks.

4.1.10 Nominal Nb_{50}:Cr_{30}:Pt_{20}, Sample 10

The nominal Nb_{50}:Cr_{30}:Pt_{20} alloy was really brittle and had many cracks. As can be seen in Figure 4.48, the sample was very inhomogeneous, showing unmelted pure Pt (light) and pure Nb (dark) regions. The EDX analyses on the unmelted pure Pt (light) and pure Nb (dark) contrast regions, confirmed they were pure Pt and Nb. This alloy had different microstructures and each part was analysed separately (a to f). There were different regions near to the unmelted pure Pt, a region between the unmelted pure Nb, and different regions along the edge of the alloy.

The XRD spectrum shown in Figures 4.61 to 4.64 was quite a poor spectrum with a low signal: background ratio and several sharp peaks. The existence of ~$NbCr_2$, (Nb) and (Pt) was confirmed, as can be seen in Figures 4.62 to 4.64, with some slight peak shifts varying in both ways for ~$NbCr_2$. The matches with the ICDD for (Nb) were excellent, with very minor peak shifts to the right. There were also matches for (Pt), with peak shifts to the right, and peak shifts were found to increase with the increase in angle. However, it was not possible to

check for the presence of ~$Nb_{1-X}Pt_{1+X}$, ~Nb_2Pt, τ4 and τ5 phases, because there was no data for them in the database (ICDD).

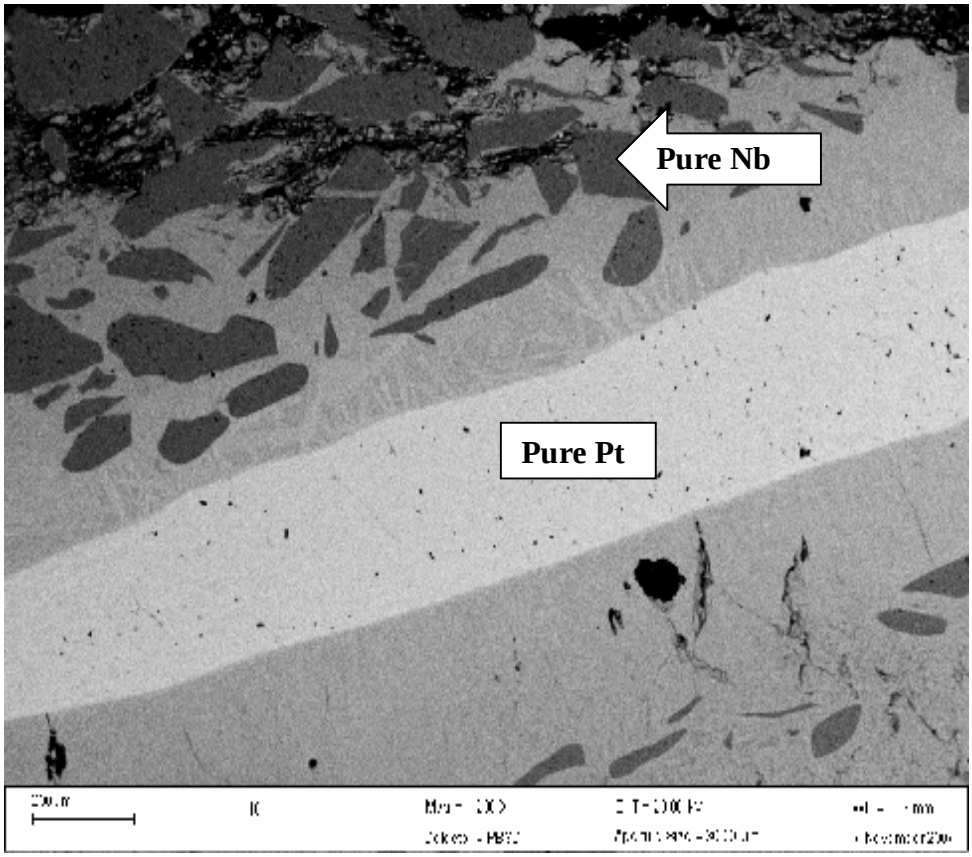

Figure 4.48. SEM-BSE image of the nominal Nb_{50}:Cr_{30}:Pt_{20} alloy in the as–cast condition, showing unmelted pure Pt (light) and pure Nb (dark) regions, together with many phases.

(a) A part of the sample near the unmelted pure light Pt showed a light ~$Nb_{1-X}Pt_{1+X}$ needle-like phase, and medium-grey ~Nb_2Pt with dark ternary phase 4 (τ4) phases between the needles, as shown in Figure 4.49. Table 4.13 gives the EDX analyses in this part of the sample. Most analyses were affected by other phases because of small size. Looking at all the other analyses and overall, it would appear there are two phases which are too small and difficult to discern, which are affecting each other. This region had high experimental errors, probably due to the inhomogeneous specimen, with small areas and difficult to distinguish phases. The phases were plotted, and fell into two groups. There were also two readings which were far away from the needles, and so could be the most accurate. These are also given in Table 4.13.

The solidification sequence deduced from the microstructure is:

$$L \rightarrow \sim Nb_{1-X}Pt_{1+X}$$

followed by the peritectic reaction

$$L + \sim Nb_{1-X}Pt_{1+X} \rightarrow \sim Nb_2Pt$$

and then another peritectic reaction

$$L + \sim Nb_2Pt \rightarrow \tau 4 \text{ (Chapter 5: Discussion)}$$

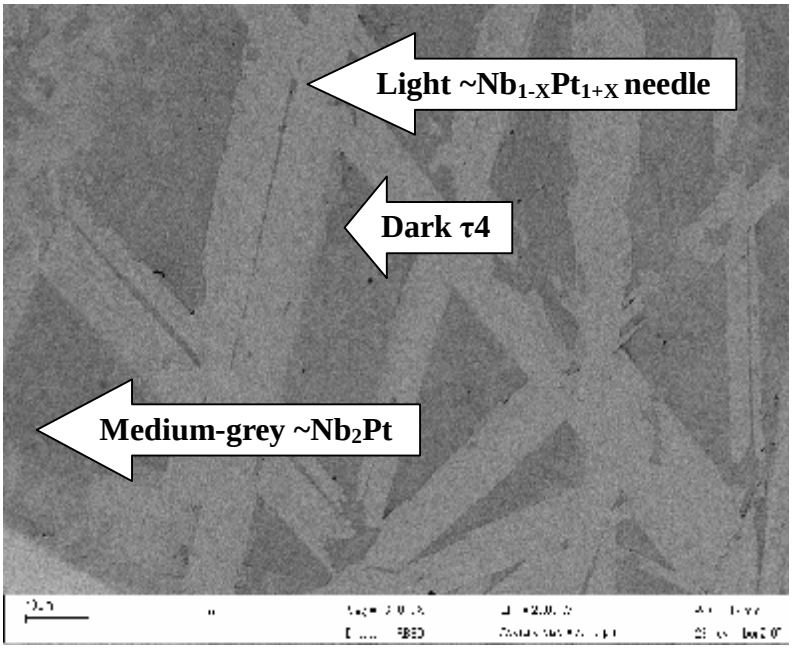

Figure 4.49. SEM-BSE image of the nominal Nb_{50}:Cr_{30}:Pt_{20} alloy in the as–cast condition, showing light $Nb_{1-X}Pt_{1+X}$ needles, and medium-grey ~Nb_2Pt with dark τ4 between the needles.

Table 4.13. EDX phase analyses for nominal $Nb_{50}:Cr_{30}:Pt_{20}$ (at.%) in the as–cast condition, as shown in Figure 4.49.

Phase contrast	Nb	Cr	Pt	Phase
Overall	45.9±1.0	8.7±0.8	45.4±1.1	-
Light (needles)	44.3±1.1	8.5±0.4	47.2±1.0	~$Nb_{1-X}Pt_{1+X}$
Medium-grey	38.1±0.8	18.4±0.7	43.5±0.5	τ5
Outlier	38.3	22.9	38.7	τ4
Dark	48.8±1.1	16.9±1.2	34.3±0.4	~Nb_2Pt
Outlier	41.1	24.5	34.3	τ4

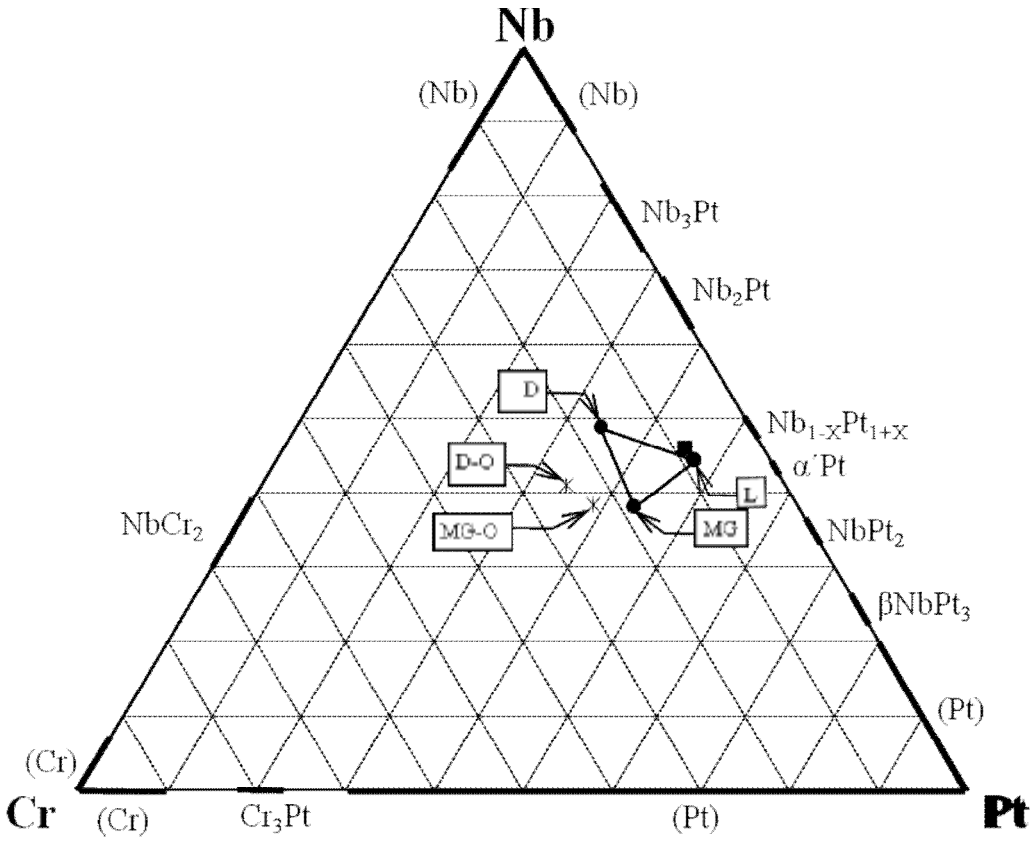

Figure 4.50. EDX phase compositions for the nominal $Nb_{50}:Cr_{30}:Pt_{20}$ (at.%) alloy in the as–cast condition: (L) light contrast; (MG) medium-grey contrast; (D) dark contrast phase; (MG-O) medium-grey outlier; (D-O) dark outlier; ■ overall composition; ● phase composition. Note that: ✸ represent outlier phase composition.

(b) Another part of the sample, near but on the other side of the unmelted pure Pt region, showed light ~$Nb_{1-X}Pt_{1+X}$ dendrites, with light ternary phase 5 (τ5) needles within some dendrites, and also medium-grey ternary phase 4 (τ4) interdendritic phase, as can be seen in Figures 4.51 a and b. This area had irregular dendrite surfaces, which indicate peritectic reactions. Table 4.14 gives the EDX phases' analyses of nominal Nb_{50}:Cr_{30}:Pt_{20} alloy, at this part of the sample and these data were plotted in Figure 4.52. Light dendrites had huge errors because only two analyses were obtained, neither of which was particularly good.

The solidification sequence deduced from the microstructure is:

$$L \rightarrow \sim Nb_{1-X}Pt_{1+X}$$

followed by the peritectic reaction

$$L + \sim Nb_{1-X}Pt_{1+X} \rightarrow \tau 5$$

And another peritectic reaction

$$L + \tau 5 \rightarrow \tau 4$$ (Chapter 5: Discussion)

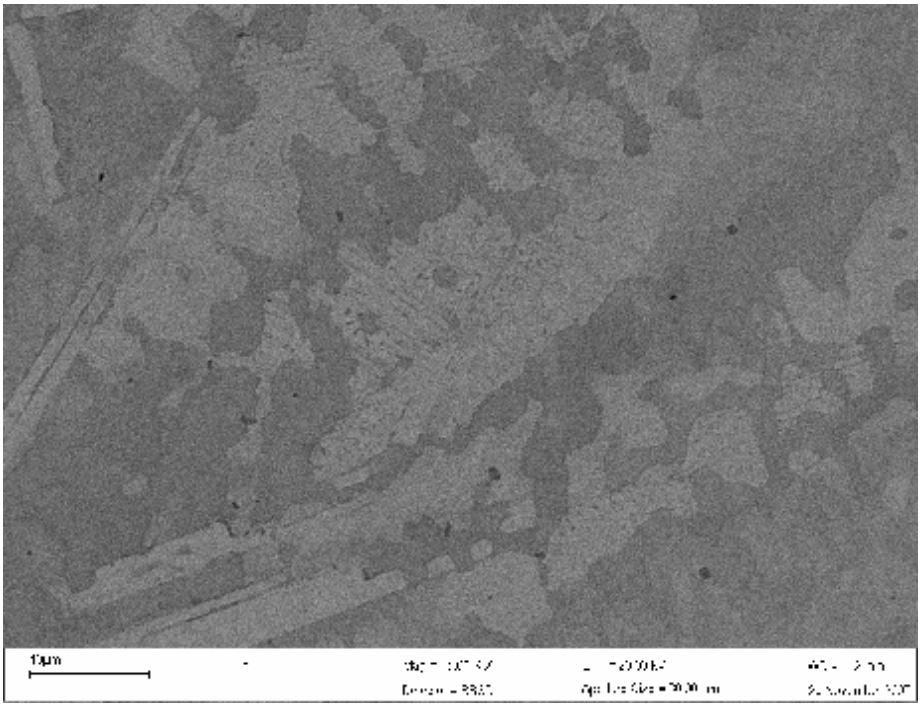

(a)

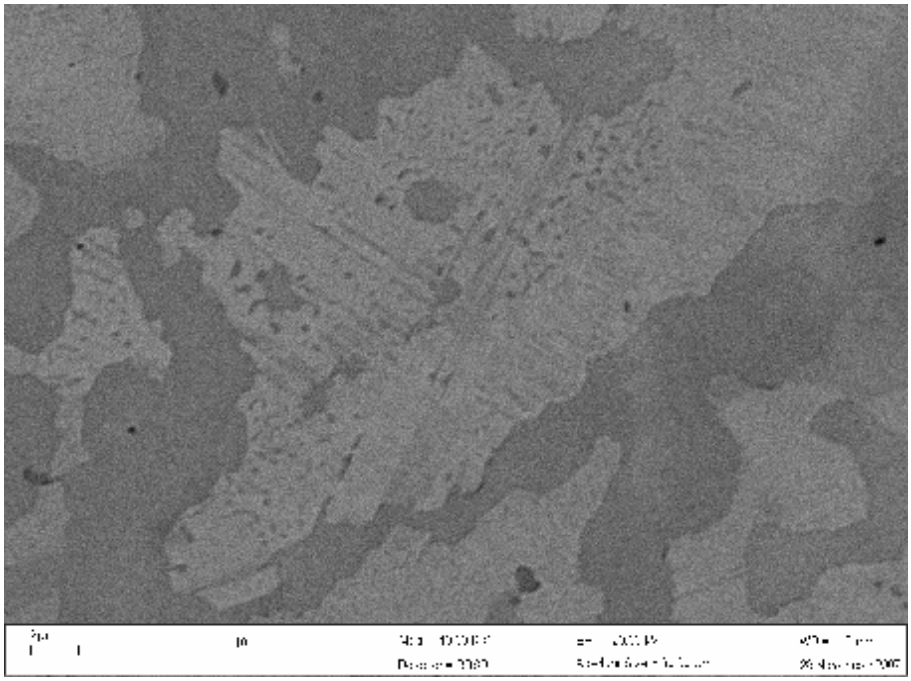

(b)

Figure 4.51 a-b. SEM-BSE image of the nominal $Nb_{50}:Cr_{30}:Pt_{20}$ alloy in the as–cast condition, showing light ~$Nb_{1-X}Pt_{1+X}$ dendrites, medium-grey τ4 interdendritic and light τ5 needles within some dendrites.

Table 4.14. EDX phase analyses for nominal $Nb_{50}:Cr_{30}:Pt_{20}$ (at.%) in the as–cast condition, as shown in Figure 4.51 (a) and (b) .

Phase contrast	**Nb**	**Cr**	**Pt**	**Phase**
Overall	40.3±1.4	20.1±0.7	39.6±0.8	-
Light (dendrites)	38.6±0.7	17.1±1.1	44.3±1.8	τ5
Decomposed light dendrites (2 phase) (DL)	40.7±2.2	15.0±1.9	44.4±0.8	~$Nb_{1-X}Pt_{1+X}$ + τ5
Light needles within some dendrites, (LN)	42.1±1.4	12.7±0.7	45.2±0.8	~$Nb_{1-X}Pt_{1+X}$
Medium-grey interdendritic (lighter-inner) (MG-LI)	50.5±0.4	13.9±0.4	35.7±0.3	~Nb_2Pt
Medium-grey interdendritic (darker-outer) (MG-DO)	46.4±0.6	18.7±0.7	34.9±1.2	τ4

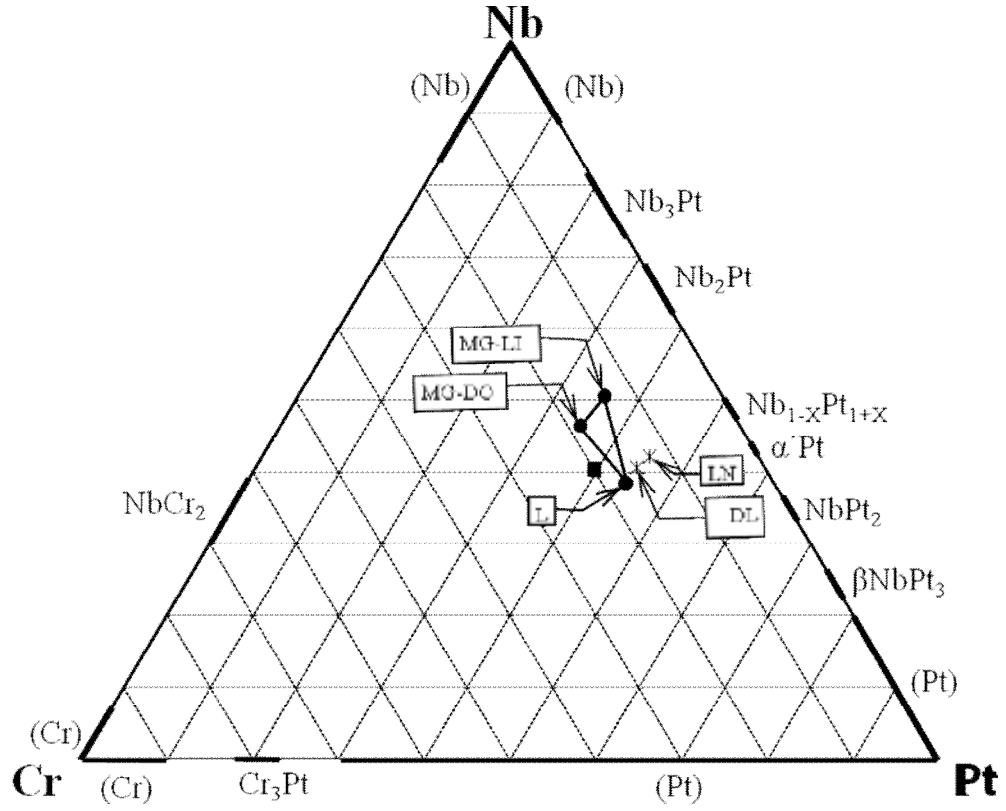

Figure 4.52. EDX phase compositions for the nominal $Nb_{50}:Cr_{30}:Pt_{20}$ (at.%) alloy in the as–cast condition: (L) light contrast; (LN) light needles within dendrites; (DL) decomposed light dendrites; (MG-LI) medium-grey lighter-inner contrast phase; (MG-DO) medium-grey dark-outer contrast phase; ■ overall composition; ● phase composition.

(c) From the region between the unmelted Nb, the alloy comprised medium-grey ~Nb_2Pt dendrites, very light ternary phase 4 (τ4) on the outside of the dendrites and a dark ~$NbCr_2$ interdendritic phase (Figures 4.53 a and b). Table 4.15 gives the EDX analyses, which are plotted in Figure 4.54, showing the overall composition to lie within the tie-triangle of the three phase compositions. There is no experimental error of the medium-grey phase because only the best analysis was used. This region had slightly high experimental errors. Ternary phase 4 (τ4) was too small to analyse.

The solidification sequence determined from these microstructures is as follows:

$$L \rightarrow \sim Nb_2Pt$$

followed by peritectic reaction

$$L + \sim Nb_2Pt \rightarrow \tau 4$$

and then ternary eutectic

$$L \rightarrow \sim Nb_2Pt + \tau 4 + \sim NbCr_2$$

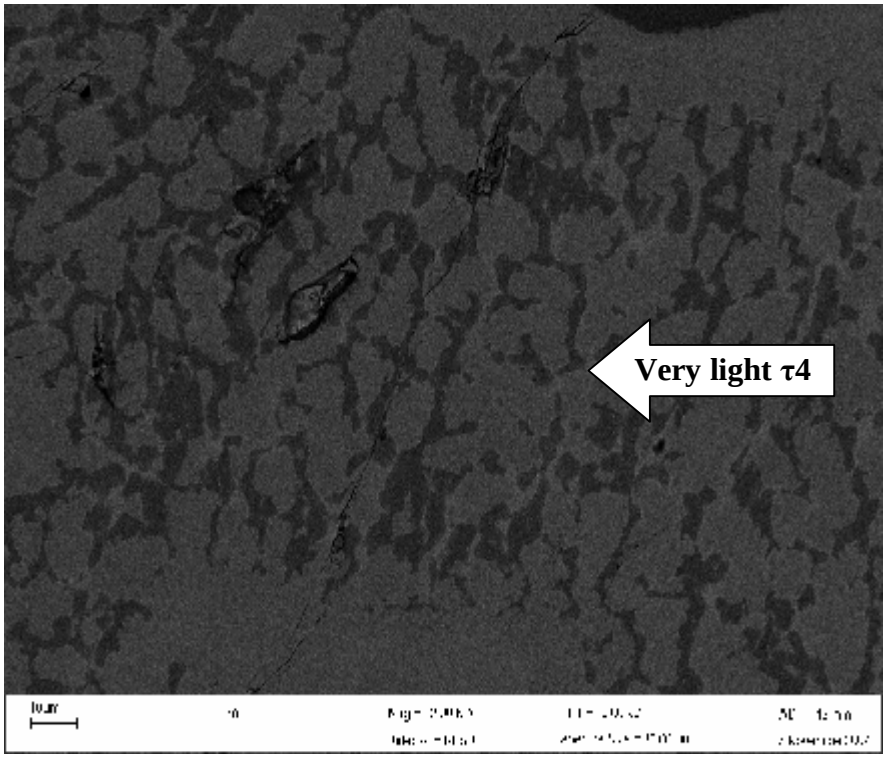

(a)

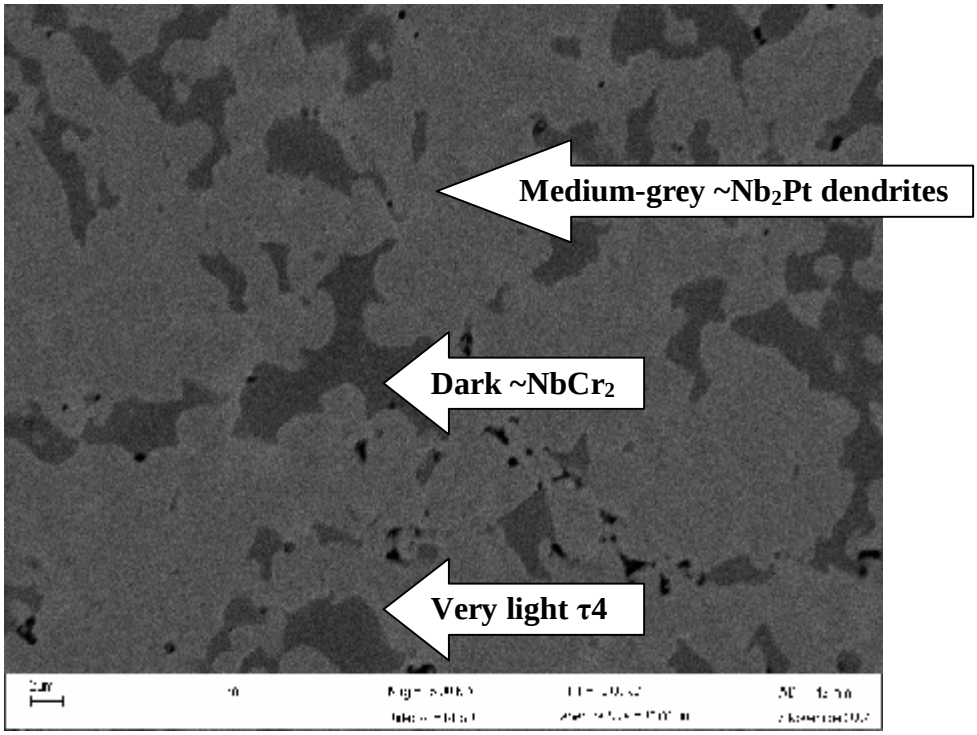

(b)

Figure 4.53 a–b. SEM-BSE images for the region between the unmelted pure Nb in nominal $Nb_{50}:Cr_{30}:Pt_{20}$ alloy in the as–cast condition, showing very light τ4, medium-grey ~Nb_2Pt dendrites and dark ~$NbCr_2$ interdendritic phase.

Table 4.15. EDX phase analyses for the region between the unmelted pure Nb in nominal $Nb_{50}:Cr_{30}:Pt_{20}$ (at.%) in the as–cast condition, as shown in Figure 4.53 (a) and (b) .

Phase contrast	**Nb**	**Cr**	**Pt**	**Phase**
Overall	45.3±1.5	33.1±0.9	21.7±0.8	-
Very light	45.7±1.2	23.2±0.5	31.2±0.7	τ4
Medium-grey (dendrites)	59.8	16.2	24.0	~Nb_2Pt
Dark (interdendritic)	33.2±0.2	49.6±0.1	17.1±0.1	~$NbCr_2$

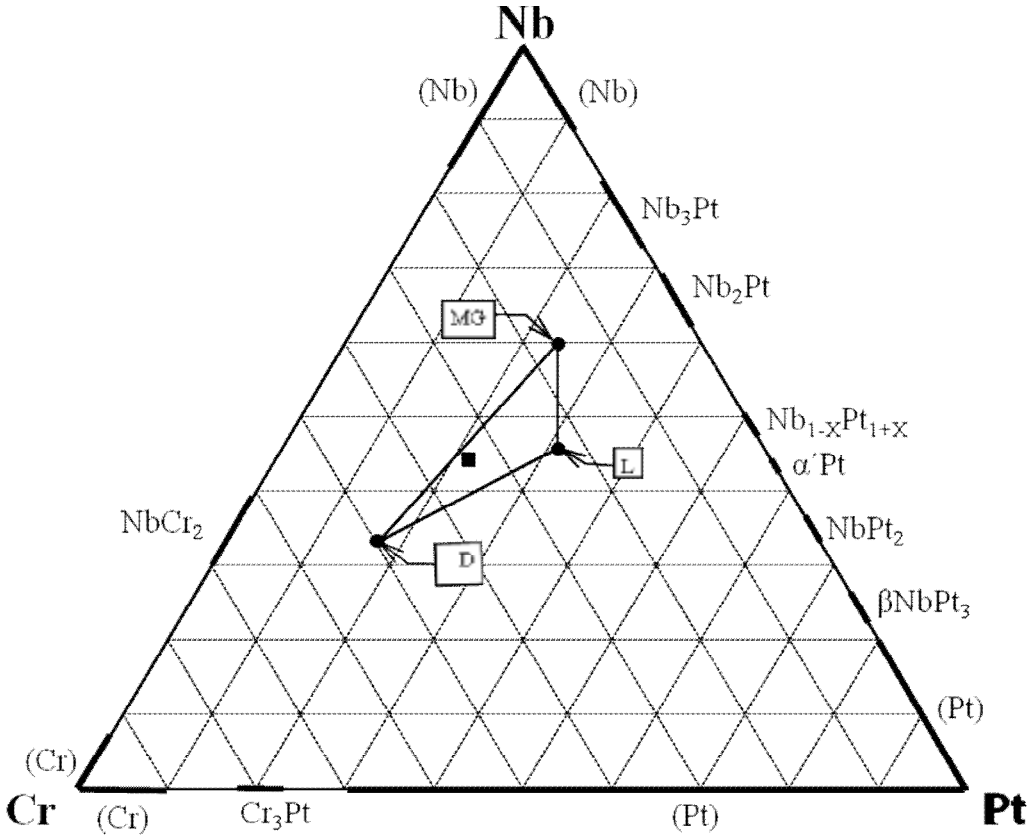

Figure 4.54. EDX phase compositions for the region between the unmelted Nb in nominal $Nb_{50}:Cr_{30}:Pt_{20}$ (at.%) alloy in the as–cast condition: (L) light contrast; (MG) medium-grey; (D) dark contrast phase; ■ overall composition; ● phase composition.

(d) From a region along the sample edge, this alloy showed a fine binary eutectic of ~$NbCr_2$ + ~Nb_2Pt, and a coarse ternary eutectic of ~$NbCr_2$ + ~Nb_2Pt + τ4, as shown in Figures 4.55 a and b.Table 4.16 gives the EDX analyses in this part of the sample, and these were plotted in Figure 4.56. Ternary phase 4 (τ4) was too small to analyse. It is likely that light phase should be extrapolated towards ~Nb_2Pt, because it was most likely affected by the surrounding dark phase. Also the dark phase was too small to analyse accurately. Only one value was used for the coarse eutectic.

The solidification sequence deduced from the microstructure was a eutectic reaction:

$$L \rightarrow \sim NbCr_2 + \sim Nb_2Pt$$

followed by a ternary eutectic

$$L \rightarrow \sim NbCr_2 + \sim Nb_2Pt + \tau 4$$ (Chapter: 5 Discussion)

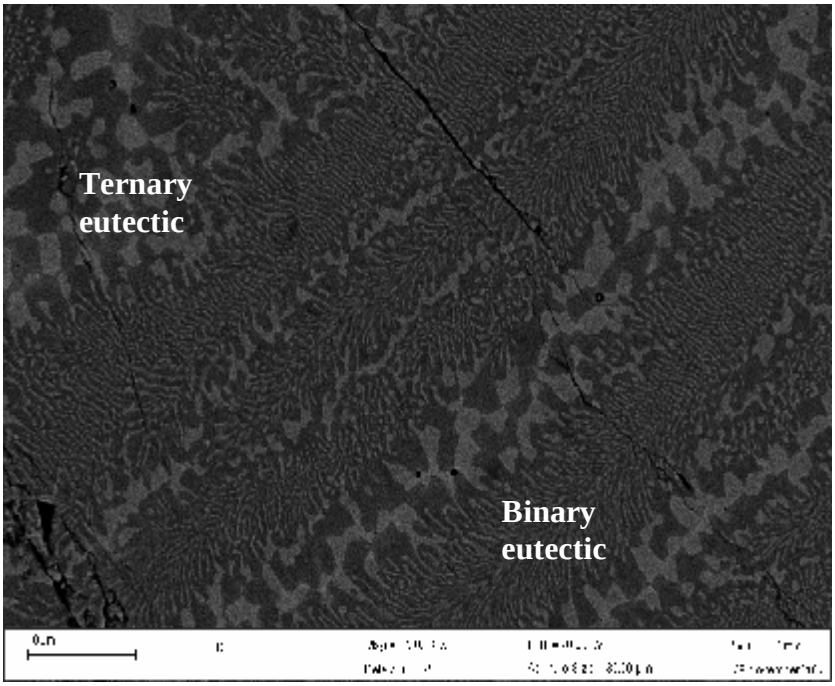

(a)

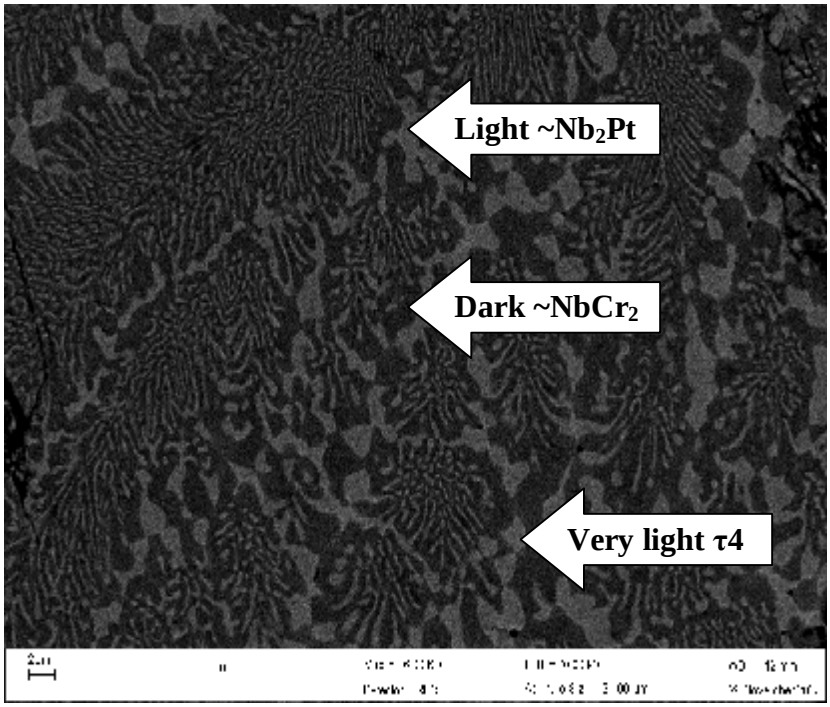

(b)

Figure 4.55. a-b SEM-BSE images of the nominal $Nb_{50}:Cr_{30}:Pt_{20}$ alloy in the as–cast condition, showing fine binary ~$NbCr_2$ (dark) + ~Nb_2Pt (light) eutectic and coarse ternary ~$NbCr_2$ + ~Nb_2Pt + τ4 (very light) eutectic.

Table 4.16. EDX phase analyses for nominal $Nb_{50}:Cr_{30}:Pt_{20}$ (at.%) in the as–cast condition, as shown in Figure 4.55 (a) and (b).

Phase contrast	**Nb**	**Cr**	**Pt**	**Phase**
Overall	42.5±0.3	38.6±0.2	18.9±0.1	-
Light	45.9±3.0	32.5±3.3	21.6±1.8	~Nb_2Pt
Dark	33.8±0.4	52.7±0.6	13.5±0.4	~$NbCr_2$
Binary eutectic overall	44.3±0.7	37.5±1.1	18.2±0.5	~$NbCr_2$ + ~Nb_2Pt
Ternary eutectic overall	44.3	35.2	20.5	~$NbCr_2$ + ~Nb_2Pt + τ4

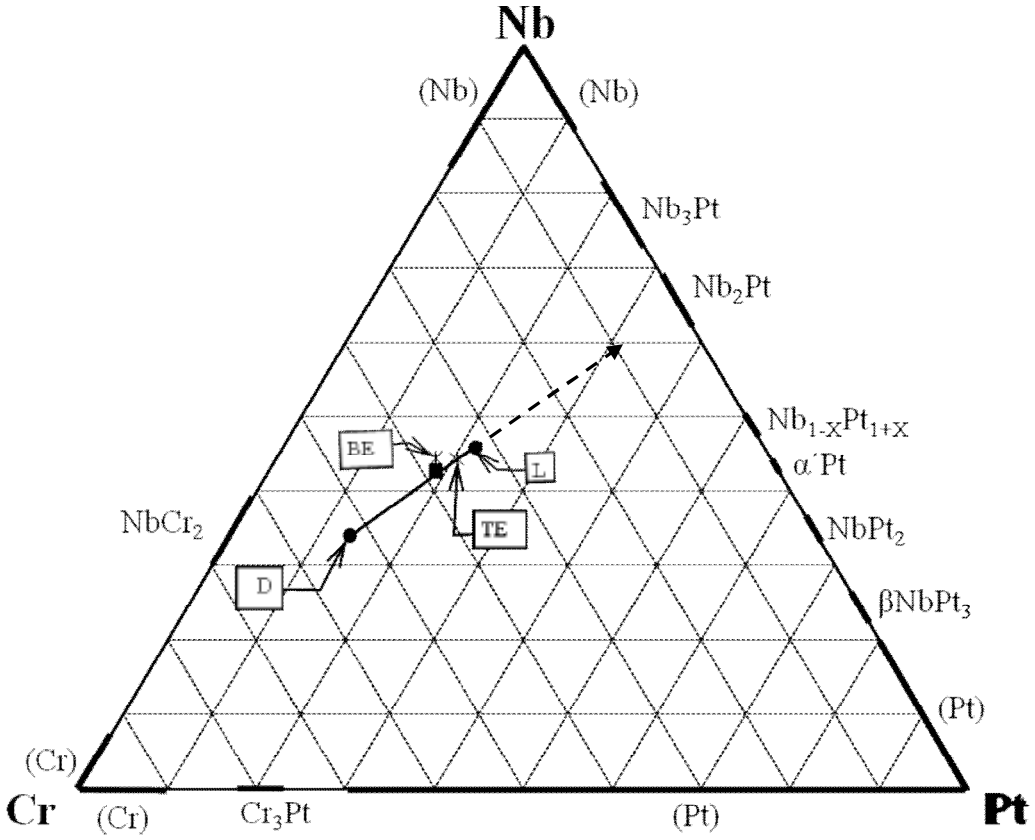

Figure 4.56. EDX phase compositions for the nominal $Nb_{50}:Cr_{30}:Pt_{20}$ (at.%) alloy in the as–cast condition. (L) light contrast; (D) dark contrast phase; (BE) binary eutectic; (TE) ternary eutectic; ■ Overall composition; ● phase composition; ✸ eutectic composition.

(e) In another part of the sample along the edge, the microstructure was different and comprised mainly medium-grey ~Nb_2Pt dendrites, light ternary phase 4 (τ4) around the dendrites and a dark interdendritic ~$NbCr_2$, as shown in Figure 4.57. The analyses of the medium-grey ~Nb_2Pt dendrites were affected by surrounding phases as shown by their small size and scatter in the data. The analysis was then extrapolated a little further to the ~Nb_2Pt boundary. Table 4.17 gives the EDX analyses and these are plotted in Figure 4.58, showing the overall composition to be slightly off the tie-line between light and dark phase. The light ternary phase 4 (τ4) phase composition had high experimental errors because of the small areas, which were too small to analyse accurately.

The solidification sequence deduced from the microstructure is as follows:

$$L \rightarrow \sim Nb_2Pt$$

followed by peritectic reaction

$$L + \sim Nb_2Pt \rightarrow \tau 4$$

and then ternary eutectic reaction

$$L \rightarrow \sim Nb_2Pt + \tau 4 + \sim NbCr_2$$ (Chapter: 5 Discussion)

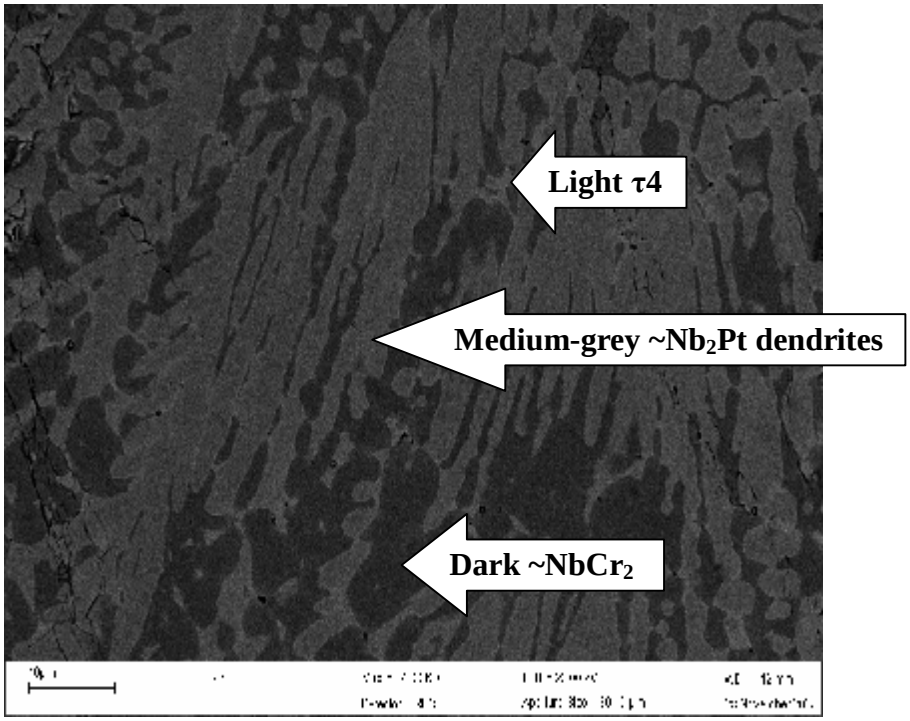

Figure 4.57. SEM-BSE image of the nominal $Nb_{50}:Cr_{30}:Pt_{20}$ alloy in the as–cast condition, showing medium-grey ~Nb_2Pt dendrites, light τ4 and dark ~$NbCr_2$ interdendritic phase.

Table 4.17. EDX phase analyses for nominal $Nb_{50}:Cr_{30}:Pt_{20}$ (at.%) in the as–cast condition, as shown in Figure 4.57.

Phase contrast	Nb	Cr	Pt	Phase
Overall	41.5±1.6	39.8±1.6	18.8±0.4	-
Light	45.3±3.3	28.1±3.2	26.6±1.1	τ4
Medium-grey (dendrites)	53.8±0.4	24.0±0.4	22.2±0.5	~Nb_2Pt
Dark (interdendritic)	38.4±0.4	46.2±0.3	15.4±0.2	~$NbCr_2$

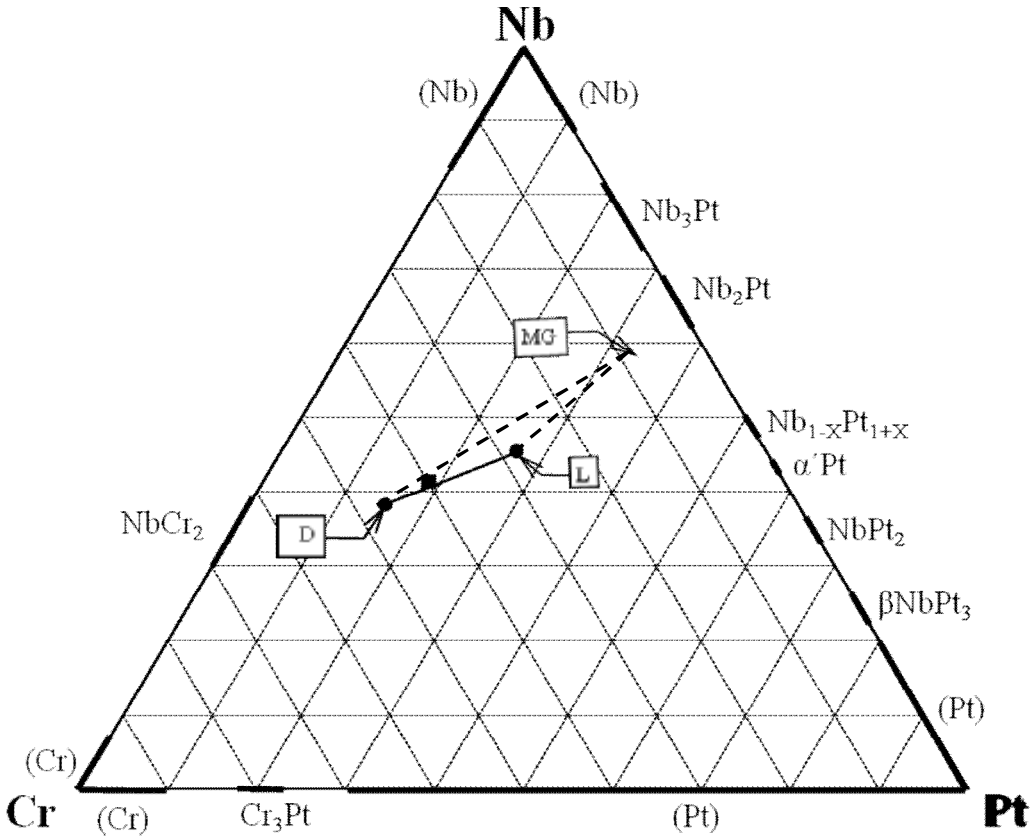

Figure 4.58. EDX phase compositions for the nominal $Nb_{50}:Cr_{30}:Pt_{20}$ (at.%) alloy in the as–cast condition: (L) light contrast; (MG) medium-grey contrast; (D) dark contrast phase; ■ overall composition; ● phase composition.

(f) There was a different microstructure along the edge, comprising of dark ~$NbCr_2$ dendrites and light ~Nb_2Pt with medium-grey ternary phase 4 (τ4) interdendritic phases, as seen in Figure 4.59. There was porosity associated with the light interdendritic phase. Table 4.18 gives the EDX analyses, which are shown in Figure 4.60. The overall composition is on the tie-line between the phase compositions, therefore this part could be in equilibrium. Conversely, the EDX experimental errors were high, and there was some porosity, which indicates that this part might not be in equilibrium. There was a very similar adjacent area with a lower proportion of dendrites and with the dendrites having fewer arms.

The solidification sequence deduced from the microstructure is:

$$L \rightarrow \sim NbCr_2$$

followed by ternary eutectic reaction

$$L \rightarrow \sim NbCr_2 + \sim Nb_2Pt + \tau 4 \text{ (Chapter: 5 Discussion)}$$

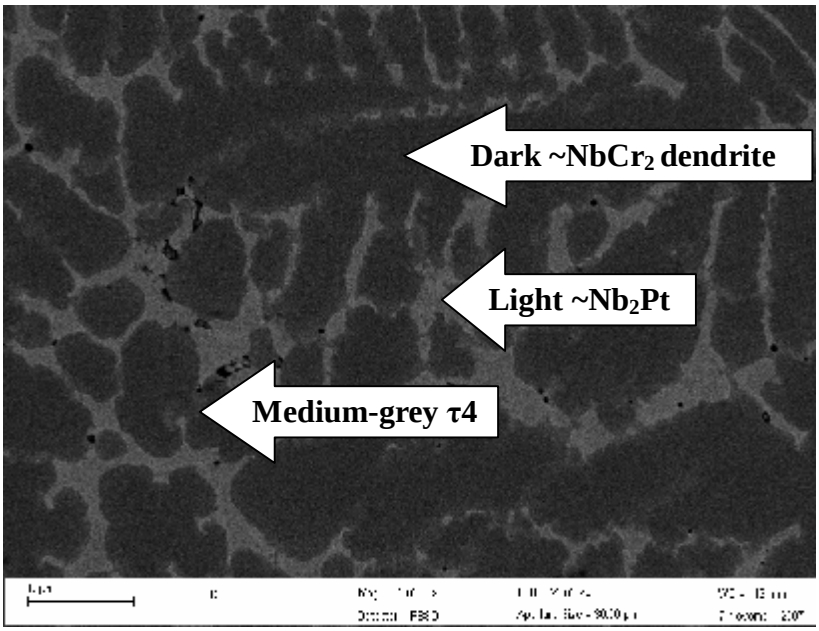

Figure 4.59. SEM-BSE image of the nominal $Nb_{50}:Cr_{30}:Pt_{20}$ alloy in the as–cast condition, showing dark ~$NbCr_2$ dendrites, and light ~Nb_2Pt with medium-grey τ4 interdendritic phases.

Table 4.18. EDX phase analyses for nominal $Nb_{50}:Cr_{30}:Pt_{20}$ (at.%) in the as–cast condition, as shown in Figure 4.59.

Phase contrast	**Nb**	**Cr**	**Pt**	**Phase**
Overall	39.3±1.0	42.4±1.5	18.3±0.5	-
Dark (dendrites)	34.3±0.5	52.2±0.8	13.4±0.5	~$NbCr_2$
Light (interdendritic)	47.7±0.7	25.9±1.3	26.5±1.5	~Nb_2Pt
Medium-grey(interdendritic)	-	-	-	τ4

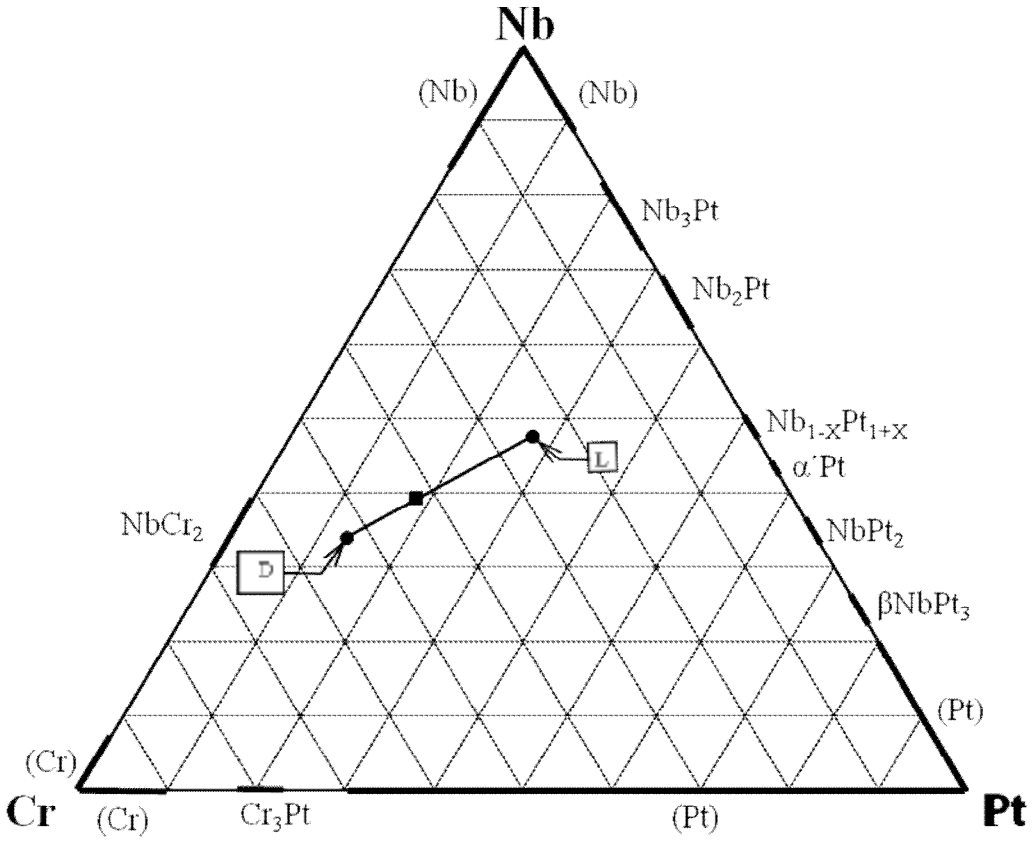

Figure 4.60. EDX phase compositions for the nominal $Nb_{50}:Cr_{30}:Pt_{20}$ (at.%) alloy in the as–cast condition: (L) light contrast; (D) dark contrast phase; ■ overall composition; ● phase composition.

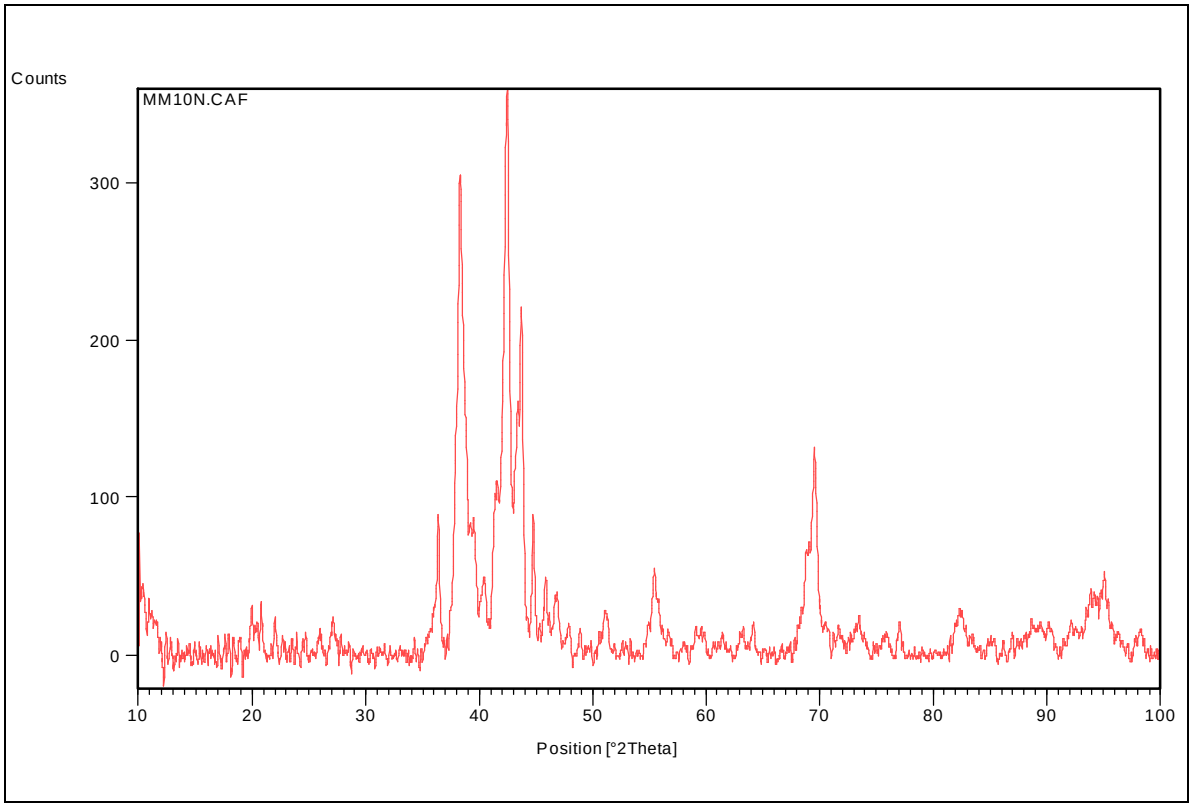

Figure 4.61. Raw XRD spectrum of nominal Nb_{50}:Cr_{30}:Pt_{20} in the as-cast condition.

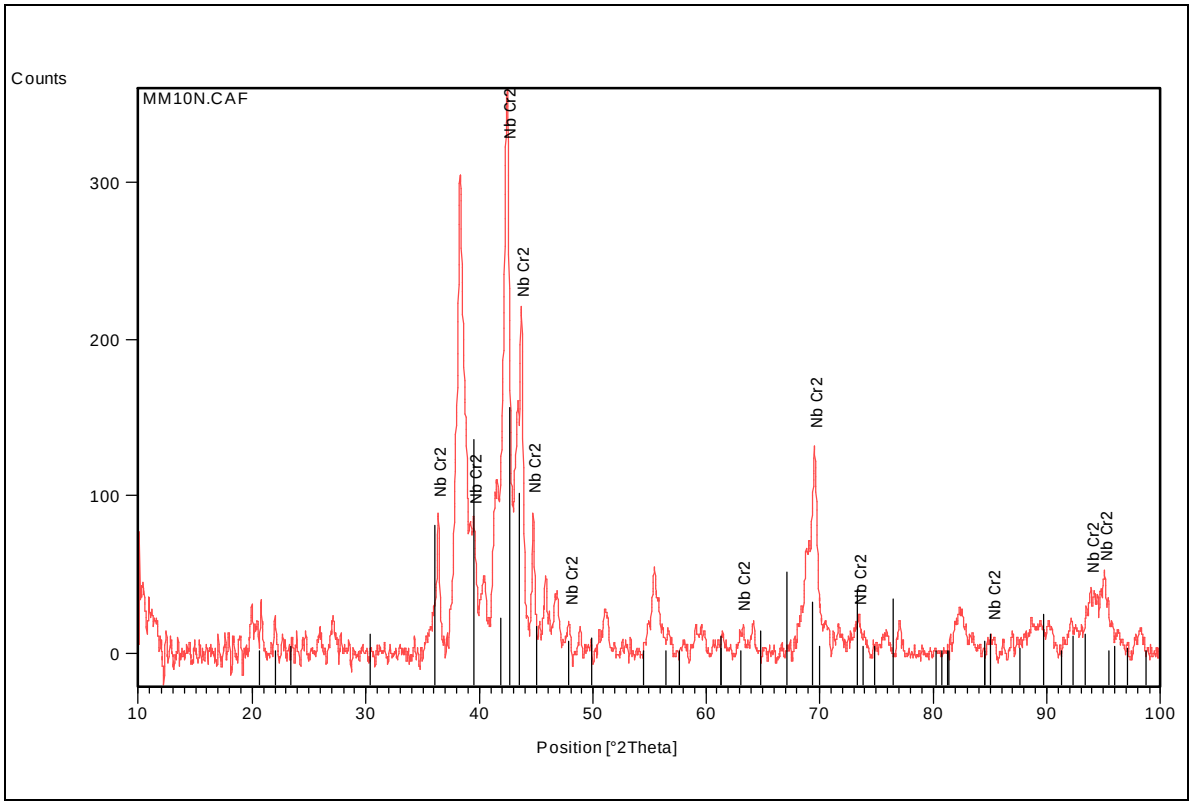

Figure 4.62. XRD spectrum of nominal Nb_{50}:Cr_{30}:Pt_{20} in the as-cast condition, showing black ~$NbCr_2$ peaks.

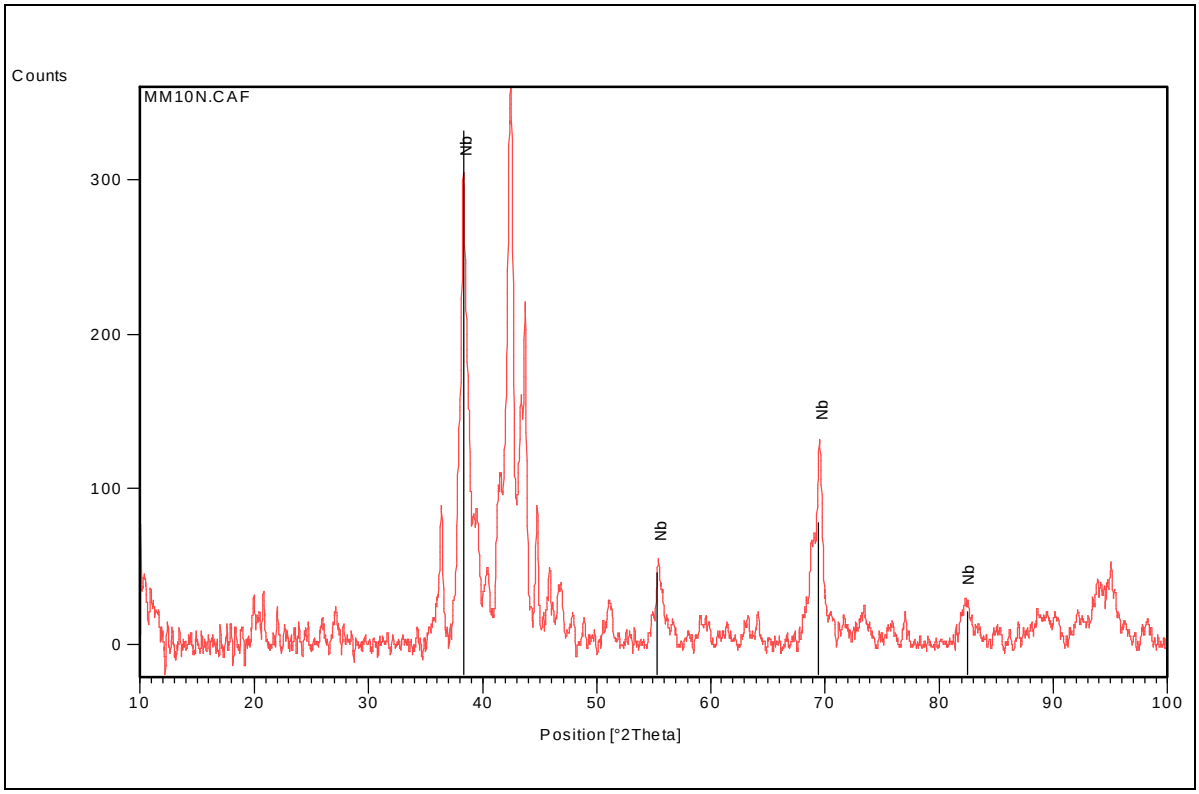

Figure 4.63. XRD spectrum of nominal Nb_{50}:Cr_{30}:Pt_{20} in the as-cast condition, showing black Nb peaks.

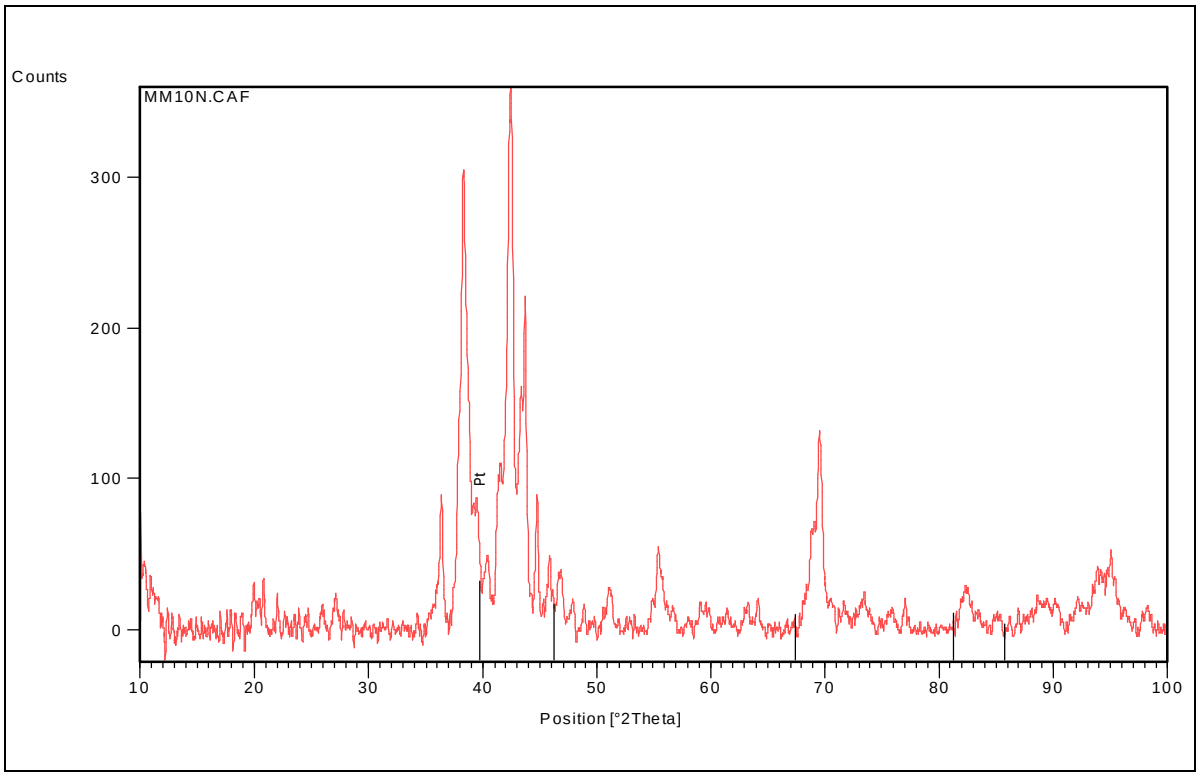

Figure 4.64. XRD spectrum of nominal Nb_{50}:Cr_{30}:Pt_{20} in the as-cast condition, showing black Pt peaks.

4.1.11 Nominal Nb_{35}:Cr_{30}:Pt_{35}, Sample 11

The nominal Nb_{35}:Cr_{30}:Pt_{35} alloy microstructure comprised mainly light cored (Pt) dendrites, with a dark interdendritic phase, as shown in Figures 4.65 a and b. The dark phase was identified as the ternary phase 2 (τ2), and there was some porosity. Table 4.19 gives the EDX analyses of this alloy, which are plotted in Figure 4.66, showing overall composition to lie between all the analysed compositions, and nearer to the light phase composition, which is expected since τ2 was in a minor proportion. There were high experimental errors for the dark phase because of its small areas. The XRD spectrum shown in Figures 4.67 to 4.68 was quite good, with a high signal: background ratio. The existence of (Pt) was confirmed by XRD, as shown in Figure 4.68, with some minor peak shifts to the right. A major peak at position $^{o}2\theta$ = 46.545 was found, which matched (Pt), but was not the maximum peak for pure Pt. However, it was not possible to check for the presence of τ2 phase, because there were no data for it in the database (ICDD). The unidentified peaks in the spectrum are assumed to be from τ2.

The solidification sequence deduced from the microstructure is as follows:

$$L \rightarrow \text{cored (Pt)}$$

followed by peritectic reaction

$$L + (Pt) \rightarrow \tau 2 \text{ (Chapter 5: Discussion)}$$

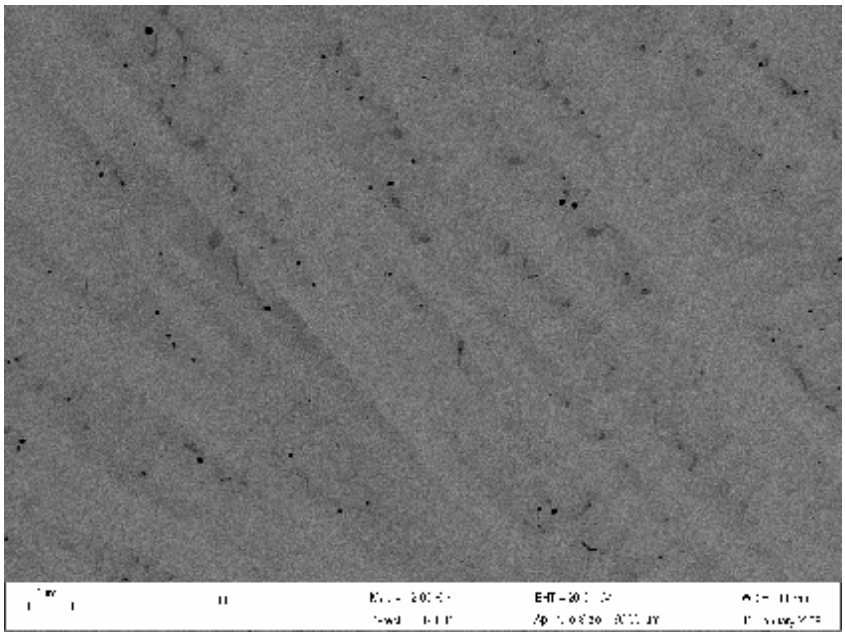

(a)

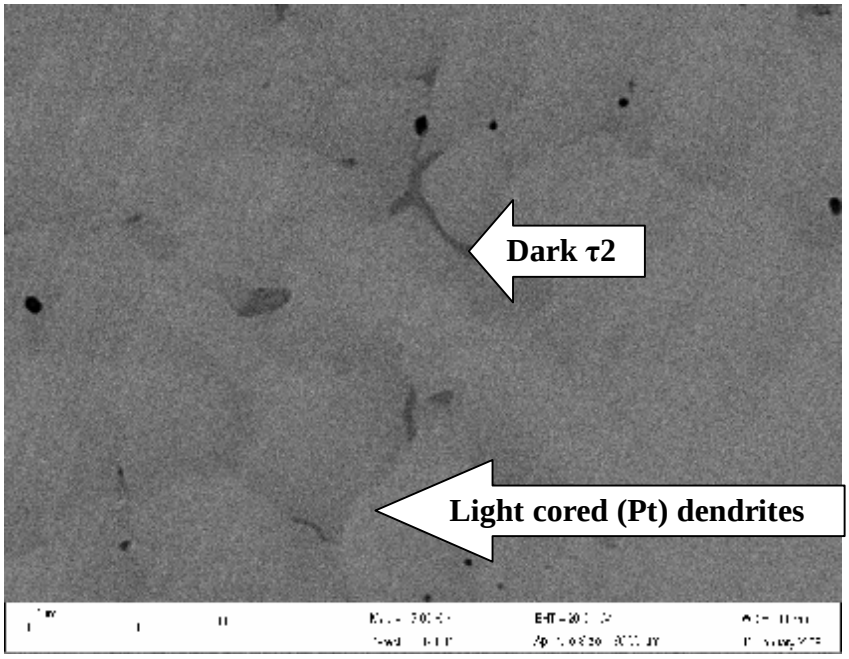

(b)

Figure 4.65 a-b. SEM-BSE images of the nominal Nb_{35}:Cr_{30}:Pt_{35} alloy in the as–cast condition, showing light cored (Pt) dendrites and interdendritic dark τ2 phase.

Table 4.19. EDX phase analyses for nominal Nb_{35}:Cr_{30}:Pt_{35} (at.%) in the as–cast condition, as shown in Figure 4.65 (a) and (b).

Phase contrast	**Nb**	**Cr**	**Pt**	**Phase**
Overall	18.9±0.2	38.3±0.2	42.8±0.2	-
Light (dendrites)	18.6±0.5	36.0±2.0	45.3±1.5	Cored (Pt)
Medium-grey	18.4±0.3	41.9±0.2	39.8±0.1	Cored (Pt)
Dark	22.3±0.5	50.3±1.0	27.4±0.5	τ2

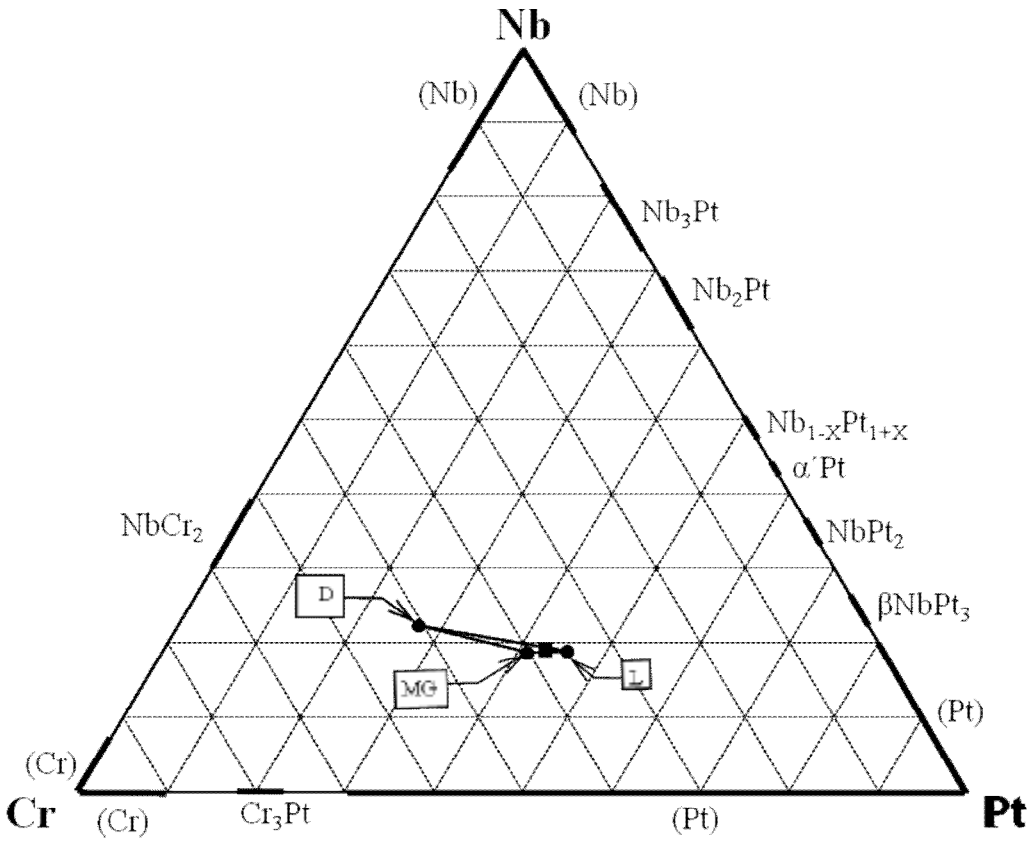

Figure 4.66. EDX phase compositions for the nominal $Nb_{35}:Cr_{30}:Pt_{35}$ (at.%) alloy in the as–cast condition: (L) light contrast; (MG) medium-grey contrast; (D) dark contrast phase; ■ overall composition; ● phase composition.

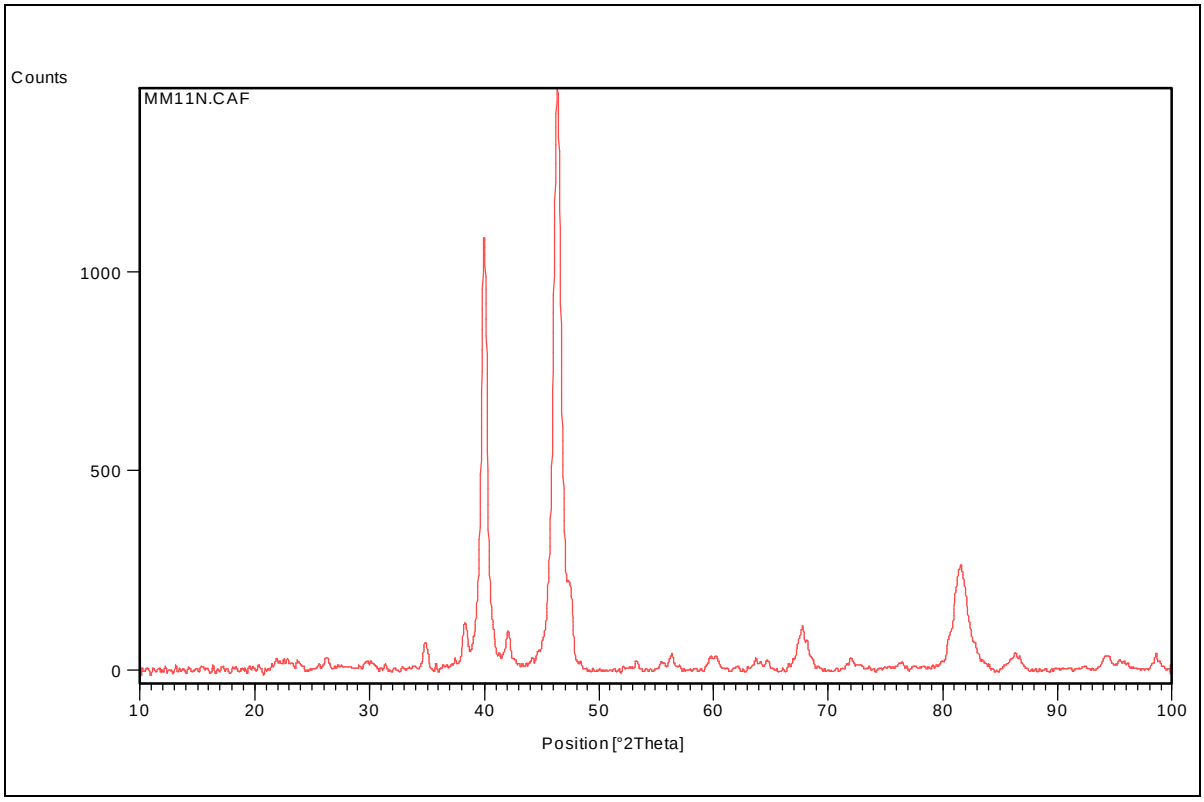

Figure 4.67. Raw XRD spectrum of nominal Nb_{35}:Cr_{30}:Pt_{35} in the as-cast condition.

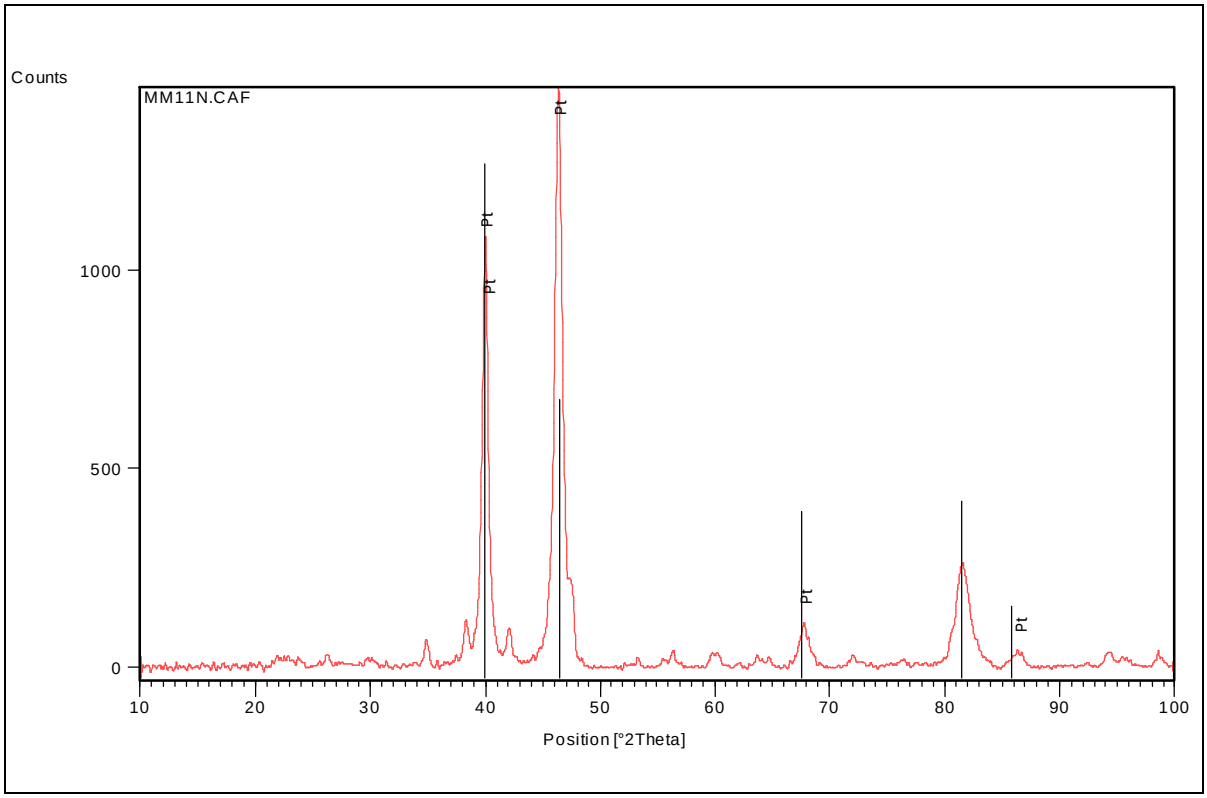

Figure 4.68. XRD spectrum of nominal Nb_{35}:Cr_{30}:Pt_{35} in the as-cast condition, showing black Pt peaks.

4.1.12 Nominal Nb_{20}:Cr_{50}:Pt_{30}, sample 12

The nominal Nb_{20}:Cr_{50}:Pt_{30} alloy possessed a very slightly porous microstructure of mainly light (Pt) dendrites, with a (Pt) + τ1 eutectic, as shown in Figure 4.69. Table 4.20 gives the EDX analyses, and these are plotted in Figure 4.70. The overall composition was between the light (Pt) phase composition and the eutectic overall composition which meant that the dark eutectic component could be estimated by extrapolation through the eutectic overall from the known component. There were low experimental errors for all the analyses. The XRD spectrum shown in Figures 4.71 to 4.72 was quite poor, with a low signal: background ratio and broad peaks. There were matches for (Pt), with fairly large peak shifts to the right, as expected because it was not pure. It was not possible to check for the presence of τ1 phase, because there were no data for it in the database (ICDD). The unidentified peaks were assumed to be from the τ1 phase. No exact matches were made for Cr_3Pt (Figure 4.72b).

The solidification sequence deduced from the microstructure is as follows:

$$L \rightarrow (Pt)$$

followed by a eutectic reaction

$$L \rightarrow (Pt) + \tau1 \text{ (Chapter 5: Discussion)}$$

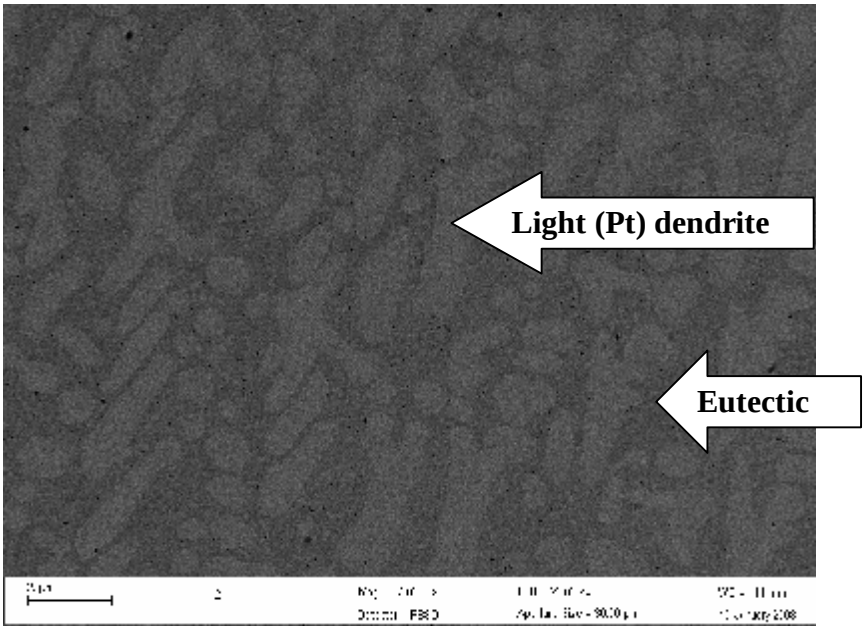

Figure 4.69. SEM-BSE image of nominal Nb_{20}:Cr_{50}:Pt_{30} alloy in the as–cast condition, showing light (Pt) dendrites and (Pt) + τ1 eutectic.

Table 4.20. EDX phase analyses for the nominal $Nb_{20}:Cr_{50}:Pt_{30}$ (at.%) alloy in the as–cast condition.

Phase contrast	Nb	Cr	Pt	Phase
Overall	14.7±0.2	56.4±0.4	28.9±0.3	-
Light (dendrites)	12.6±0.3	54.1±0.2	33.3±0.2	(Pt)
Eutectic overall	16.3±0.6	58.3±0.2	25.4±0.6	(Pt) + τ1

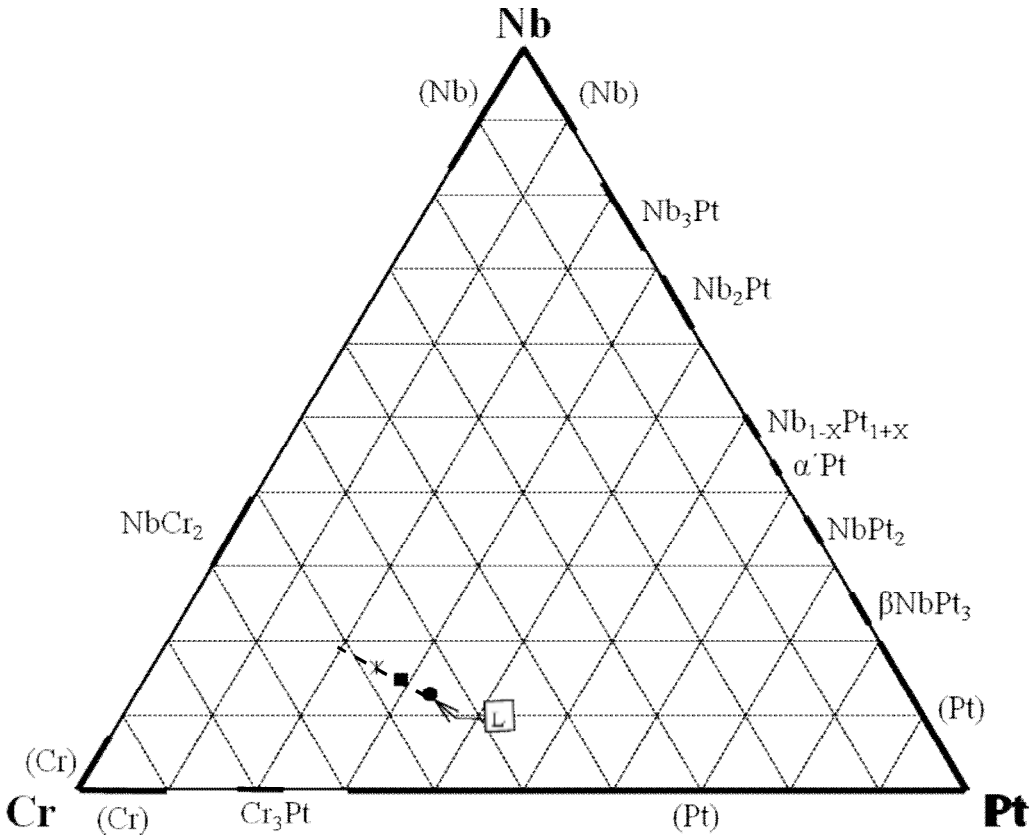

Figure 4.70. EDX phases compositions for the nominal $Nb_{20}:Cr_{50}:Pt_{30}$ (at.%) alloy in the as–cast condition: (L) light contrast phase; ■ overall composition; ● phase composition; ✹ eutectic composition.

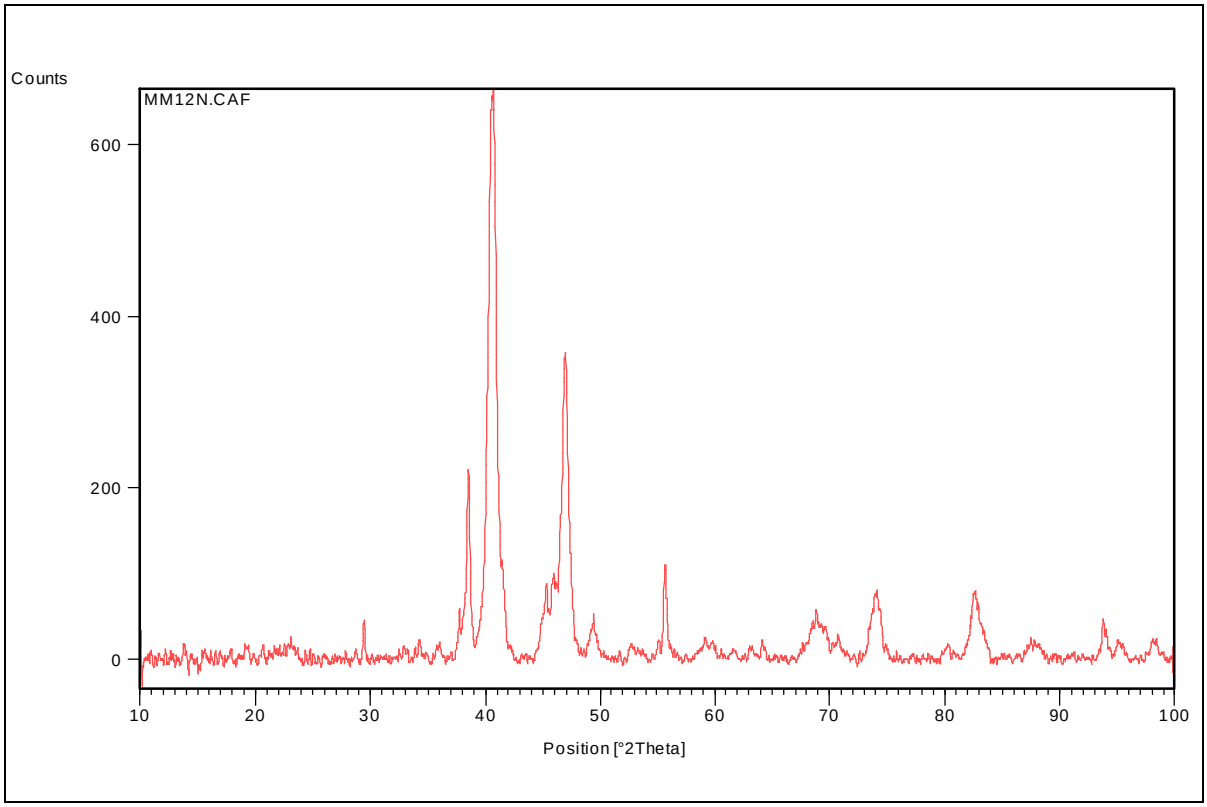

Figure 4.71. Raw XRD spectrum of nominal Nb_{20}:Cr_{50}:Pt_{30} in the as-cast condition.

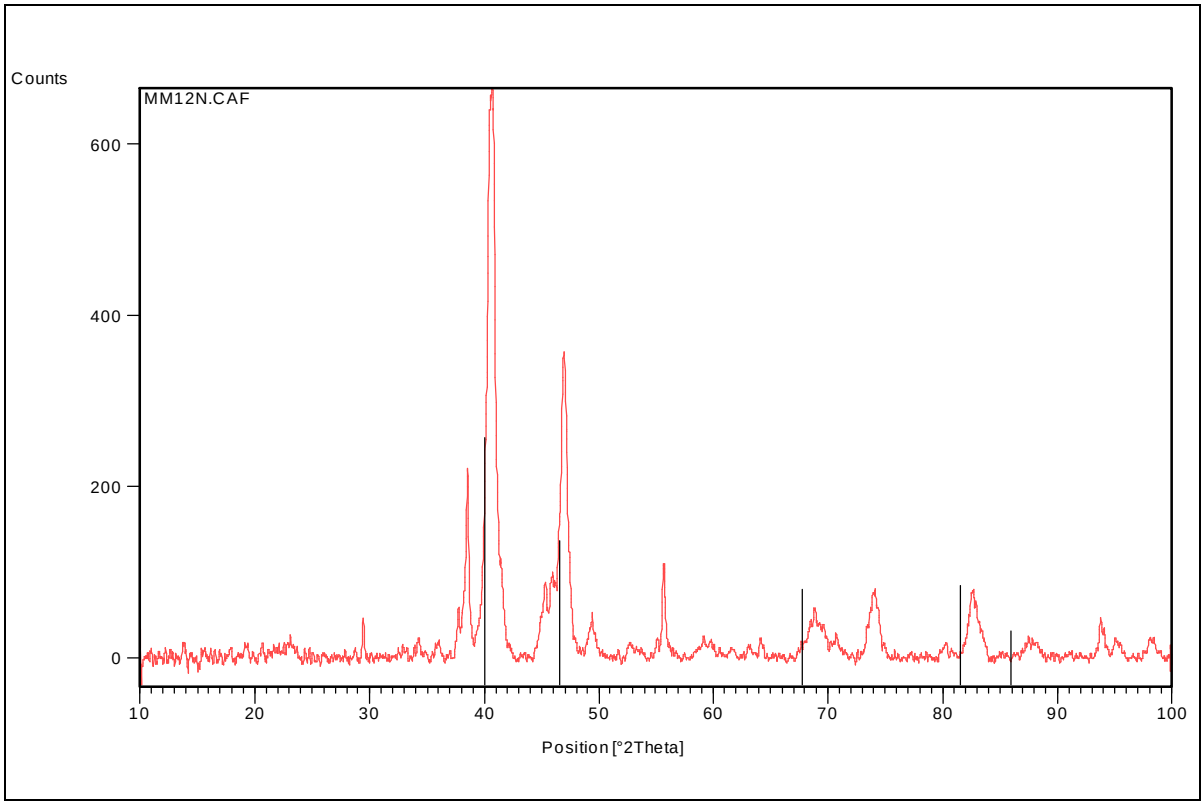

Figure 4.72 a. XRD spectrum of nominal Nb_{20}:Cr_{50}:Pt_{30} in the as-cast condition, showing black Pt peaks.

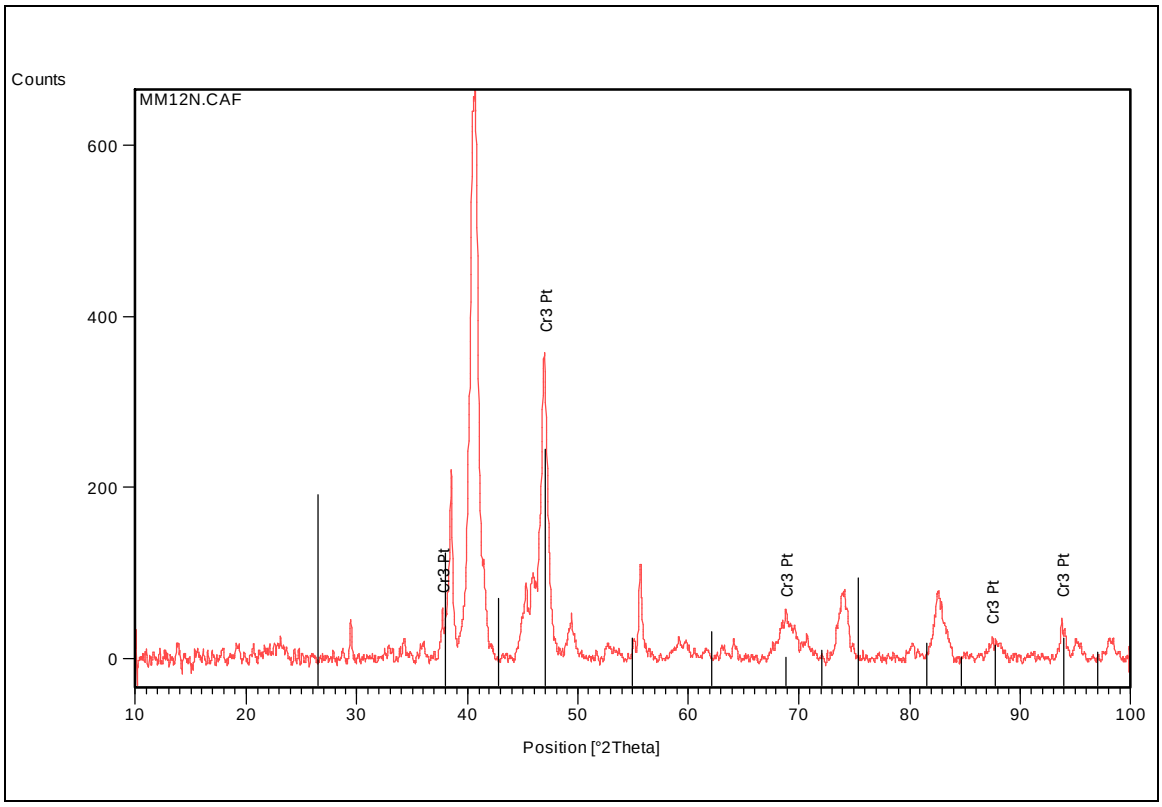

Figure 4.72 b. XRD spectrum of nominal $Nb_{20}:Cr_{50}:Pt_{30}$ in the as-cast condition, showing black Cr_3Pt peaks.

4.1.13 Nominal $Nb_{30}:Cr_{20}:Pt_{50}$, Sample 13

The nominal $Nb_{30}:Cr_{20}:Pt_{50}$ alloy possessed a two-phase microstructure of light ~$NbPt_2$ dendrites and medium-grey ternary phase 3 (τ3), as shown in Figures 4.73 a and b. This sample was quite homogeneous, but with some pores, which are associated with fast cooling. Table 4.21 gives the EDX analyses, and these are plotted in Figure 4.74. The overall composition was on the tie-line between the two phase compositions. The medium-grey analyses probably need to be extrapolated as small areas were analysed.

The XRD spectrum shown in Figures 4.75 to 4.76 was a good spectrum, with a reasonable signal: background ratio. The existence of ~$NbPt_2$ phase was confirmed by XRD, as shown in Figure 4.76. There were some small peak shifts to the right (relative to the database) for ~$NbPt_2$. However, it was not possible to check for the presence of τ3 phase, because there were no data for it in the database (ICDD), and so unidentified peaks were assumed to be from τ3.

The solidification sequence deduced from the microstructure is as follows:

$$L \rightarrow \sim NbPt_2$$

followed by a peritectic reaction

$$L + \sim NbPt_2 \rightarrow \tau 3 \text{ (Chapter 5: Discussion)}$$

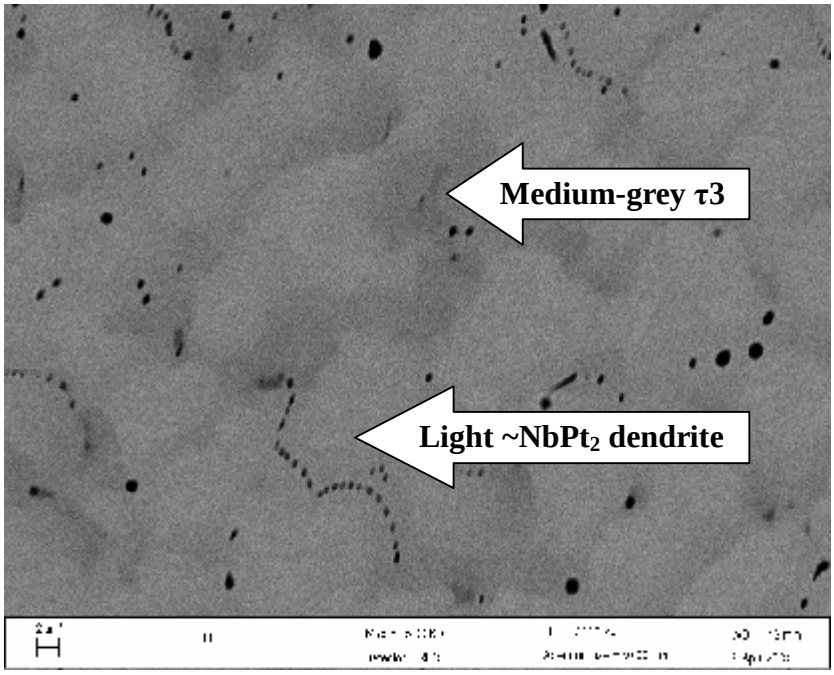

Figure 4.73. SEM-BSE image of the nominal Nb_{30}:Cr_{20}:Pt_{50} alloy in the as-cast condition, showing light ~$NbPt_2$ dendrites and a medium-grey τ3 phase.

Table 4.21. EDX phase analyses for the nominal Nb_{30}:Cr_{20}:Pt_{50} (at.%) in the as-cast condition.

Phase contrast	**Nb**	**Cr**	**Pt**	**Phase**
Overall	29.7±0.3	21.9±0.3	48.4±0.3	-
Light (dendrites) lighter inner	30.0±0.5	18.9±0.4	51.0±0.4	Cored ~$NbPt_2$
Light (dendrites) darker outer	29.3±0.3	21.6±0.5	49.1±0.5	Cored ~$NbPt_2$
Medium-grey phase	29.1±0.4	28.0±0.8	42.9±0.5	τ3

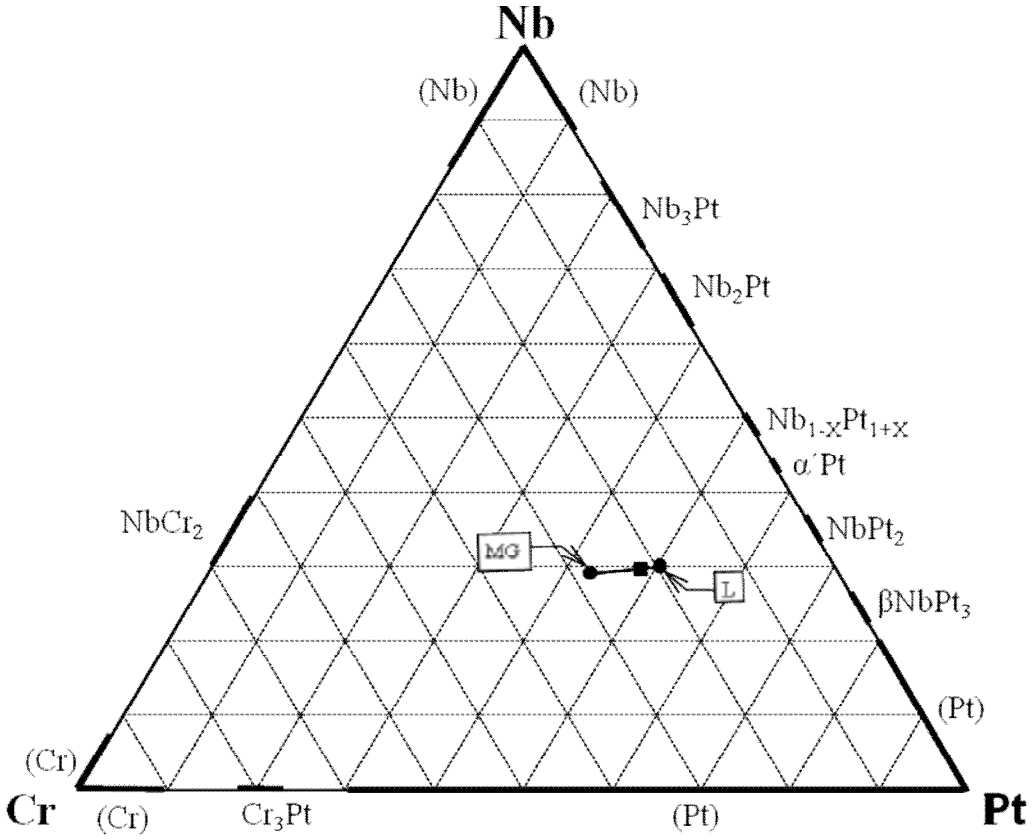

Figure 4.74. EDX phase compositions for the nominal $Nb_{30}:Cr_{20}:Pt_{50}$ (at.%) alloy in the as-cast condition: (L) light contrast; (MG) medium-grey contrast phase; ■ overall composition; ● phase composition.

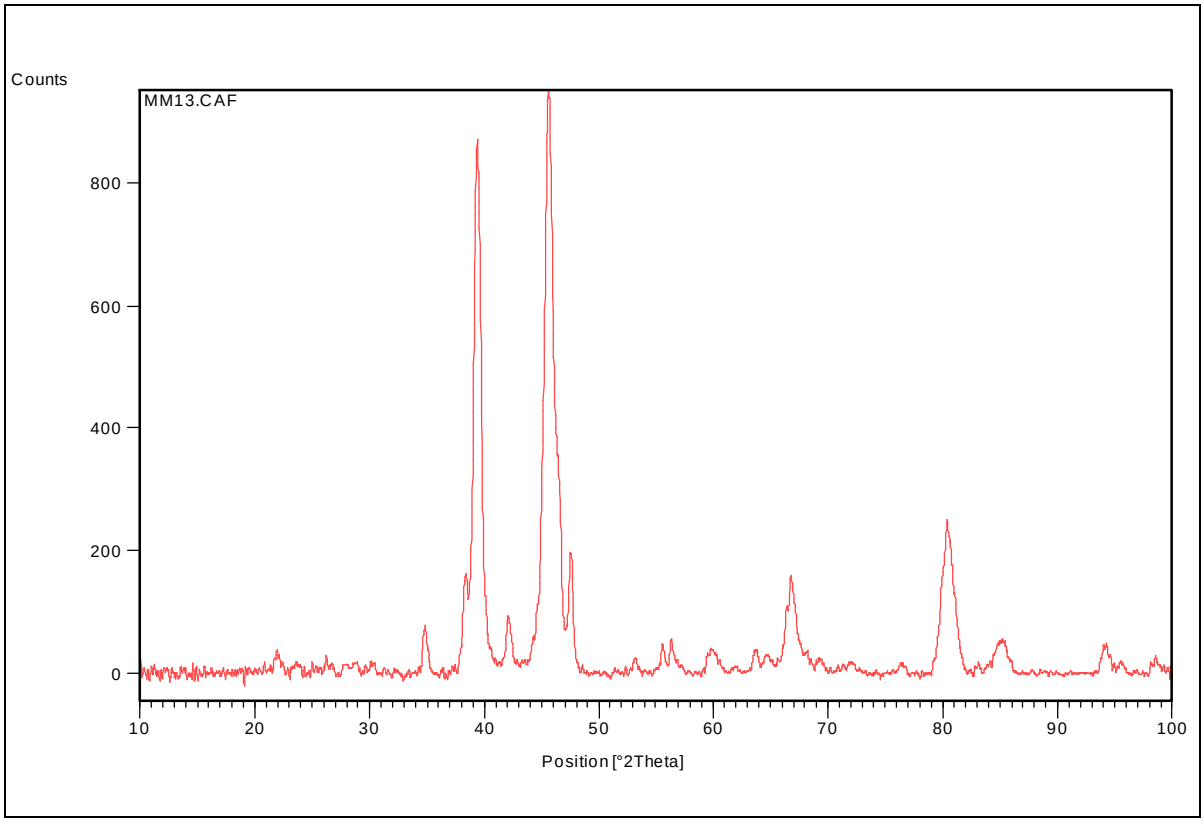

Figure 4.75. Raw XRD spectrum of nominal $Nb_{30}:Cr_{20}:Pt_{50}$ in the as-cast condition.

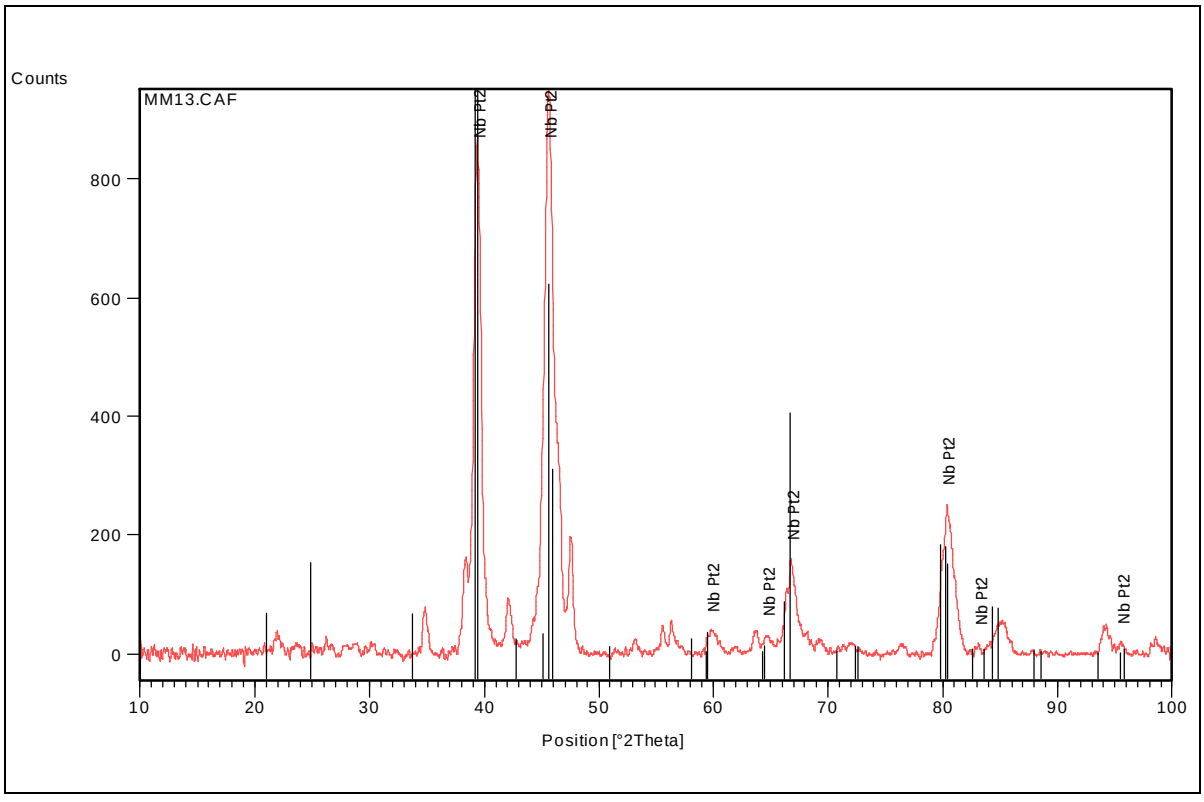

Figure 4.76. XRD spectrum of nominal $Nb_{30}:Cr_{20}:Pt_{50}$ in the as-cast condition, showing black $NbPt_2$ peaks.

4.1.14 Nominal Nb_{25}:Cr_{45}:Pt_{30}, Sample 14

The nominal Nb_{25}:Cr_{45}:Pt_{30} alloy microstructure at low magnification showed different regions around a lump of unmelted light pure platinum, as shown in Figure 4.77. These different regions were analysed individually (a to c).

The XRD spectrum was a good spectrum, with a high signal: background ratio, as shown in Figures 4.84 to 4.85. The presence of (Pt) phase was confirmed by X-ray diffraction, as shown in Figure 4.85. There were good matches for (Pt) with the ICDD lines, with some fairly small shifts to the right. However, it was not possible to check for the presence of τ2 phase, because there were no data for it in the database (ICDD). The unidentified peaks were assumed to be from τ2 phase.

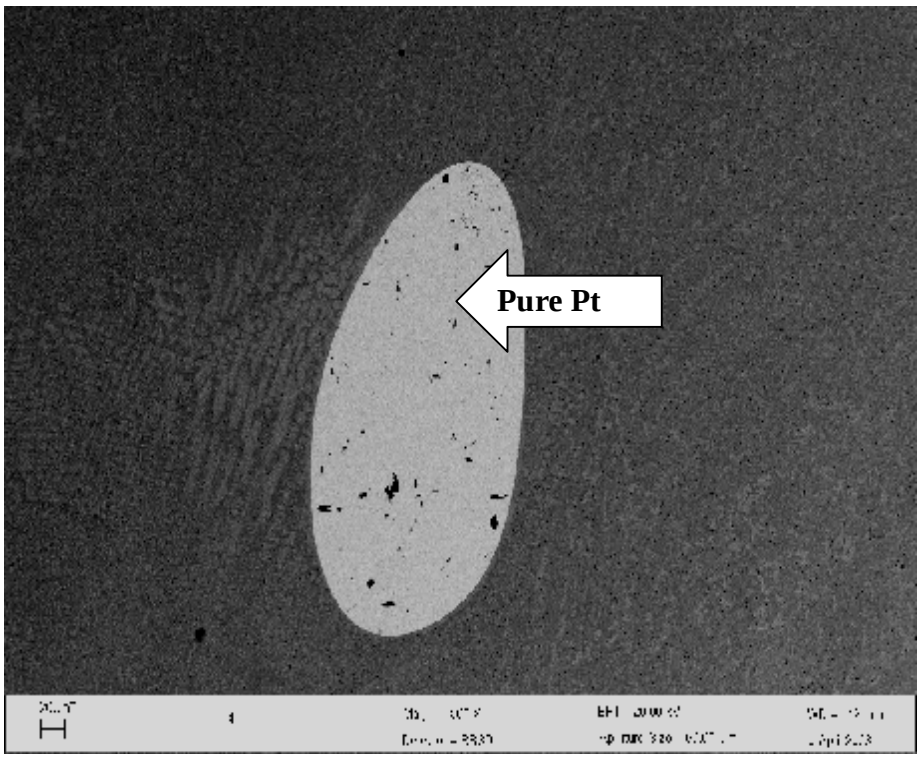

Figure 4.77. SEM-BSE image for the light unmelted pure Pt in nominal Nb_{25}:Cr_{45}:Pt_{30} alloy in the as-cast condition at low magnification, surrounded by different regions.

(a) Near the edge of the sample, the major part of the sample was found to comprise medium-grey ternary phase 2 (τ2) dendrites and interdendritic light (Pt) (Figures 4.78 a and b). There was porosity usually associated with phase boundaries. Table 4.22 and Figure 4.79 gives the EDX analyses. These results were good because of small errors and the overall composition lying on the tie-line, with the overall lying close to the medium-grey phase, which agrees with the micrograph. The analyses of the light phase were probably affected by the surrounding medium-grey phase, because of their small size.

The solidification sequence was deduced as:

$$L \rightarrow \tau 2$$

followed by a peritectic reaction

$$L + \tau 2 \rightarrow (Pt)$$

or possibly, a sparse eutectic:

$$L \rightarrow \tau 2 + (Pt)$$ (Chapter 5: Discussion)

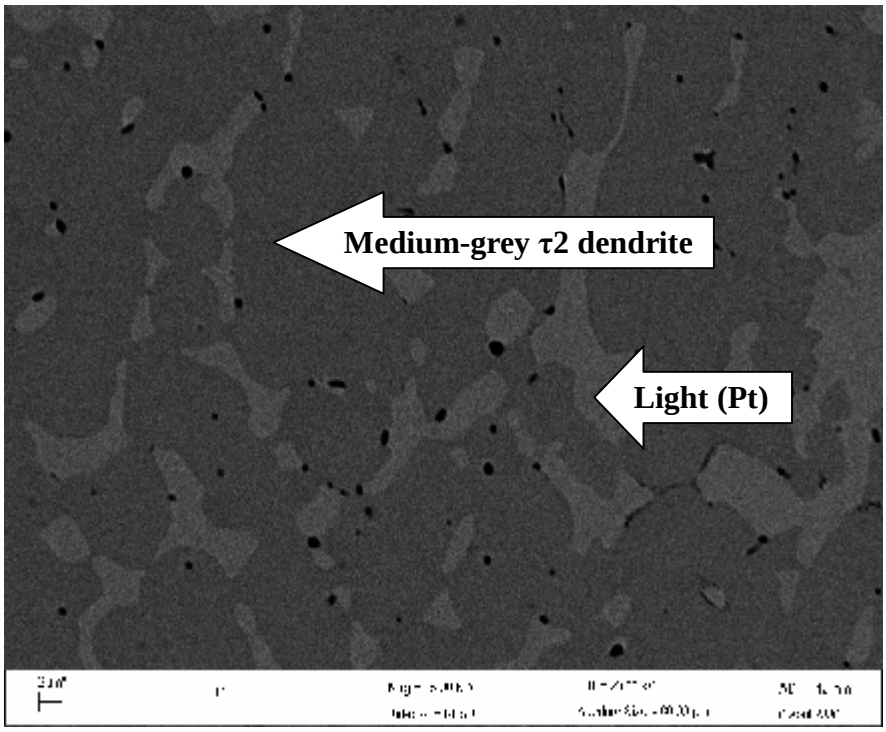

Figure 4.78. SEM-BSE image for the major part of Nb_{25}:Cr_{45}:Pt_{30} alloy in the as-cast condition, near the edge, showing medium-grey τ2 dendrites and light (Pt) interdendritic phase.

Table 4.22. EDX phase analyses for the major part of nominal $Nb_{25}:Cr_{45}:Pt_{30}$ (at.%) in the as-cast condition, near the edge as shown in Figures 4.78.

Phase contrast	Nb	Cr	Pt	Phase
Overall	23.3±0.2	47.9±0.1	28.8±0.2	-
Light (interdendritic)	21.3±0.2	43.2±0.1	35.5±0.2	(Pt)
Medium-grey (dendrites)	24.0±0.2	48.5±0.2	27.5±0.2	τ2

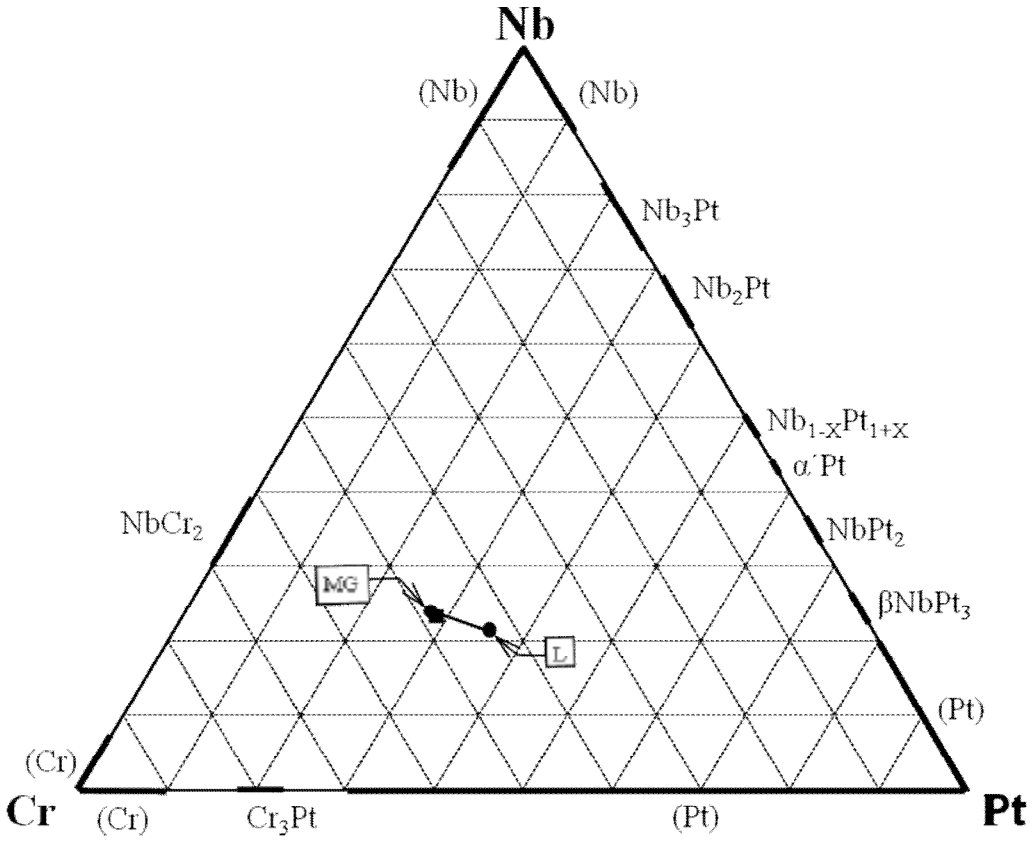

Figure 4.79. EDX phase compositions for the major part in nominal $Nb_{25}:Cr_{45}:Pt_{30}$ (at.%) alloy in the as-cast condition, near the edge: (L) light contrast; (MG) medium-grey contrast phase; ■ overall composition; ● phase composition.

(b) A minor region near the unmelted pure platinum possessed a microstructure of mainly light (Pt) dendrites and medium-grey τ2 interdendritic phase, which is different from the previously discussed section, with some porosity, as shown in Figure 4.80. Table 4.23 gives the EDX analyses and these had fairly large errors for overall and light contrast phase compositions. When plotted (Figure 4.81), the overall composition was on the tie-line between the two phases' analyses.

The solidification sequence deduced from the microstructure is as follows, and is different from previous region described:

$$L \rightarrow (Pt)$$

followed by a eutectic reaction

$$L \rightarrow (Pt) + \tau 2 \text{ (Chapter 5: Discussion)}$$

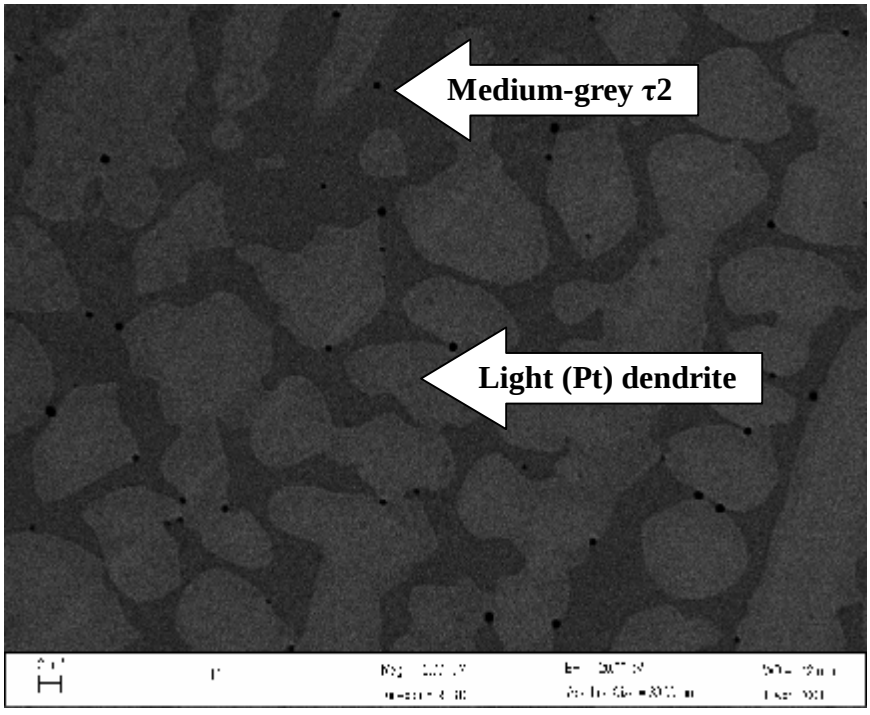

Figure 4.80. SEM-BSE image for the minor region, near the unmelted Pt in nominal Nb_{25}:Cr_{45}:Pt_{30} in the as-cast condition, showing light (Pt) dendrites and a medium-grey τ2 interdendritic phase.

Table 4.23. EDX phase analyses for the minor region, near the unmelted Pt in nominal $Nb_{25}:Cr_{45}:Pt_{30}$ (at.%) in the as-cast condition, as shown in Figure 4.80.

Phase contrast	Nb	Cr	Pt	Phase
Overall	22.6±0.4	45.2±1.3	32.2±1.7	-
Light (dendrites)	21.4±0.5	41.8±0.8	36.9±1.2	(Pt)
Medium-grey (interdendritic)	23.5±0.2	49.3±0.2	27.2±0.1	(Pt) + τ2

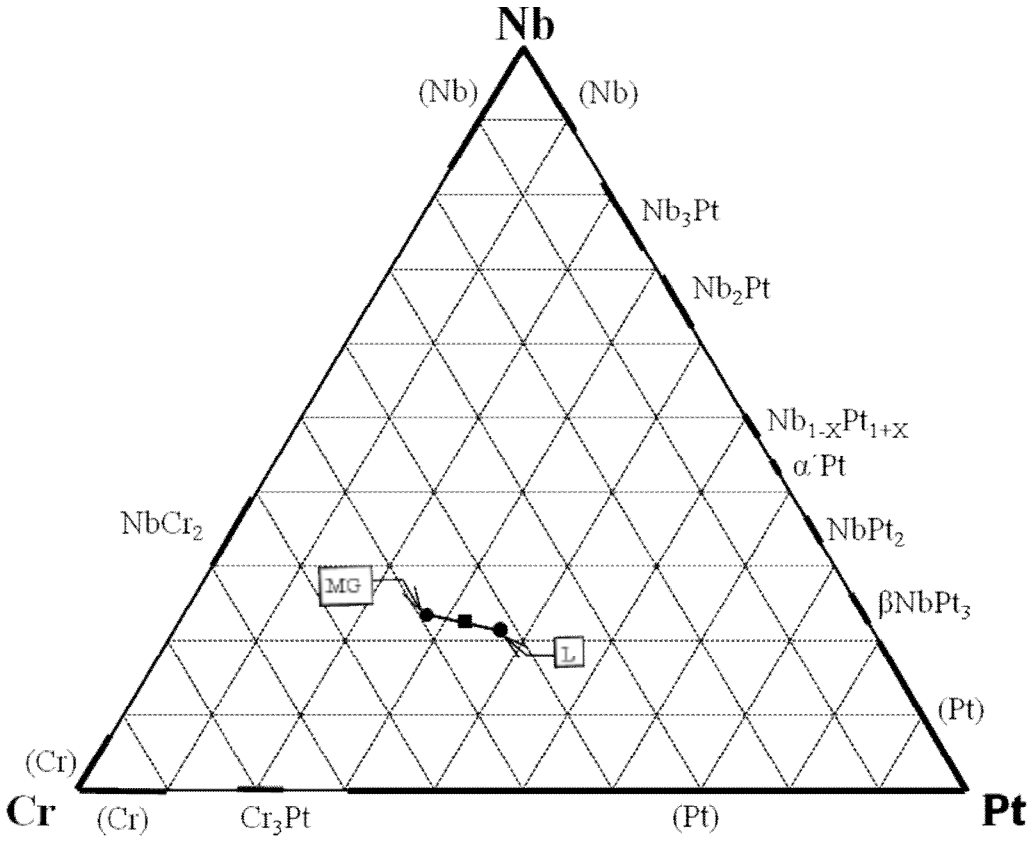

Figure 4.81. EDX phase compositions for the minor region, near the unmelted Pt in nominal $Nb_{25}:Cr_{45}:Pt_{30}$ (at.%) alloy in the as-cast condition: (L) light contrast; (MG) medium-grey contrast phase; ■ overall composition; ● phase composition.

(c) In another region, near the unmelted Pt, a better defined eutectic of (Pt) + τ2 was found, as shown in Figure 4.82 (b). Table 4.24 and Figure 4.83 gives the EDX analyses. The analyses of the two phases in the eutectic are assumed to be the same as the dark and light phases in the previous section.

The solidification sequence derived from the microstructure is as follows:

$$L \rightarrow (Pt)$$

followed by a eutectic reaction

$$L \rightarrow (Pt) + \tau 2$$

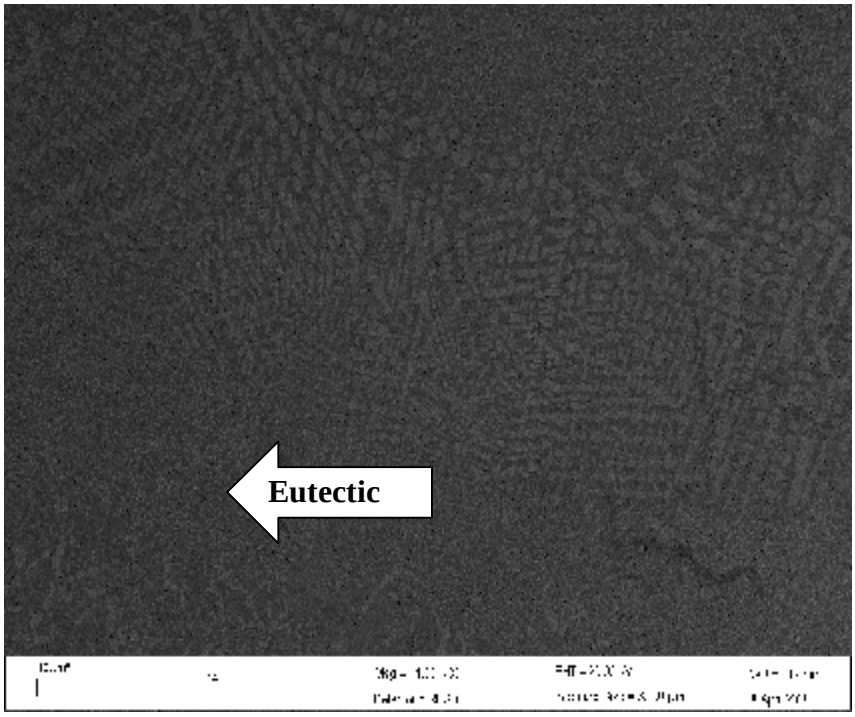

(a)

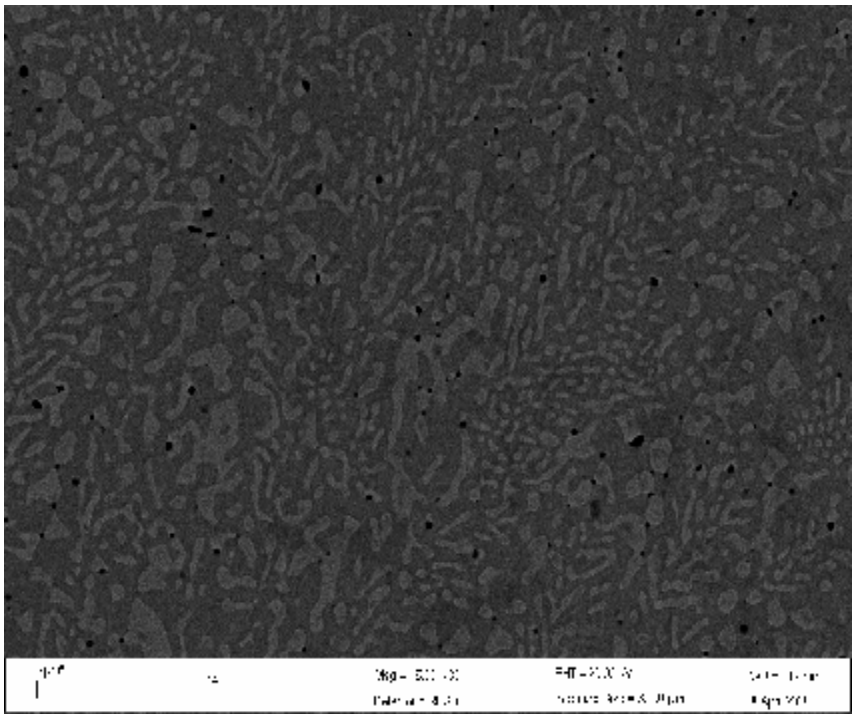

(b)

Figure 4.82 a-b. SEM-BSE images of nominal $Nb_{25}:Cr_{45}:Pt_{30}$ alloy in the as-cast condition for the region near the unmelted Pt, showing (a) the different regions and (b) eutectic of (Pt) + τ2.

Table 4.24. EDX phase analyses of nominal $Nb_{25}:Cr_{45}:Pt_{30}$ (at.%) in the as-cast condition for the region near the unmelted Pt, as shown in Figures 4.82 (a) and (b).

Phase contrast	**Nb**	**Cr**	**Pt**	**Phase**
Eutectic overall	23.0±0.3	46.8±0.4	30.2±0.4	(Pt) + τ2

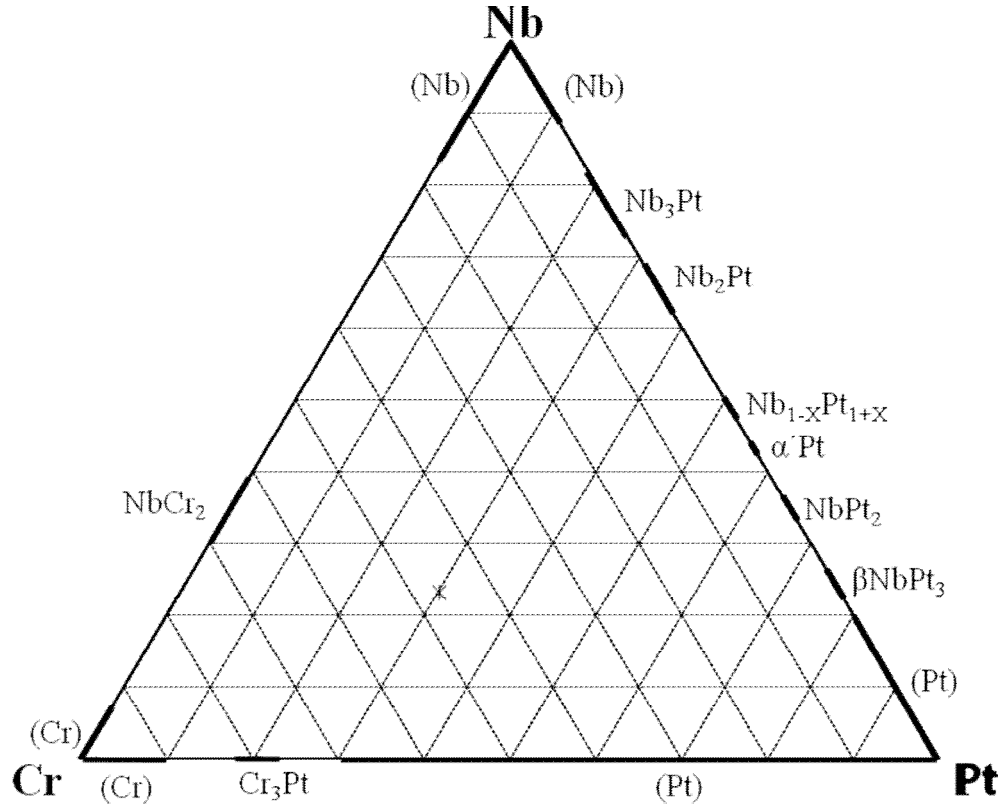

Figure 4.83. EDX phase compositions for the region near the unmelted Pt in nominal $Nb_{25}:Cr_{45}:Pt_{30}$ (at.%) alloy in the as-cast condition: ✸ eutectic composition.

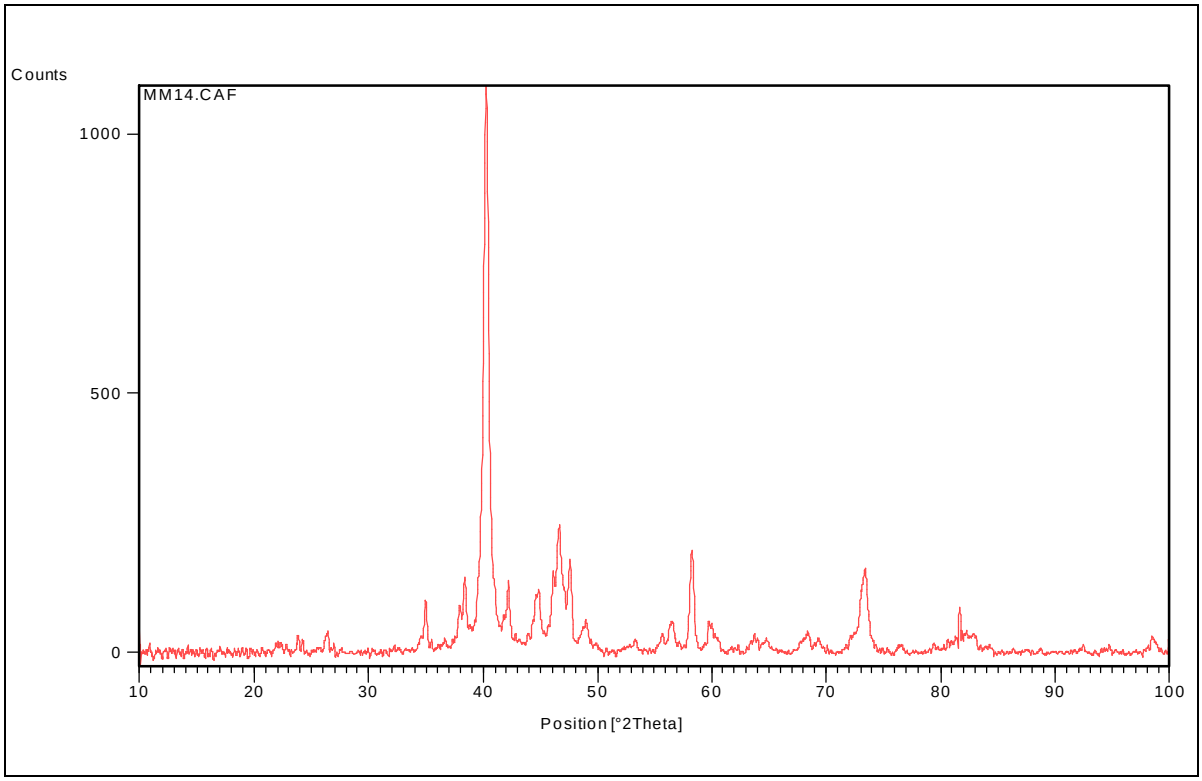

Figure 4.84. Raw XRD spectrum of nominal $Nb_{25}:Cr_{45}:Pt_{30}$ in the as-cast condition.

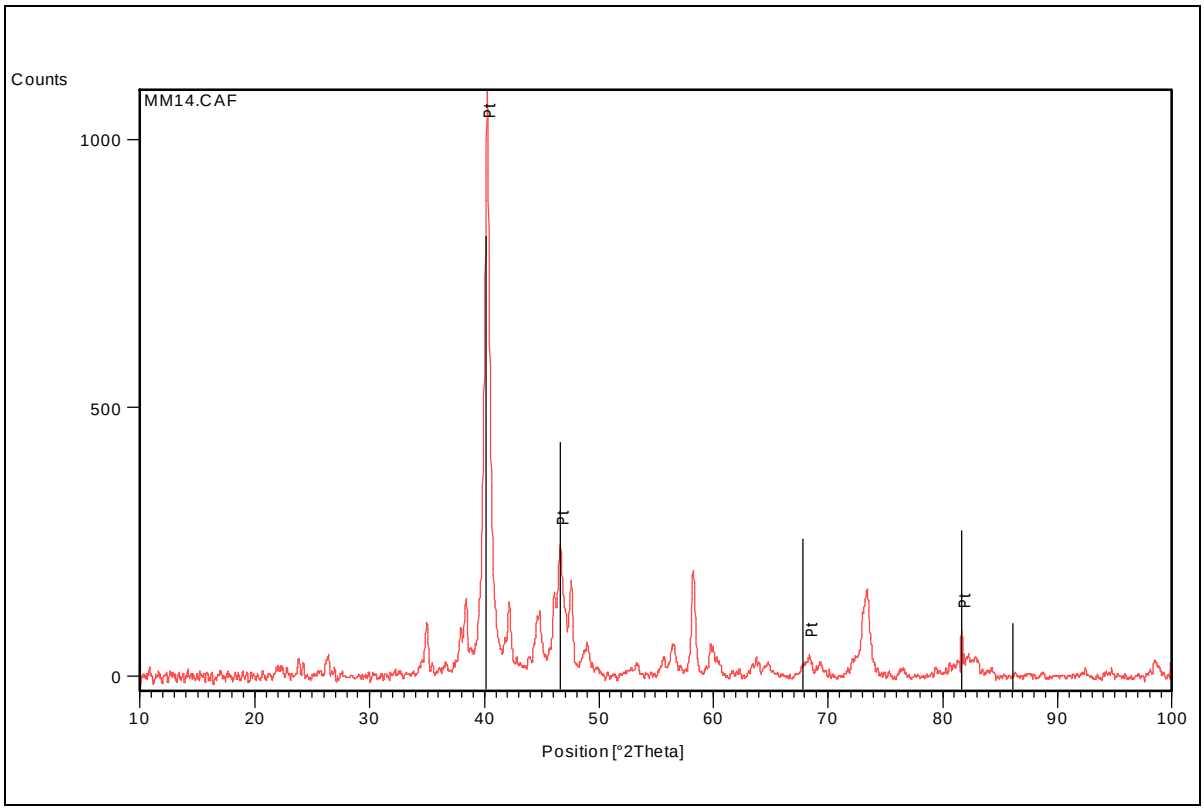

Figure 4.85. XRD spectrum of nominal $Nb_{25}:Cr_{45}:Pt_{30}$ in the as-cast condition, showing black Pt peaks.

4.1.15 Nominal Nb_{20}:Cr_{60}:Pt_{20}, Sample 15

The nominal Nb_{20}:Cr_{60}:Pt_{20} alloy at low magnification (Figure 4.86) showed different regions and some cracks mainly near to the unmelted pure light Pt. Thus, alloy was totally inhomogeneous, and was analysed in different parts (a to c).

The X-ray diffraction spectrum shown in Figures 4.93 to 4.96 was quite a poor spectrum with a low signal: background ratio, probably due to the cracks in sample. Matches for (Cr), (Pt) and ~Cr_3Pt with the ICDD lines were found, with some peak shifts. There were good fits for (Cr) with small peak shifts to the right, but there was not such a good fit for (Pt) except for two peaks. There were also good matches for ~Cr_3Pt, with minor peak shifts to the right. However, it was not possible to check for the presence of τ1 phase, because there were no data for it in the database (ICDD). The unidentified peaks were assumed to be from the τ1 phase.

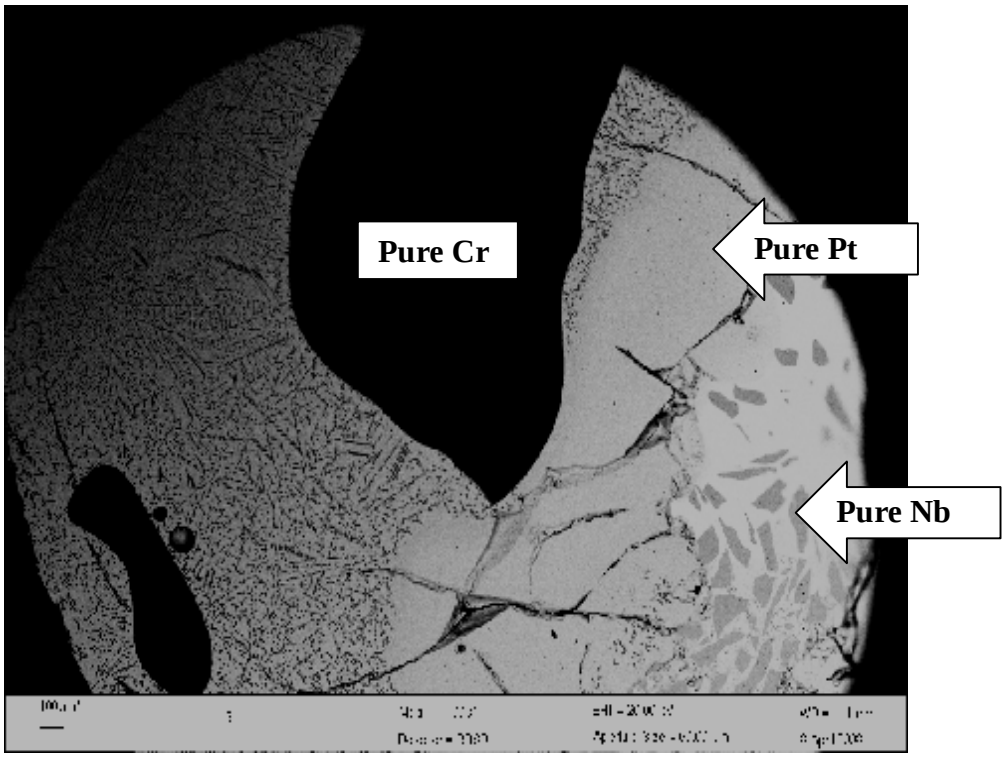

Figure 4.86. SEM-BSE image of the nominal Nb_{20}:Cr_{60}:Pt_{20} alloy in the as-cast condition at low magnification, showing large regions of unmelted Cr (dark), Pt (light) and smaller regions of Nb (medium-grey), together with different regions.

(a) The nominal Nb_{20}:Cr_{60}:Pt_{20} alloy microstructure, between the unmelted dark chromium, as shown in Figures 4.86 and 4.87 a and b, was found to be mainly a three phase region. These phases were dark (Cr) dendrites, medium-grey ~Cr_3Pt and light ternary phase 1 (τ1) matrix. Table 4.25 gives the EDX analyses and Figure 4.88 gives the plot, showing the overall composition lying within the tie-triangle of the phase compositions. The medium-grey phase had small errors and the dark phase was on the limit. Thus, the analyses of this region should only be taken as a guide.

The solidification sequence derived from these microstructures was as follows:

$$L \rightarrow (Cr)$$

followed by a peritectic reaction

$$L + (Cr) \rightarrow \sim Cr_3Pt$$

and by another peritectic reaction

$$L + \sim Cr_3Pt \rightarrow \tau 1$$

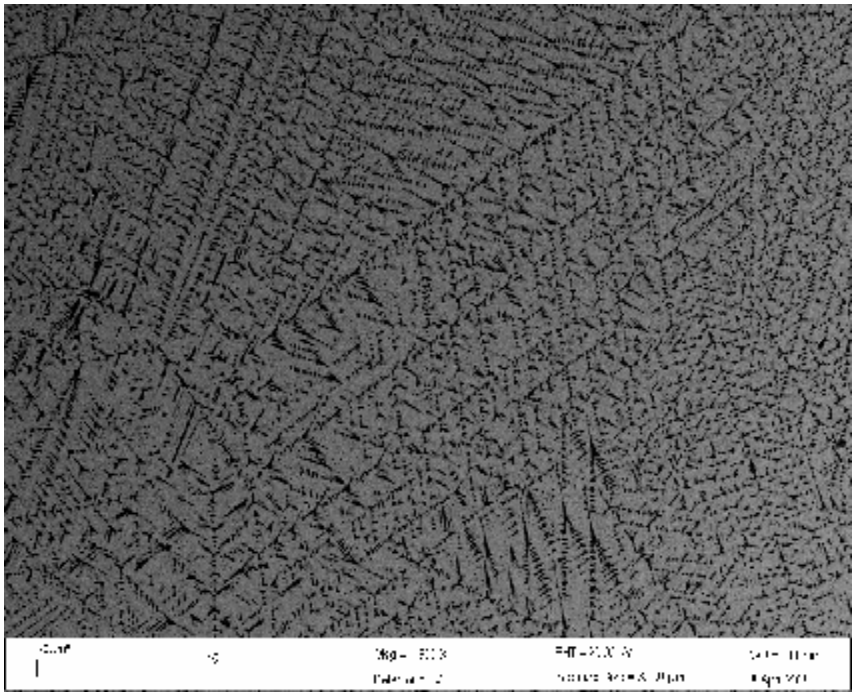

(a)

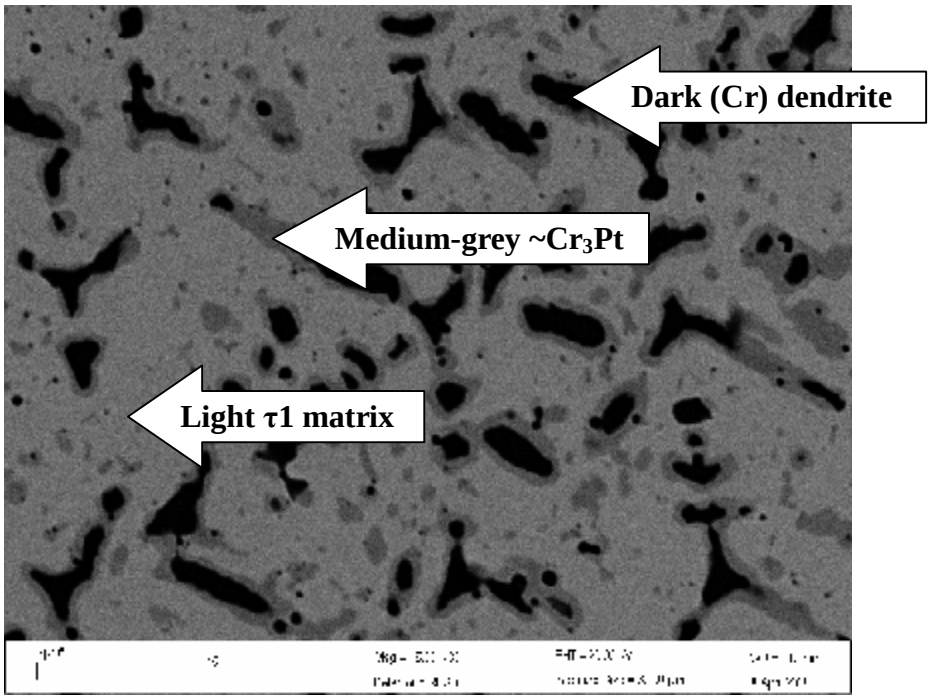

(b)

Figure 4.87 a-b. SEM-BSE images for the region between the unmelted dark Cr in nominal $Nb_{20}:Cr_{60}:Pt_{20}$ alloy in the as-cast condition, showing dark (Cr) dendrites, surrounded by medium-grey ~Cr_3Pt and light τ1 matrix.

Table 4.25. EDX phase analyses of nominal $Nb_{20}:Cr_{60}:Pt_{20}$ (at.%) in the as-cast condition for the region between the unmelted dark Cr, as shown in Figures 4.87 (a) and (b).

Phase contrast	Nb	Cr	Pt	Phase
Overall	13.1±0.3	70.1±0.4	16.8±0.2	-
Dark (dendrites)	1.6±0.2	93.0±0.7	5.4±0.5	(Cr)
Medium-grey	6.8±0.2	77.4±0.2	15.8±0.0	~Cr_3Pt
Light matrix	17.1±0.3	63.2±0.3	19.8±0.1	τ1

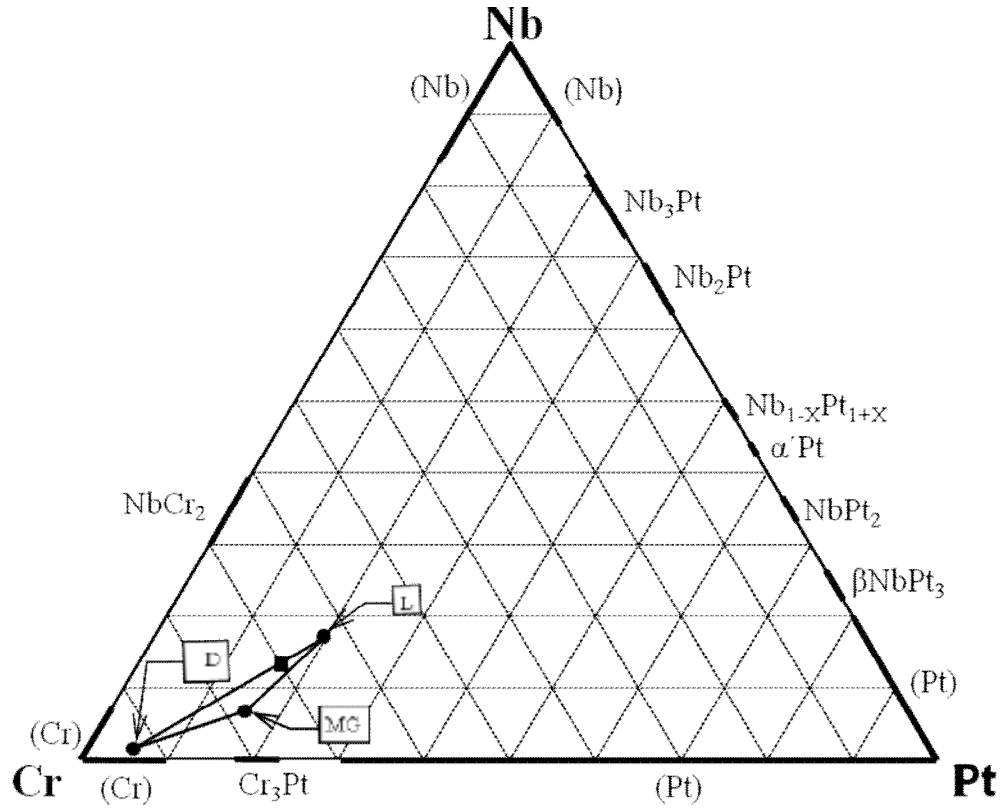

Figure 4.88. EDX phase compositions of nominal $Nb_{20}:Cr_{60}:Pt_{20}$ (at.%) alloy in the as-cast condition for the region between the unmelted Cr: (L) light contrast; (MG) medium-grey contrast; (D) dark contrast phase; ■ overall composition; ● phase composition.

(b) In a minor part of the alloy, between the unmelted niobium and platinum (Figure 4.86), the alloy comprised medium-grey ternary phase 1 (τ1) dendrites and interdendritic light (Pt), as shown in Figure 4.89. This part of the sample had many pores. Table 4.26 and Figure 4.90 gives the EDX analyses, and the overall composition was slightly off the tie-line, and much closer to the medium-grey phase composition, as expected from the microstructure.

The microstructure solidified as follows:

$$L \rightarrow \tau 1$$

followed by peritectic reaction

$$L + \tau 1 \rightarrow (Pt)$$

or possibly, a sparse eutectic

$$L \rightarrow \tau 1 + (Pt)$$

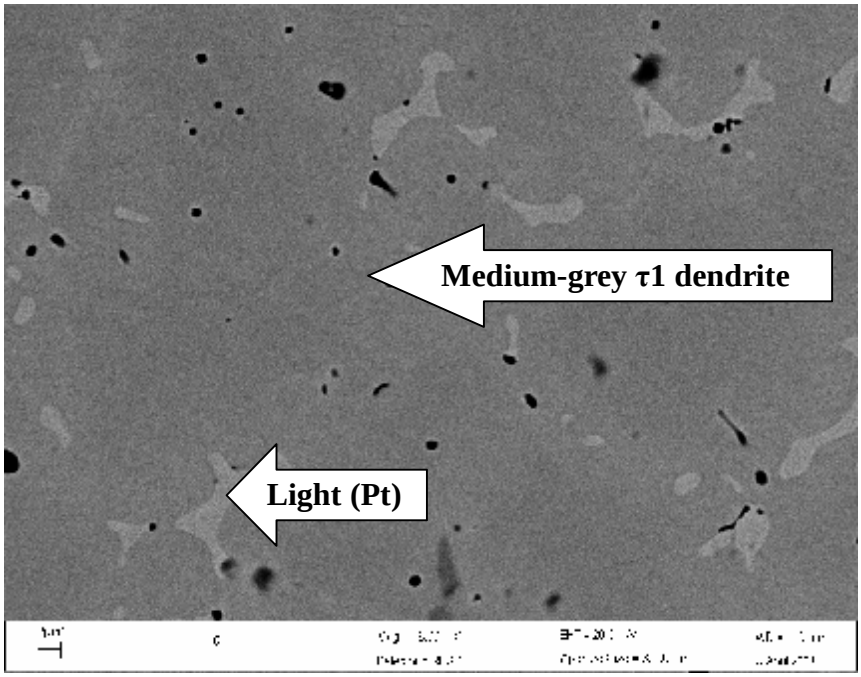

Figure 4.89. SEM-BSE image of nominal Nb_{20}:Cr_{60}:Pt_{20} alloy in the as-cast condition for the minor region near the unmelted Nb, showing medium-grey τ1 dendrites and light interdendritic (Pt).

Table 4.26. EDX phase analyses of nominal $Nb_{20}:Cr_{60}:Pt_{20}$ (at.%) in the as-cast condition for the minor region near the unmelted Nb, as shown in Figure 4.89.

Phase contrast	Nb	Cr	Pt	Phase
Overall	17.6±0.4	60.5±0.7	21.9±0.2	-
Light (interdendritic)	10.9±0.3	61.3±0.3	27.8±0.1	(Pt)
Medium-grey (dendrites)	17.1±1.3	61.3±0.8	21.6±0.5	τ1

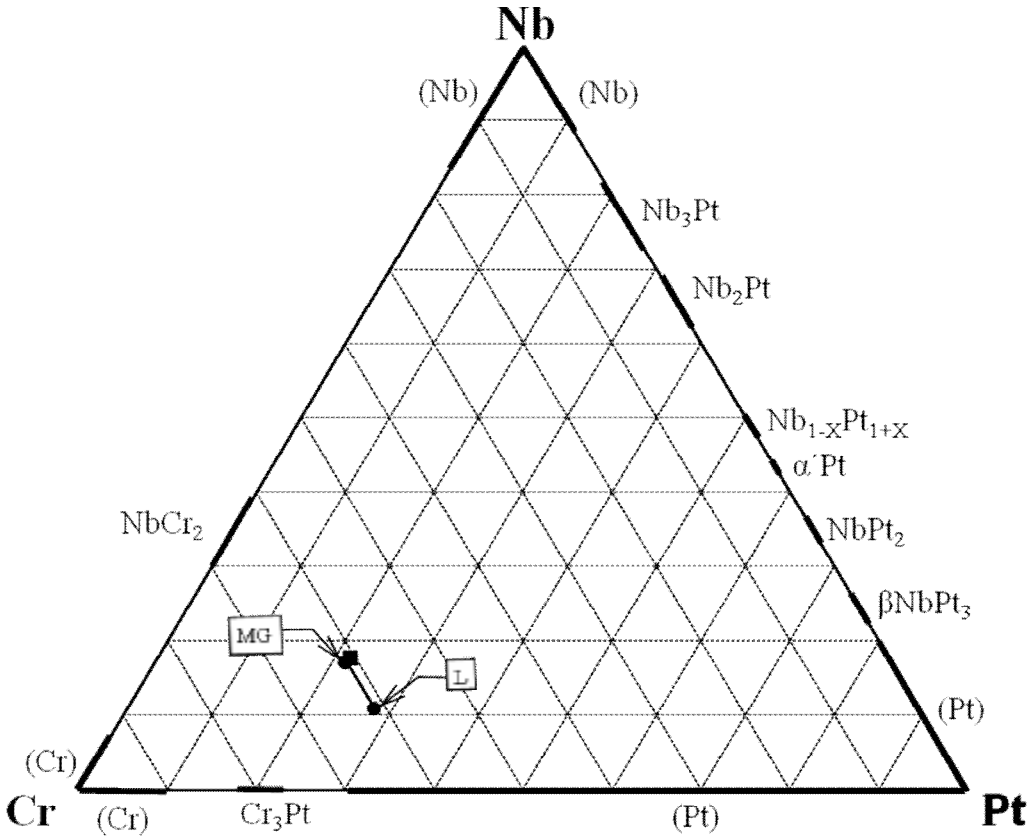

Figure 4.90. EDX phase compositions of nominal $Nb_{20}:Cr_{60}:Pt_{20}$ (at.%) alloy in the as-cast condition for the minor region near the unmelted Nb: (L) light contrast; (MG) medium-grey contrast phase; ■ overall composition; ● phase composition.

(c) From another minor part of the nominal Nb_{20}:Cr_{60}:Pt_{20} alloy, nearer the unmelted Nb than (b) (Figure 4.86), the alloy had cored light/medium-grey ternary phase 1 (τ1) dendrites with a τ1 + ~Cr_3Pt (dark) eutectic, as shown in Figure 4.91. Table 4.27 gives EDX analyses and these data are plotted in Figure 4.92. The overall composition was slightly off the tie-line and much closer to ~$NbCr_2$, and is within experimental error.

The solidification sequence is as follows:

$$L \rightarrow \tau 1$$

followed by a eutectic reaction

$$L \rightarrow \tau 1 + \sim Cr_3Pt$$

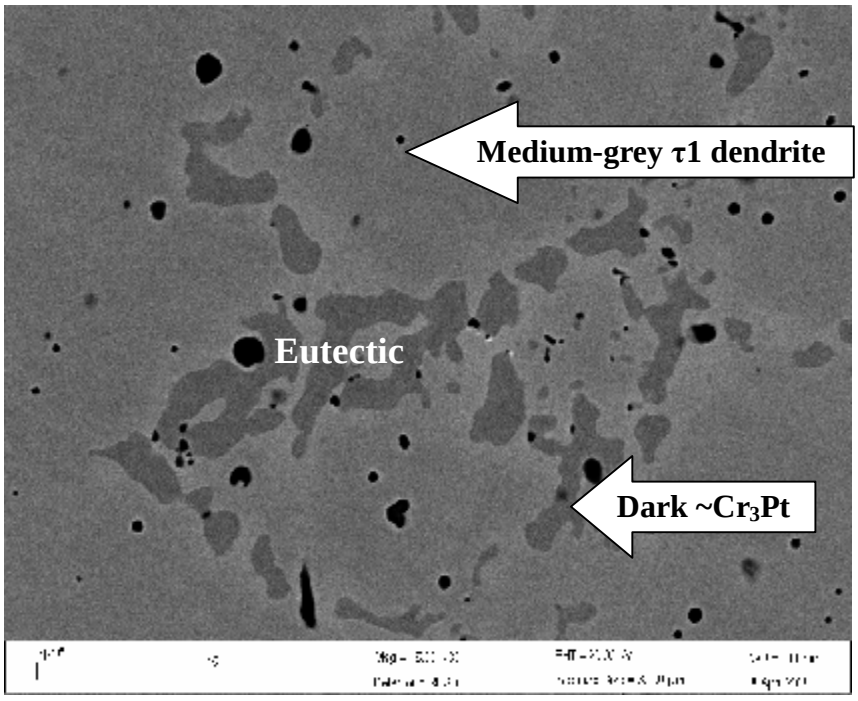

Figure 4.91. SEM-BSE image of nominal Nb_{20}:Cr_{60}:Pt_{20} alloy in the as-cast condition for another minor region near the unmelted Nb, showing medium-grey τ1 dendrites and a τ1 + dark ~Cr_3Pt eutectic.

Table 4.27. EDX phase analyses of nominal $Nb_{20}:Cr_{60}:Pt_{20}$ (at.%) in the as-cast condition for another minor region near the unmelted Nb, as shown in Figure 4.91.

Phase contrast	**Nb**	**Cr**	**Pt**	**Phase**
Overall	16.6±0.7	63.0±1.1	20.4±0.5	-
Light/Medium-grey matrix	17.8±0.4	61.1±0.1	21.2±0.3	τ1
Dark	8.9±0.4	70.1±0.4	21.0±0.1	~Cr_3Pt

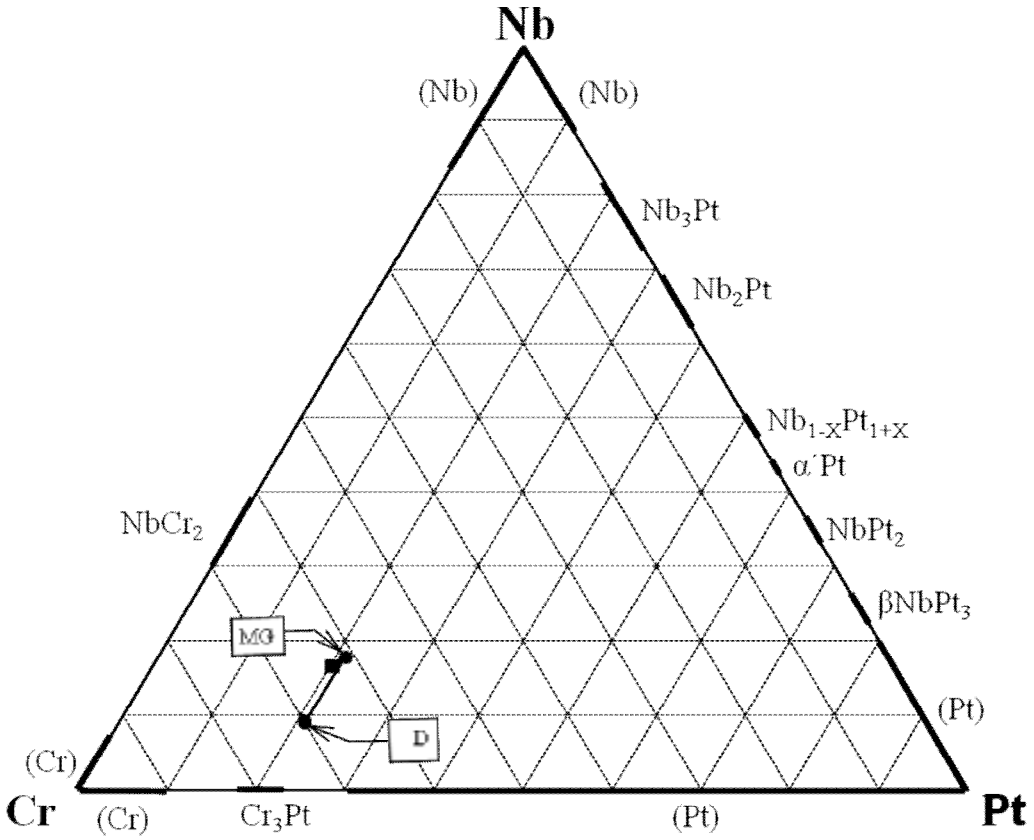

Figure 4.92. EDX phase compositions of nominal $Nb_{20}:Cr_{60}:Pt_{20}$ (at.%) alloy in the as-cast condition for another minor region near the unmelted Nb: (MG) medium-grey contrast; (D) dark contrast phase; ■ overall composition; ● phase composition.

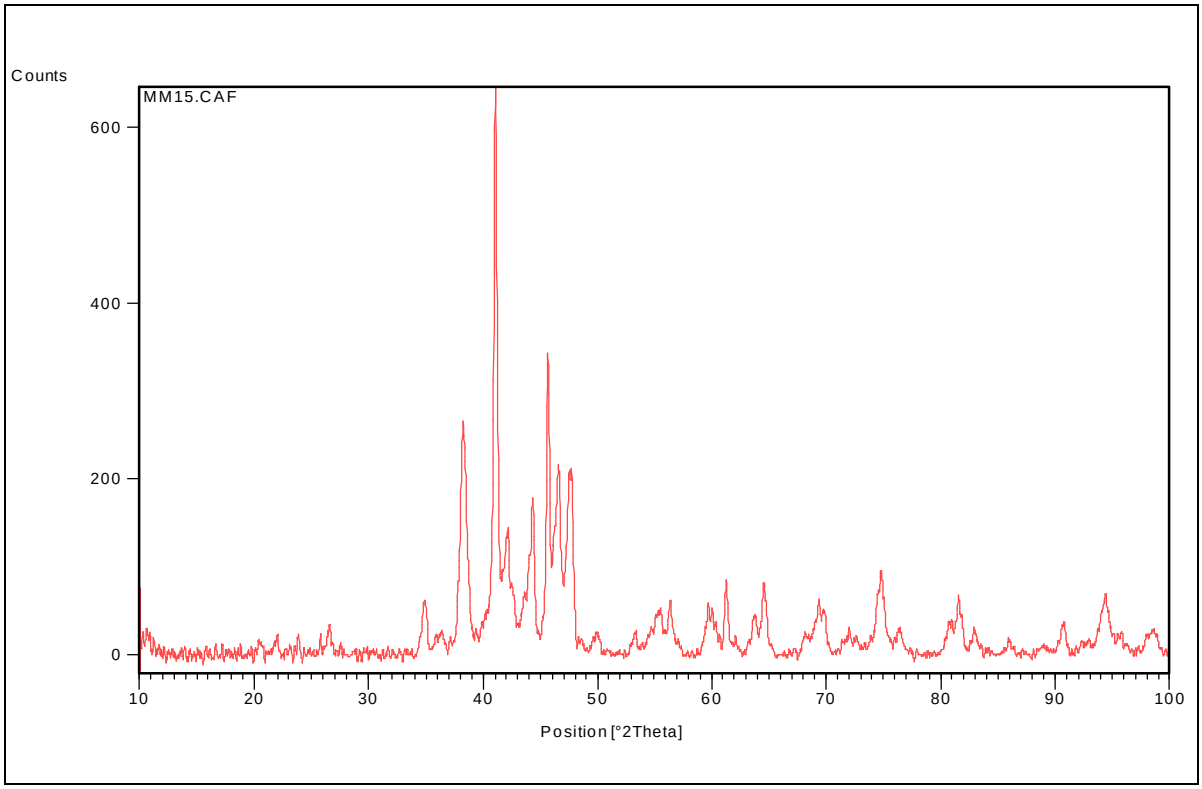

Figure 4.93. Raw XRD spectrum of nominal Nb_{20}:Cr_{60}:Pt_{20} in the as-cast condition.

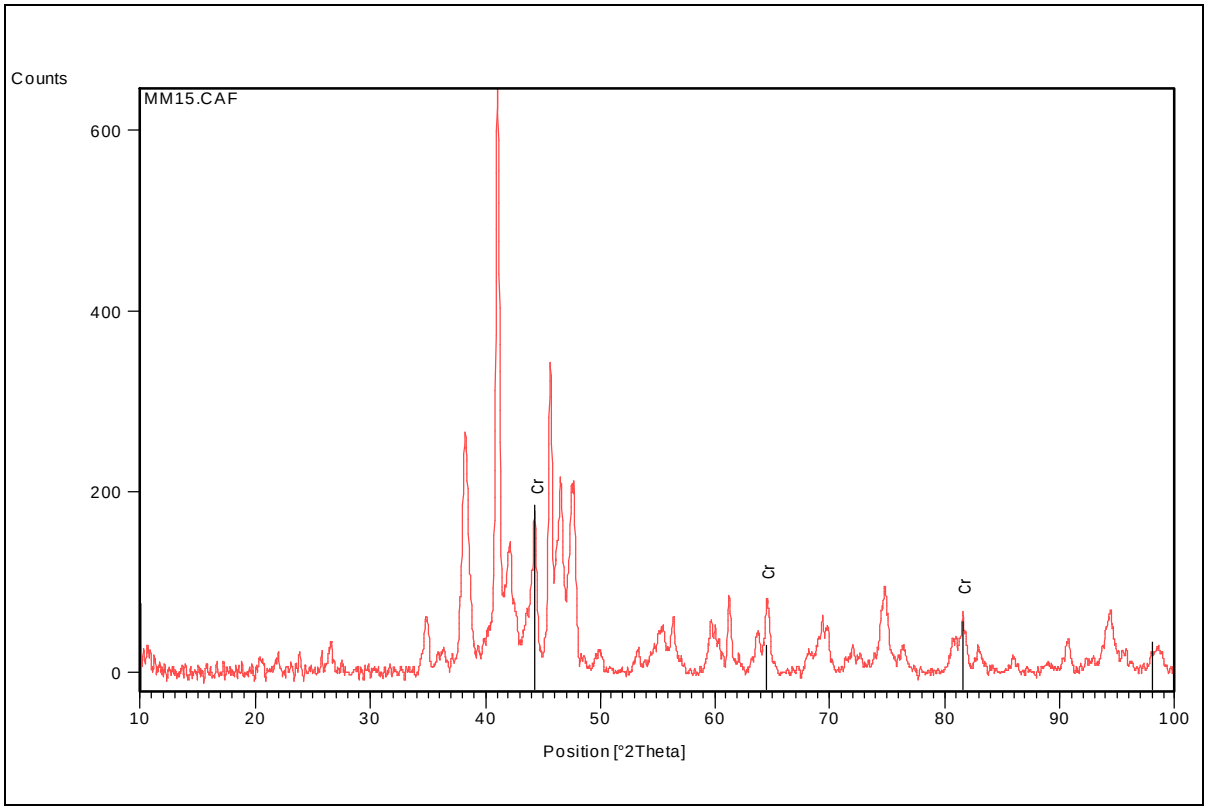

Figure 4.94. XRD spectrum of nominal Nb_{20}:Cr_{60}:Pt_{20} in the as-cast condition, showing black Cr peaks.

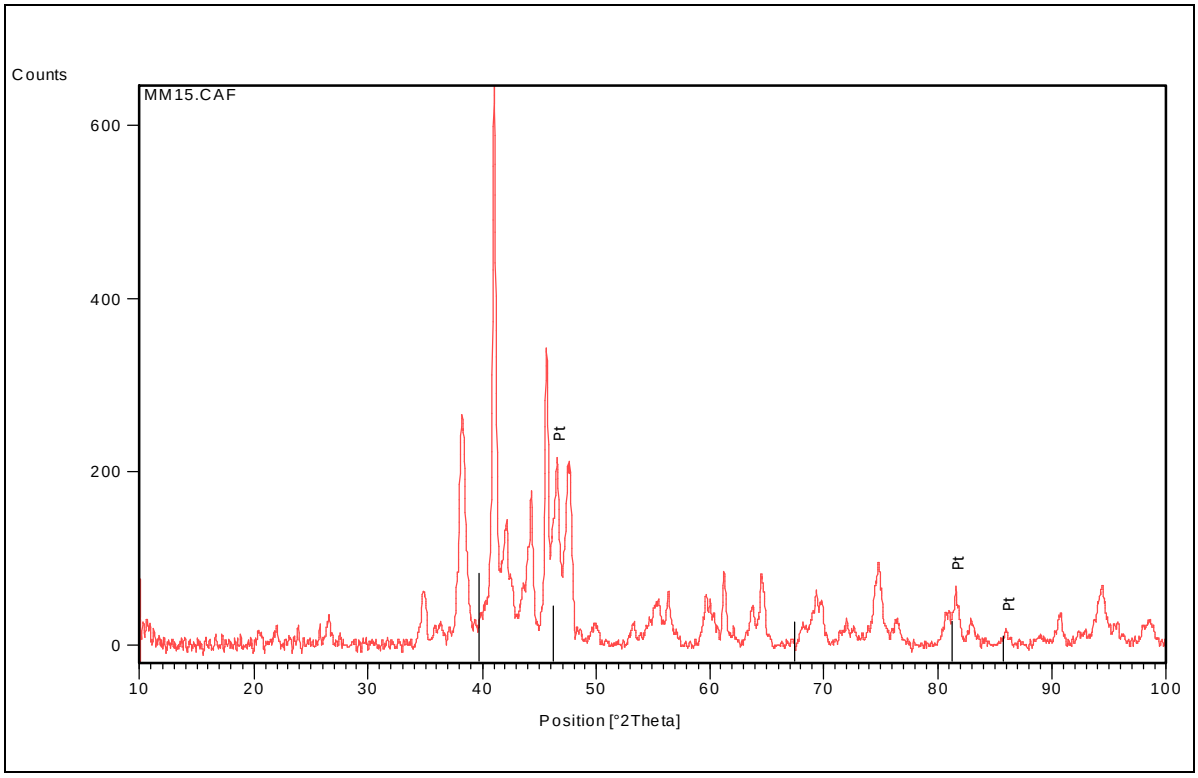

Figure 4.95. XRD spectrum of nominal Nb_{20}:Cr_{60}:Pt_{20} in the as-cast condition, showing black Pt peaks.

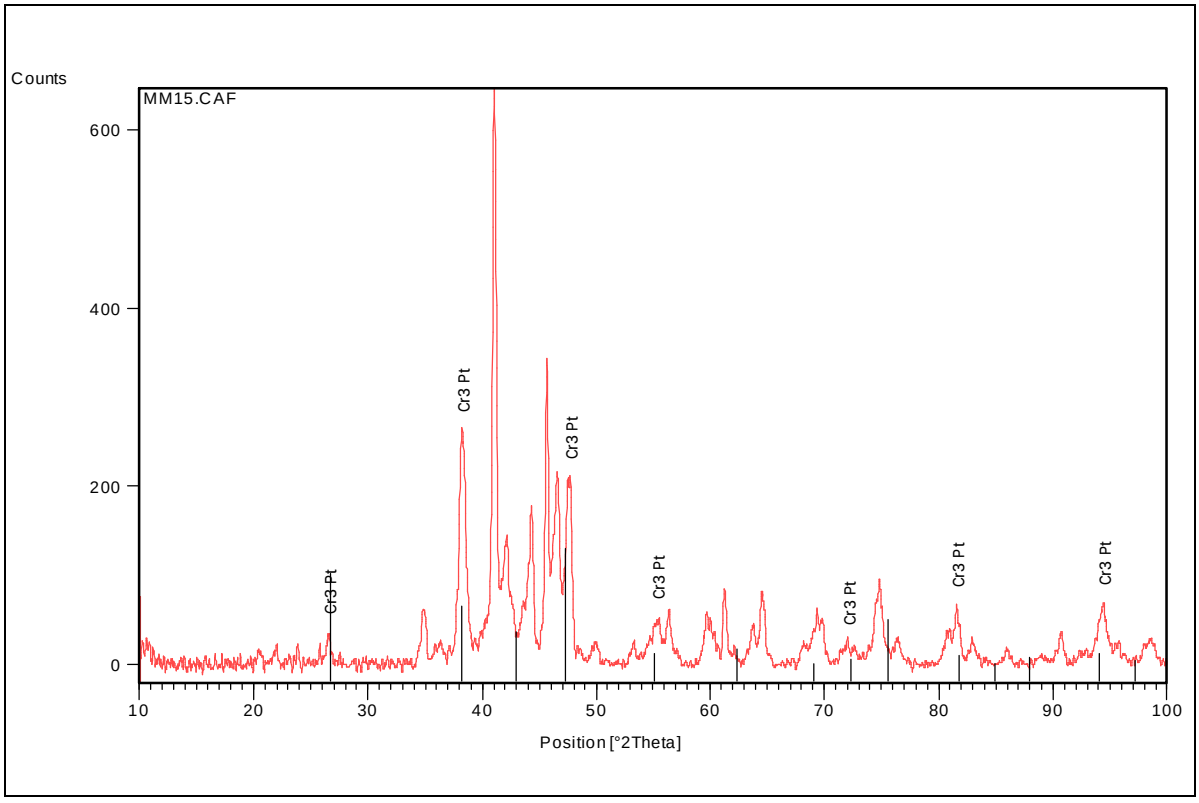

Figure 4.96. XRD pattern of nominal Nb_{20}:Cr_{60}:Pt_{20} in the as-cast condition, showing black Cr_3Pt peaks.

4.1.16 Nominal Nb_{35}:Cr_{40}:Pt_{25}, Sample 16

The nominal Nb_{35}:Cr_{40}:Pt_{25} alloy microstructure at low magnification showed unmelted pure Pt, many cracks, and different inhomogeneous regions which were analysed individually (a–b). EDX analysis on the unmelted light contrast portion confirmed it was pure Pt, as shown in Figure 4.97.

The XRD spectrum shown in Figures 4.102 and 4.103 was a poor spectrum with a low signal: background ratio, although there were many clear peaks. The existence of ~$NbCr_2$ was confirmed, as shown in Figure 4.103, with some slight peak shifts varying in both directions. However, it was not possible to check for the presence of τ2, τ3 and τ4 phases, because there were no data for them in the database (ICDD), and the unidentified peaks were assumed to be from these phases.

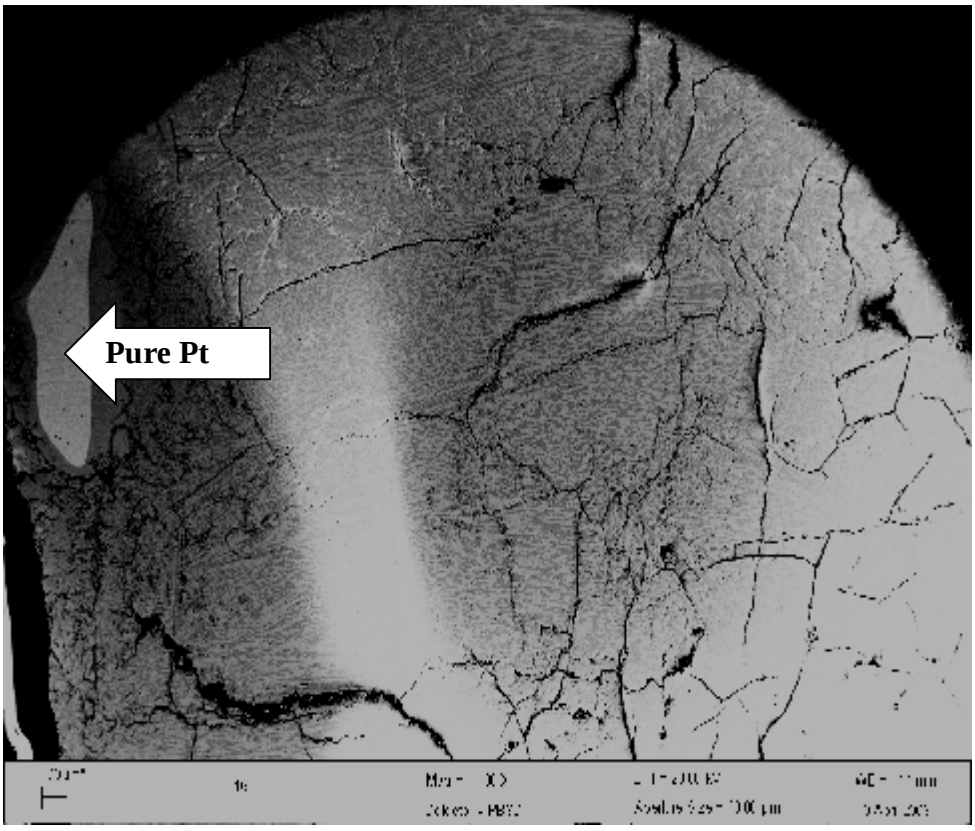

Figure 4.97. SEM-BSE image of the nominal Nb_{35}:Cr_{40}:Pt_{25} alloy in the as-cast condition at low magnification, showing many cracks, unmelted pure light Pt and different regions.

(a) The major part of the nominal Nb_{35}:Cr_{40}:Pt_{25} alloy microstructure mostly comprised dark ~$NbCr_2$ dendrites, with interdendritic medium-grey ternary phase 4 (τ4) and a light ternary phase 2 (τ2) (Figures 4.98). In local small regions, this alloy had parallel cracks. Table 4.28 gives the EDX analyses, which are plotted in Figure 4.99. The overall composition was between the three phases. The light and medium-grey phase compositions had high errors, because it was extremely difficult to distinguish between them, and they were next to each other. The best light phase composition was selected which was least affected by the medium-grey phase, and thus there is no experimental error.

The solidification sequence derived from the microstructure was as follows:

$$L \rightarrow \sim NbCr_2$$

followed by a peritectic reaction

$$L + \sim NbCr_2 \rightarrow \tau 4$$

and then another peritectic reaction

$$L + \tau 4 \rightarrow \tau 2$$ (Chapter 5: Discussion)

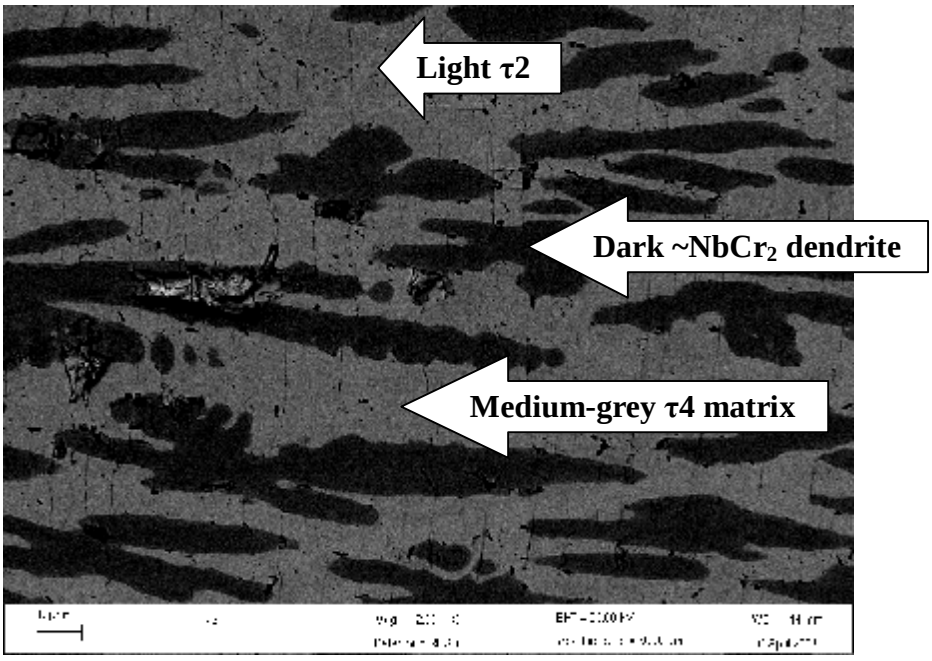

Figure 4.98. SEM-BSE image for the major part in nominal Nb_{35}:Cr_{40}:Pt_{25} alloy in the as-cast condition, showing dark ~$NbCr_2$ dendrites, medium-grey τ4 matrix and a light τ2 phase.

Table 4.28. EDX phase analyses for the major part in nominal $Nb_{35}:Cr_{40}:Pt_{25}$ (at.%) in the as-cast condition, as shown in Figures 4.98.

Phase contrast	**Nb**	**Cr**	**Pt**	**Phase**
Overall	37.4±0.3	38.1±0.4	24.5±0.2	-
Light	32.2	38.2	29.6	τ2
Medium-grey (matrix)	43.2±1.6	28.0±0.9	28.8±0.9	τ4
Dark (dendrites)	36.5±0.3	44.8±0.4	18.7±0.2	~$NbCr_2$

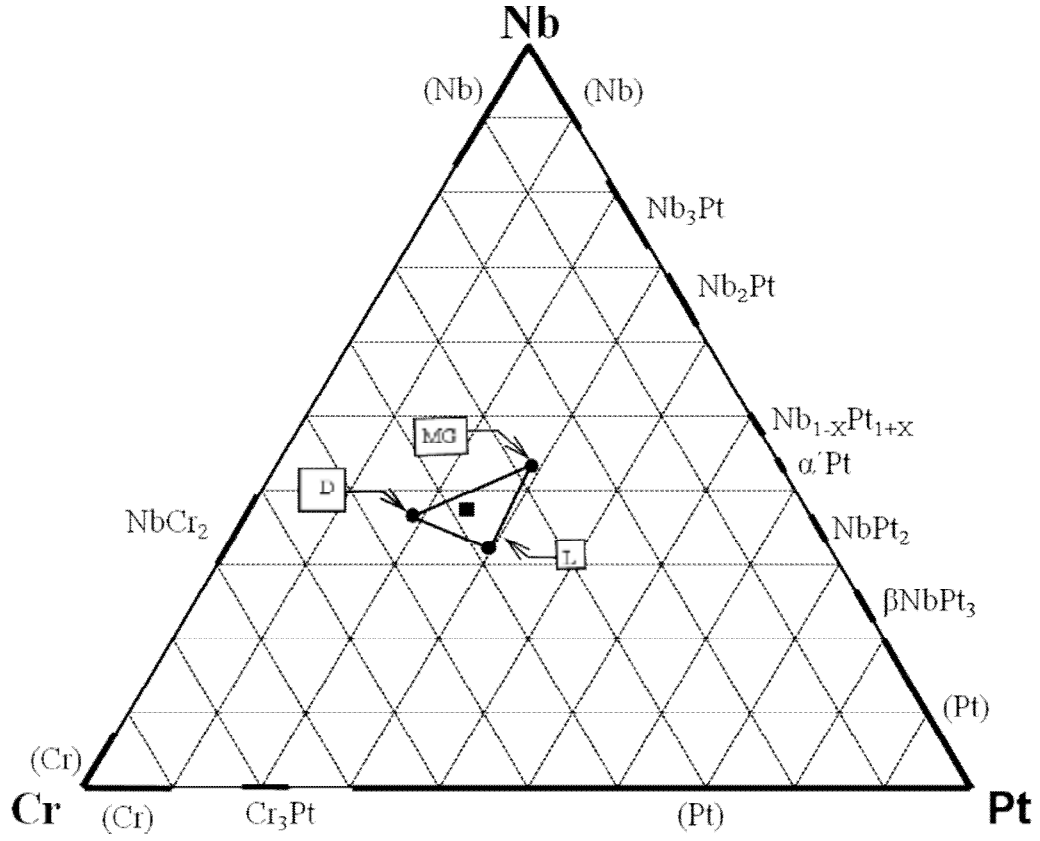

Figure 4.99. EDX phase compositions for the major part in nominal $Nb_{35}:Cr_{40}:Pt_{25}$ (at.%) alloy in the as-cast condition: (L) light contrast; (MG) medium-grey contrast; (D) dark contrast phase; ■ overall composition; ● phase composition.

(b) From a minor part of the alloy, near to the unmelted Pt, the alloy had mainly medium-grey ternary phase 2 (τ2) dendrites with pores at the dendrite edges, and interdendritic light ternary phase 3 (τ3), as shown in Figure 4.100. Table 4.29 gives the EDX analyses, and these are plotted in Figure 4.101, showing the overall composition to be on the tie-line, and much closer to the medium-grey phase composition. There was no error for overall composition because the region was small and only one analysis was made. The light phase was affected by surrounding medium-grey phase because of small area size.

The solidification sequence presumed was as follows:

$$L \rightarrow \tau 2$$

followed by a peritectic reaction

$$L + \tau 2 \rightarrow \tau 3$$

or possibly, a sparse eutectic

$$L \rightarrow \tau 2 + \tau 3$$ (Chapter 5: Discussion)

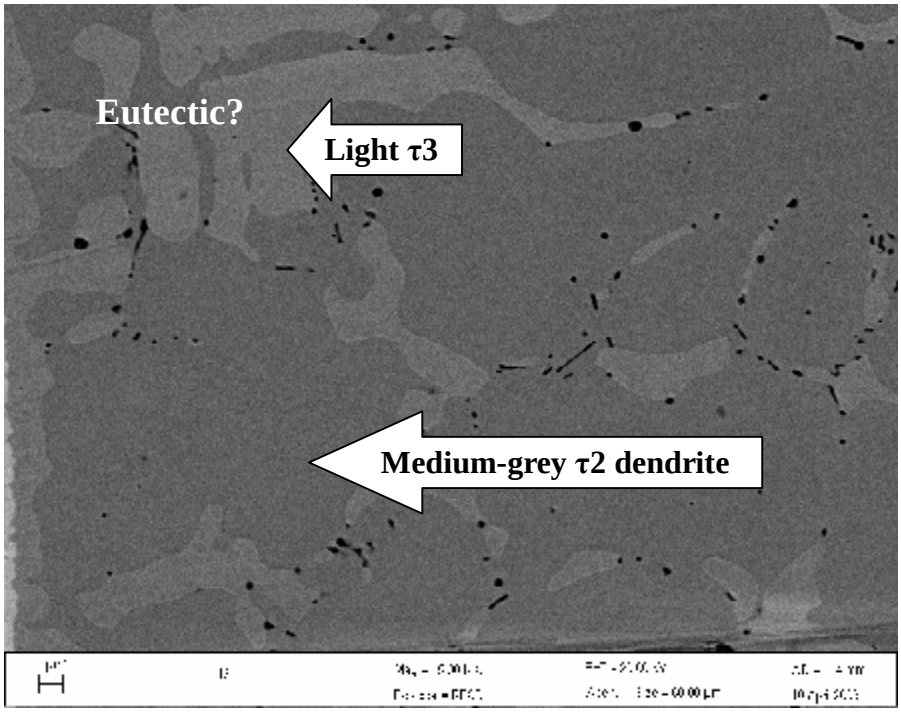

Figure 4.100. SEM-BSE image for the minor part near the unmelted Pt in nominal Nb_{35}:Cr_{40}:Pt_{25} alloy in the as-cast condition, showing medium-grey τ4 dendrites and light τ3 interdendritic phase.

Table 4.29. EDX phase analyses for the minor part near the unmelted Pt in nominal $Nb_{35}:Cr_{40}:Pt_{25}$ (at.%) in the as-cast condition, as shown in Figures 4.100.

Phase contrast	Nb	Cr	Pt	Phase
Overall (one analysis)	31.7	37.5	30.8	-
Light (interdendritic)	29.8±0.3	31.2±0.8	39.0±0.6	τ3
Medium-grey (dendrites)	32.0±0.3	37.7±0.2	30.2±0.4	τ2

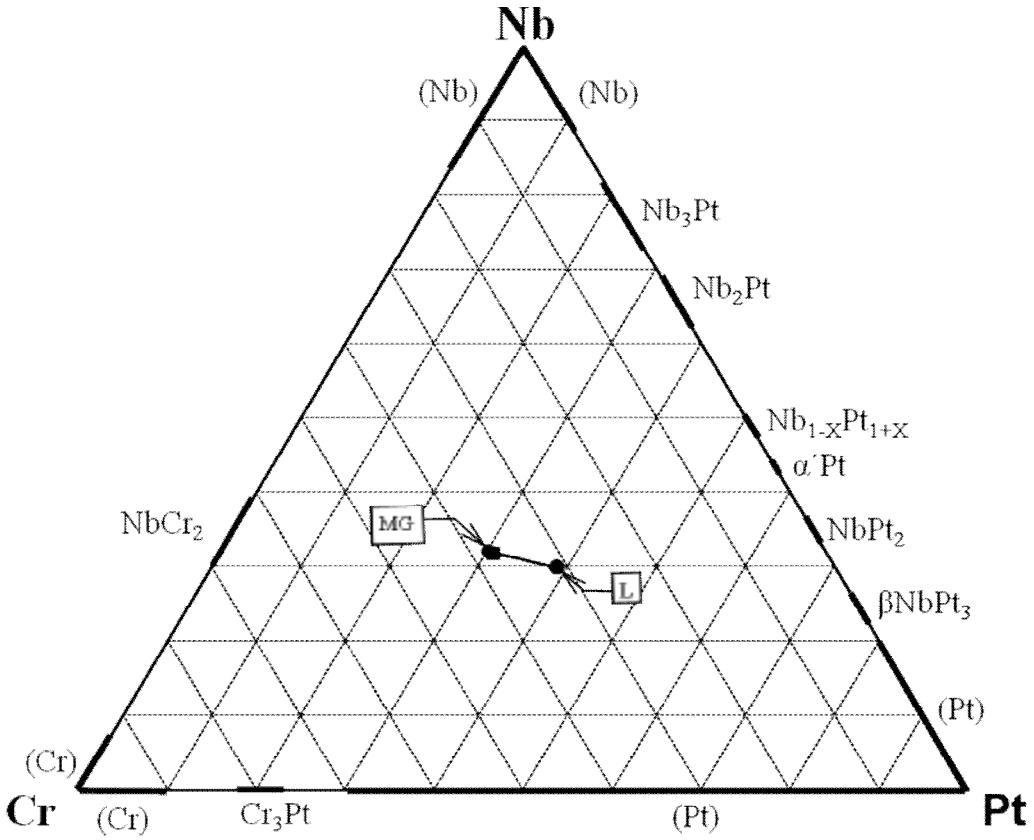

Figure 4.101. EDX phase compositions for the minor part near the unmelted Pt in nominal $Nb_{35}:Cr_{40}:Pt_{25}$ (at.%) alloy in the as-cast condition: (L) light contrast; (MG) medium-grey contrast phase; ■ overall composition; ● phase composition.

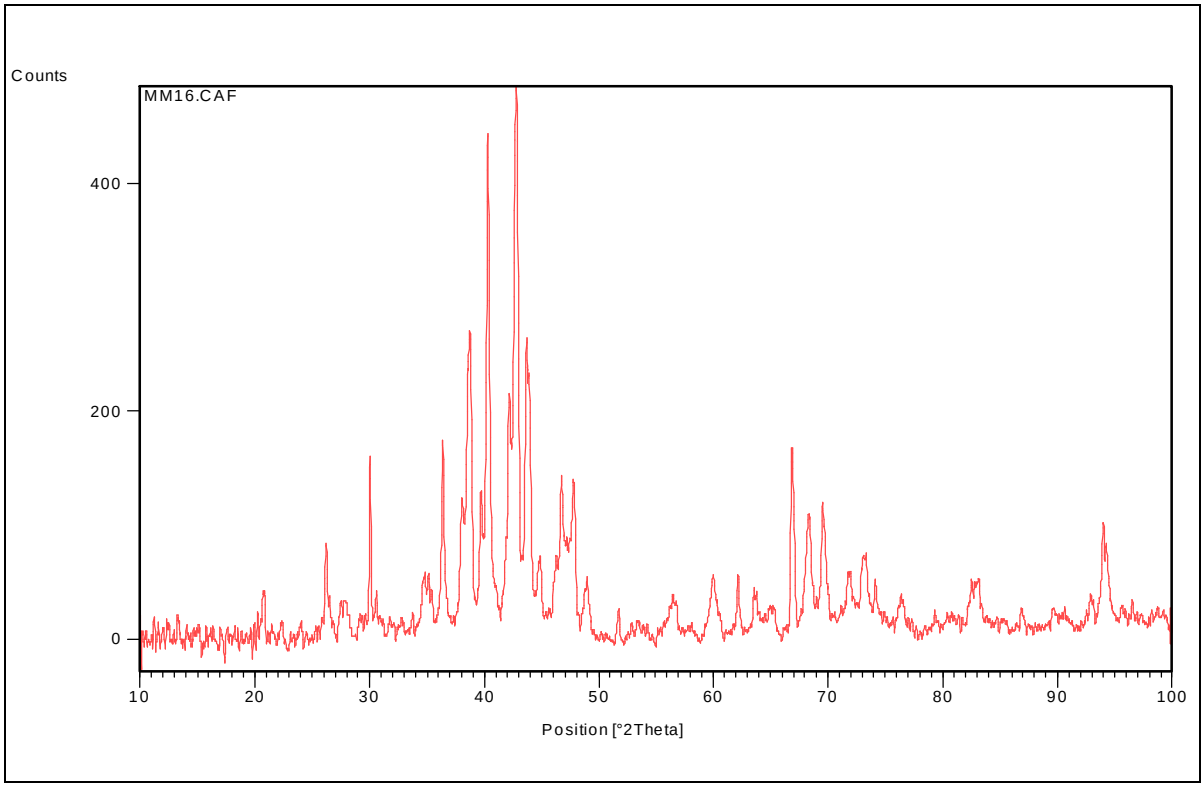

Figure 4.102. Raw XRD spectrum of nominal Nb_{35}:Cr_{40}:Pt_{25} in the as-cast condition.

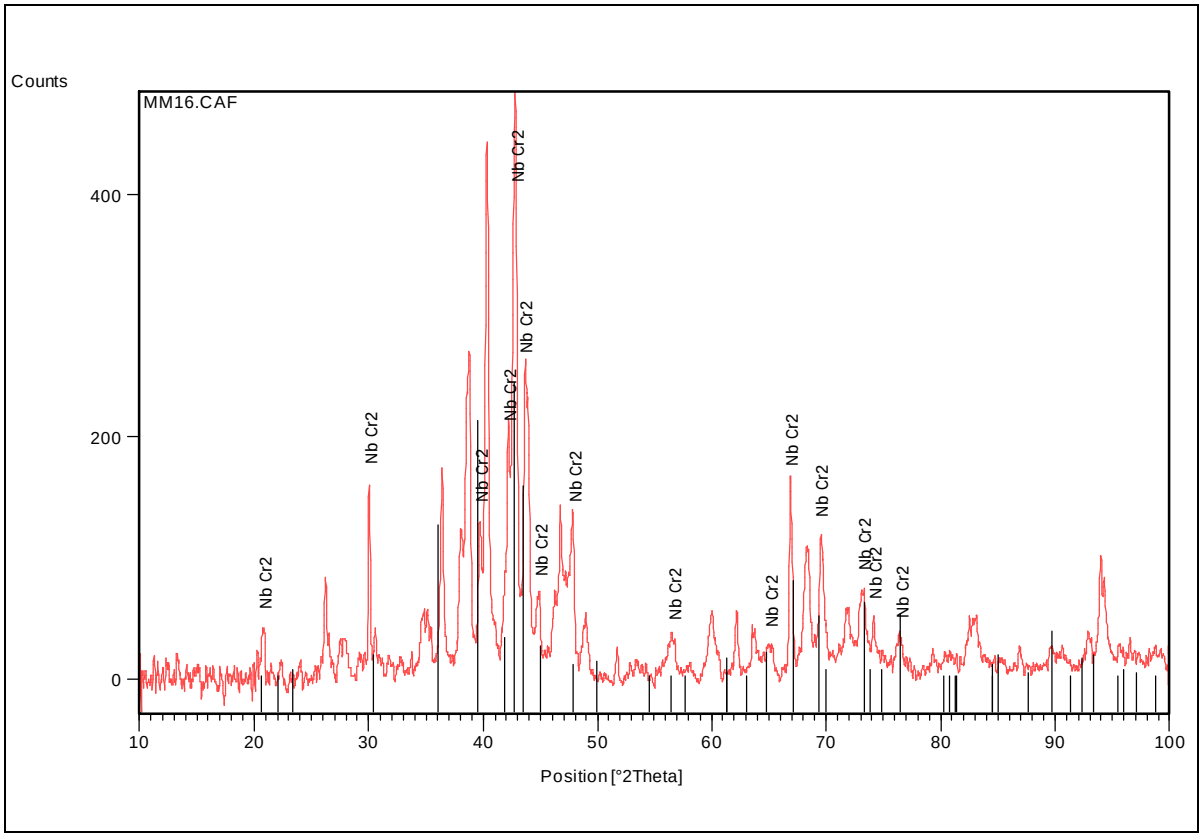

Figure 4.103. XRD spectrum of nominal Nb_{35}:Cr_{40}:Pt_{25} in the as-cast condition, showing black $NbCr_2$ peaks.

4.1.17 Nominal Nb_{40}:Cr_{25}:Pt_{35}, Sample 17

The nominal Nb_{40}:Cr_{25}:Pt_{35} alloy microstructure comprised mainly cored light ternary phase 3 (τ3) dendrites with very irregular edges and cored medium-grey ternary phase 4 (τ4), as shown in Figures 4.104 a and b, where the contrast and coring varied across the sample. Table 4.30 and Figure 4.105 give the EDX analyses. The overall composition was slightly off the tie-line between the two phases compositions, and these analyses had high errors, probably due to both coring and small area sizes. In particular, the darker phase had a wide range of analyses, and showed a darker region nearer the dendrites and a lighter region further away from the dendrites. The XRD spectrum shown in Figure 4.106 was poor, with a low signal: background ratio. None of the peaks could be identified from the database (ICDD), but they would be due to τ3 and τ4.

The microstructure was deduced to have solidified as follows:

$$L \rightarrow \tau 3$$

followed by a peritectic reaction

$$L + \tau 3 \rightarrow \tau 4 \text{ (Chapter 5: Discussion)}$$

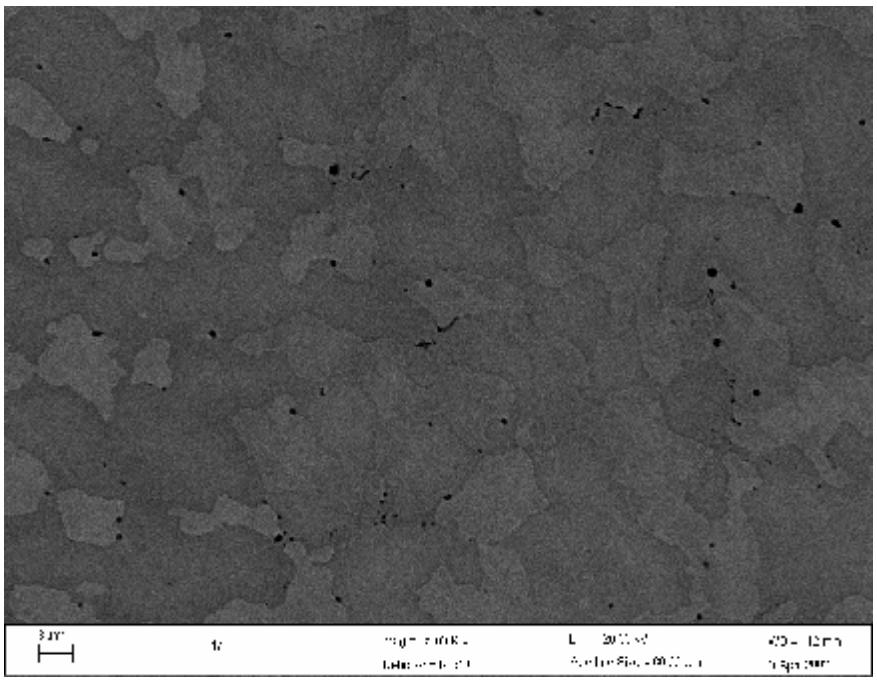

(a)

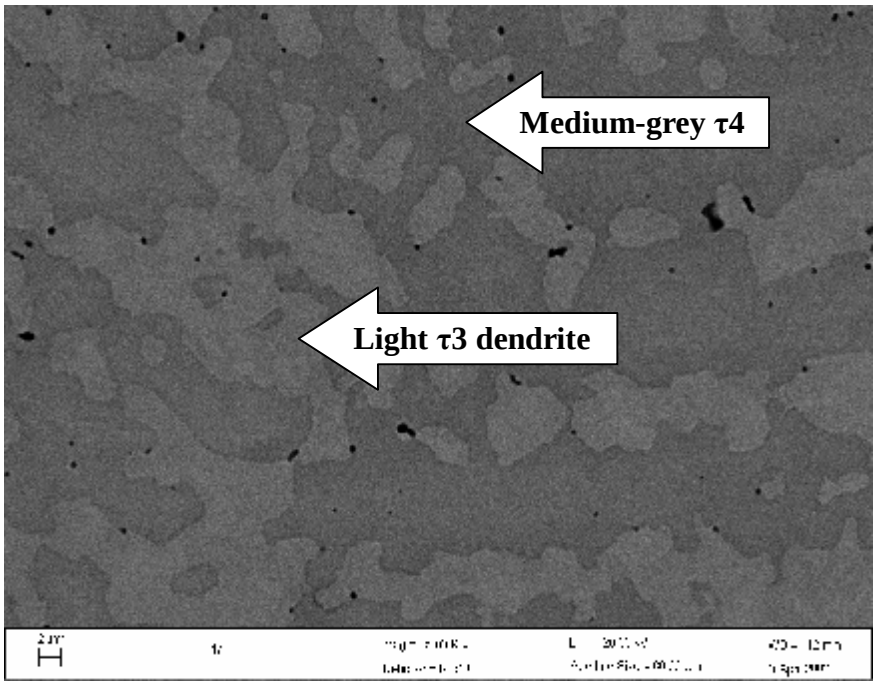

(b)

Figure 4.104 a-b. SEM-BSE images of the nominal $Nb_{40}:Cr_{25}:Pt_{35}$ alloy in the as-cast condition, showing light τ3 dendrites and medium-grey interdendritic τ4.

Table 4.30. EDX phase analyses for nominal $Nb_{40}:Cr_{25}:Pt_{35}$ (at.%) in the as-cast condition.

Phase contrast	**Nb**	**Cr**	**Pt**	**Phase**
Overall	36.8±0.2	28.9±0.3	34.4±0.3	-
Light (dendrites)	33.2±0.2	26.3±0.4	40.5±0.3	τ3
Medium-grey (interdendritic) darker	37.2±3.0	31.8±3.6	30.9±0.6	Cored τ4
Medium-grey (interdendritic) lighter	42.2±0.5	25.5±0.7	32.3±0.4	Cored τ4
Outlier	33.8	36.0	30.2	τ2??

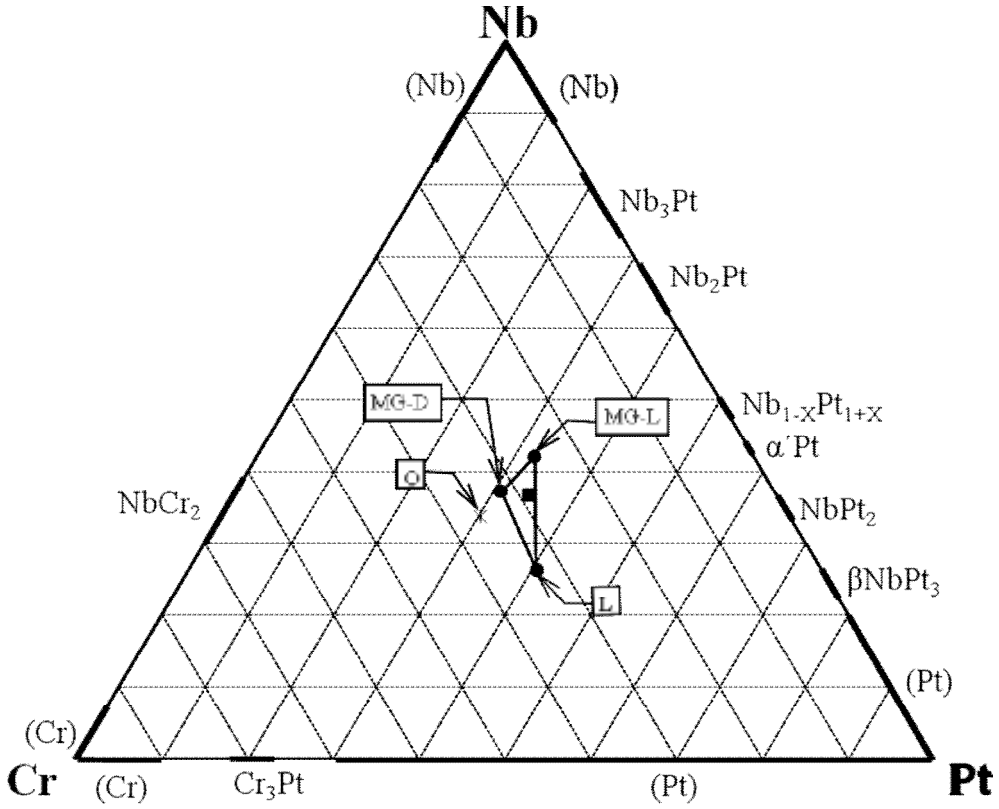

Figure 4.105. EDX phase compositions for the nominal $Nb_{40}:Cr_{25}:Pt_{35}$ (at.%) alloy in the as-cast condition: (L) light contrast; (MG-L) medium-grey lighter contrast phase; (MG-D) medium-grey darker contrast phase; (O) Outlier; ■ overall composition; ● phase composition.

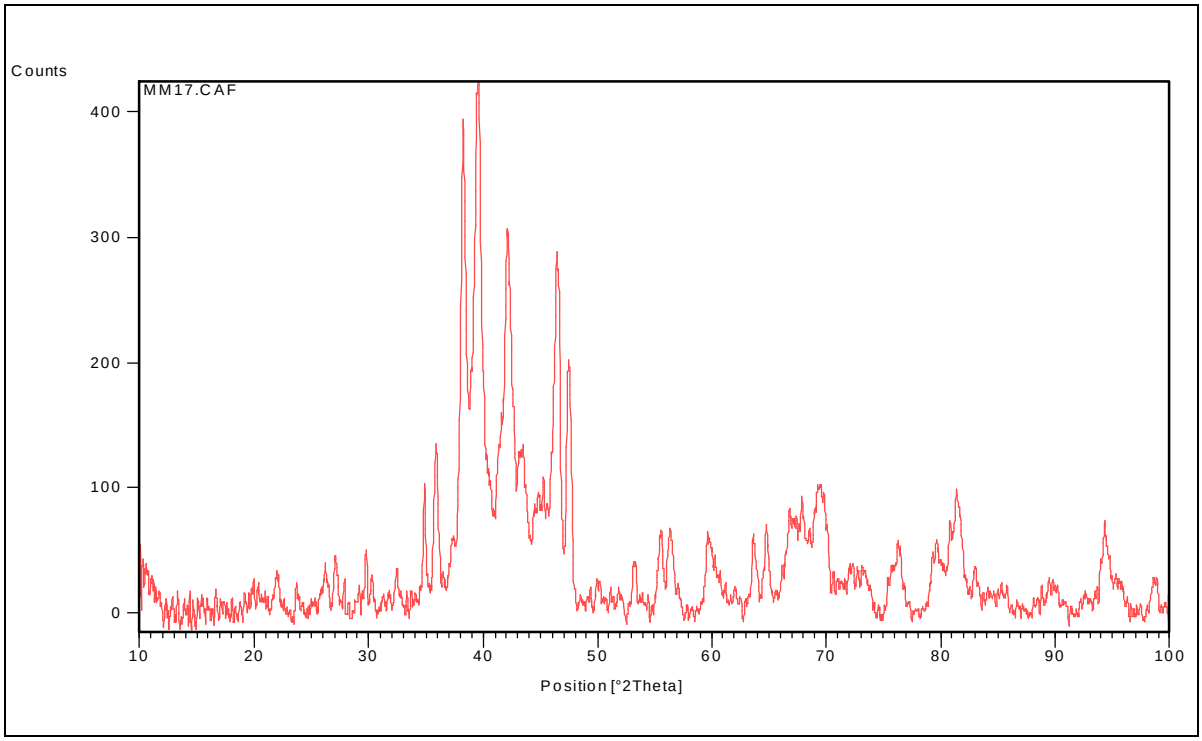

Figure 4.106. Raw XRD spectrum of nominal $Nb_{40}:Cr_{25}:Pt_{35}$ in the as-cast condition.

4.1.18 Nominal Nb_{57}:Cr_{18}:Pt_{25}, Sample 18

The nominal Nb_{57}:Cr_{18}:Pt_{25} alloy had a very inhomogeneous and many cracks (Figure 4.107), with unmelted Nb and different regions. Only one part of this sample was analysed. EDX analysis on the unmelted dark contrast portion confirmed it was pure Nb.

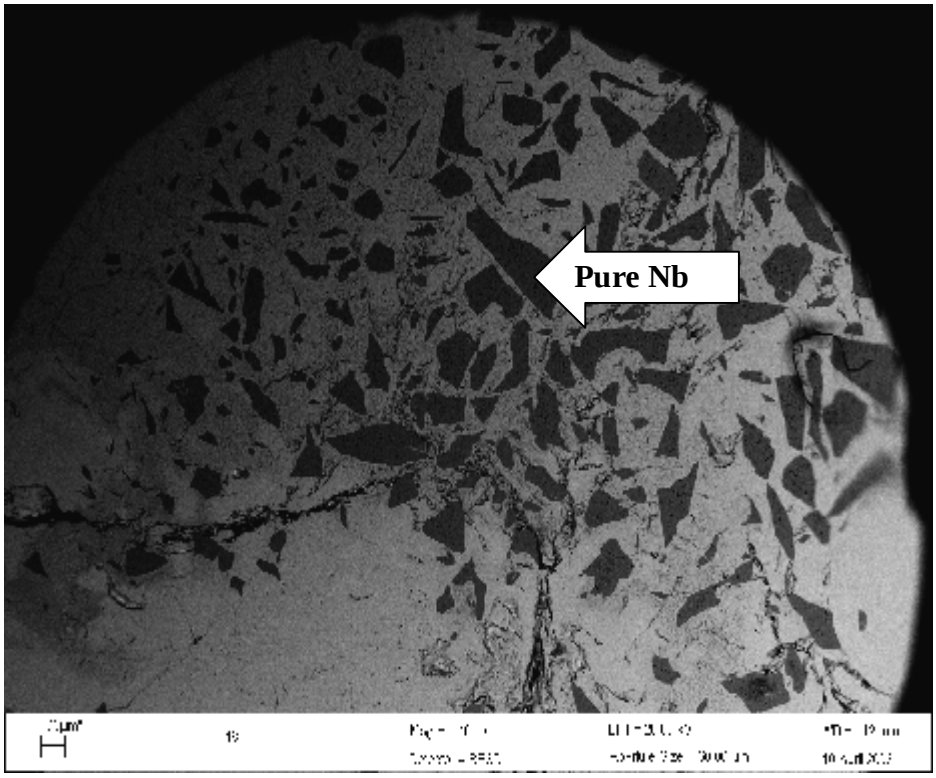

Figure 4.107. SEM-BSE image for the unmelted pure dark Nb in nominal Nb_{57}:Cr_{18}:Pt_{25} alloy in the as-cast condition at low magnification, showing unmelted pure dark Nb and different regions.

The microstructure was mainly medium-grey ternary phase 4 (τ4) dendrites, surrounded by light ~Nb_2Pt with dark interdendritic ~$NbCr_2$, as shown in Figures 4.108 a and b. Table 4.31 and Figure 4.109 gives the EDX analyses. The overall composition was on the tie-line between the medium-grey and dark contrast phase compositions, and the dark and medium-grey phases had high errors. The most Nb-rich analysis was taken for the light phase.

The XRD spectrum in Figures 4.110 and 4.111 was a poor spectrum with low signal: background ratio, but had many peaks. There were matches for $NbCr_2$ phase, with very large peak shifts varying in both ways. It was not possible to check for the presence of ~Nb_2Pt and τ4 because they are not in the ICDD database. The unidentified peaks in the spectrum are assumed to be from ~Nb_2Pt and τ4 phases.

The solidification sequence determined from the microstructure is as follows:

$$L \rightarrow \tau4$$

followed by a peritectic reaction

$$L + \tau4 \rightarrow \sim Nb_2Pt$$

and another peritectic reaction

$$L + \sim Nb_2Pt \rightarrow \sim NbCr_2$$ (Chapter 5: Discussion)

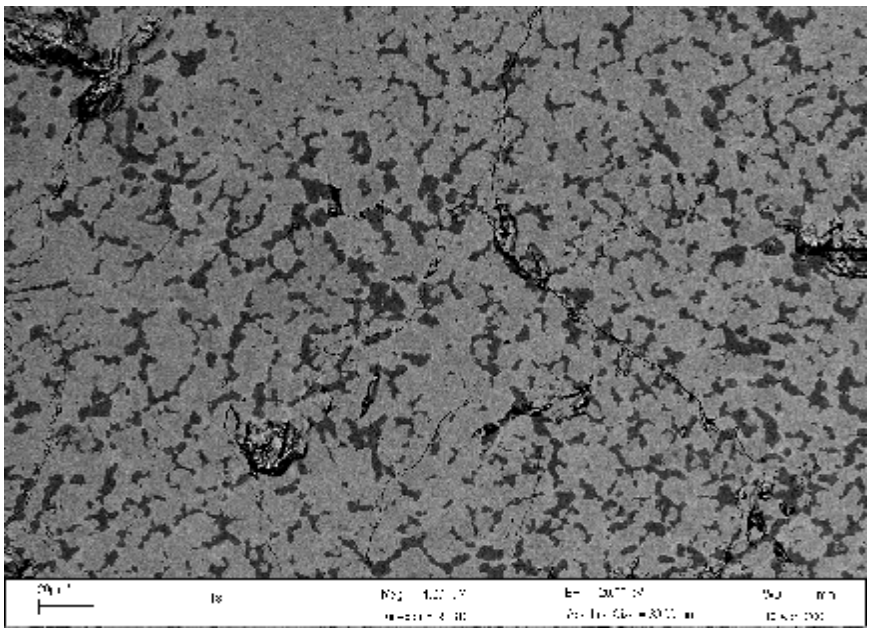

(a)

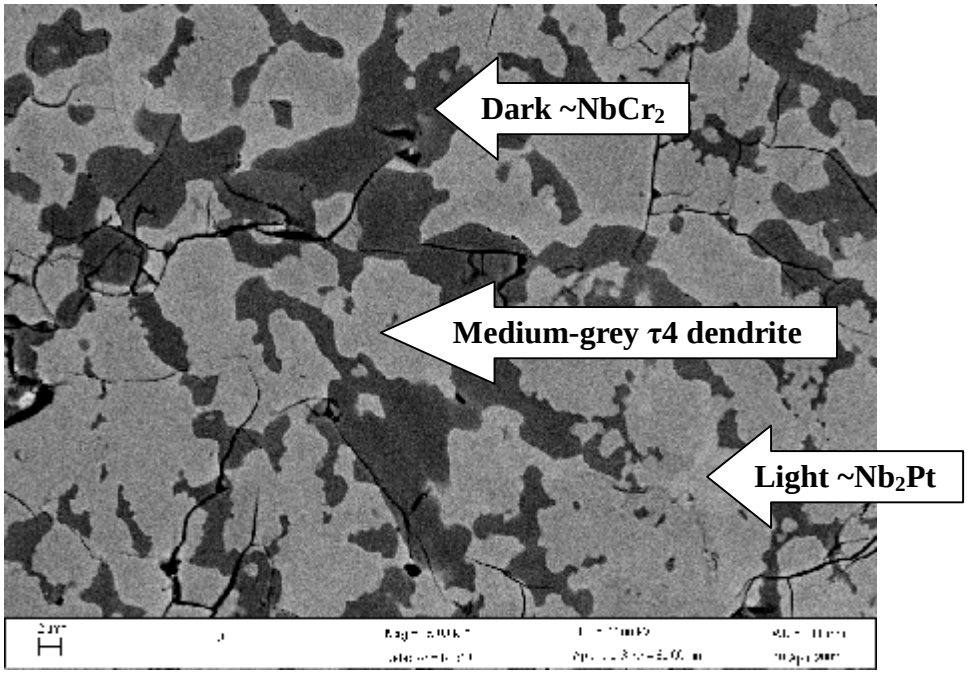

(b)

Figure 4.108 a-b. SEM-BSE images of the nominal $Nb_{57}:Cr_{18}:Pt_{25}$ alloy in the as-cast condition, showing medium-grey τ4 dendrites, light ~Nb_2Pt and dark ~$NbCr_2$.

Table 4.31. EDX phase analyses for nominal $Nb_{57}:Cr_{18}:Pt_{25}$ (at.%) in the as-cast condition.

Phase contrast	**Nb**	**Cr**	**Pt**	**Phase**
Overall	43.3±0.3	34.1±0.8	22.6±1.0	-
Light	59.0	16.1	25.0	~Nb_2Pt
Medium-grey (dendrites)	46.5±0.8	29.2±0.9	24.4±0.3	τ4
Dark (interdendritic)	33.4±0.3	50.1±0.6	16.5±0.6	~$NbCr_2$

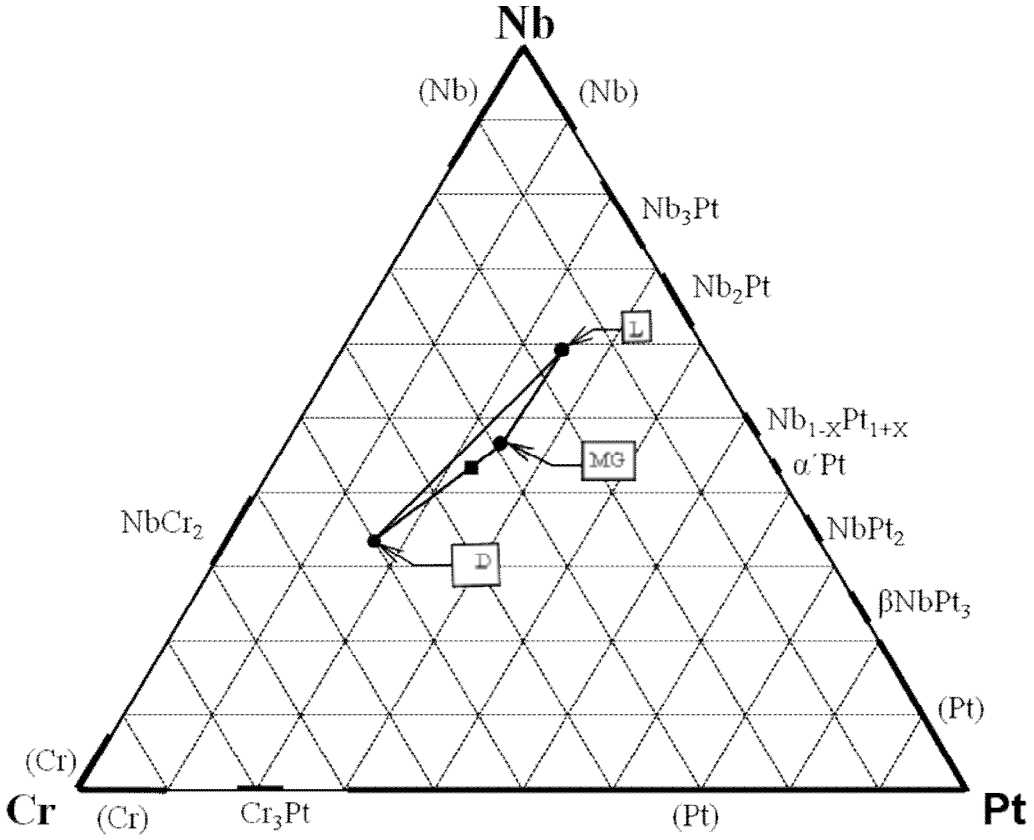

Figure 4.109. EDX phase compositions for the nominal $Nb_{57}:Cr_{18}:Pt_{25}$ (at.%) alloy in the as-cast condition: (L) light contrast; (MG) medium-grey contrast; (D) dark contrast phase; ■ overall composition; ● phase composition.

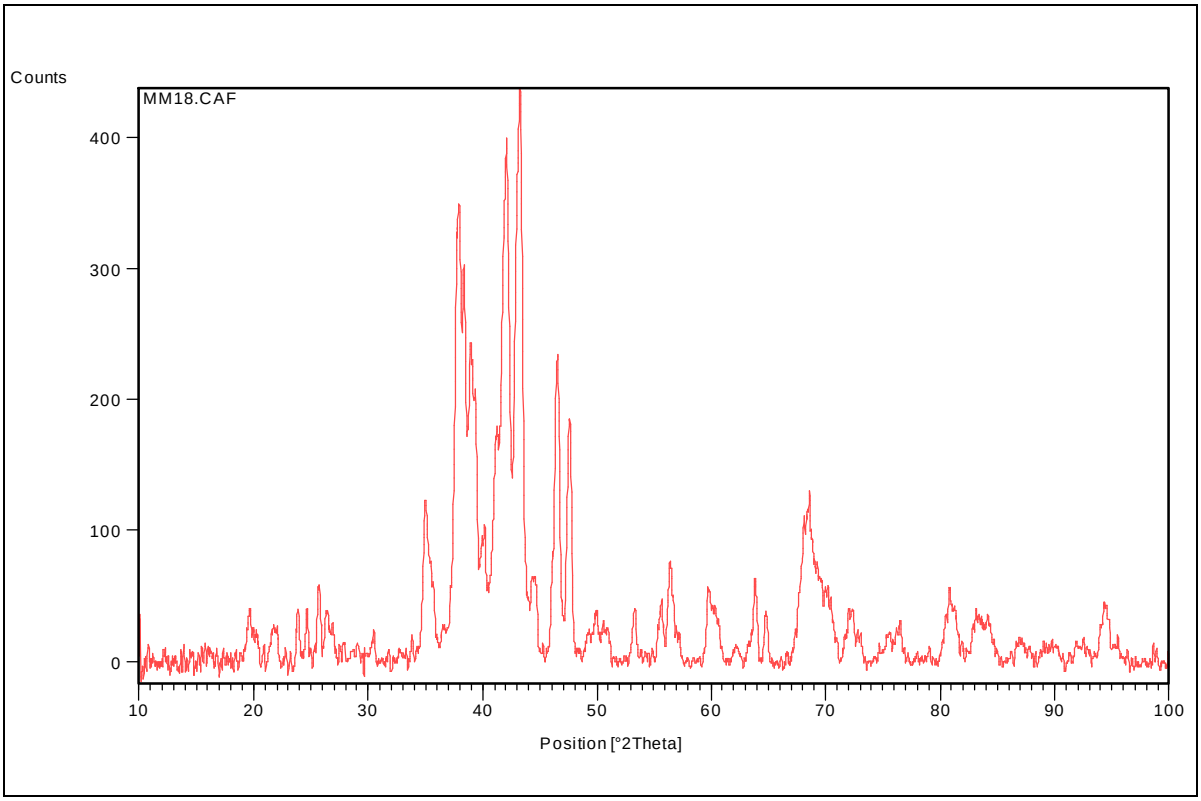

Figure 4.110. Raw XRD spectrum of nominal Nb_{57}:Cr_{18}:Pt_{25} in the as-cast condition.

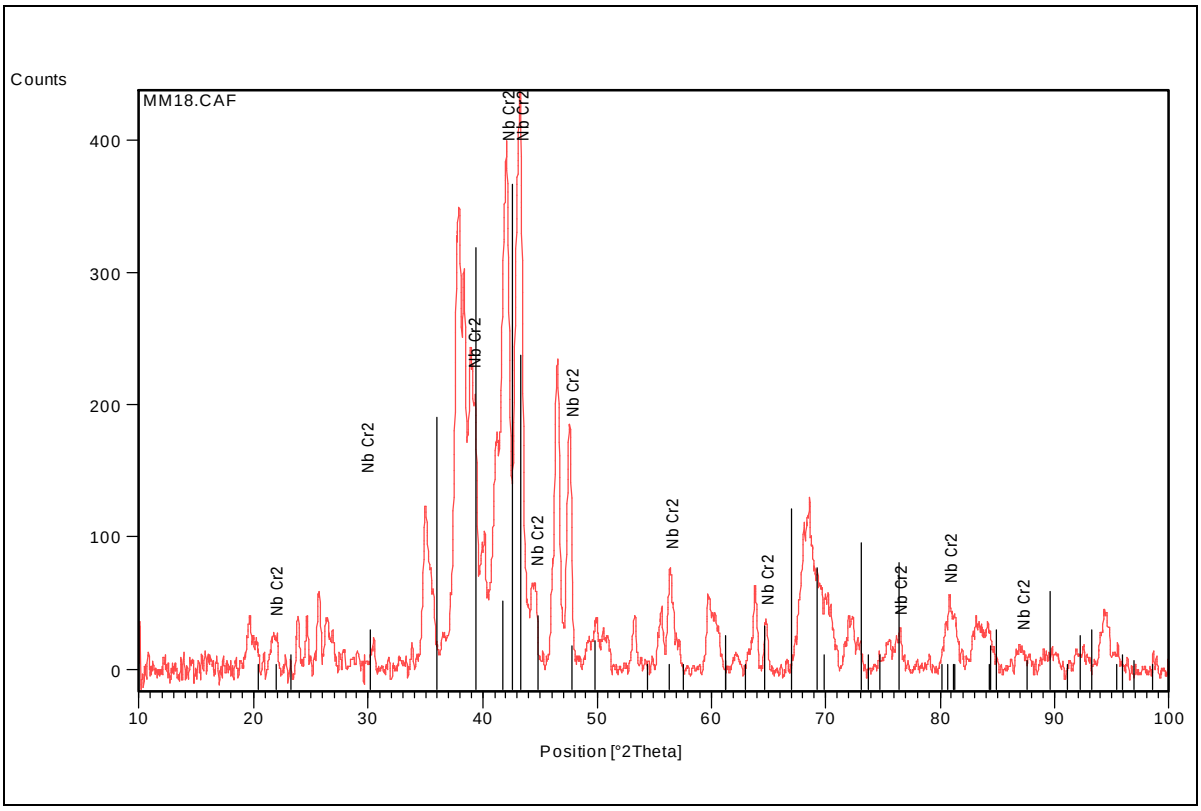

Figure 4.111. XRD spectrum of nominal Nb_{57}:Cr_{18}:Pt_{25} in the as-cast condition, showing black $NbCr_2$ peaks.

4.2 Mechanical properties

4.2.1 Hardness

The results of the Vickers macrohardness tests that were carried out on the ternary Nb-Cr-Pt as-cast samples are presented in Table 4.32.

Table 4.32. Macrohardness measurements of ternary Nb-Cr-Pt alloys using a 5kg load.

Sample name	**Alloy composition (at.%)**	**Hardness (HV_5)**	**Phases**	**Cracks?**	**Ductile/Brittle**
1	Nb_{15}:Cr_{15}:Pt_{70}	716±51	(Pt)	No cracks	Ductile
2	Nb_{15}:Cr_{40}:Pt_{45}	642±20	(Pt)	No cracks	Ductile
3	Nb_{40}:Cr_{15}:Pt_{45}	601±8	~$Nb_{1-X}Pt_{1+X}$, ~Nb_2Pt, τ4 and τ5	No cracks	Ductile
4	Nb_{15}:Cr_{70}:Pt_{15}	783±109	(Cr), ~$NbCr_2$, τ1, ~Nb_3Pt and (Nb)	Corner cracks	Brittle
5	Nb_{40}:Cr_{45}:Pt_{15}	738±63	~$NbCr_2$ and ~Nb_2Pt	Corner cracks	Brittle
6	Nb_{70}:Cr_{15}:Pt_{15}	762±93	(Nb), ~Nb_3Pt and ~$NbCr_2$	Corner cracks	Brittle
7	Nb_{30}:Cr_{10}:Pt_{60}	527±24	~β$NbPt_3$ and (Pt)	Minor cracks	Slightly brittle
8	Nb_{60}:Cr_{10}:Pt_{30}	745±102	~Nb_3Pt, ~Nb_2Pt and τ5	Corner cracks	Brittle
9	Nb_{24}:Cr_{23}:Pt_{53}	456±19	~$NbPt_2$ and (Pt)	No cracks	Ductile
10 Local regions	Nb_{44}:Cr_{12}:Pt_{44} $Nb_{40.3}$:$Cr_{20.1}$:$Pt_{39.6}$	332±91	~$Nb_{1-X}Pt_{1+X}$, ~Nb_2Pt, τ4 and τ5	Minor cracks	Slightly brittle
	$Nb_{44.1}$:$Cr_{34.1}$:$Pt_{21.9}$	507±84	~Nb_2Pt, ~$NbCr_2$ and τ4	Corner cracks	Brittle
	$Nb_{42.5}$:$Cr_{38.6}$:$Pt_{18.9}$	795±0	~Nb_2Pt, ~$NbCr_2$ and τ4	Corner cracks	Brittle

Table 4.32. Macrohardness measurements of ternary Nb-Cr-Pt alloys using a 5kg load (continued).

Sample name	Alloy composition (at.%)	Hardness (HV5)	Phases	Cracks?	Ductile/ Brittle
10 Local regions continued.	$Nb_{41.5}$:$Cr_{39.8}$:$Pt_{18.8}$	795±0	~Nb_2Pt, ~$NbCr_2$ and τ4	Corner cracks	Brittle
	$Nb_{39.3}$:$Cr_{42.4}$:$Pt_{18.3}$	795±0	~Nb_2Pt, ~$NbCr_2$ and τ4	Corner cracks	Brittle
	Unmelted Pt	113±16	Pt	No cracks	Ductile
11	Nb_{35}:Cr_{30}:Pt_{35}	642±8	(Pt) and τ2	Minor cracks	Ductile
12	Nb_{20}:Cr_{50}:Pt_{30}	739±14	(Pt) and τ1	Minor cracks	Ductile
13	Nb_{30}:Cr_{20}:Pt_{50}	655±8	~$NbPt_2$ and τ3	No cracks	Ductile
14	Nb_{25}:Cr_{45}:Pt_{30}	934±26	(Pt) and τ2	Corner cracks	Brittle
15 Local regions	$Nb_{13.1}$:$Cr_{70.1}$:$Pt_{16.8}$	966±35	(Cr), ~Cr_3Pt and τ1	Corner cracks	Brittle
	$Nb_{17.6}$:$Cr_{60.5}$:$Pt_{21.9}$ $Nb_{16.6}$:$Cr_{63.0}$:$Pt_{20.4}$	511±15	(Pt), ~Cr_3Pt and τ1	Minor corner cracks	Slightly brittle
16	Nb_{35}:Cr_{40}:Pt_{25}	690±60	~$NbCr_2$, τ2, τ3 and τ4	Corner cracks	Brittle
17	Nb_{40}:Cr_{25}:Pt_{35}	936±67	τ3 and τ4 or τ2?	Corner cracks	Brittle
18	Nb_{57}:Cr_{18}:Pt_{25}	870±79	~Nb_2Pt, ~$NbCr_2$ and τ4	Corner cracks	Brittle

Regarding the Vickers macrohardness measurements, the following explanations were made on the alloys:

- The alloys in the (Pt)-rich region had an average hardness of 679 HV_5, and these alloys are nominal ~Nb_{15}:Cr_{15}:Pt_{70} and ~Nb_{15}:Cr_{40}:Pt_{45}. This region was a single phase (Pt) region. There were no cracks found on the indentations of these alloys, and they were ductile.

- The alloy containing ~Nb_2Pt, ~$Nb_{1-X}Pt_{1+X}$, τ4 and τ5 phases had a hardness of 601±8 HV_5. This nominal ~Nb_{40}:Cr_{15}:Pt_{45} alloy was ductile, with no cracks on the indentations.
- The nominal ~Nb_{15}:Cr_{70}:Pt_{15}, ~Nb_{40}:Cr_{45}:Pt_{15} and ~Nb_{70}:Cr_{15}:Pt_{15} alloys had an average hardness of 761 HV_5, and they were found to be sitting on the same Pt (at.%) composition along the Nb-Cr binary system, and also having some common phases. The common phases were ~$NbCr_2$, ~Nb_3Pt and (Nb) for nominal ~Nb_{40}:Cr_{45}:Pt_{15} and ~Nb_{70}:Cr_{15}:Pt_{15} alloys. The ~$NbCr_2$ phase was common for all of these alloys. These alloys were brittle and had corner cracks in the indentations.
- The only ~β$NbPt_3$ and (Pt) phase containing alloy had a hardness of 527±24 HV_5. This nominal ~Nb_{30}:Cr_{10}:Pt_{60} alloy was slightly brittle, with minor cracks.
- The alloy containing ~Nb_3Pt, ~Nb_2Pt and τ5 phases had a fairly high hardness of 745±102 HV_5, and this nominal ~Nb_{60}:Cr_{10}:Pt_{30} alloy was found to be brittle and had corner cracks in the indentations.
- The nominal ~Nb_{24}:Cr_{23}:Pt_{53} alloy had a hardness of 456±19 HV_5, and this alloy was found ductile, with no cracks on the indentations. The alloy had ~$NbPt_2$ and (Pt) phases.
- The nominal ~Nb_{50}:Cr_{30}:Pt_{20} alloy had ~$Nb_{1-X}Pt_{1+X}$, ~Nb_2Pt, ~$NbCr_2$, τ4 and τ5 phases. This alloy had varying hardness values because it had different regions, with different phases and phase proportions. Overall, the alloy was brittle and had corner cracks in the indentations. The unmelted Pt was found to be ductile with no cracks on the indentations, and had a hardness of 113±16 HV_5. The regions with overall compositions of ~Nb_{44}:Cr_{12}:Pt_{44} and ~$Nb_{40.3}$:$Cr_{20.1}$:$Pt_{39.6}$ had an average hardness of 332±91 HV_5. These regions were near to the unmelted Pt, and had four phases: ~$Nb_{1-X}Pt_{1+X}$, ~Nb_2Pt, τ4 and τ5. There were cracks in the indentations and the samples were brittle. The regions containing ~Nb_2Pt, ~$NbCr_2$ and τ4 phases had a hardness value of 795 HV_5. The overall compositions of these regions were ~$Nb_{42.5}$:$Cr_{38.6}$:$Pt_{18.9}$, ~$Nb_{41.5}$:$Cr_{39.8}$:$Pt_{18.8}$ and ~$Nb_{39.3}$:$Cr_{42.4}$:$Pt_{18.3}$, had corner cracks. The ~$Nb_{44.1}$:$Cr_{34.1}$:$Pt_{21.9}$ region was found to have hardness of 507±84 HV_5, but with similar phases as the above regions. It had high experimental error because it was inhomogeneous. The reason for a smaller hardness is likely to be the coarser microstructure. This region was also brittle and had corner cracks in the indentations.

- The nominal ~Nb_{35}:Cr_{30}:Pt_{35} and ~Nb_{20}:Cr_{50}:Pt_{30} alloys had hardnesses of 642±8 and 739±14 HV_5. The phases were (Pt) and τ2, and (Pt) and τ1. These alloys were ductile and had no cracks on the indentations.
- The alloy containing ~$NbPt_2$ and τ3 had a hardness of 655±8 HV_5. This nominal ~Nb_{30}:Cr_{20}:Pt_{50} alloy was ductile and had no cracks on the indentations.
- The nominal ~Nb_{25}:Cr_{45}:Pt_{30} alloy had an overall hardness value of 934±26 HV_5. This alloy had different microstructures, but with the same (Pt) and τ2 phases. It was a very hard alloy, brittle and had corner cracks in the indentations.
- The nominal ~Nb_{20}:Cr_{60}:Pt_{20} alloy had (Cr), (Pt), ~Cr_3Pt and τ1 phases, and an overall hardness value of 706±244 HV_5. This alloy had varying hardness values because of different regions with different phases and phase proportions. There was a high experimental error on the overall hardness value because of those different regions. There were corner cracks in the indentations and it was brittle. The region with an overall composition of ~$Nb_{13.1}$:$Cr_{70.1}$:$Pt_{16.8}$ had a hardness of 966±35 HV_5, was very hard and brittle. This was a three-phase region of (Cr), ~Cr_3Pt and τ1. The ~$Nb_{17.6}$:$Cr_{60.5}$:$Pt_{21.9}$ and ~$Nb_{16.6}$:$Cr_{63.0}$:$Pt_{20.4}$ overall regions had a hardness of 511±15 HV_5, and was not as hard as the above region. These regions were brittle with minor corner cracks in the indentations. There phases were (Pt), ~Cr_3Pt and τ1.
- The alloy containing ~$NbCr_2$, τ2, τ3 and τ4 phases had a hardness value of 690±60 HV_5. This nominal ~Nb_{35}:Cr_{40}:Pt_{25} alloy had corner cracks in the indentations, showing its brittleness.
- The nominal ~Nb_{40}:Cr_{25}:Pt_{35} alloy had a hardness of 936±67 HV_5, and was very hard, brittle and had corner cracks in the indentations. The alloy had τ3 and τ4 phases.
- The nominal ~Nb_{57}:Cr_{18}:Pt_{25} alloy was also very hard, at 870±79 HV_5. This alloy had ~Nb_2Pt, ~$NbCr_2$ and τ4 phases. It had corner cracks in the indentations and was very brittle.

4.2.2 Toughness

In order to obtain a qualitative evaluation of the alloys' toughness, photographs were taken of the hardness indentations. Cracking around an indentation is an indication of brittleness, while the slip mode around the indentations shows whether the alloy has reasonable toughness (planar slip) or even better resistance against cracking (wavy slip). Figure 4.112 gives examples of the different toughnesses, showing the relevant hardness indentations and slip modes.

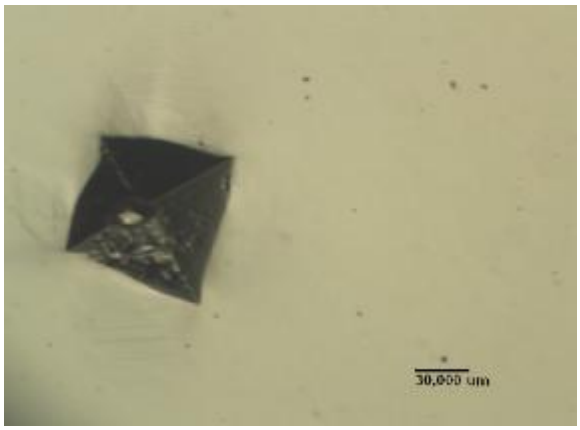

Nominal Nb_{15}:Cr_{15}:Pt_{70} (Alloy 1)
Planar slip

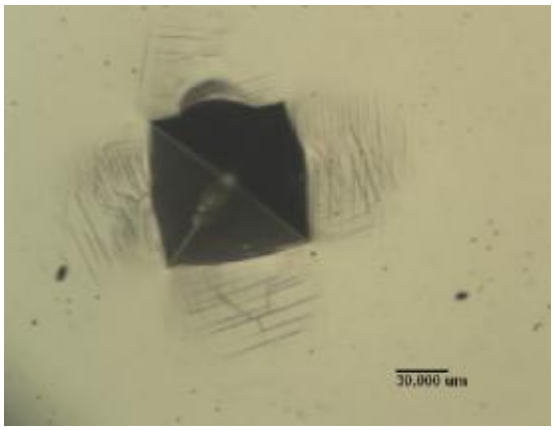

Nominal Nb_{15}:Cr_{40}:Pt_{45} (Alloy 2)
Wavy slip

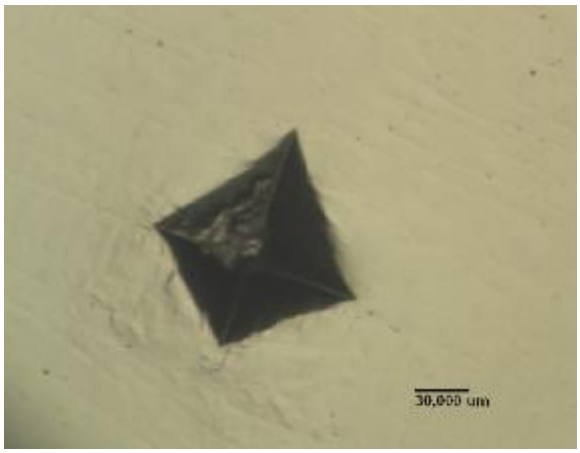

Nominal Nb_{40}:Cr_{15}:Pt_{45} (Alloy 3)
Planar slip

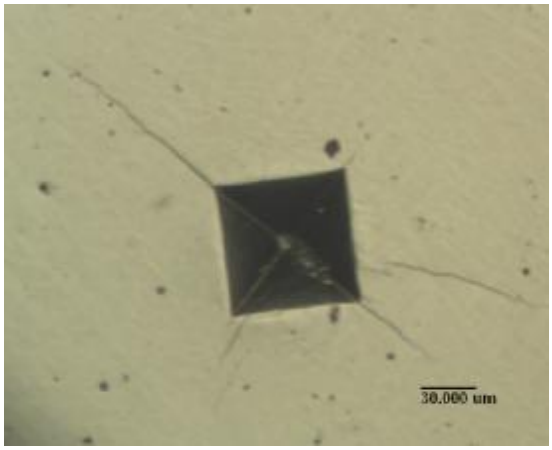

Nominal Nb_{15}:Cr_{70}:Pt_{15} (Alloy 4)
Cracking

Figure 4.112. Optical micrographs for comparison of the macrohardness indentations in the as-cast Nb-Cr-Pt alloys.

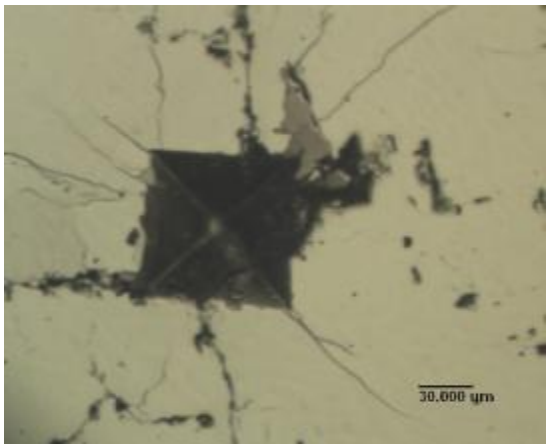

Nominal Nb_{40}:Cr_{45}:Pt_{15} (Alloy 5)
Major cracking

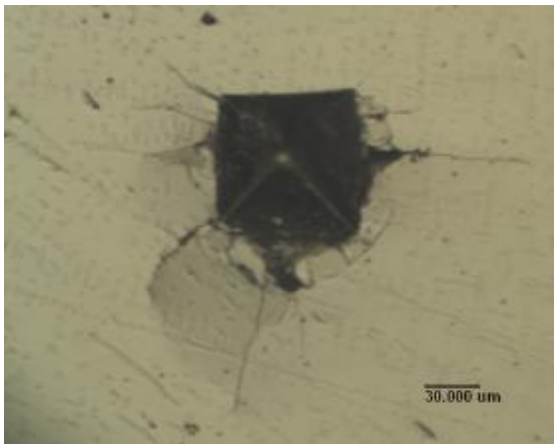

Nominal Nb_{70}:Cr_{15}:Pt_{15} (Alloy 6)
Major Cracking

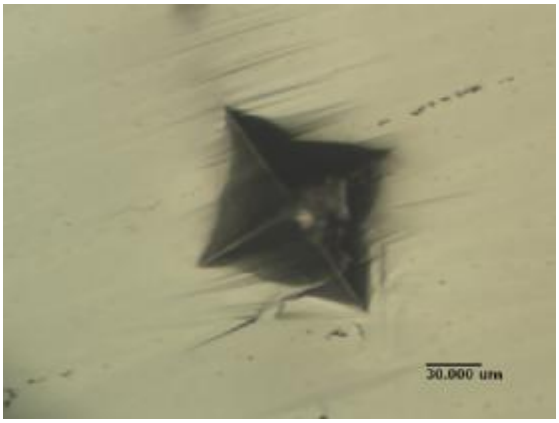

Nominal Nb_{30}:Cr_{10}:Pt_{60} (Alloy 7)
Wavy slip

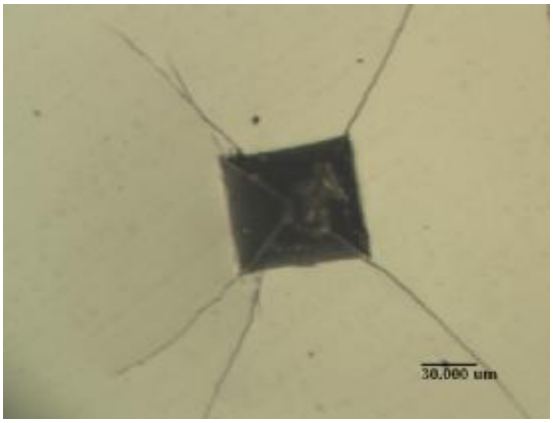

Nominal Nb_{60}:Cr_{10}:Pt_{30} (Alloy 8)
Major cracking

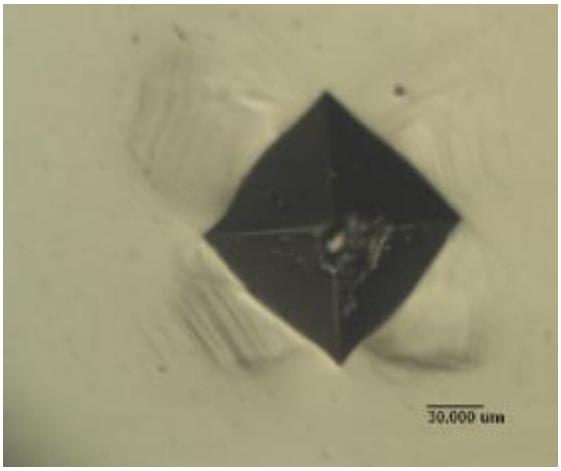

Nominal Nb_{24}:Cr_{23}:Pt_{53} (Alloy 9)
Wavy slip

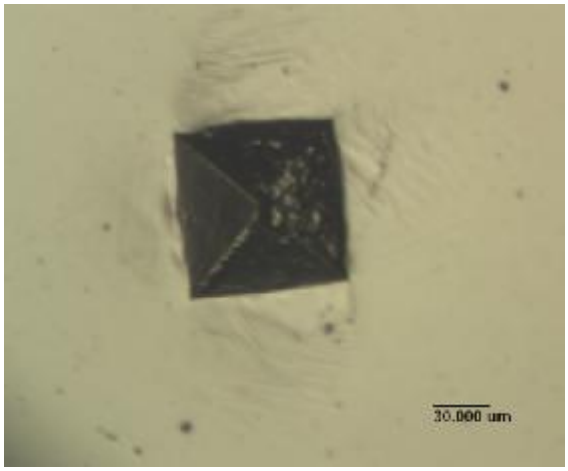

Nominal Nb_{35}:Cr_{30}:Pt_{35} (Alloy 11)
Wavy slip

Figure 4.112. Optical micrographs for comparison of the macrohardness indentations in the as-cast Nb-Cr-Pt alloys (continued).

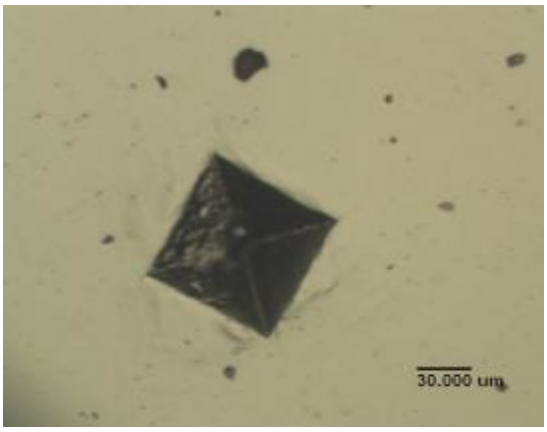

Nominal Nb_{20}:Cr_{50}:Pt_{30} (Alloy 12)
Planar slip

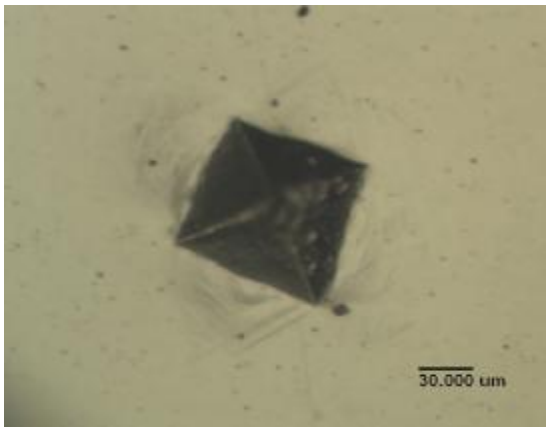

Nominal Nb_{30}:Cr_{20}:Pt_{50} (Alloy 13)
Wavy slip

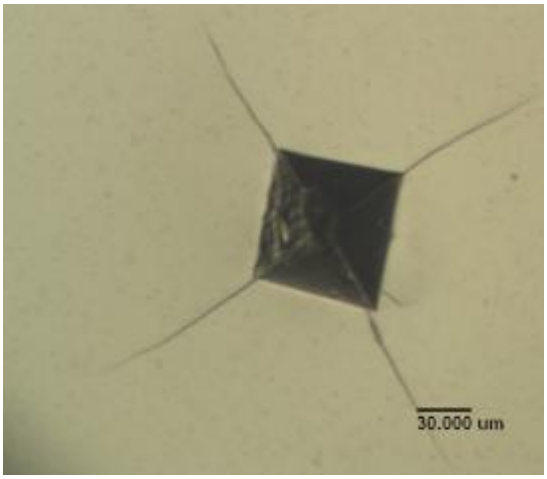

Nominal Nb_{25}:Cr_{45}:Pt_{30} (Alloy 14)
Major cracking

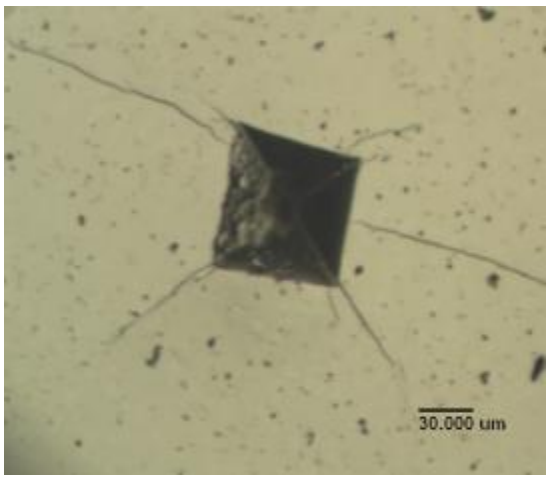

Nominal Nb_{20}:Cr_{60}:Pt_{20} (Alloy 15(a))
Major cracking

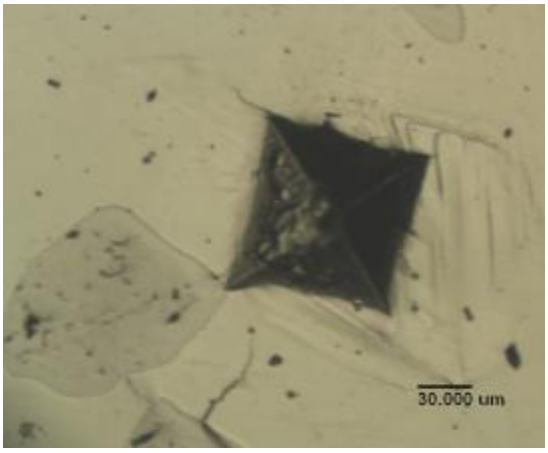

Nominal Nb_{20}:Cr_{60}:Pt_{20} (Alloy 15(b))
Wavy slip and minor cracking

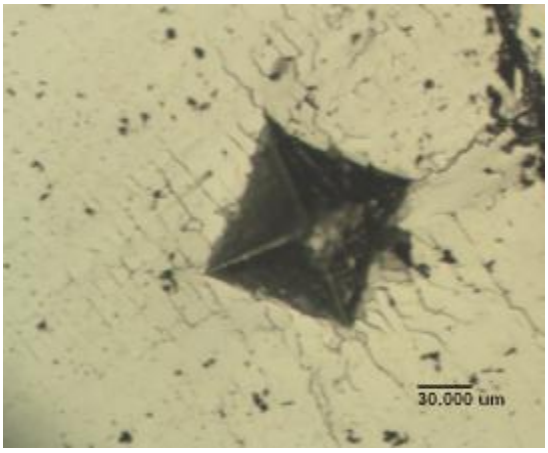

Nominal Nb_{35}:Cr_{40}:Pt_{25} (Alloy 16)
Cracking

Figure 4.112. Optical micrographs for comparison of the macrohardness indentations in the as-cast Nb-Cr-Pt alloys (continued).

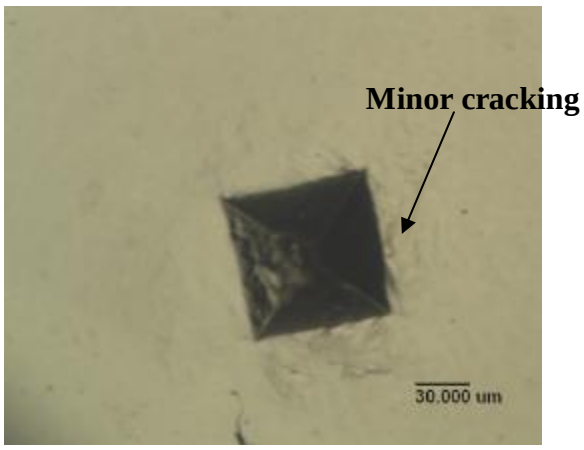

Nominal $Nb_{40}:Cr_{25}:Pt_{35}$ (Alloy 17(a))
Wavy slip and minor cracking

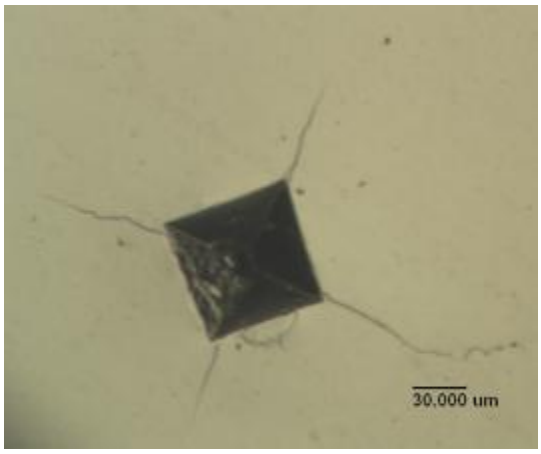

Nominal $Nb_{40}:Cr_{25}:Pt_{35}$ (Alloy 17(b))
Cracking

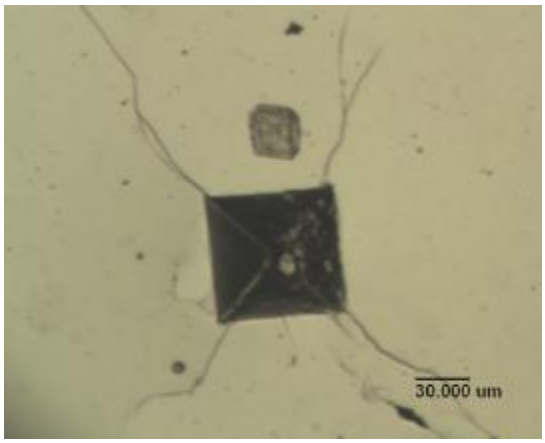

Nominal $Nb_{57}:Cr_{18}:Pt_{25}$ (Alloy 18)
Major cracking

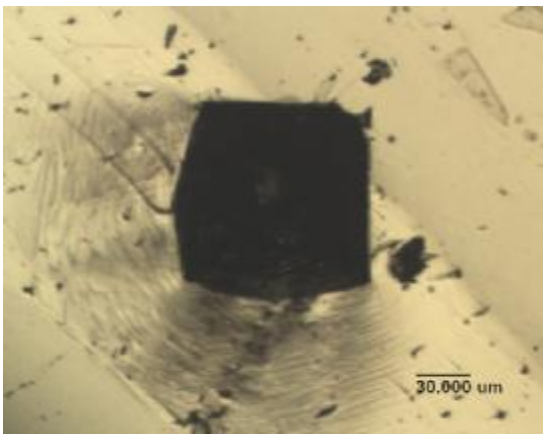

Nominal $Nb_{50}:Cr_{30}:Pt_{20}$ (Alloy 10(a))
Major wavy slip

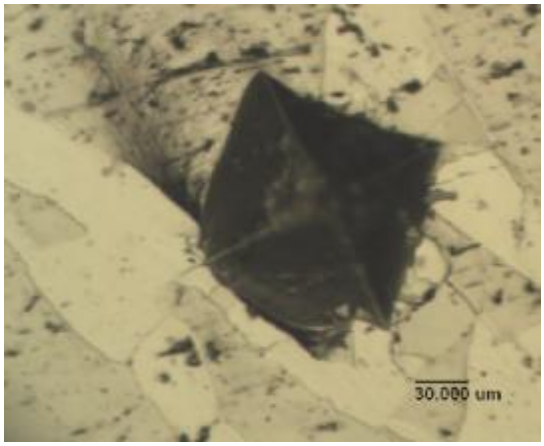

Nominal $Nb_{50}:Cr_{30}:Pt_{20}$ (Alloy 10(b))
Cracking

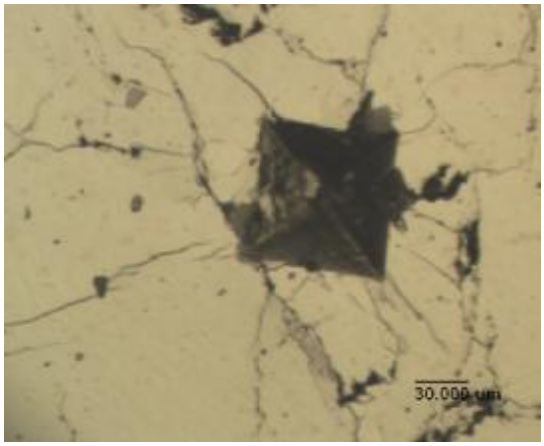

Nominal $Nb_{50}:Cr_{30}:Pt_{20}$ (Alloy 10(c))
Major cracking

Figure 4.112. Optical micrographs for comparison of the macrohardness indentations in the as-cast Nb-Cr-Pt alloys (continued).

Nominal ~Nb_{15}:Cr_{40}:Pt_{45}, ~Nb_{30}:Cr_{10}:Pt_{60}, ~Nb_{35}:Cr_{30}:Pt_{35}, Nb_{30}:Cr_{20}:Pt_{50}, and ~Nb_{24}:Cr_{23}:Pt_{53} showed wavy slip, and ~Nb_{50}:Cr_{30}:Pt_{20} (a) which is from pure Pt showing major wavy slip, indicating plastic deformation. Planar slip was observed in nominal ~Nb_{15}:Cr_{15}:Pt_{70}, ~Nb_{20}:Cr_{50}:Pt_{30} and ~Nb_{40}:Cr_{15}:Pt_{45}, indicating reasonable toughness. Brittleness was observed in nominal ~Nb_{15}:Cr_{70}:Pt_{15}, ~Nb_{35}:Cr_{40}:Pt_{25} and a local region in nominal ~Nb_{40}:Cr_{25}:Pt_{35} (b) by cracks. Nominal ~Nb_{40}:Cr_{45}:Pt_{15}, ~Nb_{40}:Cr_{45}:Pt_{15}, ~Nb_{70}:Cr_{15}:Pt_{15}, ~Nb_{60}:Cr_{10}:Pt_{30}, ~Nb_{25}:Cr_{45}:Pt_{30}, ~Nb_{57}:Cr_{18}:Pt_{25}, and local regions of nominal ~Nb_{50}:Cr_{30}:Pt_{20} (b)-(c) and ~Nb_{40}:Cr_{60}:Pt_{20} showed major cracking. Nominal and local regions in nominal ~Nb_{20}:Cr_{60}:Pt_{20} and ~Nb_{40}:Cr_{25}:Pt_{35} showed wavy slip behaviour with minor cracks.

4.2.3 Fracture Toughness (K_{IC})

The results of the Palmqvist fracture toughness (K_{IC}) measurements that were carried out on some of the brittle as-cast Nb-Cr-Pt samples are presented in Table 4.33. In some alloys, the cracks were all around the indentations and they were unmeasurable.

Table 4.33. The Palmqvist fracture toughness (MPa√m) values measured from the as-cast Nb-Cr-Pt alloys.

Sample Name	**Alloy composition (at.%)**	**Fracture toughness (MPa√m)**	**Phases**
4	Nb_{15}:Cr_{70}:Pt_{15}	1.6±0.2 (±0.24 to 2 sig. Fig.)	Cr, ~$NbCr_2$, ~Nb_3Pt, τ1 and (Nb)
6	Nb_{70}:Cr_{15}:Pt_{15}	1.3±0.1 (±0.05 to 2 sig. Fig.)	(Nb), ~Nb_3Pt and ~$NbCr_2$
8	Nb_{60}:Cr_{10}:Pt_{30}	1.1±0.0 (±0.04 to 2 sig. Fig.)	~Nb_3Pt, ~Nb_2Pt and τ5
14	Nb_{25}:Cr_{45}:Pt_{30}	1.7±0.1 (±0.07 to 2 sig. Fig)	(Pt) and τ2
15 Local region	$Nb_{13.1}$:$Cr_{70.1}$:$Pt_{16.8}$	1.6±0.0 (±0.03 to 2 sig. Fig.)	(Cr), ~Cr_3Pt and τ1
17	Nb_{40}:Cr_{25}:Pt_{35}	1.8±0.1 (±0.06 to 2 sig. Fig.)	T3 and τ4 or τ2??
18	Nb_{57}:Cr_{18}:Pt_{25}	1.4±0.1 (±0.06 to 2 sig. fig.)	~Nb_2Pt, ~$NbCr_2$ and τ4

The following explanations were made on the alloys:

- The nominal ~Nb_{60}:Cr_{10}:Pt_{30} had a comparatively low fracture toughness of 1.1±0.0 MPa√m. The phases present in the alloy were ~Nb_3Pt, ~Nb_2Pt and ternary phase 5 (τ5).
- The highest fracture toughness value was found in a nominal ~Nb_{40}:Cr_{25}:Pt_{35} alloy and the value was 1.8±0.1 MPa√m. This alloy had two ternary phases, namely τ3 and τ4.
- The nominal ~Nb_{15}:Cr_{70}:Pt_{15} and ~$Nb_{13.1}$:$Cr_{70.1}$:$Pt_{16.8}$ alloys had a fracture toughness value of 1.6 MPa√m. These alloys had a three-phase regions of (Cr), ~$NbCr_2$ and τ1 for nominal ~Nb_{15}:Cr_{70}:Pt_{15}, and (Cr), ~Cr_3Pt and τ1 for nominal ~$Nb_{13.1}$:$Cr_{70.1}$:$Pt_{16.8}$. They had (Cr) and τ1 as common phases.
- The alloy with the second highest fracture toughness was the nominal ~Nb_{25}:Cr_{45}:Pt_{30} and it had a value of 1.7±0.1 MPa√m fracture toughness. The phases in this alloy were (Pt) solid solution and τ2.
- The alloy containing ~Nb_2Pt, ~$NbCr_2$ and τ4 phases had a fracture toughness of 1.4±0.1 MPa√m. This alloy is the nominal ~Nb_{57}:Cr_{18}:Pt_{25}.
- The nominal ~Nb_{70}:Cr_{15}:Pt_{15} alloy had a fracture toughness of 1.3±0.1 MPa√m, and the phases present were (Nb), ~Nb_3Pt and ~$NbCr_2$.

CHAPTER 5:

DISCUSSION

5.1 Phase investigations of the Nb-Cr-Pt alloys

The nominal ~Nb_{15}:Cr_{15}:Pt_{70} (Alloy 1) and ~Nb_{15}:Cr_{40}:Pt_{45} (Alloy 2) alloys were the two alloys which were found to be completely in the (Pt) phase field. There was coring in the nominal ~Nb_{15}:Cr_{40}:Pt_{45}, whereas nominal ~Nb_{15}:Cr_{15}:Pt_{70} only formed a single phase microstructure of (Pt) grains of different orientations. The XRD spectra were found to be almost the same as Pt.

Ternary phase τ1 was identified in nominal ~Nb_{15}:Cr_{70}:Pt_{15} (Alloy 4) and nominal ~Nb_{20}:Cr_{60}:Pt_{20} (Alloy 15), and was between the ~$NbCr_2$, ~Cr_3Pt and (Pt) phases, and found with them.

Nominal ~Nb_{20}:Cr_{50}:Pt_{30} (Alloy 12) was found to have two phases: τ1 and (Pt), and had a simpler XRD spectrum than ~Nb_{15}:Cr_{70}:Pt_{15} (Alloy 4), which had three phases: (Cr), ~$NbCr_2$ and τ1; and ~Nb_{20}:Cr_{60}:Pt_{20} (Alloy 15) with four phases: (Cr), ~Cr_3Pt, τ1 and (Pt). Nominal ~Nb_{20}:Cr_{60}:Pt_{20} (Alloy 15) was more complex, being more inhomogeneous and with more phases, than nominal ~Nb_{15}:Cr_{70}:Pt_{15} (Alloy 4), and this is evident from their XRD spectra.

The τ1 composition of nominal ~Nb_{20}:Cr_{50}:Pt_{30} (Alloy 12) was obtained by extrapolation through the eutectic overall from (Pt), assuming a 50/50 proportion of the (Pt) + τ1 eutectic. The τ2 phase was found in nominal ~Nb_{25}:Cr_{45}:Pt_{30} (Alloy 14) and ~Nb_{35}:Cr_{40}:Pt_{25} (Alloy 16). The τ5 phase was identified in nominal ~Nb_{40}:Cr_{15}:Pt_{45} (Alloy 3), ~Nb_{60}:Cr_{10}:Pt_{30} and locally in Alloy 10 at regions of overall compositions ~$Nb_{40.3}$:$Cr_{20.1}$:$Pt_{39.6}$ and ~$Nb_{44.1}$:$Cr_{34.1}$:$Pt_{21.9}$.

In a local area of nominal ~Nb_{15}:Cr_{70}:Pt_{15} (Alloy 4), the outer light ~Nb_3Pt and inner medium-grey ~$NbCr_2$ formed an apparent eutectic, and the outer light phase was inaccurate because of its small area size.

The reason why the (Pt) analyses in (Alloy 15) agreed with each other is because they were picking up the same proportions of τ1, and should have been slightly further in the (Pt) phase field, as can be seen in the solidification projection. In nominal ~Nb_{20}:Cr_{50}:Pt_{30} (Alloy 12),

there are lighter regions within the dark phase, assumed to be different compositions of the same phase, because the overall composition falls between the light (Pt) phase and eutectic (Pt) + τ1.

The nominal ~Nb_{50}:Cr_{30}:Pt_{20} (Alloy 10) had two different eutectics in a small area, which were binary eutectic colonies, L → ~$NbCr_2$ + ~Nb_2Pt and then a ternary eutectic L → ~$NbCr_2$ + ~Nb_2Pt + τ4.

Another ternary phase was identified near to nominal ~Nb_{25}:Cr_{45}:Pt_{30} (Alloy 14) and ~Nb_{35}:Cr_{40}:Pt_{25} (Alloy 16). This ternary phase was formed in local regions of these alloys, and it was named τ2.

Only the nominal ~Nb_{30}:Cr_{10}:Pt_{60} sample (Alloy 7) had the ~β$NbPt_3$ phase. This alloy was two-phase, having ~β$NbPt_3$ and (Pt), with coring in the latter. The ~$NbPt_2$ phase was found in nominal ~Nb_{24}:Cr_{23}:Pt_{53} (Alloy 9) and ~Nb_{30}:Cr_{20}:Pt_{50} (Alloy 13), and this phase had a good XRD signal. (Pt) also had good matches in nominal ~Nb_{24}:Cr_{23}:Pt_{53} (Alloy 9). Alloy 13 formed a two-phase microstructure of ~$NbPt_2$ and a new ternary phase, τ3.

The ternary τ5 was identified in nominal ~Nb_{40}:Cr_{15}:Pt_{45} (Alloy 3), ~Nb_{60}:Cr_{10}:Pt_{30} (Alloy 8) and in (Alloy 10) at local regions of overall compositions ~$Nb_{40.3}$:$Cr_{20.1}$:$Pt_{39.6}$ and ~$Nb_{44.1}$:$Cr_{34.1}$:$Pt_{21.9}$.

The ~Nb_3Pt phase was in a higher proportion than (Nb) in the nominal ~Nb_{70}:Cr_{15}:Pt_{15} (Alloy 6), and through extrapolation and comparison of the phase contrasts, the eutectic was identified to be between ~Nb_3Pt and ~$NbCr_2$. The ~Nb_2Pt and ~$NbCr_2$ phases were found to be common phases in the nominal ~Nb_{40}:Cr_{45}:Pt_{15} (Alloy 5), ~Nb_{57}:Cr_{18}:Pt_{25} (Alloy 18) and some of the nominal ~Nb_{50}:Cr_{30}:Pt_{20} (Alloy 10) local regions. The ~$NbCr_2$ + ~Nb_2Pt binary eutectic was formed in Alloy 5 and 10, and ~$NbCr_2$ + ~Nb_2Pt + τ4 ternary eutectic been formed only in Alloy 10 local regions.

The ternary phase τ4 was identified locally in nominal ~Nb_{40}:Cr_{15}:Pt_{45} (Alloy 3), ~Nb_{50}:Cr_{30}:Pt_{20} (Alloy 10), ~Nb_{35}:Cr_{40}:Pt_{25} (Alloy 16) and ~Nb_{57}:Cr_{18}:Pt_{25} (Alloy 18).

As nominal Nb_{50}:Cr_{30}:Pt_{20} was arc-melted and then cooled fast, τ4 is always on the edges and appears to be peritectic rather than eutectic. This is the 'halo' formation described by Chadwick [1972Cha]. In halo formation, the liquid becomes too rich in one phase to form the

eutectic normally. Thus, that phase must precipitate out first, usually as a 'halo' surrounding the primary grains. Halo formation is caused by the solute 'pile-up' of the second component at the solid-liquid interface due to the inability of the primary phase to nucleate the second phase, possibly due to an asymmetric coupled zone. The pile-up of the second component can shift the composition of the liquid beyond the composition range in which co-operative (coupled) growth is possible. Once the halo has formed, the composition is returned to the 'coupled zone' [1972Cha] and normal eutectic growth can occur. This explains the usual microstructure seen.

The XRD peaks that were not identified by comparison to the ICDD were tabulated and are assumed to be, due to the other phases identified by EDX. All the phases which were not found or there were no data for them in the database (ICDD) will need to be modelled and compared with the tabulated data. These phases are: ~$Nb_{1-X}Pt_{1+X}$, ~Nb_2Pt, τ1, τ2, τ3, τ4 and τ5.

Since the τ1 phase is a major phase in ~Nb_{15}:Cr_{70}:Pt_{15} (Alloy 4), it can be assumed that the unidentified peaks in the alloy's spectrum belong to this phase. The peaks are given in Table 5.1.

Table 5.1. XRD peaks assumed to be from τ1 phase in nominal Nb_{15}:Cr_{70}:Pt_{15} (Alloy 4).

Peak No	2θ (degree)	d-spacing (Å)	Relative intensity (%)
1	36.29	2.48	9.22
2	40.48	2.21	100
3	45.78	1.98	18.01
4	47.86	1.90	10.18
5	66.82	1.40	4.23
6	71.62	1.32	4.28
7	74.58	1.27	14.56

The unidentified XRD peaks from nominal Nb_{40}:Cr_{45}:Pt_{15} (Alloy 5) spectrum were compared with those from plasticine, and it was found that not all unidentified peaks were from the plasticine, so it was assumed that the other peaks come from ~Nb_2Pt. The peak lists are presented in Tables 5.2 to 5.3.

Table 5.2. XRD plasticine peaks found to match with nominal $Nb_{40}:Cr_{45}:Pt_{15}$ (Alloy 5).

Peak No	Plasticine			Alloy 5		
	2θ (degree)	**d-spacing (Å)**	**Relative intensity (%)**	**2θ (degree)**	**d-spacing (Å)**	**Relative intensity (%)**
1	26.65	3.35	2.68	26.80	3.33	8.05
2	27.39	3.26	4.53	28.18	3.16	7.0
3	47.47	1.92	13.19	47.48	1.91	21.14
4	58.12	1.59	0.71	58.70	1.56	7.14
5	70.23	1.34	1.52	70.5	1.35	14.69
6	83.66	1.16	1.12	83.83	1.15	6.62

Table 5.3. XRD peaks assumed to be from ~Nb_2Pt in nominal $Nb_{40}:Cr_{45}:Pt_{15}$ (Alloy 5).

Peak No	2θ (degree)	d-spacing (Å)	Relative intensity (%)
1	36.04	2.49	69.71
2	37.75	2.38	80.88
3	40.0	2.25	21.52
4	46.08	1.97	15.25
5	72.81	1.30	14.69

Since nominal $Nb_{35}:Cr_{30}:Pt_{35}$ (Alloy 11) had a two-phase microstructure, the identified peaks from the XRD spectrum were of (Pt), with the unidentified peaks to be assumed to be from ternary phase τ2. Table 5.4 shows the peaks assumed to be from τ2.

Table 5.4. XRD peaks assumed to be from τ2 in nominal $Nb_{35}:Cr_{30}:Pt_{35}$ (Alloy 11).

Peak No	2θ (degree)	d-spacing (Å)	Relative intensity (%)
1	26.29	3.39	2.10
2	29.87	2.99	1.19
3	34.84	2.57	4.69
4	38.26	2.35	7.42
5	42.21	2.14	4.82
6	53.36	1.72	1.67
7	56.46	1.63	2.69
8	60.13	1.54	2.24
9	64.83	1.44	1.17
10	71.97	1.31	1.70
11	76.41	1.27	1.10

The minor unidentified XRD peaks of nominal Nb_{15}:Cr_{40}:Pt_{45} (Alloy 2) show reasonable matches to τ2, and peak list is given in Table 5.5.

Table 5.5. XRD peaks assumed to be from τ2 in nominal Nb_{15}:Cr_{40}:Pt_{45} (Alloy 2).

Peak No	2θ (degree)	d-spacing (Å)	Relative intensity (%)
1	28.04	3.18	2.98
2	37.78	2.38	2.36
3	52.77	1.73	2.59
4	59.47	1.55	1.86

The unidentified peaks in nominal Nb_{20}:Cr_{50}:Pt_{30} (Alloy 12) XRD spectrum are assumed to be from the τ1 phase, and are given in Table 5.6.

Table 5.6. XRD peaks assumed to be from τ1 in nominal Nb_{20}:Cr_{50}:Pt_{30} (Alloy 12).

Peak No	2θ (degree)	d-spacing (Å)	Relative intensity (%)
1	29.45	3.03	7.32
2	34.19	2.62	2.24
3	35.92	2.50	2.48
4	37.70	2.39	8.14
5	45.28	2.00	14.10
6	45.67	1.98	15.49
7	49.35	1.85	7.41
8	52.67	1.74	2.30
9	55.62	1.65	14.46
10	64.17	1.45	3.43
11	70.71	1.33	3.35
12	74.04	1.28	12.27
13	80.31	1.20	2.74

In nominal Nb_{30}:Cr_{20}:Pt_{50} (Alloy 13) spectrum, the unidentified XRD peaks were assumed to be from τ3 phase, and the peaks are presented in Table 5.7.

Table 5.7. XRD peaks assumed to be from τ3 in nominal Nb_{30}:Cr_{20}:Pt_{50} (Alloy 13).

Peak No	2θ (degree)	d-spacing (Å)	Relative intensity (%)
1	38.34	2.35	16.57
2	47.51	1.91	20.20
3	53.21	1.72	2.63
4	55.58	1.65	4.84
5	56.35	1.63	6.02
6	63.70	1.46	3.41

Nominal Nb_{25}:Cr_{45}:Pt_{30} (Alloy 14), had only two phases: (Pt) and τ2. The (Pt) peaks was identified using ICDD, whereas the unidentified peaks were assumed to be τ2, and are given in Table 5.8.

Table 5.8. XRD peaks assumed to be from τ2 in nominal Nb_{25}:Cr_{45}:Pt_{30} (Alloy 14).

Peak No	2θ (degree)	d-spacing (Å)	Relative intensity (%)
1	23.95	3.72	1.63
2	26.34	3.38	3.15
3	34.96	2.57	8.66
4	38.39	2.34	12.40
5	42.19	2.14	12.32
6	44.74	2.03	10.15
7	46.61	1.95	22.62
8	47.57	1.91	16.22
9	49.00	1.86	5.06
10	53.39	1.72	1.92
11	56.52	1.63	5.09
12	58.27	1.58	18.35
13	59.83	1.55	5.17
14	63.72	1.46	2.43
15	64.76	1.44	2.10
16	73.43	1.29	13.86
17	81.66	1.18	6.47

The unidentified peaks in nominal Nb_{20}:Cr_{60}:Pt_{20} (Alloy 15) XRD spectrum are assumed to be from the τ1 phase, and are given in Table 5.9.

Table 5.9. XRD peaks assumed to be from τ1 in Nb_{20}:Cr_{60}:Pt_{20} nominal (Alloy 15).

Peak No	2θ (degree)	d-spacing (Å)	Relative intensity (%)
1	35.05	2.56	7.52
2	36.33	2.47	3.99
3	40.99	2.20	100
4	42.18	2.14	22.26
5	45.63	1.99	54.82
6	47.64	1.91	32.95
7	53.24	1.72	3.23
8	56.41	1.63	9.62
9	59.76	1.55	8.10
10	63.85	1.46	6.73
11	69.86	1.35	6.44
12	76.41	1.25	4.62

In nominal Nb_{60}:Cr_{10}:Pt_{30} (Alloy 8), the unidentified XRD peaks were assumed to be from the ~Nb_2Pt and τ5 phases. Peaks at position 2θ = 35.51°, 37.90°, 45.94° and 72.09° were found to be from ~Nb_2Pt phase, as they were also found in nominal Nb_{40}:Cr_{15}:Pt_{15} (Alloy 5) for the same phase. The peak list is given in Table 5.10.

Table 5.10. XRD peaks assumed to be from ~Nb_2Pt and τ5 in nominal Nb_{60}:Cr_{10}:Pt_{30} (Alloy 8).

Peak No	2θ (degree)	d-spacing (Å)	Relative intensity (%)
1	20.00	4.44	2.15
2	27.02	3.30	6.28
3	27.77	3.21	5.75
4	32.87	2.73	1.35
5	35.51	2.53	2.96
6	37.90	2.37	100
7	41.98	2.15	41.42
8	45.94	1.98	5.61
9	46.94	1.94	5.96
10	55.84	1.65	6.50
11	59.29	1.56	2.51
12	69.96	1.34	15.11
13	72.09	1.31	2.57
14	76.00	1.25	1.58
15	80.30	1.19	18.30
16	95.21	1.04	2.65

In nominal Nb_{35}:Cr_{40}:Pt_{25} (Alloy 16) spectrum, the unidentified XRD peaks were assumed to be from τ2, τ3 and τ4 phases, and the peaks are presented in Table 5.11. Peaks at position 2θ = 26.23°, 34.82°, 38.00°, 60.01°, 63.65° and 71, 85° were from τ2 as they matched with those in Nb_{35}:Cr_{30}:Pt_{35} (Alloy 11), and peaks at 2θ = 38.00° and 46, 72° were from τ3 because they matched with those in nominal Nb_{30}:Cr_{20}:Pt_{50} (Alloy 13). The remaining peaks at position 2θ = 28.46°, 40.32°, 48.91°, 51.76°, 68.45°, 83.05° and 93.98° were assumed to be from τ4.

Table 5.11. XRD peaks assumed to be from τ2, τ3 and τ4 in nominal Nb_{35}:Cr_{40}:Pt_{25} (Alloy 16).

Peak No	2θ (degree)	d-spacing (Å)	Relative intensity (%)
1	26.23	3.40	19.03
2	28.46	3.14	93.80
3	34.82	2.58	9.32
4	38.00	2.37	25.07

Table 5.11. XRD peaks assumed to be from τ2, τ3 and τ4 in nominal Nb_{35}:Cr_{40}:Pt_{25} (Alloy 16) continued.

Peak No	2θ (degree)	d-spacing (Å)	Relative intensity (%)
5	40.32	2.24	100
6	46.72	1.94	31.49
7	48.91	1.86	10.89
8	51.76	1.77	5.50
9	60.01	1.54	12.47
10	63.65	1.46	8.01
11	68.45	1.37	22.89
12	71.85	1.31	12.43
13	83.05	1.16	8.40
14	93.98	1.05	18.71

Since none of the peaks in nominal Nb_{40}:Cr_{25}:Pt_{35} (Alloy 17) XRD spectrum were identified, the unidentified peaks were assumed to be from τ3 and τ4 phases, and Peaks are given in Table 5.12. Peaks at position 2θ = 38.22°, 46.65°, 47.39°, 53.29°, 55.58°, 56.45° and 63.67° were from τ3, as they matched with those in Alloy 13 and 16, whereas peaks at position 2θ = 28.33°, 39.68°, 49.87°, 69.43°, 83.08° and 94.33° were from τ4, as they matched with those in Alloy 16.

Table 5.12. XRD peaks assumed to be from τ3 and τ4 in nominal Nb_{40}:Cr_{25}:Pt_{35} (Alloy 17).

Peak No	2θ (degree)	d-spacing (Å)	Relative intensity (%)
1	22.11	4.02	3.30
2	27.05	3.30	6.61
3	28.33	3.15	100
4	29.78	3.00	7.75
5	32.53	2.75	3.35
6	34.89	2.57	14.94
7	35.88	2.50	19.55
8	38.22	2.35	60.90
9	39.68	2.27	54.95
10	42.03	2.15	34.81
11	46.65	1.95	30.59
12	47.39	1.92	28.22
13	49.87	1.83	2.87
14	53.29	1.72	7.10
15	55.58	1.65	11.44
16	56.45	1.63	11.01
17	59.65	1.55	9.42
18	63.67	1.46	9.56

Table 5.12. XRD peaks assumed to be from τ3 and τ4 in nominal $Nb_{40}:Cr_{25}:Pt_{35}$ (Alloy 17) continued.

Peak No	2θ (degree)	d-spacing (Å)	Relative intensity (%)
19	64.82	1.44	10.46
20	66.89	1.40	10.96
21	69.43	1.35	14.65
22	76.39	1.25	9.40
23	79.48	1.21	7.83
24	81.40	1.18	15.46
25	83.08	1.16	3.64
26	94.33	1.15	10.56

The unidentified peaks in nominal $Nb_{57}:Cr_{18}:Pt_{25}$ (Alloy 18) XRD spectrum are assumed to be from ~Nb_2Pt and τ4 phases, and are given in Table 5.13. Peaks at position 2θ = 37.74°, 46.45° and 72.15° matched ~Nb_2Pt, whereas 2θ = 94.39° matched τ4. It was interesting to find peaks at position 2θ = 46.45°, 53.32°, 55.69° and 63.90° to be matching with those of τ3 in Alloy 13, 16 and 17.

Table 5.13. XRD peaks assumed to be from ~Nb_2Pt and τ4 in nominal $Nb_{57}:Cr_{18}:Pt_{25}$ (Alloy 18).

Peak No	2θ (degree)	d-spacing (Å)	Relative intensity (%)
1	19.82	4.48	4.42
2	23.85	3.73	6.02
3	25.68	3.47	8.95
4	37.74	2.38	50.31
5	46.45	1.96	34.66
6	53.32	1.71	6.10
7	55.69	1.65	7.29
8	59.75	1.55	8.34
9	63.90	1.46	9.04
10	72.15	1.31	5.32
11	94.39	1.05	6.46

In the XRD spectrum of nominal $Nb_{24}:Cr_{23}:Cr_{53}$ (Alloy 9), there were some unidentified peaks at positions 2θ = 37.7°, 41.5°, 47°, 53°, 55°, 56.5° and 63°. Peaks at position 2θ = 37.7° and 56.5° matched with those in the plasticine spectrum, and the remaining peaks could be from an as-yet unidentified phase.

X-ray diffraction peaks at position 2θ = 38°, 45°, 49°, 56° and 74° from nominal ~Nb_{15}:Cr_{70}:Pt_{15} (Alloy 4), ~Nb_{20}:Cr_{50}:Pt_{30} (Alloy 12) and ~Nb_{20}:Cr_{60}:Pt_{20} (Alloy 15) were interpretted to be from τ1. XRD peaks at position 2θ = 38°, 48°, 55° and 56° from nominal ~Nb_{30}:Cr_{20}:Pt_{50} (Alloy 13), ~Nb_{35}:Cr_{40}:Pt_{25} (Alloy 16) and ~Nb_{40}:Cr_{25}:Pt_{35} (Alloy 17) were deduced to be from τ3.

Since none of the peaks in nominal Nb_{40}:Cr_{15}:Pt_{45} (Alloy 3) XRD spectrum were identified, the unidentified peaks were assumed to be from ~$Nb_{1-X}Pt_{1+X}$, τ4 and τ5 phases, and peaks are given in Table 5.14. Peaks at position 2θ = 83.76°, 93.99° and 94.00° were found to be from τ4, as they matched with some of those in Alloy 17 and 18.

Table 5.14. XRD peaks assumed to be from ~$Nb_{1-X}Pt_{1+X}$, τ4 and τ5 in nominal Nb_{40}:Cr_{15}:Pt_{45} (Alloy 3).

Peak No	2θ (degree)	d-spacing (Å)	Relative intensity (%)
1	27.81	3.21	2.39
2	32.08	2.79	3.88
3	34.32	2.61	2.70
4	39.16	2.30	100
5	42.08	2.15	16.29
6	43.09	2.10	12.03
7	44.65	2.03	21.08
8	45.92	1.98	30.20
9	47.01	1.93	9.87
10	51.56	1.77	3.13
11	56.00	1.64	4.67
12	59.32	1.56	2.83
13	65.96	1.42	19.85
14	80.59	1.19	6.37
15	83.76	1.15	4.02
16	93.99	1.05	2.75
17	94.00	1.05	3.50
18	95.39	1.04	1.99
19	98.22	1.02	2.28

5.2 Solidification reactions of the Nb-Cr-Pt system

Solidification sequences were determined for all the alloys from their microstructures. These solidification reaction sequences are presented in Table 5.15.

Table 5.15. Solidification reaction sequences for the Nb-Cr-Pt alloys.

Sample name	**Alloy composition (at.%)**	**Solidification reaction**
6	~$Nb_{69.9}$:$Cr_{16.1}$:$Pt_{14.0}$	L → (Nb) L + (Nb) → ~Nb_3Pt L → ~Nb_3Pt + ~$NbCr_2$
5	~$Nb_{42.4}$:$Cr_{42.6}$:$Pt_{15.0}$	L → ~$NbCr_2$ L → ~$NbCr_2$ + ~Nb_2Pt
10 Local regions	(a) ~Nb_{44}:Cr_{12}:Pt_{44}	L → ~$Nb_{1-X}Pt_{1+X}$ L + ~$Nb_{1-X}Pt_{1+X}$ → ~Nb_2Pt L + ~Nb_2Pt → τ4
	(b) ~$Nb_{40.3}$:$Cr_{20.1}$:$Pt_{39.6}$	L → ~$Nb_{1-X}Pt_{1+X}$ ~$Nb_{1-X}Pt_{1+X}$ → L + τ5 L + τ5 → τ4 Locally: L + ~$Nb_{1-X}Pt_{1+X}$ → τ5?? (Solid state precipitation in ~$Nb_{1-X}Pt_{1+X}$ of τ3.)
	(c) ~$Nb_{44.1}$:$Cr_{34.1}$:$Pt_{21.9}$	L → ~Nb_2Pt L + ~Nb_2Pt → τ4 L → ~Nb_2Pt + τ4 + ~$NbCr_2$
	(d) ~$Nb_{42.5}$:$Cr_{38.6}$:$Pt_{18.9}$	L → ~$NbCr_2$ + ~Nb_2Pt L → ~$NbCr_2$ + ~Nb_2Pt + τ4
	(e) ~$Nb_{41.5}$:$Cr_{39.8}$:$Pt_{18.8}$	L → ~Nb_2Pt L + ~Nb_2Pt → τ4 L → ~Nb_2Pt + τ4 + ~$NbCr_2$
	(f) ~$Nb_{39.3}$:$Cr_{42.4}$:$Pt_{18.3}$	L → ~$NbCr_2$ L → ~$NbCr_2$ + ~Nb_2Pt + τ4
18	~$Nb_{43.3}$:$Cr_{34.1}$:$Pt_{22.6}$	L → τ4 L + τ4 → ~Nb_2Pt L + ~Nb_2Pt → ~$NbCr_2$ (or sparse eutectic?)
4	(a) ~$Nb_{13.6}$:$Cr_{73.1}$:$Pt_{13.3}$	L → (Cr) L + (Cr) → ~$NbCr_2$ L + ~$NbCr_2$ → τ1

Table 5.15. Solidification reaction sequences for the Nb-Cr-Pt alloys (continued).

Sample name	**Alloy composition (at.%)**	**Solidification reaction**
4 continued.	(b) No overall	L → ~$NbCr_2$ + ~Nb_3Pt (Smaller region, locally. Unlikely to be in equilibrium)
15 Local regions	(a) ~$Nb_{13.1}$:$Cr_{70.1}$:$Pt_{16.8}$	L → (Cr) L + (Cr) → ~Cr_3Pt L + ~Cr_3Pt → τ1
	(b) ~$Nb_{17.6}$:$Cr_{60.5}$:$Pt_{21.9}$	L → τ1 L + τ1→ (Pt) (or sparse eutectic?)
	(c) ~$Nb_{16.6}$:$Cr_{63.0}$:$Pt_{20.4}$	L → τ1 L → τ1 + ~Cr_3Pt
12	~$Nb_{14.7}$:$Cr_{56.4}$:$Pt_{28.9}$	L → (Pt) L → (Pt) + τ1
14 Local regions	(a) ~$Nb_{23.3}$:$Cr_{48.0}$:$Pt_{28.7}$	L → τ2 L + τ2 → (Pt) (or sparse eutectic)
	(b) ~$Nb_{22.6}$:$Cr_{47.7}$:$Pt_{32.2}$	L → (Pt) L → (Pt) + τ2 (Non-equilibrium)
	(c) ~$Nb_{22.3}$:$Cr_{47.7}$:$Pt_{30.0}$	L → (Pt) L → (Pt) + τ2
11	~$Nb_{18.9}$:$Cr_{38.0}$:$Pt_{43.1}$	L → (Pt) L + (Pt) → τ2
2	~$Nb_{15.4}$:$Cr_{38.9}$:$Pt_{45.7}$	L → (Pt)
16 Local regions	(a) ~$Nb_{37.4}$:$Cr_{38.1}$:$Pt_{24.5}$	L → ~$NbCr_2$ L + ~$NbCr_2$ → τ4 L + τ4 → τ2? (Difficult to see τ2)
	(b) ~$Nb_{31.7}$:$Cr_{37.5}$:$Pt_{30.8}$	L → τ2 L + τ2 → τ3
17	~$Nb_{36.8}$:$Cr_{28.9}$:$Pt_{34.4}$	L → τ3 L + τ3 → τ4
8	~$Nb_{56.5}$:$Cr_{9.0}$:$Pt_{34.5}$	L → ~Nb_3Pt L + ~Nb_3Pt → ~Nb_2Pt L + ~Nb_2Pt → ~$Nb_{1-X}Pt_{1+X}$ Or L + ~Nb_2Pt → τ5
3 Local regions	(a) ~$Nb_{40.8}$:$Cr_{13.5}$:$Pt_{45.7}$	L → ~$Nb_{1-X}Pt_{1+X}$ L + ~$Nb_{1-X}Pt_{1+X}$ → τ5 L + τ5 → τ4
	(b) ~$Nb_{40.6}$:$Cr_{13.1}$:$Pt_{46.3}$	L → ~$Nb_{1-X}Pt_{1+X}$ L + ~$Nb_{1-X}Pt_{1+X}$ → τ5 L + τ5 → τ4

Table 5.15. Solidification reaction sequences for the Nb-Cr-Pt alloys (continued).

Sample name	Alloy composition (at.%)	Solidification reaction
9	~$Nb_{21.7}$:$Cr_{23.6}$:$Pt_{54.7}$	L → ~$NbPt_2$ L + ~$NbPt_2$ → (Pt)
7	~$Nb_{20.9}$:$Cr_{8.6}$:$Pt_{70.4}$	L → ~β$NbPt_3$ L + ~β$NbPt_3$ → (Pt)
1	~$Nb_{14.6}$:$Cr_{16.0}$:$Pt_{69.5}$	(Pt)

5.3 Solidification projection for the Nb-Cr-Pt system

Using analyses from reasonable phase sizes (where possible, greater than 3μm) and with good reproducibility, the best phase results were plotted. The solidification projection for the Nb-Cr-Pt system is shown in Figures 5.1 a and b, and is based on the results and data in Chapter 4. The phase boundary extents of the binary phases were drawn using the experimental measured compositions. All binary phases were found to extend into the ternary, except for α´Pt, which was not identified in this investigation. Five ternary phases were identified on the basis of the phase contrasts in the microstructures and the fact that the plotted compositions could not be an extension of a binary phase because that binary phase was already present in a sample.The phase boundaries of the ternary phases were also drawn using the experimental data. The (Pt) binary phase was found to have the largest extent.

The extensions of the binary phases were determined as:

- (Cr): having at least ~2 at.% Nb extension;
- (Pt): ~24 at.% Nb;
- (Nb): ~12 at.% Pt and ~17 at.% Cr;
- ~$NbPt_2$: ~20 at.% Cr;
- ~$NbCr_2$: ~18 at.% Pt;
- ~Cr_3Pt: ~10 at.% Nb;
- ~β$NbPt_3$: ~4 at.% Cr;
- ~$Nb_{1-X}Pt_{1+X}$: ~13 at.% Cr;
- ~Nb_3Pt: ~10 at.% Cr;
- ~Nb_2Pt: ~26 at.% Cr.

The ternary phases and their approximate compositions are:

- (τ1): ~Nb_{17}:Cr_{64}:Pt_{19};
- (τ2): ~Nb_{28}:Cr_{45}:Pt_{27};
- (τ3): ~Nb_{30}:Cr_{30}:Pt_{40};
- (τ4): ~Nb_{45}:Cr_{27}:Pt_{28};
- (τ5): ~Nb_{40}:Cr_{18}:Pt_{42}.

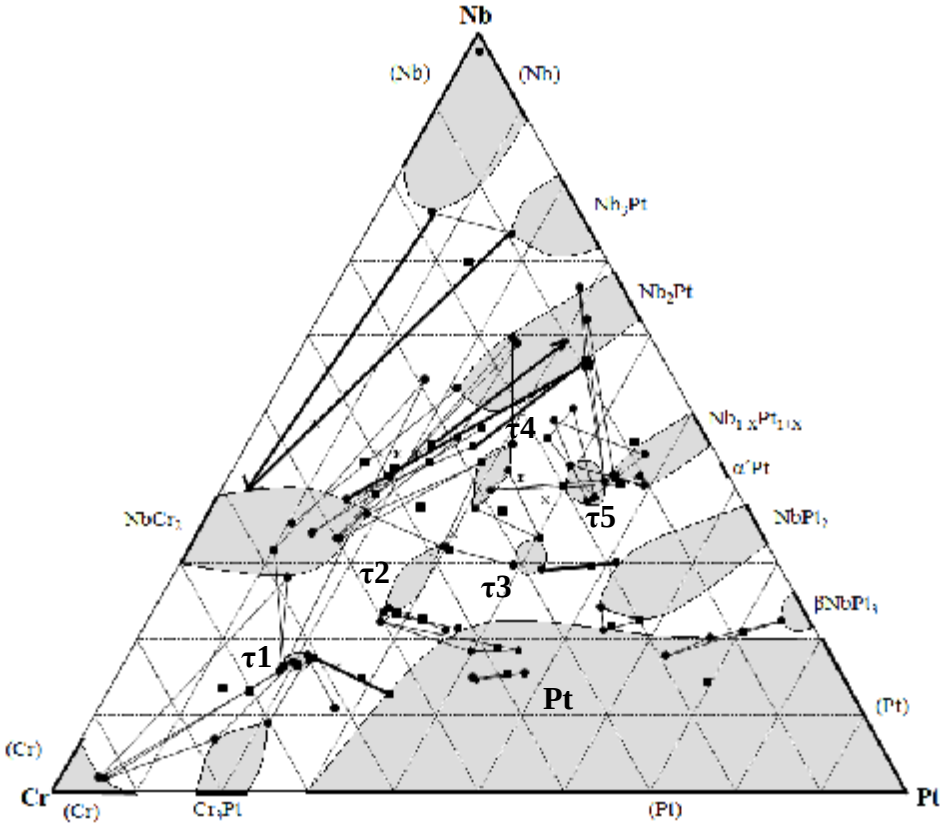

Figure 5.1 a. Solidification projection diagram of the Nb-Cr-Pt system. (Note that bold lines indicate extrapolation)

Using the tie-lines shown in Figure 5.1 a, the remaining two- and three-phase regions were deduced and are shown in Figure 5.1 b.

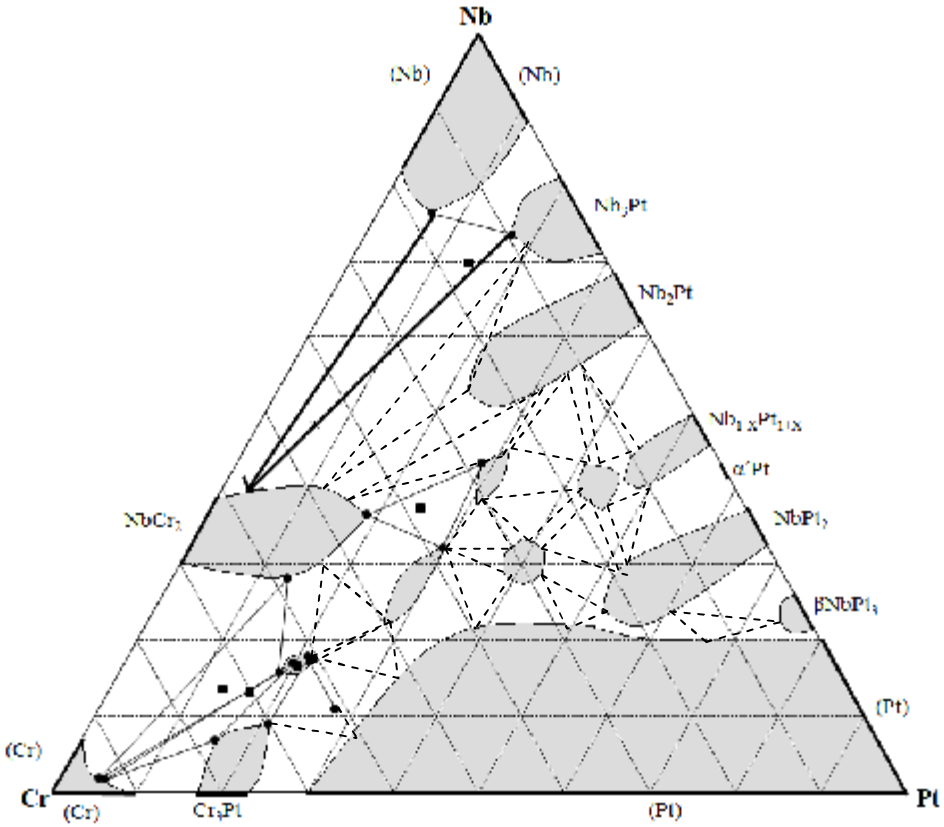

Figure 5.1 b. Solidification projection diagram of the Nb-Cr-Pt system, showing two- and three-phase regions (Note that bold lines indicate extrapolations and dashed lines were determined using the experimental tie-lines).

5.4 Liquidus surface of the Nb-Cr-Pt system

The experimental ternary liquidus surface projection was plotted using the binary phase diagrams, primary phases identified in the Nb-Cr-Pt alloys, following the solidification sequences, and the solidification projection. The eutectic compositions were also used as a guideline. The proposed experimental liquidus surface projection is presented in Figure 5.2, with the alloy's overall compositions and reactions from the binary phase diagrams. Table 5.16 shows the ternary invariant reactions deduced for the Nb-Cr-Pt system.

Table 5.16. Ternary invariant reactions of the Nb-Cr-Pt system.

Reaction Number	Reaction	Composition
A	$L + (Nb) \rightarrow {\sim}Nb_3Pt + {\sim}NbCr_2$	${\sim}Nb_{53}:Cr_{40}:Pt_7$
B	$L + {\sim}Nb_3Pt \rightarrow {\sim}NbCr_2 + {\sim}Nb_2Pt$	${\sim}Nb_{50}:Cr_{40}:Pt_{10}$
C	$L + {\sim}Nb_2Pt + {\sim}Nb_{1-X}Pt_{1+X} \rightarrow \tau5$	${\sim}Nb_{50}:Cr_{14}:Pt_{36}$
D	$L + \tau5 + {\sim}Nb_{1-X}Pt_{1+X} \rightarrow \tau4$	${\sim}Nb_{42}:Cr_{19}:Pt_{39}$
E	$L + \tau5 \rightarrow {\sim}Nb_2Pt + \tau4$	${\sim}Nb_{45}:Cr_{25}:Pt_{30}$
F	$L \rightarrow {\sim}NbCr_2 + {\sim}Nb_2Pt + \tau4$	${\sim}Nb_{43}:Cr_{38}:Pt_{19}$
G	$L + {\sim}Nb_{1-X}Pt_{1+X} + \tau4 \rightarrow \tau3$	${\sim}Nb_{40}:Cr_{20}:Pt_{40}$
H	$L + \alpha´Pt \rightarrow {\sim}Nb_{1-X}Pt_{1+X} + {\sim}NbPt_2$	${\sim}Nb_{50}:Cr_4:Pt_{46}$
I	$L + {\sim}Nb_{1-X}Pt_{1+X} \rightarrow {\sim}NbPt_2 + \tau3$	${\sim}Nb_{31}:Cr_{24}:Pt_{45}$
J	$L + (Pt) \rightarrow \tau1 + {\sim}Cr_3Pt$	${\sim}Nb_{12}:Cr_{63}:Pt_{25}$
K	$L + {\sim}Cr_3Pt \rightarrow (Cr) + \tau1$	${\sim}Nb_{15}:Cr_{65}:Pt_{20}$
L	$L + (Cr) \rightarrow {\sim}NbCr_2 + \tau1$	${\sim}Nb_{18}:Cr_{64}:Pt_{18}$
M	$L + \tau1 + {\sim}NbCr_2 \rightarrow \tau2$	${\sim}Nb_{27}:Cr_{53}:Pt_{20}$
N	$L + {\sim}NbCr_2 \rightarrow \tau2 + \tau4$	${\sim}Nb_{40}:Cr_{34}:Pt_{26}$
O	$L + \tau4 \rightarrow \tau2 + \tau3$	${\sim}Nb_{40}:Cr_{30}:Pt_{30}$
P	$L + {\sim}\beta NbPt_3 \rightarrow (Pt) + {\sim}NbPt_2$	${\sim}Nb_{20}:Cr_{22}:Pt_{58}$
Q	$L + {\sim}NbPt_2 \rightarrow (Pt) + \tau3$	${\sim}Nb_{20}:Cr_{29}:Pt_{51}$
R	$L + \tau3 \rightarrow (Pt) + \tau2$	${\sim}Nb_{22}:Cr_{36}:Pt_{42}$
S	$L + \tau2 \rightarrow (Pt) + \tau1$	${\sim}Nb_{21}:Cr_{52}:Pt_{27}$

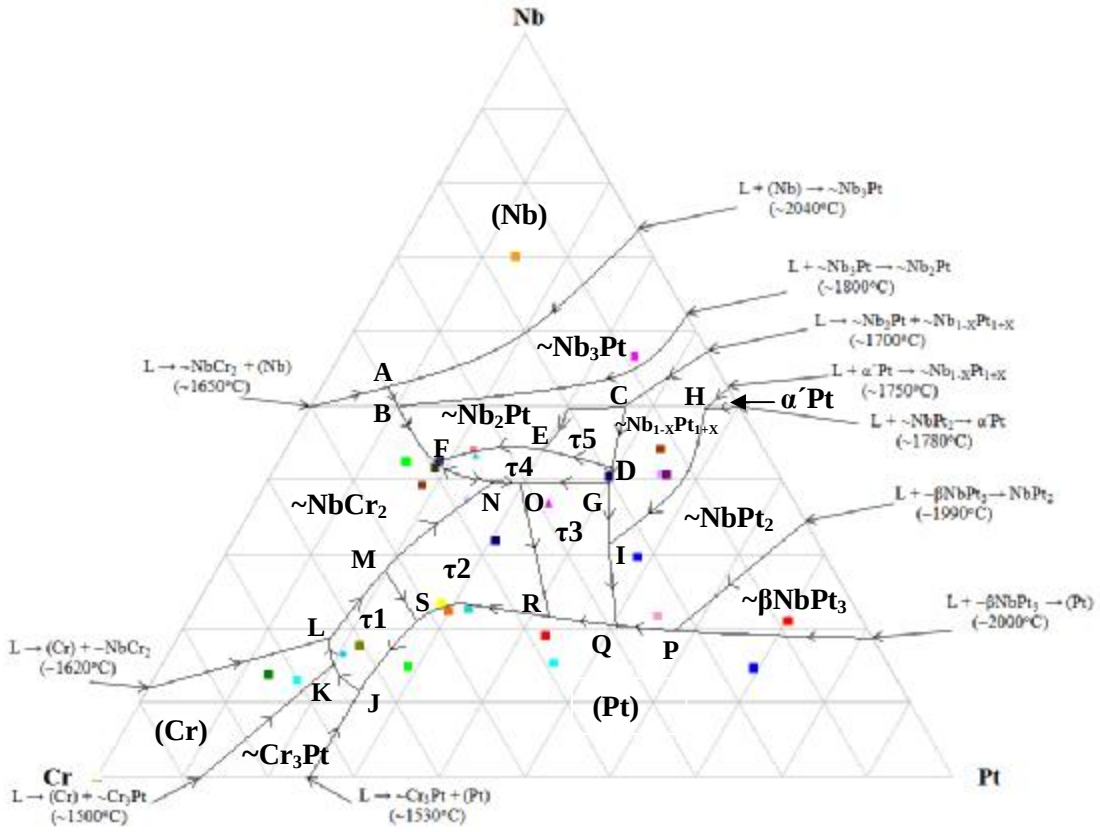

Figure 5.2. Experimental liquidus surface projection for the Nb-Cr-Pt alloys.

The (Pt) liquidus surface was found to be the largest. The ~βNbPt$_3$ liquidus surface extended to ~24 at.% Cr. The reaction separating (Pt), ~βNbPt$_3$ and ~NbPt$_2$ liquidus surfaces was a peritectic reaction, and was seen in nominal ~Nb$_{20.9}$:Cr$_{8.6}$:Pt$_{70.4}$ (Alloy 7) and ~Nb$_{21.7}$:Cr$_{23.6}$:Pt$_{54.7}$ (Alloy 9). In these alloys, (Pt) was a common phase in both alloys, and it formed after ~βNbPt$_3$ and ~NbPt$_2$ phases, therefore it could be assumed that the peritectic reaction proceeds in a direction away from the Nb-Pt binary.

The ~NbPt$_2$ liquidus surface extended to ~28 at.% Cr from the Nb-Pt binary. The reaction separating (Pt), ~NbPt$_2$ and τ3 surfaces was a peritectic reaction, and was seen in nominal ~Nb$_{29.7}$:Cr$_{21.9}$:Pt$_{48.4}$ (Alloy 13) and ~Nb$_{21.7}$:Cr$_{23.6}$:Pt$_{54.7}$ (Alloy 9). In these, alloys (Pt) and τ3 were formed after ~NbPt$_2$.

The weak ternary peritectic L + τ2 → (Pt) + τ1 (S) at ~Nb$_{21}$:Cr$_{52}$:Pt$_{27}$ was found in nominal ~Nb$_{14.7}$:Cr$_{56.4}$:Pt$_{28.9}$ (Alloy 12) and a region ~Nb$_{22.3}$:Cr$_{47.7}$:Pt$_{30.0}$ (Alloy 14(c)). The reaction separating the (Cr), ~Cr$_3$Pt and τ1 surfaces was peritectic and was seen in ~Nb$_{13.1}$:Cr$_{70.1}$:Pt$_{16.8}$, local region of Alloy 15(a).

The reaction separating (Cr), ~$NbCr_2$ and τ1 was a weak peritectic, and was found in nominal ~$Nb_{13.6}$:$Cr_{73.1}$:$Pt_{13.3}$ (Alloy 4), as L + (Cr) → ~$NbCr_2$ + τ1 (L) at ~Nb_{18}:Cr_{64}:Pt_{18}.

The ~$NbCr_2$ liquidus surface extended to ~26 at.% Pt from the Nb-Cr binary. A peritectic reaction was found to be separating τ1, τ2 and ~$NbCr_2$ surfaces at ~Nb_{27}:Cr_{53}:Pt_{20} as L + τ1 + ~$NbCr_2$ → τ2 (M). The reaction separating τ2, τ4 and ~$NbCr_2$ surfaces was also peritectic and was seen in ~$Nb_{37.4}$:$Cr_{38.1}$:$Pt_{24.5}$, local region of Alloy 16 (a). This reaction was at ~Nb_{40}:Cr_{34}:Pt_{26} (N).

The ternary eutectic L → ~$NbCr_2$ + ~Nb_2Pt + τ4 at ~Nb_{43}:Cr_{38}:Pt_{19} (F) was found locally in Alloy 10 and these local regions were ~$Nb_{42.5}$:$Cr_{38.6}$:$Pt_{18.9}$ and ~$Nb_{39.3}$:$Cr_{42.4}$:$Pt_{18.3}$.

Liquidus surfaces of τ2, τ3, and τ4 were separated by peritectic reaction at ~Nb_{40}:Cr_{30}:Pt_{30} (O). This reaction was seen in nominal ~$Nb_{36.8}$:$Cr_{28.9}$:$Pt_{34.4}$ (Alloy 17) and locally in ~$Nb_{31.7}$:$Cr_{37.5}$:$Pt_{30.8}$ (Alloy 16 (b)).

The ~Nb_3Pt liquidus surface extended to ~40 at.% Cr from the Nb-Pt binary. The reaction separating (Nb), ~$NbCr_2$ and ~Nb_3Pt surfaces was a peritectic, and it was found in nominal ~$Nb_{69.9}$:$Cr_{16.1}$:$Pt_{14.0}$ (Alloy 6). This reaction was found at ~Nb_{53}:Cr_{40}:Pt_7.

A peritectic L + ~Nb_3Pt → ~$NbCr_2$ + ~Nb_2Pt at ~Nb_{50}:Cr_{40}:Pt_{10} (B), is the reaction separating ~$NbCr_2$, ~Nb_3Pt and ~Nb_2Pt surfaces, and was seen in nominal ~$Nb_{42.4}$:$Cr_{42.6}$:$Pt_{15.0}$ (Alloy 5) and ~$Nb_{69.9}$:$Cr_{16.1}$:$Pt_{14.0}$ (Alloy 16).

The ~$Nb_{1-X}Pt_{1+X}$ liquidus surface extended to ~24 at.% Cr from the Nb-Pt binary. A weak peritectic reaction separating ~Nb_2Pt, τ4 and τ5 surfaces was determined at ~Nb_{45}:Cr_{25}:Pt_{30} (E), and another peritectic was derived at ~Nb_{50}:Cr_{14}:Pt_{36} (C), separating ~Nb_2Pt, ~$Nb_{1-X}Pt_{1+X}$ and τ5 surfaces.

The reaction separating the ~$Nb_{1-X}Pt_{1+X}$, τ4 and τ5 surfaces was peritectic, and occurred at ~Nb_{42}:Cr_{19}:Pt_{39} (D). This reaction was seen in nominal ~Nb_{40}:Cr_{15}:Pt_{45} (Alloy 3) and in local region (b) of ~$Nb_{40.3}$:$Cr_{20.1}$:$Pt_{39.6}$ (Alloy 10).

The α´Pt liquidus surface was drawn to extend to ~5 at.% Cr from the Nb-Pt binary. A peritectic reaction separating ~$Nb_{1-X}Pt_{1+X}$, τ3 and τ4 surfaces was derived at ~Nb_{40}:Cr_{20}:Pt_{40} (G), and another peritectic separates α´Pt, ~$Nb_{1-X}Pt_{1+X}$ and $NbPt_2$ surfaces at ~Nb_{50}:Cr_4:Pt_{46}

(H). The α´Pt phase was not found in the ternary. This was not surprising since the nearest alloy comprised at least 10% Cr, so would not be expected to follow the Nb-Pt binary. Additionally, the α´Pt phase only exists in a short temperature range in the Nb-Pt system, and would only form from the liquid in a very limited range: ~47-50 at.% Pt. Thus, this phase is unlikely to extend far into the ternary.

5.5 Mechanical properties of the ternary Nb-Cr-Pt alloys

5.5.1 Hardness

Table 5.17 shows the mechanical behaviour of individual phases in the as-cast Nb-Cr-Pt alloys. The average Vickers macrohardnesses of the ternary Nb-Cr-Pt alloys are superposed on the (simplified) solidification projection in Figure 5.3, and variations of the Vickers macrohardness measurements with platinum, chromium and niobium contents (at.%) are plotted in Figures 5.2 to 5.4.

The main findings of the investigation into the hardness of the Nb-Cr-Pt alloys were:

- The alloys in the (Pt)-rich region were ductile with no cracks on the indentations.
- All the Nb-Cr-Pt alloys containing >40 at.% Pt had low hardnesses, and were mostly ductile.
- The samples with high chromium and niobium contents were found to have high hardnesses, and they were extremely brittle.
- Three alloys had extremely high hardnesses, between 934 and 966 HV_5. One alloy had a three-phase region of (Cr) + ~Cr_3Pt + τ1, while the other two alloys had two-phase regions of (Pt) + τ2 and τ3 + τ4.
- Alloys which had eutectics were all found to be brittle, except for one alloy which had (Pt) solid solution (Alloy 12).

Table 5.17. Mechanical behaviour of individual phases in the as-cast Nb-Cr-Pt system.

Very brittle	**Brittle**	**Slightly brittle**	**Ductile**
(Nb) ~Nb_2Pt ~Nb_3Pt $NbCr_2$ τ4	(Cr) ~Cr_3Pt τ1 τ2	~β$NbPt_3$ ~$Nb_{1-X}Pt_{1+X}$ τ3 τ5	(Pt) ~$NbPt_2$

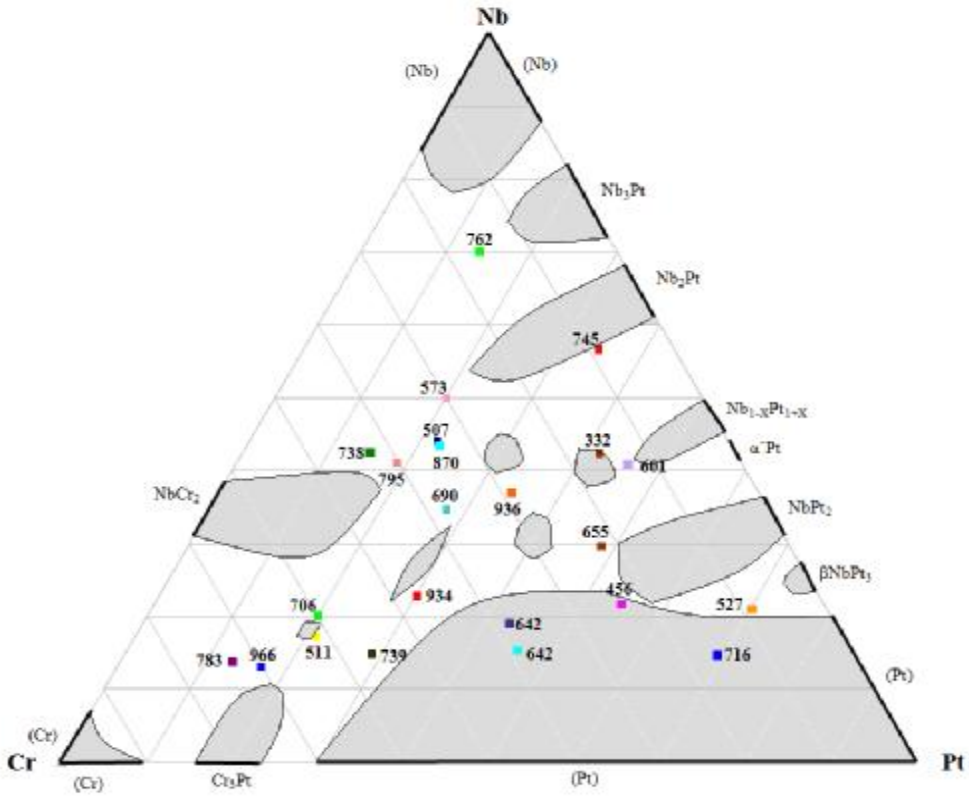

Figure 5.3 Vickers macrohardnesses of the ternary Nb-Cr-Pt alloys.

Figures 5.4–5.6 show the variations of the Vickers macrohardness measurements, with platinum, chromium and niobium contents in the Nb-Cr-Pt alloys. The hardnesses decreased

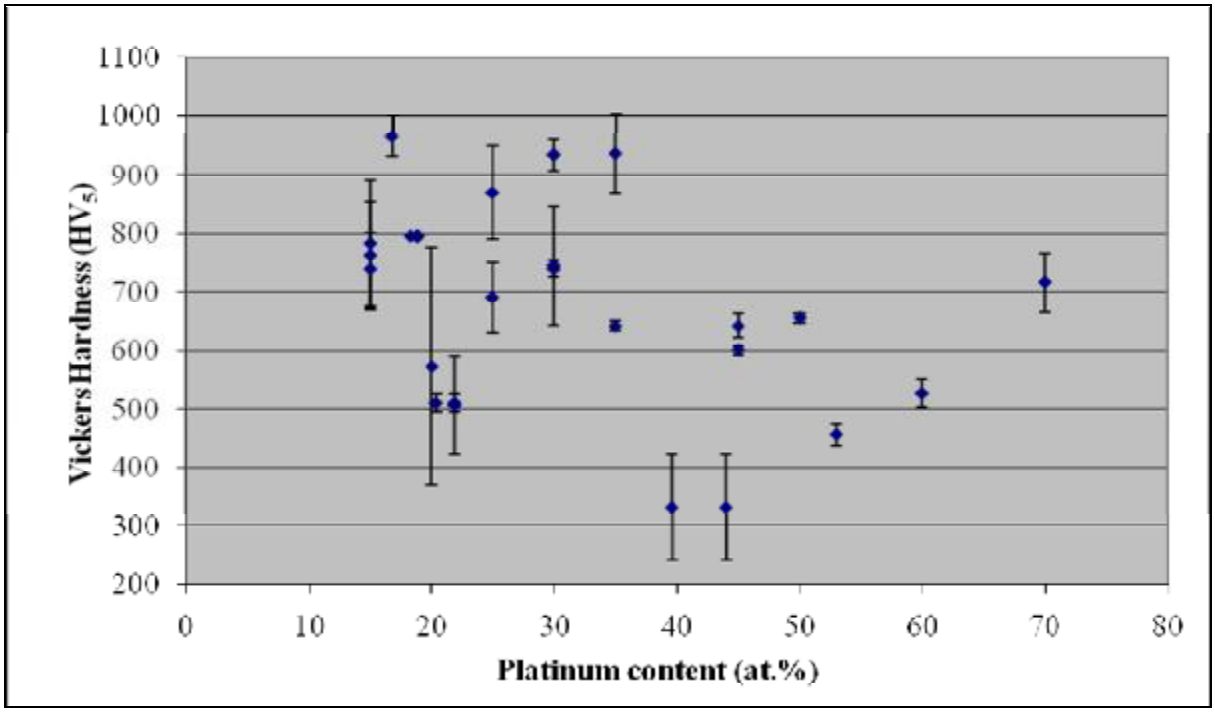

Figure 5.4. Variations of the Vickers macrohardness (HV_5) with platinum content (at.%).

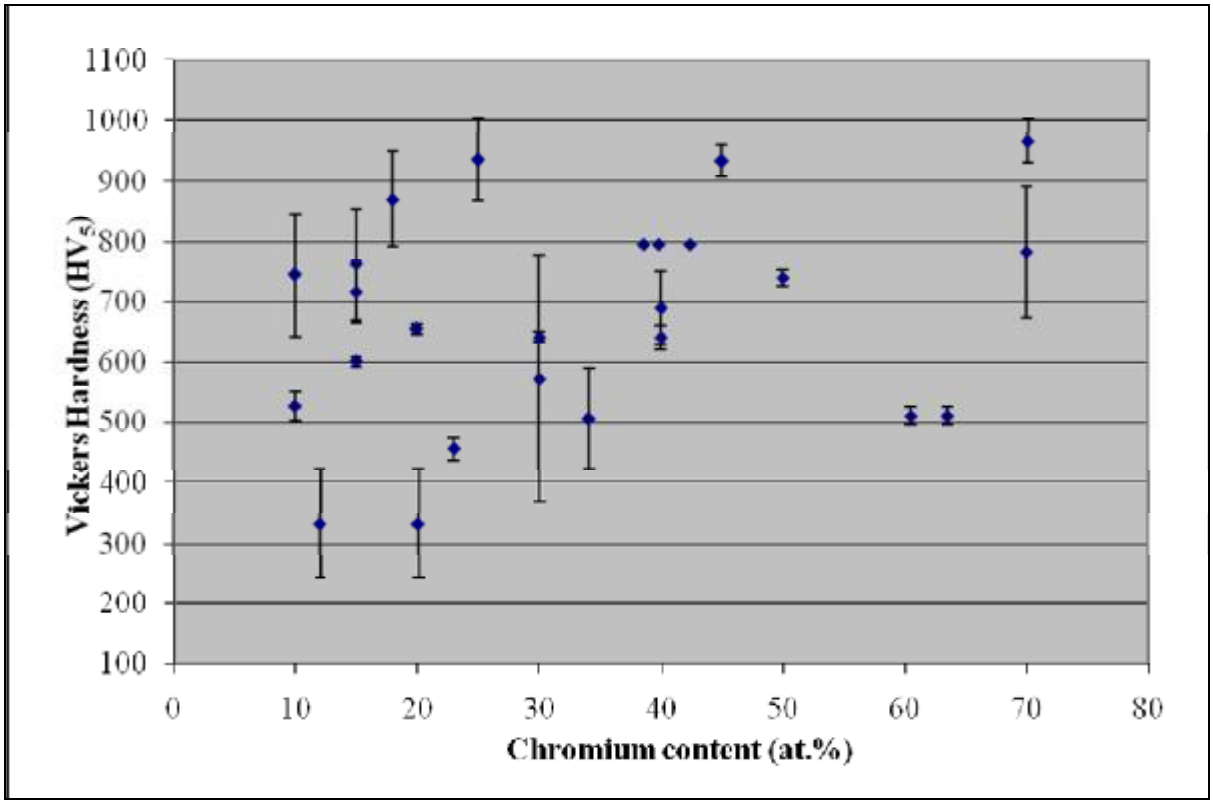

Figure 5.5. Variations of the Vickers macrohardness (HV_5) with chromium content (at.%).

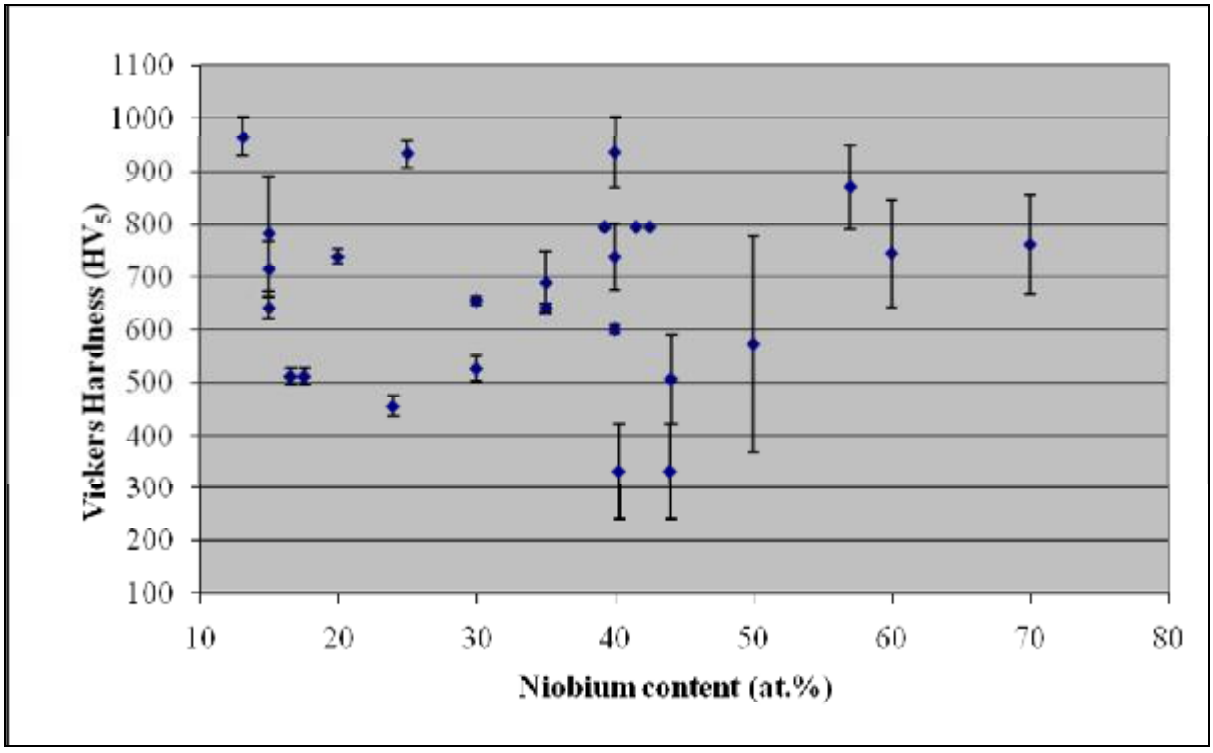

Figure 5.6. Variations of the Vickers macrohardness (HV_5) with niobium content (at.%).

with increased platinum content, and they increased with increased chromium content, although with much scatter. It was difficult to see a relationship of hardness with niobium contents because there was much scatter.

5.5.2 Toughness

The different slip modes of the as-cast Nb-Cr-Pt alloys are superposed on the solidification projection in Figure 5.7 and the mechanical behaviours are shown in Figure 5.8.

Alloys with a single phase (Pt) showed planar or wavy slip. The alloys with about ≥45 at.% Pt exhibited planar slip, wavy slip, or wavy slip with minor cracks, while those with ≤20 at.% Pt had cracks, showing their brittleness. Some alloys had major cracks showing their high brittleness. The newly-identified ternary phases showed planar and wavy slip, together with cracks. Alloys with (Pt) and ~$NbPt_2$ phases were found to have good toughness.

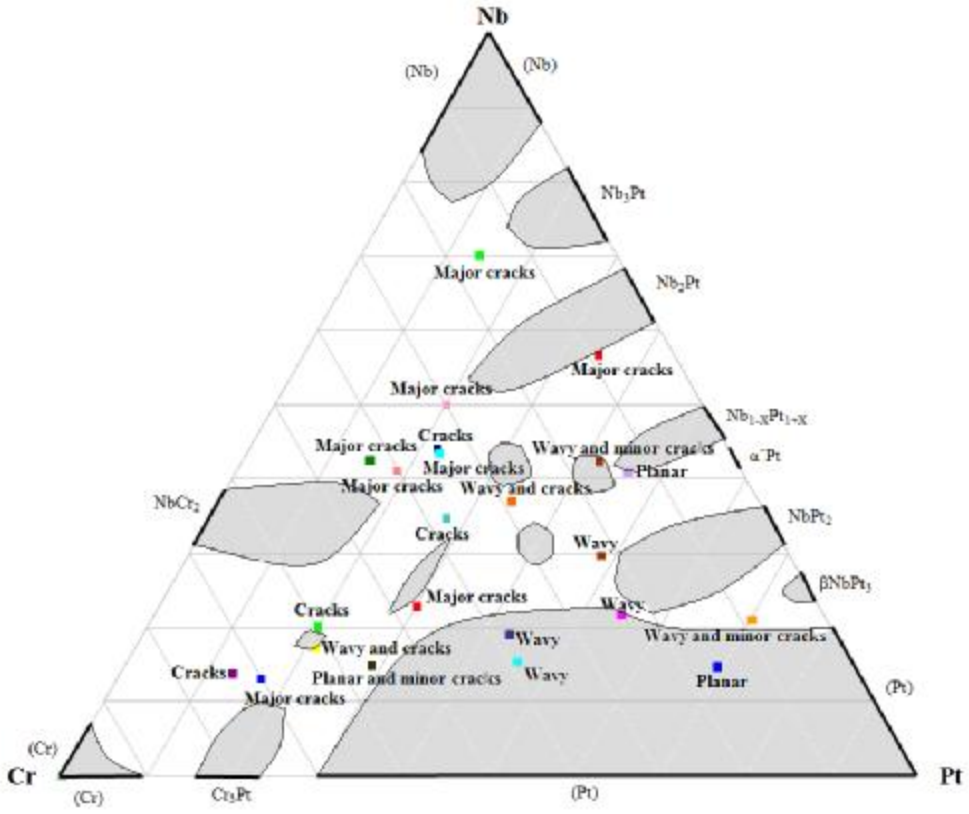

Figure 5.7. Summary of the slip modes of as-cast Nb-Cr-Pt alloys, superposed on the solidification projection.

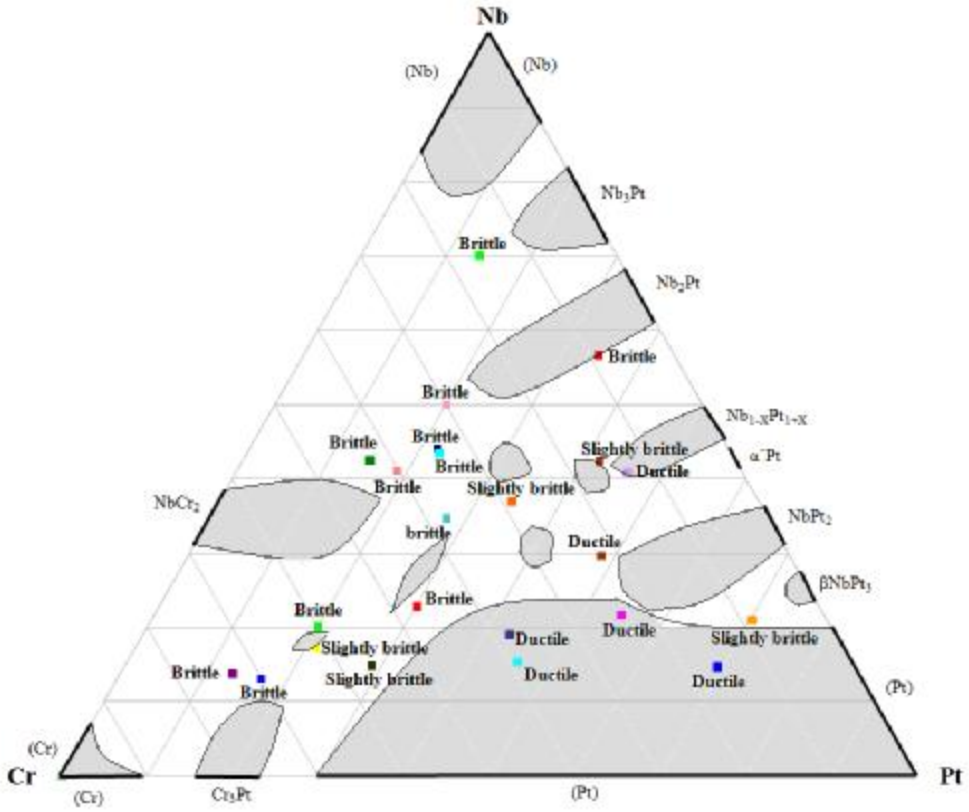

Figure 5.8. Summary of the mechanical behaviour of the as-cast Nb-Cr-Pt alloys, superposed on the solidification projection.

5.5.3 Fracture toughness (K_{IC})

In general, fracture toughness (K_{IC}) is low for brittle materials and high for ductile materials. This is supported by fracture toughness (K_{IC}) values given in Table 5.18 [1993Dow, 1994Cal].

***Table 5.18. Examples of room-temperature plane strain fracture toughness values* [1993Dow, 1994Cal].**

Materials	**Fracture toughness ($MPa.m^{-1/2}$)**
Metals	
2024-T351 Aluminum alloy	36
4340 Steel (tempered at 260°C)	50
Titanium alloy (Ti-6Al-4V)	44-66
Ceramics	
Aluminium oxide	3.0-5.3
Silicon carbide	3.0-5.0
Soda-lime glass	0.7-0.8
Concrete	0.2-1.4

Figure 5.9 shows the Palmqvist fracture toughness values of the as-cast Nb-Cr-Pt alloys superposed on the solidification projection. Fracture toughnesses of the Nb-Cr-Pt alloys were found to be very low when compared to other metal alloys, as can be seen in Table 5.18, and were only comparable to some of the ceramics.

The main findings of the fracture toughness in the Nb-Cr-Pt alloys were:

- The highest fracture toughness 1.8±0.1 MPa√m was found between three ternary phases (τ3, τ4 and τ5), but was much closer to τ4.
- The second highest fracture toughness was found near to τ2.
- The lowest fracture toughness was 1.1±0.0 (±0.04 rounded to 2 decimal places) MPa√m, and was at about 60 at.% Nb.
- High fracture toughnesses were also observed at high chromium content.
- All the alloys with which fracture toughness was undertaken had cracks and ternary phases, except for one alloy (Alloy 6), which did not have a ternary phase.

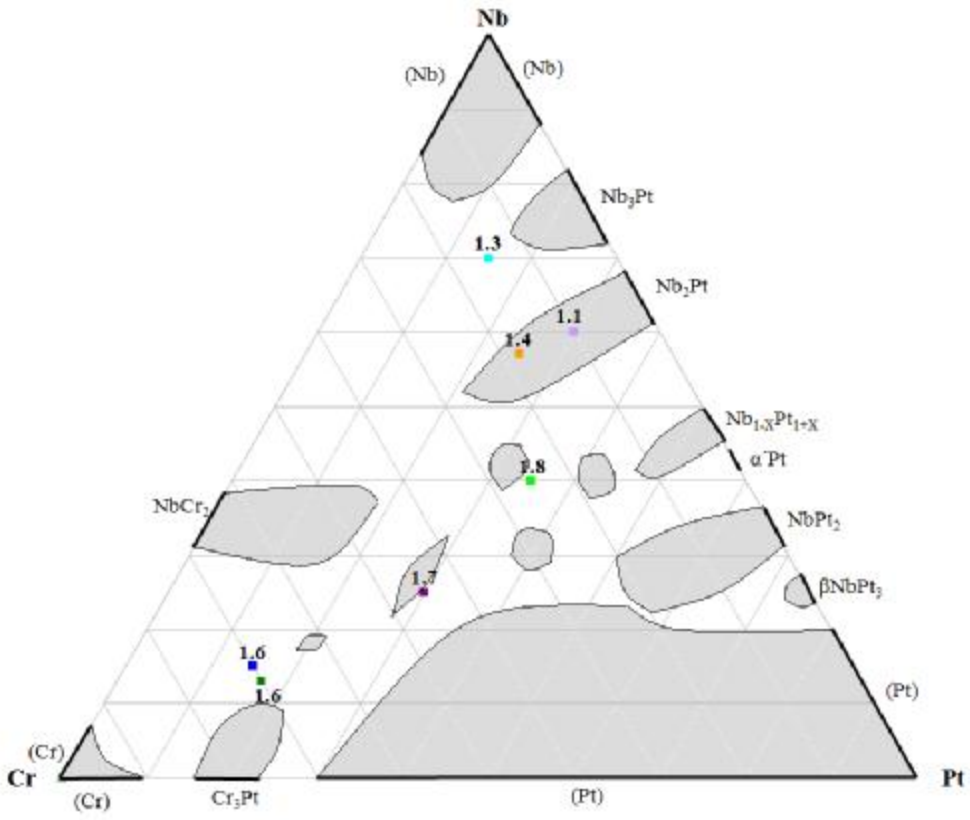

Figure 5.9. The Palmqvist fracture toughness (K_{IC}) values of the as-cast Nb-Cr-Pt alloys superposed on the solidification projection.

Figure 5.10 shows the relationship between fracture toughness and chromium content in the Nb-Cr-Pt alloys. Note that the errors bars were plotted using 2 decimal places. The fracture toughness showed a peak of 1.8±0.1 at ~25 at.% Cr, with a steep increase before, and a shallower decrease afterwards to 1.6±0.2 at ~70 at.% Cr and 1.6±0.0 MPa√m at ~70.1 at.% Cr.

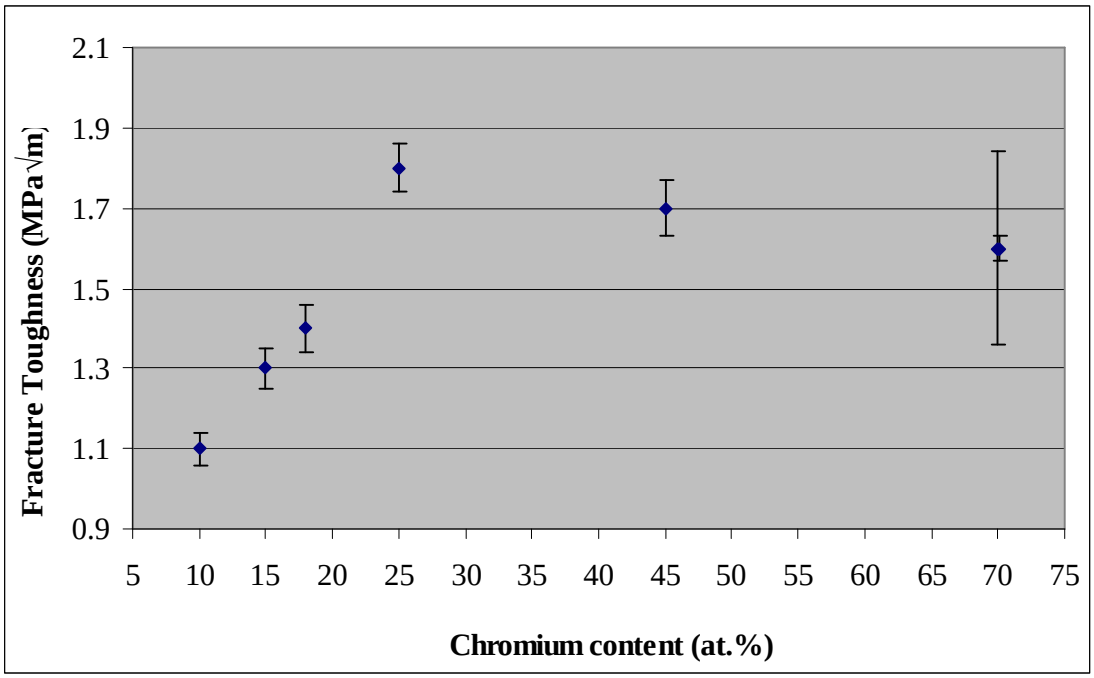

Figure 5.10. Fracture toughness (MPa√m) versus chromium content (at.%) for Nb-Cr-Pt alloys.

The relationship of fracture toughness versus niobium content is shown in Figure 5.11, and fracture toughness peaked to 1.8±0.1 MPa√m at ~40 at.% Nb (although the first four readings were similar), and then steep decreased to 1.1±0.0 at ~60 at.% Nb.

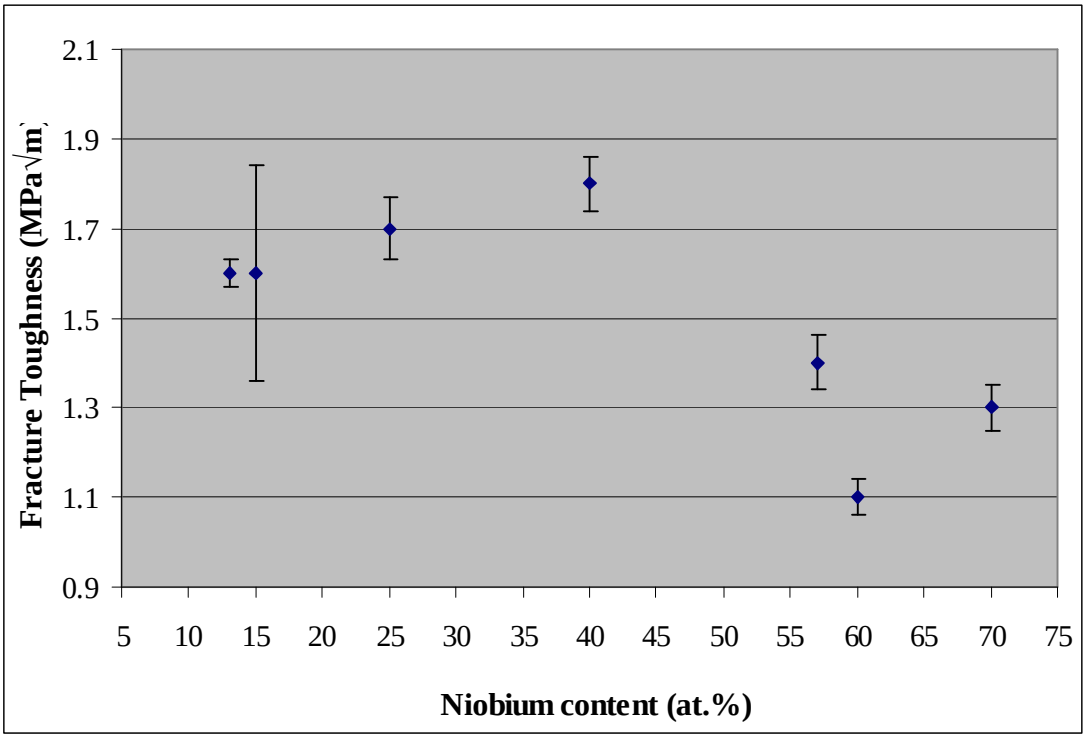

Figure 5.11. Fracture toughness (MPa√m) versus niobium content (at.%) for Nb-Cr-Pt alloys.

Figure 5.12 shows the relationship of fracture toughness versus platinum content. In this figure the fracture toughness was only measured up to ~35 at.% Pt because alloys with higher Pt content were ductile. It was difficult to see a relationship of fracture toughness with platinum content because there was much scatter. There was a lowest fracture toughness of 1.1±0.0 MPa√m at ~30 at.% Pt, and the highest fracture toughness of 1.8±0.1 MPa√m at ~35 at.% Pt. There were two different fracture toughness values at ~30 at.% Pt, which were 1.1±0.0 and 1.7±0.1 MPa√m. The difference in fracture toughness values is attributed to the different phases entailed in their alloys; there was one with 1.1±0.0 MPa√m which had (Pt) and τ2 phases, whereas there one with 1.7±0.1 MPa√m had three phases, ~Nb_3Pt, ~Nb_2Pt and τ5.

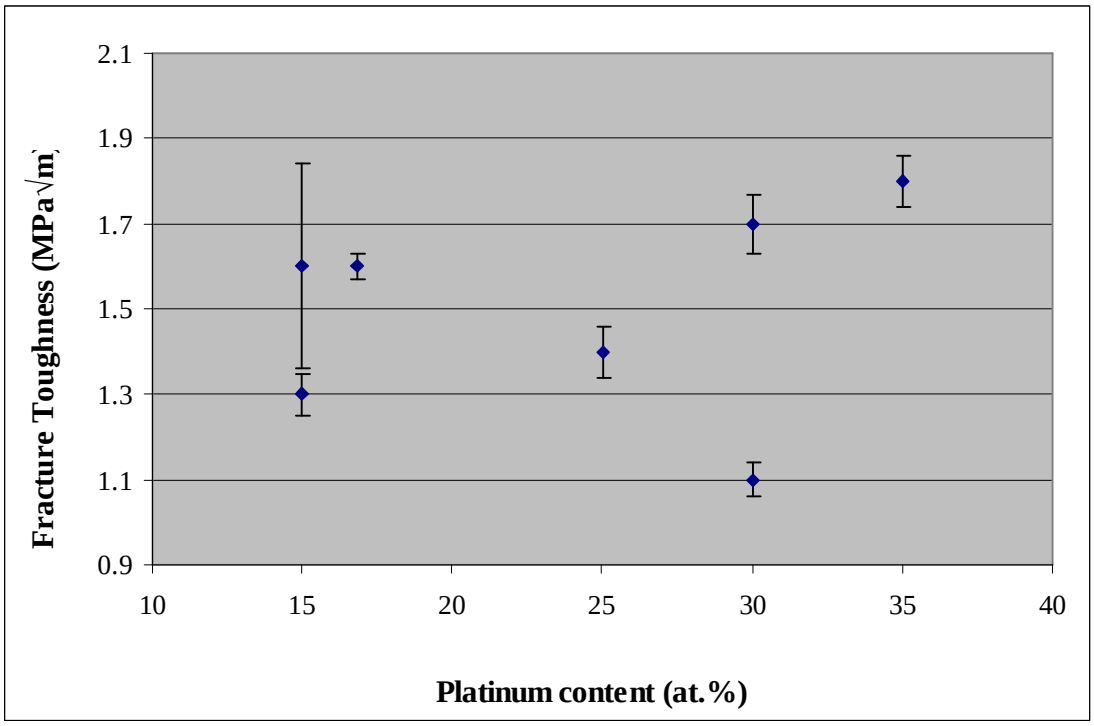

Figure 5.12. Fracture toughness (MPa.m√) versus platinum content (at.%) for Nb-Cr-Pt alloys.

CHAPTER 6:

CONCLUSIONS

Eighteen samples of different compositions were studied using SEM with EDX, and the phases were confirmed by X-ray diffraction. Other peaks were identified to belong to the phases not currently included in the ICD Database. A solidification projection was drawn, showing the phase extents into the ternary. The phase extents were:

- (Cr): a least ~2 at.% Nb;
- (Pt): ~24 at.% Nb;
- (Nb): ~12 at.% Pt and ~17 at.% Cr;
- ~$NbPt_2$: ~20 at.% Cr;
- ~$NbCr_2$: ~18 at.% Pt;
- ~Cr_3Pt: ~10 at.% Nb;
- ~$\beta NbPt_3$: ~4 at.% Cr;
- ~$Nb_{1-X}Pt_{1+X}$: ~13 at.% Cr;
- ~Nb_3Pt: ~10 at.% Cr;
- ~Nb_2Pt: ~26 at.% Cr.

Five ternary phases and their approximate compositions were identified as:

- $\tau 1$: ~Nb_{17}:Cr_{64}:Pt_{19};
- $\tau 2$: ~Nb_{28}:Cr_{45}:Pt_{27};
- $\tau 3$: ~Nb_{30}:Cr_{30}:Pt_{40};
- $\tau 4$: ~Nb_{45}:Cr_{27}:Pt_{28};
- $\tau 5$: ~Nb_{40}:Cr_{18}:Pt_{42}.

The liquidus surface projection was derived, and nineteen ternary invariant reactions were identified.

Hardness measurements were undertaken, and alloys with (Pt) and ~$NbPt_2$ were found to be ductile with reasonable hardness. Alloys containing (Cr), (Nb), ~Cr_3Pt, ~$NbCr_2$, ~Nb_3Pt and ~Nb_2Pt were extremely brittle with cracks. Fracture toughnesses of the Nb-Cr-Pt alloys were found to be very low as compared to other metal alloys. The highest fracture toughness, 1.8 ± 0.1 MPa.m^{-2}, was found in a sample containing the $\tau 3$ and $\tau 4$ ternary phases.

CHAPTER 7:

RECOMMENDATIONS FOR FUTURE WORK

- Model the XRD peaks for the missing phases in the ICD Database: $Nb_{1-X}Pt_{1+X}$ and Nb_2Pt.
- A binary alloy of Nb_{40}:Pt_{60} would be useful to confirm the α´Pt phase.
- An alloy needs to be made at ~Nb_{44}:Cr_5:Pt_{51}, for more information regarding $Nb_{1-X}Pt_{1+X}$ and τ5.
- Differential thermal analysis needs to be conducted on the alloys in order to determine the reaction temperatures and enthalpies of formation for the different phases.
- The alloys also need to be investigated after heat treatment, in a protective atmosphere, to equilibrate them and to undertake an isothermal section at the heat treatment temperature.

REFERENCES

[1930Mül] L. Müller, *Ann. Phys. (Leipzig)*, 7 (5), (1930), pp. 9–47.

[1935Fri] E. Friederich and A. Kussmann, *Phys. Z.*, 36 (6), (1935), pp. 185–192.

[1940Geb] E. Gebhardt and W. Köster, *Z. Metallkd.*, 32, (1940), pp. 262–264.

[1943Wal] H.J. Wallbamm, *Naturwissenschaften*, 31 (1943), pp. 91–92.

[1952Duw] P. Duwez and H. Martens, *Trans. AIME*, 194 (1952), pp. 72–74.

[1954Ell] R.P. Elliot, Armour Research Foundation, Chicago, I11, Technical Report 1, Technical Note OSR–TN–247, August, (1954), p. 84.

[1955Gel] S. Geller, B.T. Mathias and R. Goldstein, *J. Am. Chem. Soc.*, 77, (1955), pp. 1502–1504.

[1955Rau] E. Raub and W. Mahler, *Z. Metallkunde.*, 46 (1955), pp. 210–215.

[1956Gre] P. Greenfield and P.A. Beck, *Trans. AIME*, 206, (1956), pp. 265–276.

[1958Han] M. Hansen and K. Auderko, Constitution of Binary Alloys, McGraw–Hill Book Company, INC, (1958), pp. 541–554.

[1961Gol] H.J. Goldschmidt and J.A. Brand, *J. Less–Common Met.*, 3 (1961) , pp. 44–61.

[1961Kim] H. Kimura and A. Ito, *Trans. Natl. Res. Inst. Met. (Jpn.)*, 3, (1961), pp. 27–34.

[1961Mat] B.T. Matthias, V.B. Compton and E. Corenzwit, *Phys. Chem. Solids*, 19 (1961), pp. 130–133.

[1961Pan] V.M Pan, *Dopov, Akad. Nauk Ukr.RSR* ,(1961), pp. 332–334.

[1962Bro] W. Bronger and W. Klemm, *Z. Anorg. Allg. Chem.*, 319, (1962), pp. 58–81.

[1963Pic] S.J. Pickart and R. Nathans, *J. Appl. Phys.*, 34 (4),(1963), pp. 1203–1204.

[1964Gie] B.C. Giessen and N.J. Grant, *Acta Crystallogr.*, 17, (1964), pp. 615–616.

[1964Mal] A. Maldonado and K. Schubert, *Z. Metallkd.*, 55, (1964), pp. 619–626

[1964Sch] K. Schubert, Kristallstrukturen Zweikomponentiger Phasen, 1st edition, Springer–Verlag OHG., Berlin, (1964), p. 30.

[1965Dwi] A.E. Dwight, R.A. Conner, Jr., and J.W. Downey, *Acta Crystallogr*, 18, (1965), pp. 835–839.

[1967Sul] A.H. Sully and E.A. Brandes, Metallurgy of the Rarer Metals (Chromium), 2nd edition, Butterworth and Co (Ltd), (1967).

[1968Kus] A. Kussmann, K. Müller and E. Raub, *Z. Metallkd.*, 59, (1968), pp. 859–863.

[1968Reu] E.C. Van Reuth and R.M. Waterstrat, *Acta Crystallogr. B*, 24, (1968), pp. 186–196.

[1969Rud] E. Rudy, Tech. Rep, AFML–TR–65 (1969) 2, 21, pp. 127–130.

[1970Shu] F.A. Shunk, Constitution of Binary Alloys, McGraw-Hill, New York, (1970).

[1972Cha] G.A. Chadwick, Metallography of Phase Transformations, Butterworth, London, (1972).

[1972Ros] R.B Ross, Metallic Materials Specification Handbook, 2nd edition, E. and F.N. Spon Ltd, (1972).

[1973Bes] M. J. Besnus and A.J.P. Meyer, *Phy. Status Solidi (b)*, 58, (1973), pp. 533–542.

[1973Wat] R.M. Waterstrat, *Metall. Trans.*, 4 (1973), pp. 1585–1592.

[1977Got] T. Goto, *J. Phys. Soc. Jpn.*, 43, (1977), pp. 1848–1853.

[1978Bag1] J. Baglin, J. Dumpsey, F. d'Heurle, W. Hammer and S. Zirinsky, *Proc. Electrochem. Soc*, 78–82 (1978), pp. 185–198.

[1978Bag2] J. Baglin, F. d'Heurle, and S. Zirinsky, *J. Electrochem. Soc.*, 125, (1978), pp. 1854–1859.

[1978Sav] E. Savitsky, V. Polyakova, N. Gorina and N. Roshan, Physical Metallurgy of Platinum Metals, MIR Publishers, Moscow, (1978).

[1979Ole] A. Oles and A. Bombik, *Phys. Status Solidi (b)*, 92, K81–K83 (1979).

[1980But] A.K. Butylenko and V.V. Nevdacha, *Dop. Akad. Nauk Ukr. RSR A*, Fiz.–Mat. Tekh. , 42 (5), (1980), pp. 66–69.

[1983Wat] R.M. Waterstrat and B.C. Giessen, Alloy Chemical Comparison of Refractory Metal–Noble Metal Phase Diagrams, T_5–T_{10} (T_5 = V, Nb, Ta; T_{10} = Pd, Pt), Alloy Phase Diagrams, MRS porc., L.H. Bennet, T.B. Massalski and B.C. Giessen, Ed., North – Holland, NY, 19, (1983), pp. 423–428.

[1985She] D.K. Shetty, I.G. Wright, P.N. Mincer and A.H. Clauer, *J. Mat. Sci.*, Vol. 20, (1985), p. 1873.

[1985Wat] R.M. Waterstrat and B.C. Giessen, *Metall. Trans. A*, 16 (11), (1985), pp. 1943–1949.

[1986Mis] Y. Mishima, Y. Oya and T. Suzuki, Proceedings of the International Conference on Martensitic Transformations, Japan Institute of Metals, (1986), p. 1009–1014.

[1987Sim] C.T. Sims, N.S. Stoloff and W.C. Hagel, Superalloys II: High Temperature Materials for Aerospace and Industrial Power, Wiley–Interscience, USA, (1987).

[1988Die] G.E. Dieter, Mechanical Metallurgy, McGraw-Hill Book Company, UK, (1988)

[1988Wha] M.V. Whalen, *Plat. Metals Rev.*, 32 (1) (1988), pp. 2–10.

[1990Lup] D. Lupton, *Adv. Mater.*, 5 (1990) p. 29.

[1990Mas] T.B. Massalski, Binary Alloy Phase Diagrams, ASM International, (1990), Ohio, USA

[1990Spi] R. Spiegler, S. Schmauder and L. Sigl, *J. Hard Mater.*, 1(3), (1990), p.147.

[1990Ven] M. Venkatraman and J.P. Neumann, *Bull. Alloy Phase Diagrams*, Vol. 11 (No.1), (1990), pp. 16–21.

[1991Oka] H. Okamoto and T.B. Massalski, *J. of Phase Equilibria*, 12(2), (1991), pp. 148-168.

[1992Tho] D.J. Thoma and J.H. Perepezko, *Mat. Sci. & Eng.*, A156, (1992), pp. 97–108.

[1994Dow] N. E. Dowling, Mechanical Behavior of Materials: Engineering Methods for Deformation, Fracture, and Fatigue, Prentice Hall, (1993), pp. 287-291.

[1993Oka] H. Okamoto, *J. of Phase Equilibria*, 14(4), (1993).

[1994Cal] W. Callister, Material Science and Engineering: An Introduction, 3rd Edition, John Wiley & Sons, Inc., (1994), pp. 194-196.

[1995Tri] S.N. Tripathi, S.R. Bharadwaj and S.R. Dharwadkar, *J. of Phase Equilibria*, Vol. 16 (No.5), (1995), pp. 465–470.

[1997Yos] M. Yoshida and T. Takasugi, *Mat. Sci. & Eng*, A224 (1997), pp. 69–76.

[1999Ter] Y. Terada, K. Ohkubo, T. Mohri and T. Suzuki., *J. Alloys & Compounds*, 285 (1999), pp. 233–237.

[2000Com1] D.N. Compton, L.A. Cornish and M.J. Witcomb, Microscopy and Microanalysis 2000, volume 6, Supplement 2, 370–371, Philadelphia, Pennsylvania, USA, 13^{th} – 17^{th} August 2000.

[2000Com2] D.N. Compton, L.A. Cornish and M.J. Witcomb, Proc. Microsc. Soc. South. Afr. , Vol. 30, p. 9, Grahamstown, 6^{th} – 8^{th} December 2000.

[2000Fai] G.B. Fairbank, C.J. Humpreys, A. Kelly and C.N. Jones, *Intermetallics*, 8 (2000), pp. 1091–1100.

[2000Wol] I.M. Wolff and P.J. Hill, *Plat. Metals Rev.*, 44, (4), (2000), pp. 158–166.

[2001Com] D.N. Compton, L.A. Cornish, and M.J. Witcomb, Microscopy and Microanalysis 2001, volume 7, Supplement 2, 1248–1249, Pub. Springer–Verlag, NY, Inc. , Long Beach, California, USA, 5^{th} – 9^{th} August 2001.

[2001Hil1] P.J. Hill, Superalloy Analogues Based on Platinum for Ultra–High Temperature Applications, PhD Thesis, University of Witwatersrand, Johannesburg, South Africa, (2001).

[2001Hil2] P.J. Hill, L.A. Cornish, P. Ellis and M.J. Witcomb, *J. Alloys & Compounds*, 322 (2001), pp. 166–175.

[2001Hil3] P.J. Hill, L.A. Cornish and M.J. Witcomb, Proc. Microsc. Soc. South. Afr., Vol. 31, p. 22, Johannesburg, 5^{th} – 7^{th} December 2001.

[2001Hil4] P.J. Hill, L.A. Cornish and M.J. Witcomb, Proc. Microsc. Soc. South. Afr., Vol. 31, (2001), p. 22.

[2001Oik] K. Oikawa, G.W. Qin, T. Ikeshoji, O. Kitakami, Y. Shimida, K. Ishidaand J. Fukamichi, *J. Magnetism & Magnetic Mat.*, vol. 236, (2001), pp. 220–223.

[2001Süs] R. Süss, P.J. Hill, P. Ellis and L.A. Cornish, Proc. Microsc. Soc. South. Afr., Vol. 31, p. 21, Johannesburg, 5–7^{th} December 2001.

[2002Cor] L.A. Cornish, J. Hohls, P.J. Hill, S.N. Prins, R. Süss and D.N. Compton, *J. Mining and Metallurgy*, 38 ((3–4) B) (2002), pp. 197–204.

[2002Hil] P.J. Hill, N. Adams, T. Biggs, P. Ellis, J. Hohls, S.S. Taylor and I.M. Wolff, *Mat. Sci. & Eng.*, A329 – 339 (2002), pp. 295–304.

[2002Süs1] R. Süss, L.A. Cornish, L. Glaner and D.N. Compton, ICEM 15, Proceedings of the 15^{th} international Congress on Electron Microscopy, 1^{st} – 6^{th} September 2002, Durban, South Africa.

[2002Süs2] R. Süss, R. Völkl, D. Freund, B. Fischer, P.J. Hill, P. Ellis and I.M. Wolff, *Mat. Sci. & Eng.*, A338, (2002), pp. 133–141.

[2003Cho] L.H. Chown and L.A. Cornish, Proc. 2nd International Conference of the African Materials Society, Johannesburg, (2003), pp. 136–137.

[2003Cor] L.A. Cornish, B. Fischer and R. Völkl, *Mat. Res. Bul.*, 28 (9) (2003), pp. 632–638.

[2003Gla] L. Glaner and L.A. Cornish, Proc. Microsc. Soc. South. Afr., Vol. 33, (2003), p. 17.

[2003Hua] C. Huang, Y. Yamabe-Mitarai, K. Nishida and H. Harada, *Intermetallics*, 11, (2003), pp. 917–926.

[2003Pri] S.N. Prins, The Al–Pt–Ru Ternary Phase Diagram, MSc Dissertation, University of Pretoria, Pretoria, South Africa, (2003).

[2003Süs] R. Süss, L.A. Cornish, P.J. Hill and J. Hohls, Proceedings of Advanced Materials and Processes of Gas Turbines, 22–26 September 2002, Copper Mountain, Colorado, USA, TMS, (2003), pp. 301–308.

[2003Süs1] R. Süss, L.A. Cornish and B. Joja, Proc. Microsc. Soc. South. Afr., Vol. 33, (2003), p.13.

[2003Süs2] R. Süss, U. Glatzel, S.N. Prins and L.A. Cornish, Proc. 2nd International conference of the African Materials Society, (2003), p. 141–142.

[2003Xpe] X´pert Highscore, (PW3209), 1.0d, PANalytical B.V., Almelo, The Netherlands, 31 March, 2003.

[2004Hua1] C. Huang, Y. Yamabe–Mitarai and H. Harada, *J. Alloys and Compounds*, 366 (2004), pp. 217–221.

[2004Hua2] C. Huang, Y. Yamabe-Mitarai, S. Nakazawa and H. Harada, *Mat. Let.*, 58, (2004), pp. 483–488.

[2004Süs1] R. Süss, Investigation into the Pt–Cr–Ru System, MSc Dissertation, University of the Witwatersrand, Johannesburg, South Africa, (2004).

[2004Süs2] R. Süss, L.A. Cornish, L.H. Chown and L. Glaner, Beyond Ni-based Superalloys, TMS 2004 133rd Annual Meeting and Exhibition, Charlotte, North Carolina, USA, (2004), p. 269.

[2004Vor] S. Vorberg, M. Wenderoth, B. Fischer, U. Glatzel, and R. Völkl, *JOM*, 56(9), (2004), pp. 40–43.

[2005Hua] C. Huang, Y. Yamabe-Mitarai, X.H. Yu, S. Nakazawa and H. Harada, *Met. & Mat. Trans.*, Vol. 36A, (2005), pp. 539–545.

[2005Hül] M. Hüller, M. Wenderoth, S. Vorberg, B. Fischer, U. Glatzel and R. Völkl, *Met. & Mat. Trans.*, Vol. 36A, (2005), pp. 681–689.

[2005Süs] R. Süss and L.A. Cornish, Proc. Microsc. Soc. South. Afr., Vol. 35, (2005), p. 9.

[2005Wen] M. Wenderoth, L.A. Cornish, R. Süss, S. Vorberg, B. Fischer, U. Glatzel and R. Völkl, *Met. & Mat. Trans.*, Vol. 36A, (2005), pp. 567–575.

[2005Zha] J.-C. Zhao, X. Zheng and D.G. Cahil, *Materials Today*, October (2005), pp. 28–37.

[2006Ndl] G.F. Ndlovu, L.A. Cornish, A. Douglas, B.A. Julies and B. Joja, Proc. Microsc. Soc. South. Afr., Vol. 36, (2006), p.11.

[2006Süs] R. Süss, L.A. Cornish and M.J. Witcomb, *J. Alloys & Compounds*, 416 (2006), pp. 80–92.

[2007Dou] A. Douglas, J.H. Neethling, R. Santamarta, D. Schryvers and L.A. Cornish, *J. Alloys & Compounds*, 432, (2007), pp. 96–102.

[2007Ndl] G.F. Ndlovu, Microstructural Investigation of the Pt-Al-Nb System, MSc Dissertation, University of the Western Cape, Cape Town, South Africa, (2007).

[2008Née] http://en.wikipedia.org/wiki/N%C3%A9el-temperature.

[2008Sho] M.B. Shongwe, L.A. Cornish and R. Süss, Advanced Metals Initiative Conference, 18th–19th November 2008, CD.

[2008Süs] R. Süss, Investigation of the Pt-Al-Cr system as part of the development of the Pt-Al-Cr-Ru thermodynamic database, PhD Thesis, University of the Witwatersrand, Johannesburg, South Africa, (2008).

[2008Ukp] A.M. Ukpong, L.A. Cornish, R. Süss and A. Watson, Advanced Metals Initiative Conference, 18th–19th November 2008, CD.

APPENDICES

Appendix A Average atomic numbers for binary phases in the Nb-Cr-Pt ternary

Appendix B List of phases for X-ray diffraction from the ICD Database

Appendix C XRD data for binary phases

Appendix D XRD peaks of the binary phases

Appendix E XRD spectrum of plasticine

Appendix F EDX data for alloys' in the as-cast condition

Appendix G Papers published and presented during the course of this investigation

APPENDIX A

Table A1. Average atomic numbers for binary phases in the Nb–Cr–Pt ternary.

Phase	**Average atomic number**	**Contrast**
(Cr)	24.00	Dark ↕ Light
$NbCr_2$	29.67	
Cr_3Pt	37.50	
(Nb)	41.00	
α′Pt	45.24	
Nb_3Pt	50.25	
CrPt	51.00	
Nb_2Pt	53.33	
$Nb_{1-X}\ Pt_{1+X}$	60.61	
$CrPt_3$	64.50	
$NbPt_2$	65.67	
$NbPt_3$	68.75	
(Pt)	78.00	

APPENDIX B

Table B1. List of phases for X-ray diffraction from the database (ICDD).

Phase	**XRD data available on the database**	**Reference number**
(Cr)	Yes	00-006-0694
$NbCr_2$	Yes	00-047-1638
Cr_3Pt	Yes	00-065-3306
(Nb)	Yes	01-089-5008
α′Pt	**No**	----
Nb_3Pt	Yes	00-018-0918
CrPt	Yes	00-034-0707
Nb_2Pt	**No**	----
$Nb_{1-X}\ Pt_{1+X}$	**No**	----
$CrPt_3$	Yes	00-034-1080
$NbPt_2$	Yes	00-065-1437
$NbPt_3$	Yes	00-065-1138
(Pt)	Yes	00-004-0802

APPENDIX C

Table C1. XRD data for Pt, syn phase (Ref. No: 00-004-0802).

No.	h	k	l	d-spacing (Å)	2θ (degree)	Intensity (%)
1	1	1	1	2.26500	39.765	100
2	2	0	0	1.96160	46.244	53
3	2	2	0	1.38730	67.456	31
4	3	1	1	1.18260	81.289	33
5	2	2	2	1.13250	85.715	12
6	4	0	0	0.98080	103.512	6
7	3	3	1	0.90000	117.716	22
8	4	2	0	0.87730	122.812	20
9	4	2	2	0.80080	148.272	29

Table C2. XRD data for Nb phase (Ref. No: 01-089-5008).

No	h	k	l	d-spacing (A)	2θ (degree)	Intensity (%)
1	1	1	0	2.32978	38.614	100.0
2	2	0	0	1.64740	55.755	13.8
3	2	1	1	1.34510	69.873	23.5
4	2	2	0	1.16489	82.793	6.3

Table C3. XRD data for Cr phase (Ref. No: 00-006-0694).

No	h	k	l	d-spacing (A)	2 θ (degree)	Intensity (%)
1	1	1	0	2.03900	44.393	100.0
2	2	0	0	1.44190	64.583	16.0
3	2	1	1	1.17740	81.724	30.0
4	2	2	0	1.01950	98.150	18.0
5	3	1	0	0.91200	115.264	20.0
6	2	2	2	0.83250	135.425	6.0

Table C4. XRD data for $NbCr_2$ phase (Ref. No: 00-047-1638).

No	h	k	l	d-spacing (Å)	2θ (deg)	Intensity (%)
1	1	0	0	4.30940	20.594	1.0
2	0	0	2	4.02931	22.043	1.0
3	1	0	1	3.79992	23.392	3.0
4	1	0	2	2.94308	30.346	8.0
5	1	1	0	2.48800	36.071	52.0
6	1	0	3	2.27967	39.498	87.0
7	2	0	0	2.15457	41.896	14.0
8	1	1	2	2.11701	42.675	100.0
9	2	0	1	2.08175	43.434	65.0
10	0	0	4	2.01446	44.963	11.0
11	2	0	2	1.90017	47.830	5.0
12	1	0	4	1.82513	49.928	6.0
13	2	0	3	1.68080	54.554	1.0
14	2	1	0	1.62871	56.452	1.0
15	2	1	1	1.59640	57.701	1.0
16	2	1	2	1.51018	61.337	2.0
17	1	0	5	1.50952	61.367	7.0
18	2	0	4	1.47164	63.125	1.0
19	3	0	0	1.43654	64.853	9.0
20	2	1	3	1.39268	67.161	33.0
21	3	0	2	1.35297	69.408	21.0
22	0	0	6	1.34302	69.997	3.0
23	2	0	5	1.29054	73.294	26.0
24	1	0	6	1.28230	73.843	3.0
25	2	1	4	1.2663	74.912	3.0
26	2	2	0	1.24411	76.509	22.0
27	3	1	0	1.19521	80.255	1.0
28	2	2	2	1.18871	80.784	1.0
29	3	1	1	1.18230	81.314	1.0
30	1	1	6	1.18182	81.354	1.0
31	3	1	2	1.14589	84.479	1.0
32	2	1	5	1.14567	84.499	5.0
33	2	0	6	1.13977	85.039	8.0
34	1	0	7	1.11217	87.674	2.0
35	3	1	3	1.09203	89.721	16.0
36	4	0	0	1.07732	91.289	1.0
37	4	0	1	1.06782	92.336	7.0
38	2	2	4	1.05848	93.395	8.0
39	4	0	2	1.04079	95.482	1.0
40	2	1	6	1.03621	96.041	3.0
41	3	1	4	1.02795	97.069	2.0
42	2	0	7	1.01539	98.686	1.0

Table C5. XRD data for $NbPt_2$ phase (Ref. No: 00-065-1437).

No	h	k	l	d-spacing (Å)	2θ (deg)	Intensity (%)
1	0	2	0	4.22950	20.987	6.7
2	0	1	1	3.57977	24.852	14.8
3	1	1	0	2.65902	33.679	6.5
4	0	3	1	2.29514	39.221	98.5
5	1	0	1	2.28504	39.401	100.0
6	0	4	0	2.11475	42.723	2.4
7	1	2	1	2.01040	45.059	3.3
8	1	3	0	1.98717	45.615	60.6
9	0	0	2	1.97550	45.900	30.1
10	0	2	2	1.78988	50.981	1.1
11	1	1	2	1.58575	58.125	2.4
12	0	5	1	1.55522	59.379	0.3
13	1	4	1	1.55207	59.512	3.4
14	1	5	0	1.44815	64.271	0.2
15	0	4	2	1.44361	64.497	1.3
16	0	6	0	1.40983	66.238	8.4
17	1	3	2	1.40100	66.710	39.4
18	2	2	0	1.32951	70.815	0.4
19	2	1	1	1.30424	72.401	1.1
20	0	1	3	1.30132	72.589	1.1
21	1	6	1	1.19984	79.883	17.8
22	2	3	1	1.19550	80.231	17.5
23	0	3	3	1.19326	80.413	14.7
24	1	5	2	1.16766	82.553	0.7
25	0	7	1	1.15559	83.608	0.7
26	0	6	2	1.14757	84.326	7.6
27	2	0	2	1.14252	84.786	7.4
28	1	7	0	1.10957	87.932	0.6
29	2	2	2	1.10298	88.594	0.3
30	0	8	0	1.05737	93.523	0.1
31	2	5	1	1.04072	95.490	0.1
32	0	5	3	1.03829	95.786	0.8
33	2	4	2	1.00520	100.048	0.6
34	2	6	0	0.99359	101.660	4.7
35	0	0	4	0.98775	102.494	2.3
36	1	7	2	0.96742	105.546	0.8
37	0	2	4	0.96187	106.420	0.1
38	1	8	1	0.95961	106.781	0.1
39	2	1	3	0.95331	107.807	0.4
40	0	8	2	0.93224	111.439	0.1
41	3	1	0	0.92803	112.205	0.2
42	1	1	4	0.92593	112.593	0.4
43	0	9	1	0.91437	114.796	3.8
44	1	6	3	0.91018	115.627	7.6

Table C5. XRD data for $NbPt_2$ phase (continued).

45	3	0	1	0.90828	116.008	10.9
46	0	4	4	0.89494	118.796	0.2
47	2	7	1	0.89106	119.646	4.1
48	3	2	1	0.88837	120.245	2.1
49	2	6	2	0.88764	120.410	7.4
50	3	3	0	0.88634	120.704	3.8
51	1	3	4	0.88451	121.122	8.1
52	0	10	0	0.84590	131.184	0.2
53	2	8	0	0.84387	131.795	0.1
54	3	1	2	0.83996	133.001	0.3
55	3	4	1	0.83484	134.645	0.5
56	3	5	0	0.81744	140.892	0.1
57	1	5	4	0.81601	141.465	0.1
58	1	9	2	0.81226	143.008	6.8
59	0	6	4	0.80867	144.556	8.6
60	2	0	4	0.80719	145.223	4.9

Table C6. XRD data for Nb_3Pt phase (Ref. No: 00-018-0918).

No	**h**	**k**	**l**	**d-spacing (Å)**	**2θ (deg)**	**Intensity (%)**
1	1	1	0	3.64200	24.421	14.0
2	2	0	0	2.57500	34.813	40.0
3	2	1	0	2.30400	39.064	65.0
4	2	1	1	2.10200	42.995	100.0
5	2	2	0	1.82300	49.991	6.0
6	3	1	0	1.62900	56.441	6.0
7	2	2	2	1.48800	62.353	4.0
8	3	2	0	1.42890	65.243	16.0
9	3	2	1	1.37650	68.057	55.0
10	4	0	0	1.28860	73.422	16.0
11	4	1	1	1.21440	78.737	4.0
12	4	2	0	1.15220	83.910	16.0
13	4	2	1	1.12440	86.483	14.0
14	3	3	2	1.09830	89.072	14.0
15	4	2	2	1.05180	94.170	2.0
16	5	1	0	1.01050	99.334	6.0
17	5	2	0	0.95680	107.236	16.0
18	5	2	1	0.94080	109.924	25.0
19	4	4	0	0.91100	115.463	14.0
20	5	3	0	0.88380	121.285	4.0
21	6	0	0	0.85880	127.520	14.0
22	6	1	0	0.84700	130.858	8.0
23	6	1	1	0.83580	134.332	30.0
24	6	2	0	0.81460	142.035	1.0
25	5	4	1	0.79500	151.361	4.0

Table C7. XRD data for βNbPt$_3$ phase (Ref. No: 00-065-1138).

No	h	k	l	d-spacing (Å)	2θ (deg)	Intensity (%)
1	0	0	1	9.12152	9.689	0.6
2	1	0	0	4.79303	18.497	0.4
3	-1	0	1	4.59087	19.319	2.3
4	1	0	1	3.96374	22.412	0.3
5	-1	0	2	3.64172	24.423	3.3
6	1	1	0	3.62389	24.545	7.6
7	0	1	2	3.52032	25.279	11.0
8	1	1	1	3.22302	27.655	2.2
9	1	0	2	3.04563	29.301	4.0
10	-1	0	3	2.80170	31.917	0.4
11	0	2	0	2.76850	32.310	2.9
12	1	1	2	2.66857	33.555	0.9
13	0	2	1	2.64917	33.808	0.1
14	-1	1	3	2.49989	35.894	0.7
15	-2	0	1	2.42583	37.029	5.1
16	1	2	0	2.39652	37.498	28.7
17	-1	2	1	2.37078	37.921	35.6
18	-2	0	2	2.29544	39.215	4.8
19	0	0	4	2.28038	39.485	80.6
20	2	0	1	2.22312	40.546	51.2
21	-1	0	4	2.21715	40.660	25.6
22	-1	2	2	2.20394	40.915	100.0
23	2	1	0	2.19935	41.004	51.1
24	-2	1	2	2.12044	42.603	0.4
25	0	1	4	2.10856	42.855	0.4
26	-2	0	3	2.06866	43.723	42.4
27	2	1	1	2.06304	43.849	21.3
28	1	2	2	2.04861	44.174	83.0
29	2	0	2	1.98187	45.744	3.9
30	-1	2	3	1.96926	46.054	7.4
31	-2	1	3	1.93783	46.845	0.3
32	1	0	4	1.93082	47.025	0.1
33	2	1	2	1.86594	48.764	0.1
34	1	1	4	1.82086	50.054	6.2
35	-1	0	5	1.81519	50.221	3.3
36	2	2	0	1.81194	50.317	0.7
37	0	3	1	1.80636	50.483	10.9
38	-2	2	2	1.76705	51.688	0.1
39	0	2	4	1.76016	51.906	1.2
40	2	0	3	1.73843	52.604	1.3
41	2	2	1	1.73342	52.768	1.1
42	-1	2	4	1.73059	52.861	2.6
43	-1	1	5	1.72487	53.050	1.3
44	1	3	0	1.72238	53.132	0.8

Table C7. XRD data for βNbPt$_3$ phase (continued).

45	-1	3	1	1.71088	53.518	1.2
46	1	3	1	1.67317	54.824	0.3
47	2	1	3	1.65860	55.346	1.3
48	-1	3	2	1.64630	55.796	0.1
49	-3	0	1	1.62333	56.656	0.5
50	1	0	5	1.61151	57.110	0.1
51	-2	0	5	1.59398	57.797	1.4
52	1	2	4	1.58370	58.208	2.6
53	1	3	2	1.57845	58.420	1.3
54	-3	1	1	1.55776	59.273	0.1
55	1	1	5	1.54834	59.670	0.3
56	-1	3	3	1.54128	59.971	0.1
57	-3	1	2	1.53601	60.198	0.1
58	-2	1	5	1.53177	60.382	0.5
59	-1	0	6	1.52925	60.492	0.3
60	2	0	4	1.52282	60.774	4.7
61	-1	2	5	1.51800	60.987	9.7
62	-3	1	3	1.47500	62.965	0.7
63	3	1	1	1.47330	63.046	0.7
64	-2	3	1	1.46886	63.258	0.8
65	0	1	6	1.46600	63.396	0.8
66	2	3	0	1.46227	63.577	0.3
67	1	3	3	1.45933	63.720	0.1
68	-2	3	2	1.43837	64.761	0.1
69	0	3	4	1.43464	64.950	0.1
70	3	0	2	1.43085	65.143	0.1
71	2	3	1	1.41850	65.781	0.4
72	-2	0	6	1.40035	66.745	26.6
73	1	2	5	1.39350	67.116	0.9
74	0	4	0	1.38425	67.625	12.5
75	-2	2	5	1.38037	67.841	6.6
76	-2	3	3	1.37720	68.018	0.3
77	0	4	1	1.36858	68.506	0.1
78	-2	1	6	1.35806	69.111	0.1
79	2	3	2	1.35067	69.544	0.1
80	2	0	5	1.34159	70.083	6.5
81	-3	2	3	1.33861	70.262	16.2
82	2	2	4	1.33429	70.523	6.9
83	1	4	0	1.32990	70.791	0.3
84	0	4	2	1.32370	71.173	0.2
85	3	0	3	1.32125	71.325	0.3
86	-1	0	7	1.31790	71.534	0.1
87	1	4	1	1.30685	72.234	0.1
88	2	1	5	1.30308	72.476	0.1
89	-1	3	5	1.29393	73.071	0.3
90	-3	1	5	1.28742	73.501	0.1

Table C7. XRD data for βNbPt$_3$ phase (continued).

91	3	1	3	1.28516	73.651	0.1
92	-1	1	7	1.28209	73.857	0.1
93	3	2	2	1.27112	74.602	0.1
94	0	1	7	1.26842	74.788	0.1
95	2	3	3	1.26547	74.992	0.3
96	1	4	2	1.26019	75.361	0.4
97	-2	2	6	1.24995	76.088	0.1
98	-1	4	3	1.24070	76.758	5.9
99	1	2	6	1.23534	77.152	11.5
100	-3	3	1	1.21894	78.387	0.1
101	-4	0	1	1.21619	78.599	0.3
102	-3	0	6	1.21292	78.852	1.4
103	-2	1	7	1.21068	79.026	0.7
104	2	2	5	1.20636	79.365	0.2
105	-2	4	1	1.20228	79.688	0.7
106	2	4	0	1.19866	79.977	3.2
107	-3	2	5	1.19421	80.336	13.2
108	3	2	3	1.19241	80.482	13.6
109	-1	2	7	1.18894	80.765	10.3
110	-2	4	2	1.18539	81.057	2.7
111	3	1	4	1.18330	81.230	12.4
112	-3	3	3	1.17804	81.670	0.3
113	2	4	1	1.17507	81.921	8.5
114	4	1	0	1.17115	82.254	4.1
115	2	1	6	1.16514	82.771	0.1
116	-4	1	3	1.16178	83.063	4.4
117	-1	0	8	1.15630	83.545	0.1
118	-2	4	3	1.15044	84.068	8.0
119	-4	0	4	1.14772	84.313	4.4
120	0	0	8	1.14019	85.000	5.2
121	4	1	1	1.13702	85.293	2.6
122	2	4	2	1.13484	85.496	0.8
123	-2	2	7	1.13220	85.743	0.9
124	-4	1	4	1.12383	86.538	0.1
125	0	1	8	1.11676	87.223	0.1
126	-4	2	1	1.11348	87.545	0.1
127	4	0	2	1.11156	87.735	0.7
128	-2	0	8	1.10857	88.032	0.9
129	1	3	6	1.10456	88.435	1.0
130	0	4	5	1.10197	88.697	2.0
131	4	2	0	1.09967	88.932	0.8
132	2	2	6	1.09440	89.474	0.2
133	-4	2	3	1.09246	89.676	0.2
134	4	1	2	1.08903	90.036	0.2
135	-2	1	8	1.08698	90.252	0.2
136	2	3	5	1.08519	90.442	0.1

Table C7. XRD data for βNbPt$_3$ phase (continued).

137	2	4	3	1.08289	90.688	0.4
138	1	5	0	1.07898	91.109	0.1
139	0	5	2	1.07613	91.419	0.2
140	3	3	3	1.07363	91.692	0.2
141	4	2	1	1.07128	91.952	0.3
142	2	0	7	1.06816	92.298	0.2
143	-1	2	8	1.06697	92.432	0.3

Table C8. XRD data for Cr$_3$Pt phase (Ref. No: 00-065-3306).

No	**h**	**k**	**l**	**d-spacing (Å)**	**2θ (deg)**	**Intensity (%)**
1	1	1	0	3.32764	26.769	78.2
2	2	0	0	2.35300	38.218	50.1
3	2	1	0	2.10459	42.939	28.3
4	2	1	1	1.92122	47.274	100.0
5	2	2	0	1.66382	55.158	9.5
6	3	1	0	1.48817	62.345	12.6
7	2	2	2	1.35851	69.085	0.2
8	3	2	0	1.30521	72.339	3.9
9	3	2	1	1.25773	75.534	38.4
10	4	0	0	1.17650	81.800	7.4
11	4	1	0	1.14137	84.891	0.1
12	4	1	1	1.10921	87.968	6.2
13	4	2	0	1.05229	94.112	9.6
14	4	2	1	1.02693	97.198	2.9
15	3	3	2	1.00332	100.305	8.5
16	4	2	2	0.96061	106.622	2.8
17	4	3	0	0.94120	109.855	0.1
18	4	3	1	0.92292	113.155	7.6
19	4	3	2	0.87388	123.640	2.9
20	5	2	1	0.85919	127.413	12.5
21	4	4	0	0.83191	135.621	5.8
22	4	3	3	0.80707	145.276	4.5

APPENDIX D

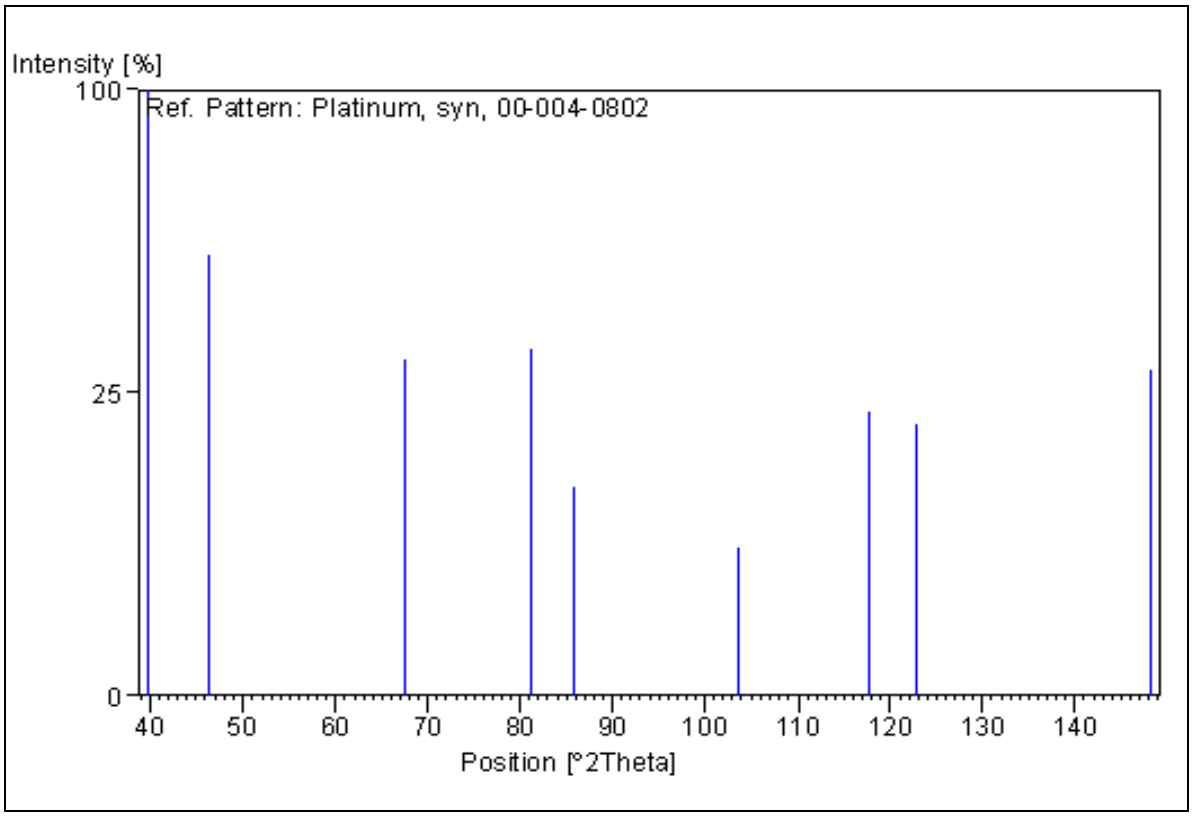

Figure D1. XRD peaks of the Pt phase.

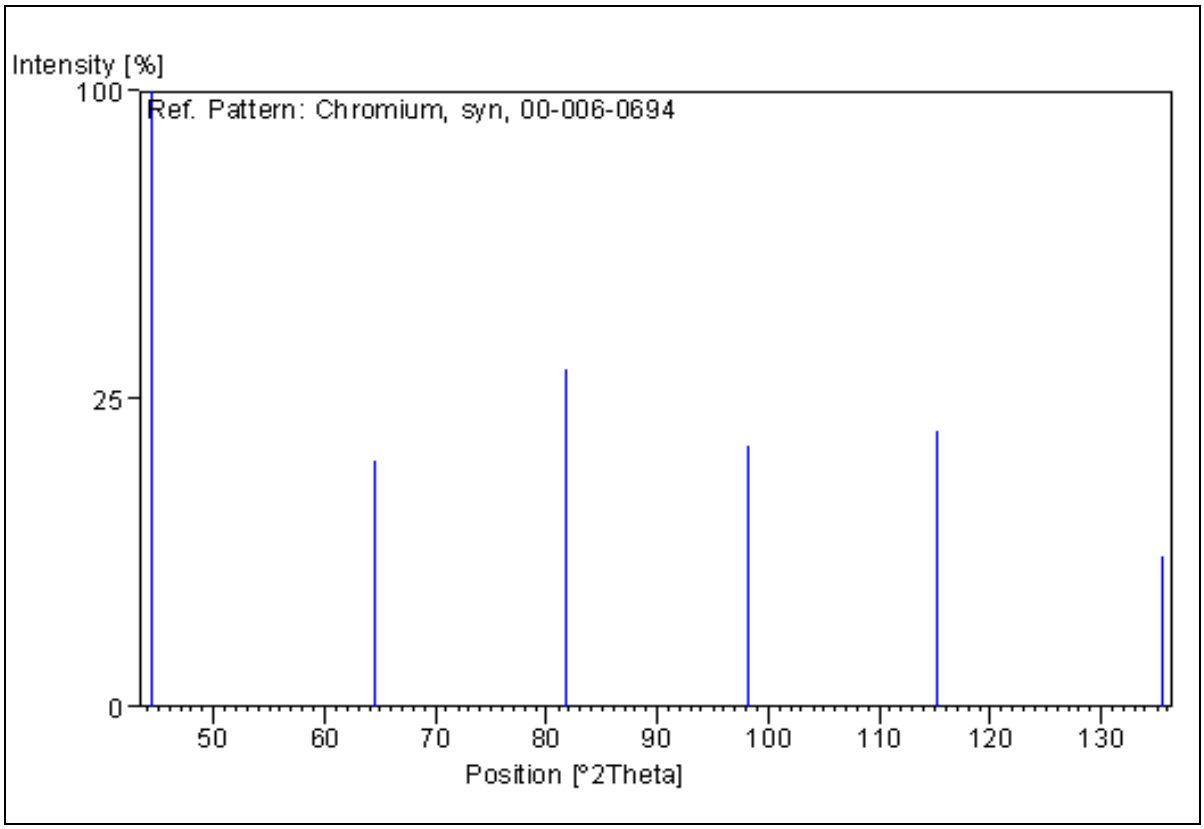

Figure D2. XRD peaks of the Cr phase.

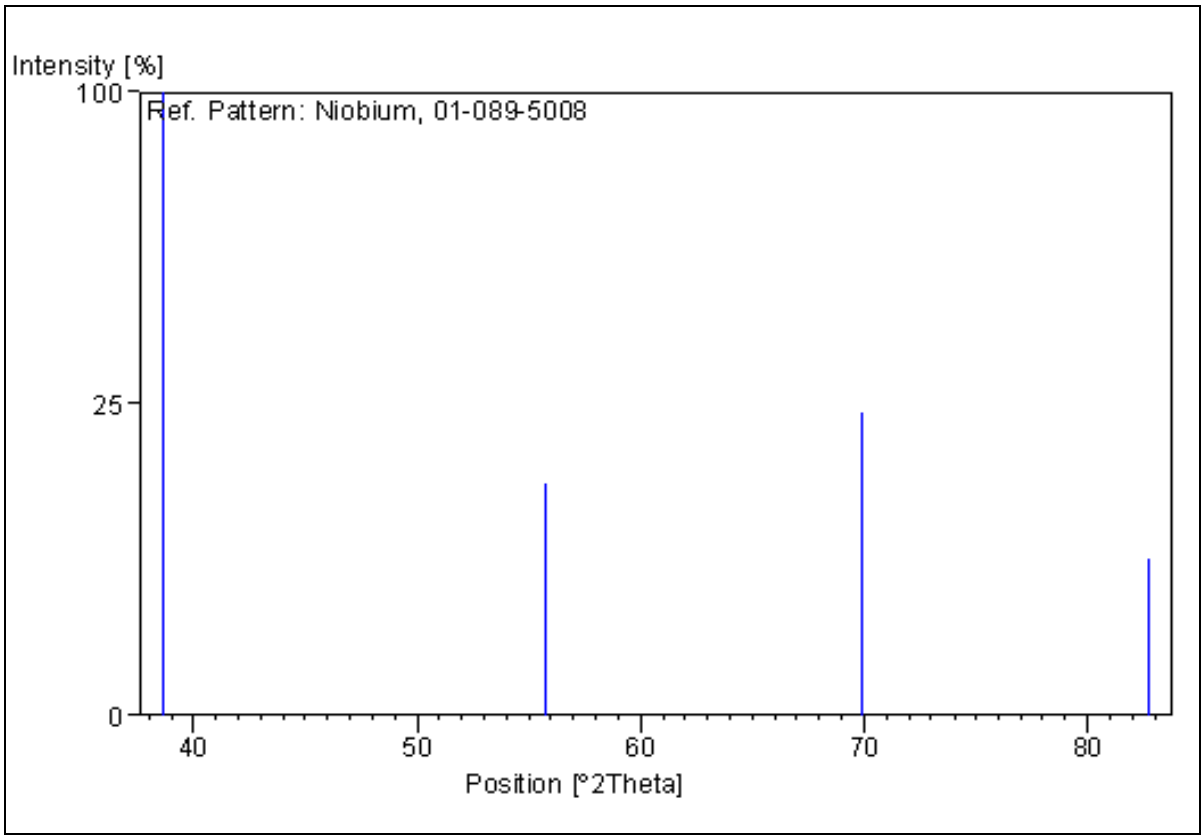

Figure D3. XRD peaks of the Nb phase.

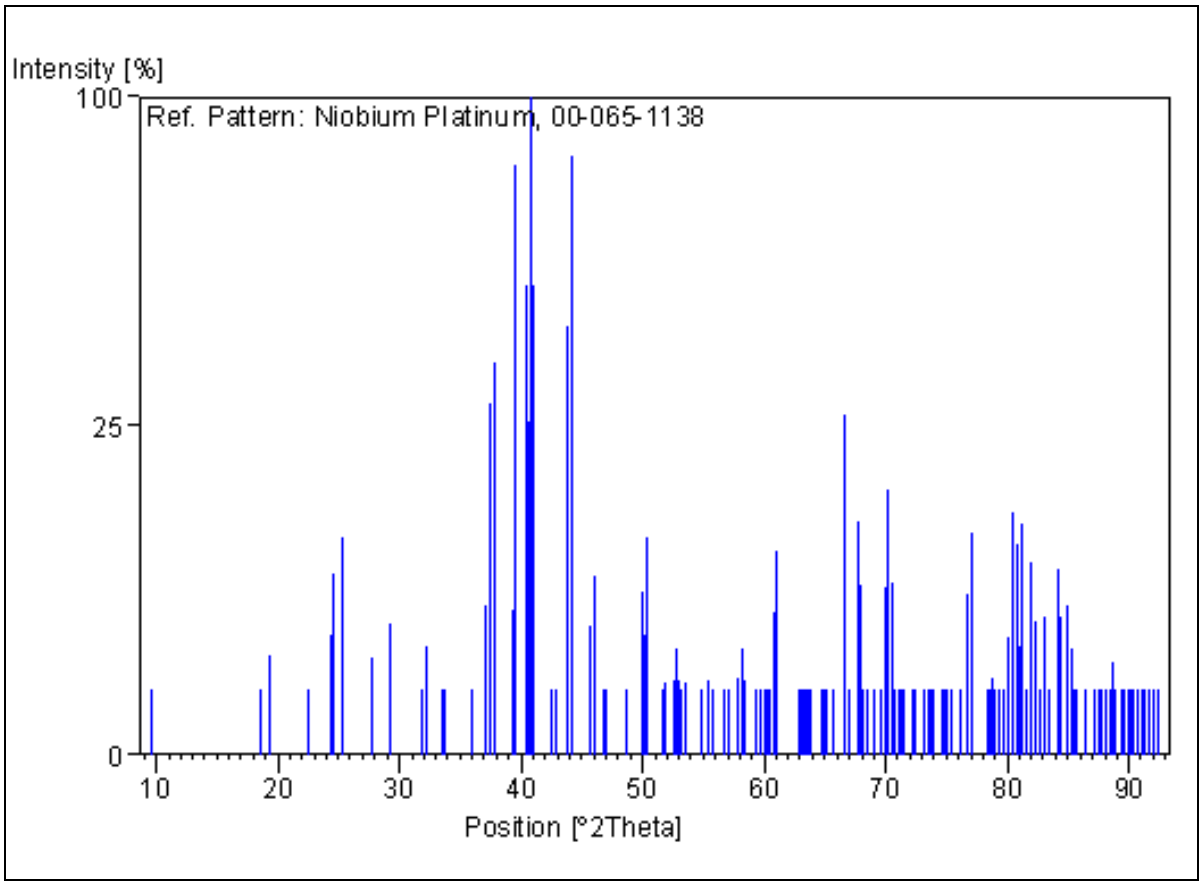

Figure D4. XRD peaks of the βNbPt$_3$ phase.

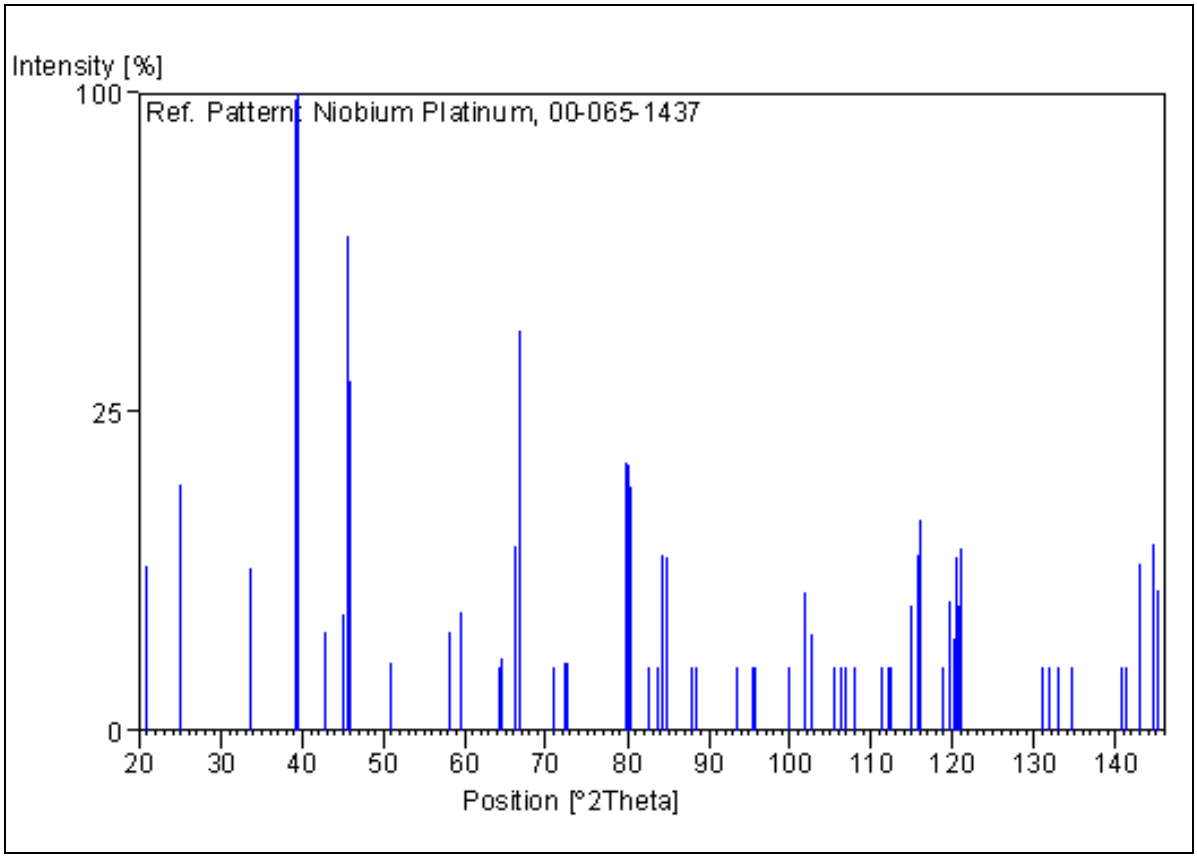

Figure D5. XRD peaks of the $NbPt_2$ phase.

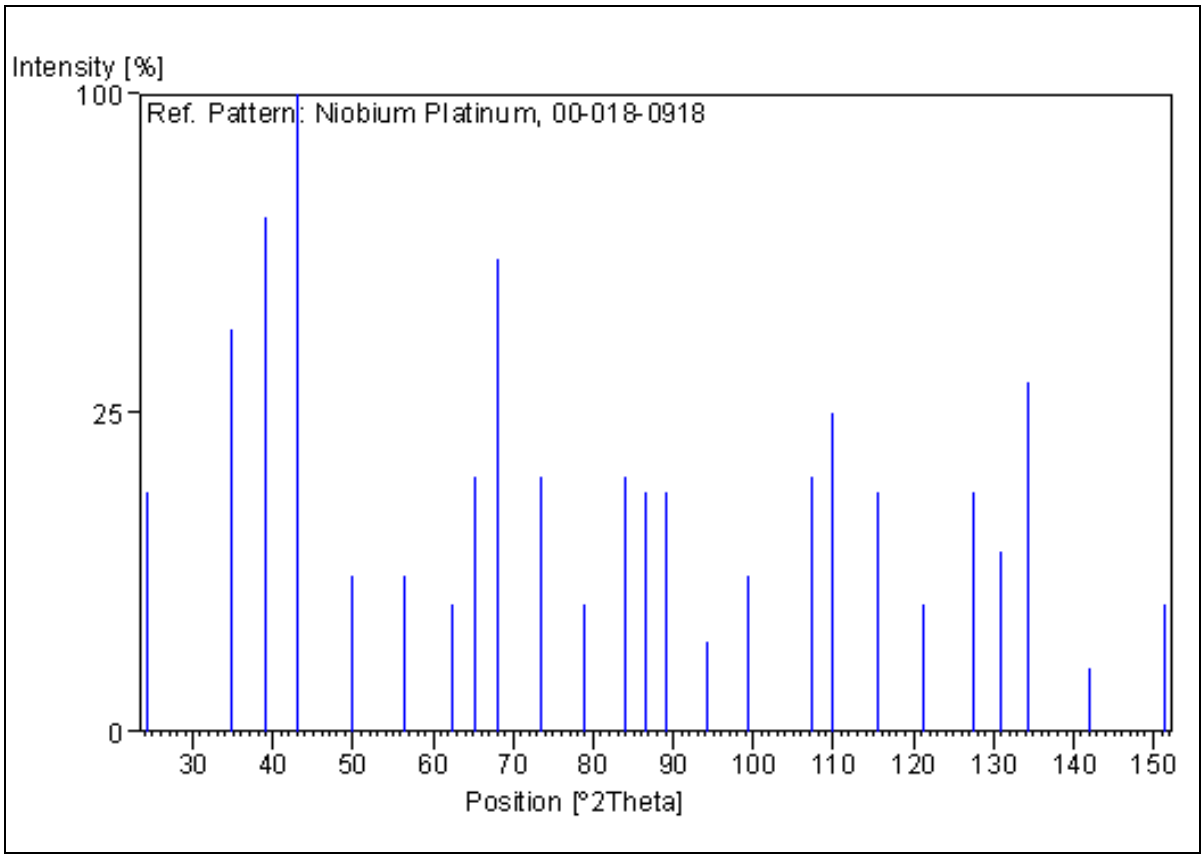

Figure D6. XRD peaks of the Nb_3Pt phase.

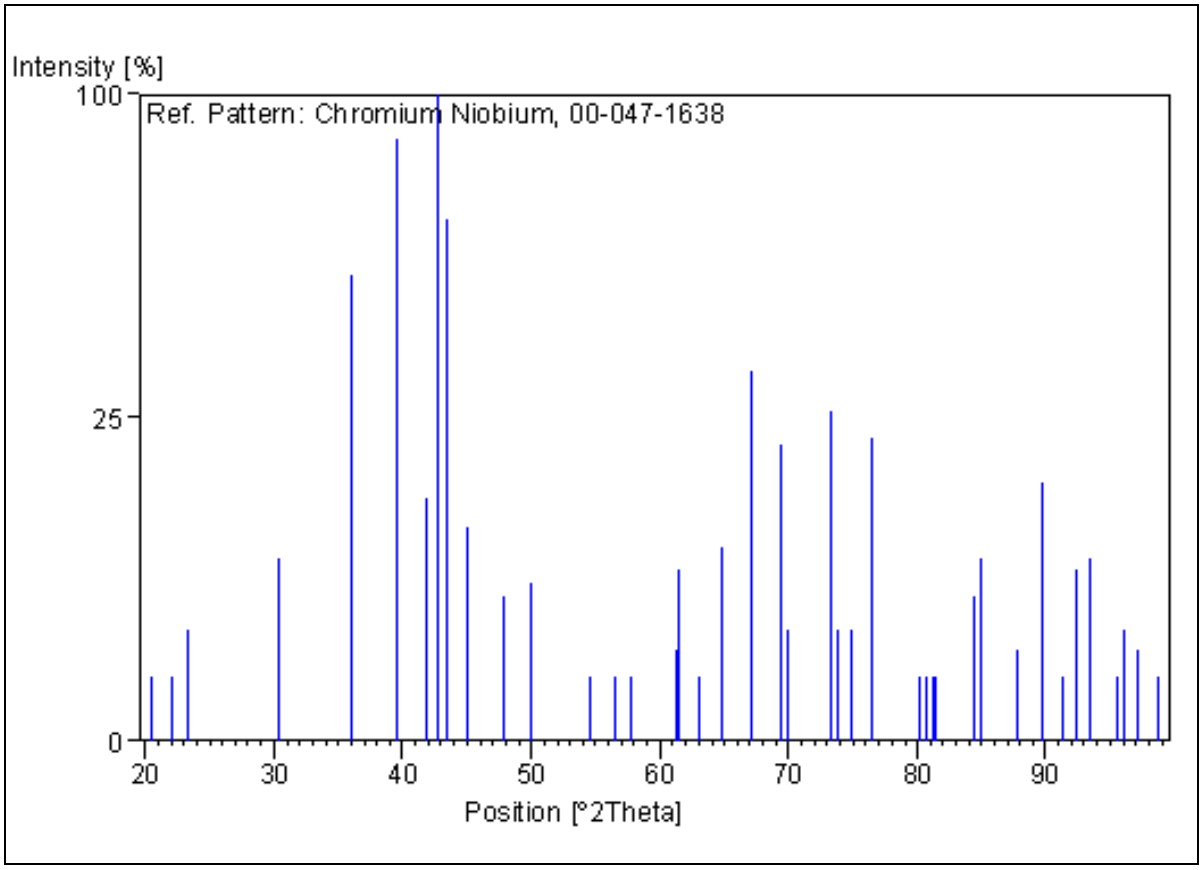

Figure D7. XRD peaks of the $NbCr_2$ phase.

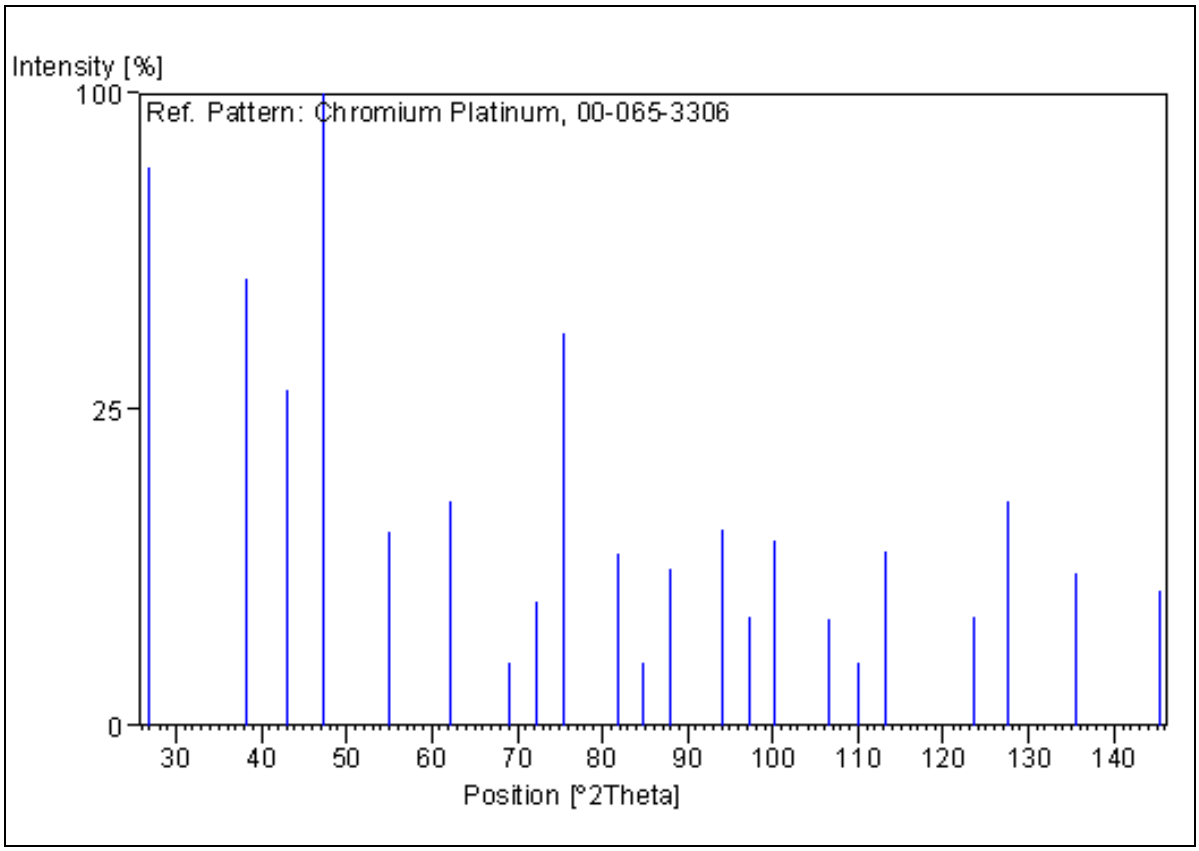

Figure D8. XRD peaks of the Cr_3Pt phase.

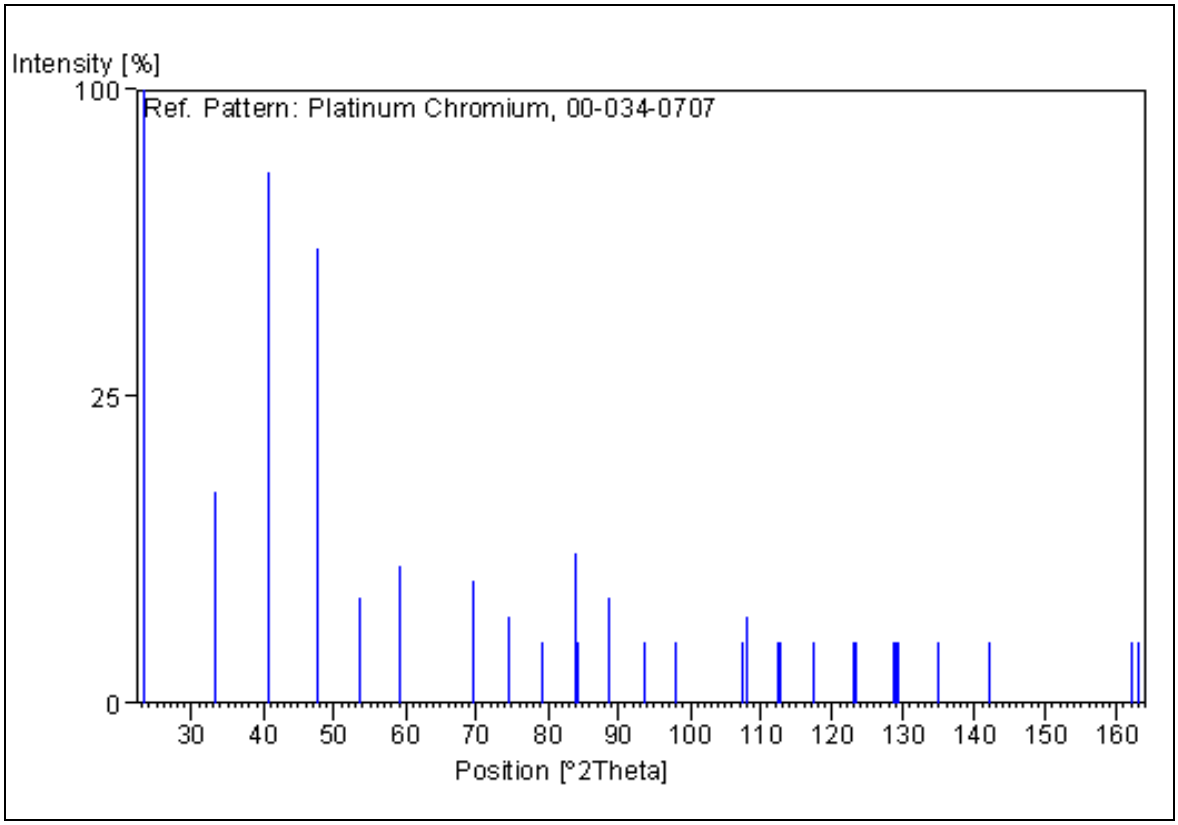

Figure D9. XRD peaks of the CrPt phase.

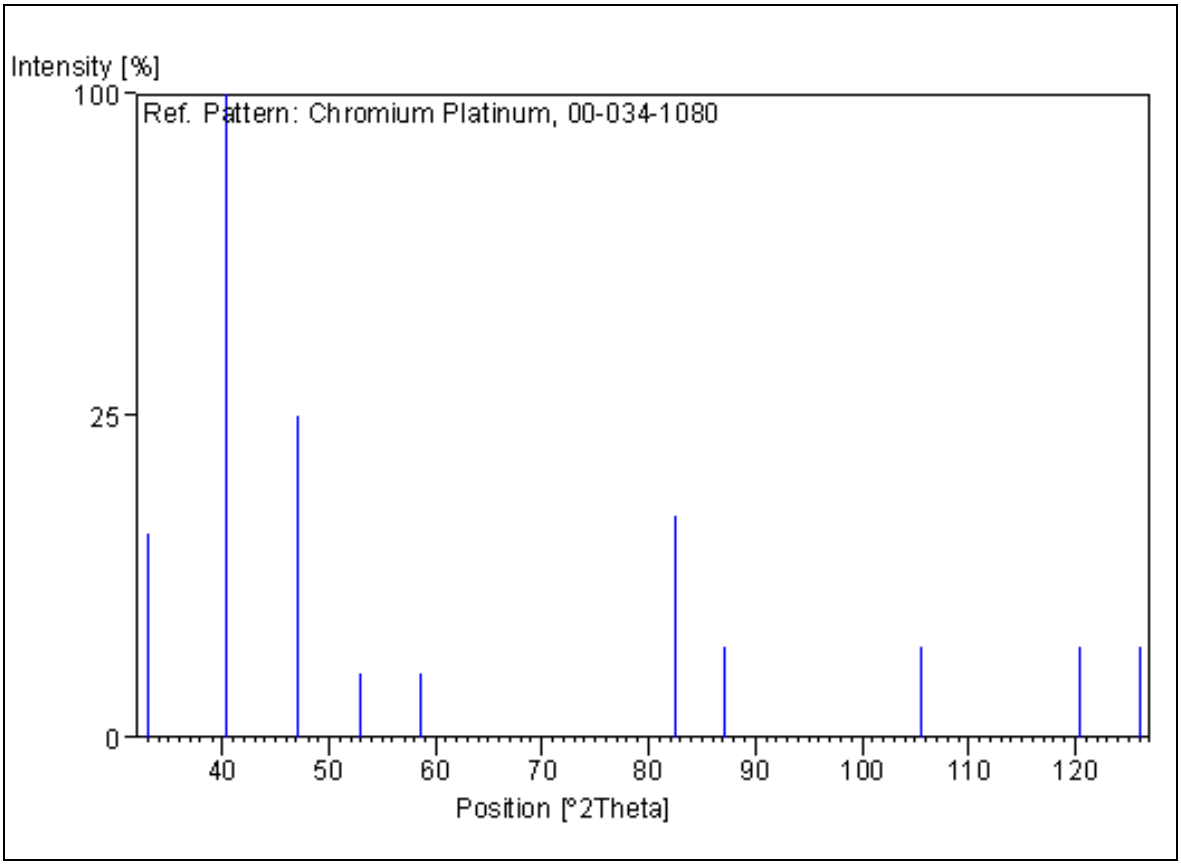

Figure D10. XRD peaks of the $CrPt_3$ phase.

APPENDIX E

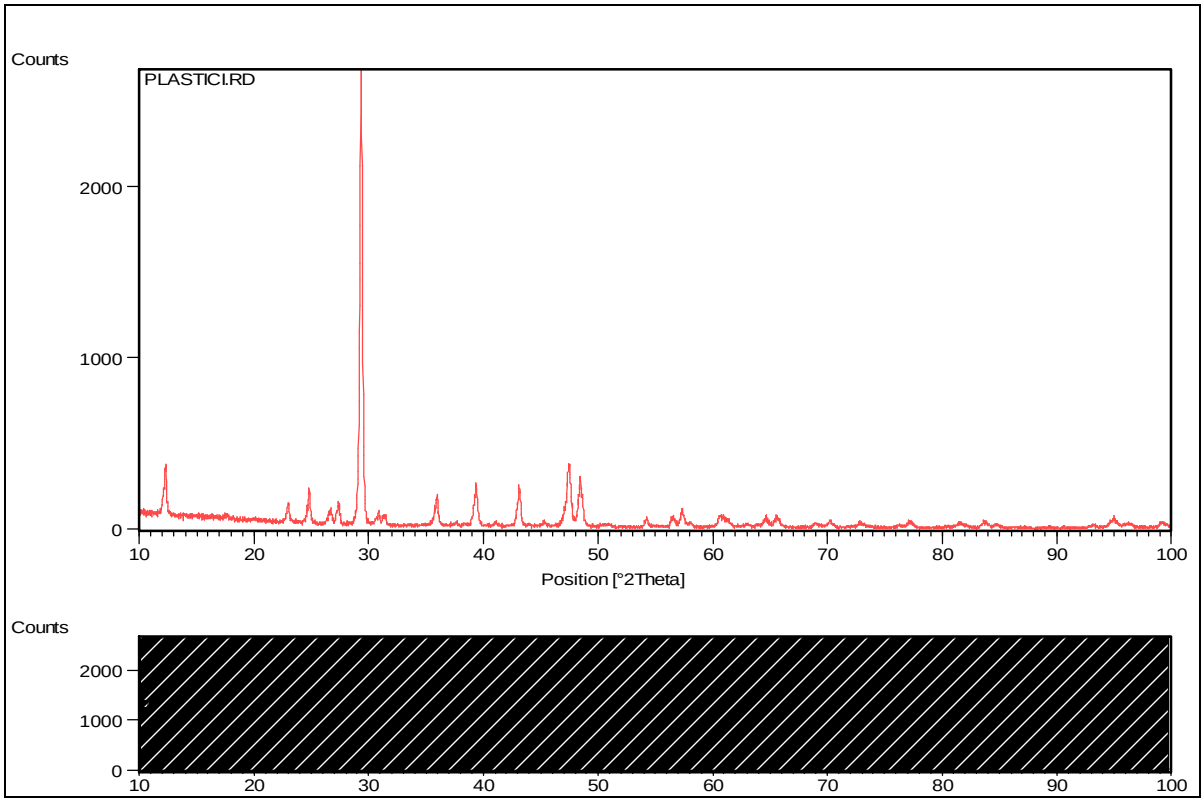

Figure E1. XRD spectrum of plasticine, top of the holder.

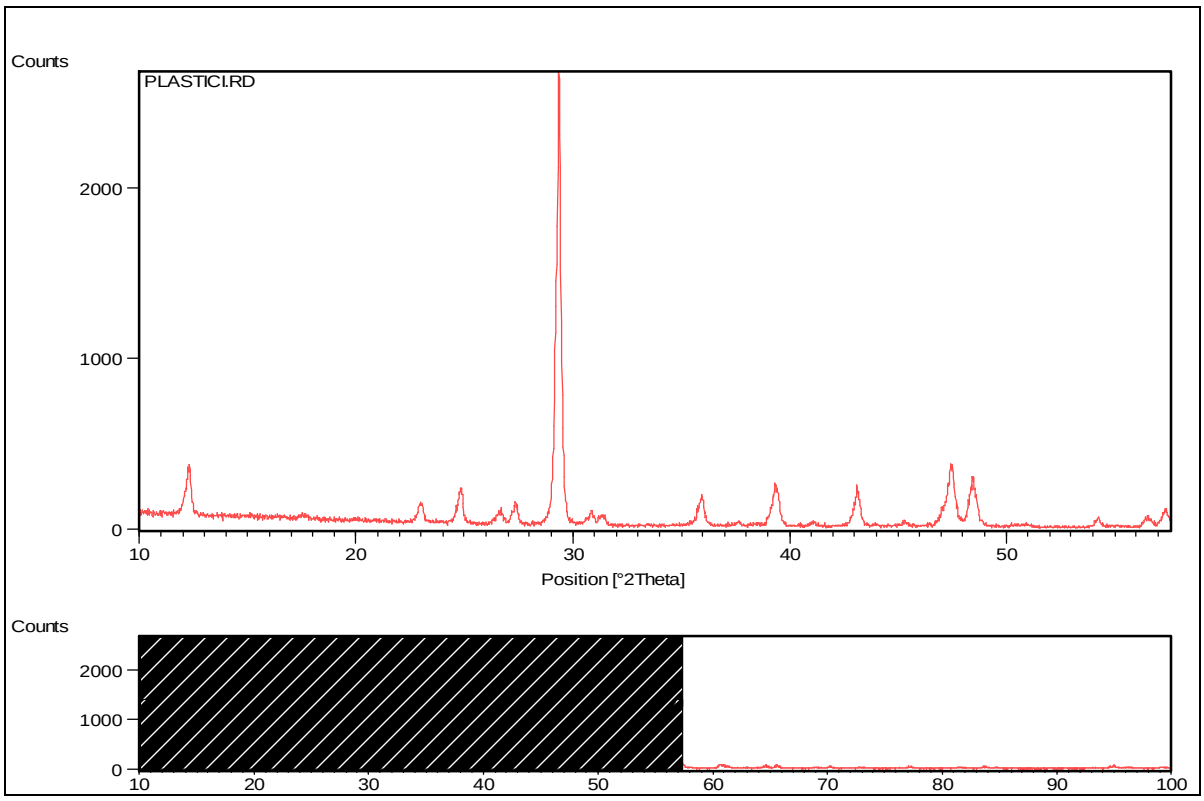

Figure E2: XRD spectrum of plasticine zoomed up to 58 (°2θ) position.

APPENDIX F (Different averages might have been used after dissertation examination)

Table F1. Energy-dispensive X-ray spectroscopy (EDX) data for nominal Nb_{15}:Cr_{15}:Pt_{70} (at.%) alloy, Sample 1.

Overall	**Area 1**	**Area 2**	**Area 3**	**Mean**	**StdDev**
Pt	70.2	70.1	68.2	**69.5**	**1.1**
Nb	13.5	13.2	17.0	**14.5**	**2.1**
Cr	16.4	16.7	14.8	**16.0**	**1.0**

Table F2. EDX data for nominal Nb_{15}:Cr_{40}:Pt_{45} (at.%) alloy in the as-cast condition, Sample 2.

Overall	Area 1	Area 2	Area 3	**Mean**	**StdDev**
Pt	47.5	44.8	44.9	**45.7**	**1.5**
Nb	16.2	15.0	14.9	**15.4**	**0.7**
Cr	36.3	40.3	40.2	**38.9**	**2.2**

Light	Area 1	Area 2	Area 3	Area 4	Area 5	Area 6	Area 7	Area 8	Area 9	Area 10	Area 11	**Mean**	**StdDev**
Pt	45.4	47.3	47.7	47.1	47.8	48.2	46.4	48.0	47.6	47.6	48.2	**47.4**	**0.8**
Nb	14.3	14.9	15.1	15.6	15.4	16.1	15.5	15.4	15.4	16.4	15.4	**15.4**	**0.6**
Cr	40.3	37.8	37.2	37.3	36.8	35.7	38.2	36.5	37.0	36.0	36.4	**37.2**	**1.3**

Dark	Area 1	Area 2	Area 3	Area 4	Area 5	Area 6	**Mean**	**StdDev**
Pt	44.1	43.4	41.9	39.6	41.7	40.4	**41.9**	**1.7**
Nb	14.6	15.4	14.6	15.7	14.4	14.6	**14.9**	**0.5**
Cr	41.3	41.2	43.5	44.7	43.9	45.0	**43.3**	**1.6**

Table F3. EDX data for nominal $Nb_{40}:Cr_{15}:Pt_{45}$ (at.%) alloy in the as-cast condition, with dendrites, Sample 3 (a).

Overall dendrites	Area 1	Area 2	Area 3	Area 4	Area 5	**Mean**	**StdDev**
Pt	45.4	45.7	46.0	45.6	45.8	**45.7**	**0.2**
Nb	41.3	40.7	40.4	40.9	40.6	**40.8**	**0.4**
Cr	13.2	13.6	13.7	13.5	13.6	**13.5**	**0.2**
Light dendrites	Area 1	Area 2	Area 3	Area 4	Area 5	**Mean**	**StdDev**
Pt	49.1	49.6	49.1	49.6	49.0	**48.5**	**1.5**
Nb	41.0	40.4	41.0	39.8	39.2	**40.6**	**0.9**
Cr	9.9	10.0	9.9	10.6	11.8	**10.9**	**1.1**
Dark interdendritic	Area 1	Area 2	Area 3	Area 4	**Mean**	**StdDev**	
Pt	44.4	35.0	39.8	38.7	**39.5**	**3.3**	
Nb	39.1	47.6	43.0	43.0	**43.2**	**3.0**	
Cr	16.5	17.3	17.2	18.3	**17.3**	**0.7**	

Table F4. EDX data for nominal $Nb_{40}:Cr_{15}:Pt_{45}$ (at.%) alloy in the as-cast condition, with needles and dendrites, Sample 3 (b).

Overall	Area 1	Area 2	Area 3	Area 4	Area 5	**Mean**	**StdDev**			
Pt	45.3	47.4	45.9	45.5	47.3	**46.3**	**1.0**			
Nb	41.1	39.5	41.4	41.4	39.7	**40.6**	**0.9**			
Cr	13.6	13.1	12.7	13.0	12.9	**13.1**	**0.3**			
Light Needles	Area 1	Area 2	Area 3	**Mean**	**StdDev**					
Pt	46.7	47.8	46.8	**47.1**	**0.6**					
Nb	41.0	42.9	41.7	**41.9**	**1.0**					
Cr	12.3	9.4	11.5	**11.0**	**1.5**					
Light dendrites	Area 1	Area 2	Area 3	Area 4	Area 5	**Mean**	**StdDev**			
Pt	44.3	44.4	46.4	45.8	45.6	**45.3**	**0.9**			
Nb	39.2	39.8	40.1	39.9	39.4	**39.7**	**0.4**			
Cr	16.6	15.9	13.5	14.3	15.0	**15.0**	**1.2**			
Medium-grey	Area 1	Area 2	**Mean**	**StdDev**						
Pt	44.0	42.3	**43.1**	**1.2**						
Nb	37.7	37.4	**37.6**	**0.3**						
Cr	18.3	20.4	**19.3**	**1.5**						
Dark	Area 1	Area 2	Area 3	Area 4	Area 5	Area 6	Area 7	Area 8	**Mean**	**StdDev**
Pt	31.9	31.6	31.3	31.8	31.3	32.1	31.6	31.6	**31.6**	**0.3**
Nb	39.7	38.9	39.7	40.0	40.0	40.3	39.3	39.7	**39.7**	**0.4**
Cr	28.4	29.5	29.1	28.2	28.8	27.6	29.1	28.7	**28.7**	**0.6**

Table F5. EDX data for nominal $Nb_{15}:Cr_{70}:Pt_{15}$ (at.%) alloy in the as-cast condition, Sample 4 (a).

Overall	**Cr**	**Nb**	**Pt**		**Light**	**Cr**	**Nb**	**Pt**
Area 1	73.0	13.5	13.5		Area 1	65.4	16.0	18.6
Area 2	73.1	13.7	13.2		Area 2	65.7	15.6	18.7
Area 3	72.8	13.9	13.4		Area 3	65.3	15.9	18.8
Area 4	73.4	13.3	13.2		Area 4	66.0	15.1	19.0
Area 5	72.6	14.5	12.9		Area 5	65.5	15.9	18.6
Area 6	73.3	13.3	13.4		Area 6	64.9	16.8	18.4
Area 7	73.2	13.6	13.2		Area 7	65.4	16.1	18.5
Area 8	73.5	13.3	13.2		Area 8	65.8	15.5	18.8
Mean	**73.1**	**13.6**	**13.3**		**Mean**	**65.5**	**15.8**	**18.7**
StdDev	**0.3**	**0.4**	**0.2**		**StdDev**	**0.3**	**0.5**	**0.2**
Medium	**Cr**	**Nb**	**Pt**		**Dark**	**Cr**	**Nb**	**Pt**
Area 1	58.8	27.8	13.5		Area 1	93.6	1.6	4.8
Area 2	57.3	28.7	14.1		Area 2	93.5	1.8	4.7
Area 3	58.5	27.9	13.6		Area 3	94.1	1.3	4.7
Area 4	57.5	28.6	14.0		Area 4	93.4	1.9	4.7
Area 5	58.7	27.8	13.5		Area 5	93.4	1.8	4.8
Area 6	58.3	28.1	13.7		Area 6	93.2	1.8	5.0
Area 7	58.6	28.2	13.2					
Mean	**58.2**	**28.1**	**13.6**		**Mean**	**93.5**	**1.7**	**4.8**
StdDev	**0.6**	**0.4**	**0.3**		**StdDev**	**0.3**	**0.2**	**0.1**

Table F6. EDX data for nominal $Nb_{15}:Cr_{70}:Pt_{15}$ (at.%) alloy in the as-cast condition, Sample 4 (b).

Inner light	Area 1	Area 2	Area 3	Area 4	**Mean**	**StdDev**		
Pt	19.7	19.3	17.8	19.4	**19.0**	**0.9**		
Nb	15.7	15.5	18.1	16.6	**16.4**	**1.2**		
Cr	64.6	65.3	64.2	64.0	**64.5**	**0.6**		
Outer light	Area 1	Area 2	Area 3	Area 4	Area 5	**Mean**	**StdDev**	
Pt	17.0	16.8	16.0	17.0	16.5	**16.7**	**0.4**	
Nb	55.7	53.3	53.8	56.1	52.3	**54.2**	**1.6**	
Cr	27.4	29.9	30.2	26.9	31.2	**29.1**	**1.9**	
Inner medium-grey	Area 1	Area 2	Area 3	Area 4	Area 5	Area 6	**Mean**	**StdDev**
Pt	9.3	9.3	8.7	11.0	10.6	12.4	**10.2**	**1.4**
Nb	34.5	33.6	34.3	29.9	30.2	27.5	**31.7**	**2.9**
Cr	56.2	57.1	57.0	59.2	59.2	60.1	**58.1**	**1.6**
Outer medium-grey	Area 1	Area 2	**Mean**	**StdDev**				
Pt	1.0	1.8	**1.4**	**0.5**				
Nb	98.0	97.2	**97.6**	**0.6**				
Cr	1.0	1.1	**1.0**	**0.1**				

Table F7. EDX data for nominal $Nb_{40}:Cr_{45}:Pt_{15}$ (at.%) alloy in the as-cast condition, Sample 5.

Overall	Area 1	Area 2	Area 3	Area 4	Area 5	**Mean**	**StdDev**
Pt	14.2	14.3	15.2	15.2	15.8	**15.0**	**0.7**
Nb	39.5	40.4	42.7	44.0	45.7	**42.4**	**2.6**
Cr	46.4	45.3	42.1	40.8	38.5	**42.6**	**3.2**
Light	Area 1	Area 2	Area 3	Area 4	Area 5	**Mean**	**StdDev**
Pt	21.15	20.3	20.45	21.31	21.57	**21.0**	**0.6**
Nb	53.53	53.31	54.45	52.1	51.44	**53.0**	**1.2**
Cr	25.32	26.4	25.1	26.59	26.99	**26.1**	**0.8**
Dark Dendrites	Area 1	Area 2	Area 3	Area 4	Area 5	**Mean**	**StdDev**
Pt	11.8	10.2	10.0	10.1	10.4	**10.5**	**0.8**
Nb	36.0	35.0	34.9	35.1	35.7	**35.3**	**0.5**
Cr	52.2	54.8	55.1	54.8	53.9	**54.2**	**1.2**
Sparse eutectic	Area 1	**Mean**	**StdDev**				
Pt	16.3	**16.3**	**-**				
Nb	44.4	**44.4**	**-**				
Cr	39.4	**39.4**	**-**				

Table F8. EDX data for alloy $Nb_{70}:Cr_{15}:Pt_{15}$ (at.%), in the as-cast conditon, Sample 6.

Overall	**Cr**	**Nb**	**Pt**	**Light interdendritic**	**Cr**	**Nb**	**Pt**
	16.3	69.9	13.8		12.5	71.2	16.4
	15.2	70.8	14.0		9.3	73.9	16.8
	16.1	69.8	14.1		9.0	73.9	17.1
	16.5	69.7	13.8		12.3	71.7	15.9
	16.2	69.7	14.1		9.8	73.1	17.1
	16.2	69.8	14.0				
	16.6	69.3	14.1	**Mean**	**10.6**	**72.8**	**16.7**
Mean	**16.2**	**69.9**	**14.0**	**StdDev**	**1.7**	**1.3**	**0.5**
StdDev	**0.4**	**0.4**	**0.1**				
Medium dendrites	**Cr**	**Nb**	**Pt**	**Eutectic**	**Cr**	**Nb**	**Pt**
	18.1	75.7	6.3		41.3	51.0	7.7
	14.2	78.0	7.9		37.5	54.4	8.1
	17.7	76.1	6.2		43.6	48.4	8.0
	15.9	77.6	6.6		46.1	47.2	6.7
	18.2	75.4	6.4		46.9	47.5	5.6
					48.2	46.6	5.2
Mean	**16.8**	**76.5**	**6.7**		45.0	48.2	6.8
StdDev	**1.8**	**1.1**	**0.7**		51.1	43.3	5.6
				Mean	**45.0**	**48.3**	**6.7**
				StdDev	**4.2**	**3.3**	**1.1**

Table F9. EDX data for alloy $Nb_{30}:Cr_{10}:Pt_{60}$ (at.%), in the as-cast condition, Sample 7.

Overall	**Cr**	**Nb**	**Pt**	**Light needles**	**Cr**	**Nb**	**Pt**
Area 1	8.6	21.9	69.5	Area 1	2.8	22.7	74.5
Area 2	8.3	21.3	70.4	Area 2	2.8	23.0	74.2
Area 3	9.5	19.6	71.0	Area 3	2.5	23.2	74.3
Area 4	8.6	22.0	69.4	Area 4	3.3	22.5	74.2
Area 5	8.4	20.2	71.5	Area 5	3.8	21.9	74.3
Area 6	8.4	20.7	70.9	Area 6	3.1	23.3	73.6
Mean	**8.6**	**20.9**	**70.4**	Area 7	3.3	21.1	75.5
StdDev	**0.4**	**1.0**	**0.8**	Area 8	3.6	21.7	74.7
					5.0	21.9	73.2
Medium-grey	**Cr**	**Nb**	**Pt**		2.6	23.3	74.1
					3.3	22.7	74.0
Area 1	14.7	19.8	65.5		3.0	21.8	75.2
Area 2	12.7	19.8	67.5		3.0	23.0	74.0
Area 3	13.0	20.7	66.4	**Mean**	**3.2**	**22.5**	**74.3**
Area 4	14.6	19.8	65.6	**StdDev**	**0.6**	**0.7**	**0.6**
Area 5	13.9	20.2	65.9				
Area 6	11.7	20.9	67.4	**Dark**	**Cr**	**Nb**	**Pt**
Area 7	14.9	19.2	65.9		17.5	18.3	64.3
Area 8	12.4	19.7	67.9		20.9	16.8	62.3
Area 9	13.0	19.7	67.3		19.1	18.3	62.6
Mean	**13.4**	**20.0**	**66.6**	**Mean**	**19.2**	**17.8**	**63.0**
StdDev	**1.1**	**0.5**	**0.9**	**StdDev**	**1.7**	**0.9**	**1.1**

Table F10. EDX data for nominal $Nb_{60}:Cr_{10}:Pt_{30}$ (at.%) alloy in the as-cast condition, Sample 8.

Overall	Area 1	Area 2	Area 3	Area 4	Area 5	**Mean**	**StdDev**
Pt	33.9	34.3	34.6	34.7	35.2	**34.5**	**0.4**
Nb	57.3	56.7	56.2	55.9	56.3	**56.5**	**0.5**
Cr	8.8	9.0	9.2	9.4	8.6	**9.0**	**0.3**
Light	Area 1	Area 2	Area 3	Area 4	Area 5	**Mean**	**StdDev**
Pt	43.3	44.8	44.5	44.6	44.4	**44.3**	**0.5**
Nb	42.7	40.7	40.7	39.9	40.7	**40.9**	**0.9**
Cr	14.1	14.6	14.8	15.5	14.9	**14.8**	**0.5**
Dark	Area 1	Area 2	Area 3	Area 4	Area 5	**Mean**	**StdDev**
Pt	28.5	28.7	29.0	28.6	28.3	**28.6**	**0.2**
Nb	66.7	66.1	65.7	66.5	66.5	**66.3**	**0.4**
Cr	4.8	5.3	5.3	4.9	5.2	**5.1**	**0.2**

Table F10. EDX data for nominal $Nb_{60}:Cr_{10}:Pt_{30}$ (at.%) alloy in the as-cast condition, Sample 8 (continued).

Medium-Grey	Area 1	Area 2	Area 3	Area 4	Area 5	Area 6	Area 7	Area 8	Area 9	Area 10	**Mean**	**StdDev**
Pt	35.2	35.4	34.8	33.4	35.4	34.6	33.1	34.6	34.1	35.1	**34.6**	**0.8**
Nb	54.6	54.0	55.9	58.9	53.8	56.2	59.1	55.3	57.2	54.5	**55.9**	**1.8**
Cr	10.3	10.6	9.3	7.8	10.8	9.2	7.8	10.1	8.7	10.4	**9.5**	**1.0**

Table F11. EDX data for nominal $Nb_{24}:Cr_{23}:Pt_{53}$ (at.%) alloy in the as-cast condition, Sample 9.

Overall	Area 1	Area 2	Area 3	Area 4	Area 5	**Mean**	**StdDev**			
Pt	54.9	55.1	54.4	55.1	54.2	**54.7**	**0.4**			
Nb	21.8	21.7	21.8	21.6	21.7	**21.7**	**0.1**			
Cr	23.3	23.3	23.8	23.3	24.2	**23.6**	**0.4**			
Light dendrites	Area 1	Area 2	Area 3	Area 4	Area 5	**Mean**	**StdDev**			
Pt	58.1	57.9	57.7	58.1	57.8	**57.9**	**0.2**			
Nb	22.1	22.7	22.3	22.3	22.7	**22.4**	**0.3**			
Cr	19.8	19.4	20.1	19.6	19.5	**19.7**	**0.3**			
Cored (Pt) light	Area 1	Area 2	Area 3	Area 4	**Mean**	**Stdev**				
Pt	51.4	53.4	51.5	52.7	**52.3**	**1.0**				
Nb	24.1	24.5	24.2	24.1	**24.2**	**0.2**				
Cr	24.5	22.1	24.4	23.3	**23.5**	**1.1**				
Dark	Area 1	Area 2	Area 3	Area 4	Area 5	Area 6	Area 7	Area 8	**Mean**	**StdDev**
Pt	52.7	54.3	55.3	54.2	52.7	55.4	53.7	53.5	**54.0**	**1.1**
Nb	21.0	22.0	21.3	21.6	21.2	20.7	21.0	21.4	**21.3**	**0.4**
Cr	26.4	23.8	23.4	24.3	26.1	23.8	25.3	25.2	**24.8**	**1.1**

Table F12. EDX data for nominal $Nb_{50}:Cr_{30}:Pt_{20}$ (at.%) alloy in the as-cast condition, Sample 10 (a).

Overall	Area 1	Area 2	Area 3	Area 4	Area 5	**Mean**	**StdDev**
Pt	44.2	46.4	45.6	41.7	42.0	**44.0**	**2.1**
Nb	46.9	45.7	44.9	40.9	41.8	**44.1**	**2.6**
Cr	8.9	7.9	9.5	17.5	16.2	**12.0**	**4.5**
Light needles	Area 1	Area 2	Area 3	**Mean**	**StdDev**		
Pt	48.3	46.9	46.3	**47.2**	**1.0**		
Nb	43.2	44.1	45.5	**44.3**	**1.1**		
Cr	8.4	8.9	8.2	**8.5**	**0.4**		

Table F13. EDX data for nominal $Nb_{50}:Cr_{30}:Pt_{20}$ (at.%) alloy in the as-cast condition, Sample 10 (b).

Overall	Area 1	Area 2	Area 3	Area 4	**Mean**	**StdDev**				
Pt	40.1	40.2	38.4	39.8	**39.6**	**0.8**				
Nb	39.4	39.9	42.3	39.5	**40.3**	**1.4**				
Cr	20.6	19.9	19.3	20.7	**20.1**	**0.7**				
Light dendrites	Area 1	Area 2	Area 3	Area 4	Area 5	Area 6	Area 7	Area 8	Area 9	**Mean**	**StdDev**
Pt	43.9	44.4	44.0	45.0	45.1	44.3	44.4	45.4	45.0	**44.6**	**0.5**
Nb	43.0	43.0	41.5	42.3	42.3	43.6	42.8	42.9	43.0	**42.7**	**0.6**
Cr	13.1	12.7	14.5	12.7	12.6	12.1	12.8	11.7	12.0	**12.7**	**0.8**
Light Mixture	Area 1	Area 2	Area 3	Area 4	Area 5	Area 6	Area 7	**Mean**	**StdDev**		
Pt	43.4	43.1	42.1	43.4	42.8	41.7	41.4	**42.5**	**0.8**		
Nb	40.0	37.7	38.9	39.7	39.1	38.2	34.8	**38.4**	**1.8**		
Cr	16.7	19.2	19.0	16.9	18.1	20.1	23.8	**19.1**	**2.4**		
Medium-grey	Area 1	**Mean**	**StdDev**								
Pt	31.9										
Nb	40.3										
Cr	27.8										

Table F14. EDX data for nominal Nb_{50}:Cr_{30}:Pt_{20} (at.%) alloy in the as-cast condition, Sample 10 (c).

Overall	Area 1	Area 2	**Mean**	**StdDev**		
Pt	20.6	23.1	**21.9**	**1.8**		
Nb	45.4	42.7	**44.1**	**2.0**		
Cr	34.0	34.2	**34.1**	**0.2**		
Light	Area 1	Area 2	Area 3	Area 4	**Mean**	**StdDev**
Pt	30.4	31.2	32.1	30.9	**31.2**	**0.7**
Nb	46.7	45.6	44.0	46.3	**45.7**	**1.2**
Cr	22.9	23.2	23.9	22.9	**23.2**	**0.5**
Medium-grey	Area 1	**Mean**	**StdDev**			
Pt	24.1	-	-			
Nb	59.8	-	-			
Cr	16.2	-	-			
Dark	Area 1	Area 2	Area 3	**Mean**	**StdDev**	
Pt	17.1	17.2	17.1	**17.1**	**0.1**	
Nb	33.4	33.1	33.1	**33.2**	**0.2**	
Cr	49.5	49.7	49.7	**49.6**	**0.1**	

Table F15. EDX data for nominal $Nb_{50}:Cr_{30}:Pt_{20}$ (at.%) alloy in the as-cast condition, Sample 10 (d).

Overall	Area 1	Area 2	**Mean**	**StdDev**								
Pt	19.0	18.9	**18.9**	**0.1**								
Nb	42.3	42.7	**42.5**	**0.3**								
Cr	38.8	38.4	**38.6**	**0.2**								
Light	Area 1	Area 2	Area 3	Area 4	Area 5	Area 6	Area 7	Area 8	Area 9	Area 10	**Mean**	**StdDev**
Pt	20.7	21.4	21.4	20.7	19.5	20.8	22.4	22.1	26.1	21.4	**21.6**	**1.8**
Nb	46.2	49.1	47.3	44.7	44.8	42.5	49.0	50.2	42.3	42.5	**45.9**	**3.0**
Cr	33.2	29.5	31.3	34.6	35.7	36.8	28.6	27.6	31.6	36.1	**32.5**	**3.3**
Dark	Area 1	Area 2	Area 3	Area 4	Area 5	Area 6	Area 7	**Mean**	**StdDev**			
Pt	13.5	12.9	13.2	13.5	13.8	14.1	14.2	**13.6**	**0.5**			
Nb	33.5	33.6	33.9	33.9	34.6	33.4	34.1	**33.8**	**0.4**			
Cr	53.0	53.5	52.9	52.7	51.7	52.5	51.7	**52.6**	**0.7**			
Binary eutectic	Area 1	Area 2	Area 3	Area 4	**Mean**	**StdDev**						
Pt	17.5	18.6	18.4	17.7	**18.0**	**0.5**						
Nb	43.1	44.6	45.0	44.1	**44.2**	**0.8**						
Cr	39.5	36.8	36.6	38.2	**37.8**	**1.3**						
Ternary eutectic	Area 1	**Mean**	**StdDev**									
Pt	20.5	-	-									
Nb	44.3	-	-									
Cr	35.2	-	-									

Table F16. EDX data for nominal $Nb_{50}:Cr_{30}:Pt_{20}$ (at.%) alloy in the as-cast condition, Sample 10 (e).

Overall	Area 1	Area 2	Area 3	Area 4	Area 5	**Mean**	**StdDev**
Pt	19.1	18.4	19.3	18.5	18.7	**18.8**	**0.4**
Nb	39.6	40.0	42.1	43.4	42.2	**41.5**	**1.6**
Cr	41.4	41.6	38.5	38.2	39.2	**39.8**	**1.6**
Light	Area 1	Area 2	Area 3	Area 4	**Mean**	**StdDev**	
Pt	26.3	26.0	25.9	28.3	**26.6**	**1.1**	
Nb	48.1	48.1	41.6	43.5	**45.3**	**3.3**	
Cr	25.6	25.9	32.5	28.2	**28.1**	**3.2**	
Dark	Area 1	Area 2	Area 3	**Mean**	**StdDev**		
Pt	15.6	15.4	15.2	**15.4**	**0.2**		
Nb	38.1	38.2	38.9	**38.4**	**0.4**		
Cr	46.3	46.4	45.9	**46.2**	**0.3**		

Table F17. EDX data for nominal $Nb_{50}:Cr_{30}:Pt_{20}$ (at.%) alloy in the as-cast condition, Sample 10 (f).

Overall	Area 1	Area 2	Area 3	Area 4	Area 5	Area 6	Area 7	Area 8	Area 9	**Mean**	**StdDev**
Pt	18.8	18.6	18.8	18.5	19.0	18.2	17.3	17.8	17.9	**18.3**	**0.6**
Nb	40.7	39.3	41.1	39.8	39.9	37.9	38.2	38.7	38.0	**39.3**	**1.2**
Cr	40.5	42.0	40.2	41.7	41.1	44.0	44.5	43.5	44.1	**42.4**	**1.6**
Light interdendrites	Area 1	Area 2	Area 3	Area 4	Area 5	Area 6	Area 7	Area 8	**Mean**	**StdDev**	
Pt	27.8	27.5	27.8	27.2	27.3	27.5	26.7	26.7	**27.3**	**0.4**	
Nb	47.0	46.7	46.6	47.5	47.6	48.5	48.2	48.2	**47.5**	**0.7**	
Cr	25.2	25.8	25.6	25.3	25.1	23.9	25.1	25.1	**25.1**	**0.6**	
Dark dendrites	Area 1	Area 2	Area 4	**Mean**	**StdDev**						
Pt	12.4	13.3	14.0	**13.6**	**1.1**						
Nb	33.7	34.0	34.2	**34.4**	**0.8**						
Cr	53.9	52.7	51.8	**52.0**	**1.8**						

Table F18. EDX data for nominal $Nb_{35}:Cr_{30}:Pt_{35}$ (at.%) alloy in the as-cast condition, Sample 11.

Overall	Area 1	Area 2	Area 3	Area 4	Area 5	**Mean**	**StdDev**				
Pt	43.2	43.4	42.7	43.0	43.0	**43.0**	**0.3**				
Nb	19.3	18.7	19.2	18.9	18.7	**18.9**	**0.3**				
Cr	37.4	37.9	38.2	38.2	38.4	**38.0**	**0.4**				
Light	Area 1	Area 2	Area 3	Area 4	Area 5	Area 6	Area 7	Area 8	Area 9	Area 10	**Mean**	**StdDev**
Pt	46.8	44.1	46.6	43.9	46.5	46.0	44.6	46.7	45.6	45.7	**45.6**	**1.1**
Nb	19.4	18.2	18.5	18.5	18.6	18.9	18.8	17.9	20.2	18.8	**18.8**	**0.6**
Cr	33.8	37.7	34.9	37.7	34.9	35.1	36.6	35.3	34.2	35.5	**35.6**	**1.3**
Medium-grey	Area 1	Area 2	Area 3	Area 4	Area 5	Area 6	Area 7	Area 8	Area 9	**Mean**	**StdDev**	
Pt	42.4	42.2	39.8	39.7	42.2	40.9	41.4	40.1	42.6	**41.3**	**1.2**	
Nb	17.8	19.6	18.1	18.6	18.4	18.9	18.6	19.5	18.5	**18.7**	**0.6**	
Cr	39.8	38.3	42.1	41.7	39.5	40.1	40.0	40.4	38.9	**40.1**	**1.2**	
Dark	Area 1	Area 2	**Mean**	**StdDev**								
Pt	26.9	27.3	**27.1**	**0.2**								
Nb	21.9	22.6	**22.3**	**0.5**								
Cr	51.2	50.1	**50.6**	**0.7**								

Table F19. EDX data for nominal $Nb_{20}:Cr_{50}:Pt_{30}$ (at.%) alloy in the as-cast condition, Sample 12.

Overall	Area 1	Area 2	Area 3	Area 4	Area 5	**Mean**	**StdDev**		
Pt	29.1	29.2	29.1	28.5	28.5	**28.9**	**0.3**		
Nb	14.8	14.7	14.8	14.4	15.1	**14.7**	**0.2**		
Cr	56.2	56.2	56.1	57.0	56.4	**56.4**	**0.4**		
Light	Area 1	Area 2	Area 3	Area 4	Area 5	Area 6	**Mean**	**StdDev**	
Pt	33.3	33.4	33.1	32.9	33.5	33.6	**33.3**	**0.2**	
Nb	12.8	12.9	12.5	13.0	12.2	12.4	**12.6**	**0.3**	
Cr	53.9	53.8	54.3	54.1	54.3	53.9	**54.1**	**0.2**	
Eutectic								**Mean**	**StdDev**
Pt	24.7	24.8	25.1	26.0	25.4	26.1	25.9	**25.4**	**0.6**
Nb	16.8	16.9	16.5	15.6	16.3	15.5	16.3	**16.3**	**0.6**
Cr	58.5	58.3	58.4	58.4	58.4	58.4	57.8	**58.3**	**0.2**

Table F20. EDX data for nominal $Nb_{30}:Cr_{20}:Pt_{50}$ (at.%) alloy in the as-cast condition, Sample 13

Overall	Area 1	Area 2	Area 3	Area 4	Area 5	**Mean**	**StdDev**
Pt	48.6	48.5	48.0	48.3	48.7	**48.4**	**0.3**
Nb	29.6	29.5	30.1	29.4	29.8	**29.7**	**0.3**
Cr	21.9	22.0	22.0	22.3	21.5	**21.9**	**0.3**
Light	Area 1	Area 2	Area 3	Area 4	Area 5	**Mean**	**StdDev**
Pt	50.9	50.8	49.7	50.9	49.9	**50.4**	**0.6**
Nb	29.7	30.7	29.2	30.3	30.0	**30.0**	**0.6**
Cr	19.4	18.5	21.1	18.8	20.2	**19.6**	**1.1**
Medium-grey	Area 1	Area 2	Area 3	Area 4	Area 5	**Mean**	**StdDev**
Pt	43.5	42.9	43.4	43.1	42.6	**43.1**	**0.4**
Nb	29.6	28.7	29.0	29.5	28.8	**29.1**	**0.4**
Cr	26.9	28.4	27.6	27.5	28.5	**27.8**	**0.7**

Table F21. EDX data for nominal $Nb_{25}:Cr_{45}:Pt_{30}$ (at.%) alloy in the as-cast condition, with medium-grey dendrites, Sample 14 (a).

Overall	Area 1	Area 2	Area 3	Area 4	Area 5	**Mean**	**StdDev**
Pt	28.5	28.8	28.7	28.8	29.1	**28.7**	**0.2**
Nb	23.4	23.2	23.4	23.5	23.1	**23.3**	**0.1**
Cr	48.1	48.0	47.9	48.1	47.8	**48.0**	**0.1**
Medium-grey dendrites	Area 1	Area 2	Area 3	Area 4	Area 5	**Mean**	**StdDev**
Pt	35.4	35.6	35.6	35.4	35.8	**35.5**	**0.2**
Nb	21.6	21.2	21.4	21.3	20.9	**21.3**	**0.2**
Cr	43.1	43.2	43.1	43.3	43.2	**43.2**	**0.1**
Light (interdendritic)	Area 1	Area 2	Area 3	Area 4	Area 5	**Mean**	**StdDev**
Pt	27.4	27.4	27.5	27.9	27.5	**27.5**	**0.2**
Nb	24.0	24.3	24.1	23.9	23.8	**24.0**	**0.2**
Cr	48.7	48.4	48.4	48.2	48.7	**48.5**	**0.2**

Table F22. EDX data for nominal $Nb_{25}:Cr_{45}:Pt_{30}$ (at.%) alloy in the as-cast condition, with Light dendrites, Sample 14 (b).

Overall	Area 1	Area 2	**Mean**	**StdDev**
Pt	33.4	31.0	**32.2**	**1.7**
Nb	22.3	22.8	**22.6**	**0.4**
Cr	44.3	46.2	**45.2**	**1.3**

Light dendrites	Area 1	Area 2	Area 3	Area 4	Area 5	Area 6	Area 7	Area 8	**Mean**	**StdDev**
Pt	36.9	37.9	38.1	37.8	37.9	35.6	35.3	35.5	**36.9**	**1.2**
Nb	20.9	21.2	21.3	21.2	20.5	22.0	22.1	21.6	**21.4**	**0.5**
Cr	42.3	40.9	40.6	41.1	41.6	42.4	42.5	42.8	**41.8**	**0.8**
Medium-grey	Area 1	Area 2	Area 3	Area 4	Area 5	Area 6	Area 7	Area 8	**Mean**	**StdDev**
Pt	27.1	27.2	27.2	27.2	27.3	27.3	28.7	27.4	**27.4**	**0.5**
Nb	23.6	23.2	23.5	23.9	23.5	23.5	23.3	23.6	**23.5**	**0.2**
Cr	49.4	49.7	49.3	48.9	49.2	49.2	48.1	49.0	**49.1**	**0.5**

Table F23. EDX data for nominal $Nb_{25}:Cr_{45}:Pt_{30}$ (at.%) alloy in the as-cast condition, with a eutectic, Sample 14 (c).

Overall	Area 1	Area 2	**Mean**	**StdDev**
Pt	30.4	29.7	**30.0**	**0.5**
Nb	22.5	22.0	**22.3**	**0.3**
Cr	47.1	48.3	**47.7**	**0.8**

Light dendrites	Area 1	Area 2	Area 3	Area 4	Area 5	Area 6	Area 7	Area 8	**Mean**	**StdDev**
Pt	36.9	37.9	38.1	37.8	37.9	35.6	35.3	35.5	**36.9**	**1.2**
Nb	20.9	21.2	21.3	21.2	20.5	22.0	22.1	21.6	**21.4**	**0.5**
Cr	42.3	40.9	40.6	41.1	41.6	42.4	42.5	42.8	**41.8**	**0.8**
Medium-grey	Area 1	Area 2	Area 3	Area 4	Area 5	Area 6	Area 7	Area 8	**Mean**	**StdDev**
Pt	27.1	27.2	27.2	27.2	27.3	27.3	28.7	27.4	**27.4**	**0.5**
Nb	23.6	23.2	23.5	23.9	23.5	23.5	23.3	23.6	**23.5**	**0.2**
Cr	49.4	49.7	49.3	48.9	49.2	49.2	48.1	49.0	**49.1**	**0.5**

Eutectic Overall	Area 1	Area 2	Area 3	Area 4	Area 5	Area 6	Area 7	**Mean**	**StdDev**
Pt	30.4	29.8	30.5	30.3	29.5	30.3	30.3	**30.2**	**0.4**
Nb	23.5	23.0	22.9	22.9	23.1	23.4	22.7	**23.1**	**0.3**
Cr	46.2	47.2	46.6	46.8	47.4	46.4	47.0	**46.8**	**0.4**

Table F24. EDX data for nominal $Nb_{20}:Cr_{60}:Pt_{20}$ (at.%) alloy in the as-cast condition, with dark (Cr) dendrites, Sample 15 (a)

Overall	Area 1	Area 2	Area 3	Area 4	Area 5	**Mean**	**StdDev**
Pt	16.6	16.7	17.0	16.7	16.8	**16.8**	**0.2**
Nb	13.0	13.0	13.3	13.6	12.7	**13.1**	**0.3**
Cr	70.5	70.3	69.7	69.7	70.5	**70.1**	**0.4**
Dark dendrites	Area 1	Area 2	Area 3	Area 4	Area 5	**Mean**	**StdDev**
Pt	5.7	5.0	5.2	6.0	5.0	**5.4**	**0.5**
Nb	1.6	1.5	1.6	2.0	1.4	**1.6**	**0.2**
Cr	92.7	93.5	93.2	92.0	93.6	**93.0**	**0.7**
Light matrix	Area 1	Area 2	Area 3	Area 4	Area 5	**Mean**	**StdDev**
Pt	19.7	19.8	19.7	19.8	19.8	**19.8**	**0.1**
Nb	17.4	16.6	17.1	16.9	17.3	**17.1**	**0.3**
Cr	62.9	63.6	63.2	63.3	62.9	**63.2**	**0.3**

Medium-grey	Area 1	Area 2	Area 3	Area 4	Area 5	Area 6	Area 7	Area 8	**Mean**	**StdDev**
Pt	18.0	18.5	18.4	15.7	15.5	15.8	18.2	17.1	**17.1**	**1.3**
Nb	9.3	11.7	12.9	6.7	7.0	6.9	9.8	7.8	**9.0**	**2.3**
Cr	72.7	69.8	68.8	77.6	77.5	77.3	72.0	75.1	**73.8**	**3.5**

Table F25. EDX data for nominal $Nb_{20}:Cr_{60}:Pt_{20}$ (at.%) alloy in the as-cast condition, with medium-grey ~$NbCr_2$ dendrites, Sample 15 (b).

Overall	Area 1	Area 2	**Mean**	**StdDev**	
Pt	21.7	22.1	**21.9**	**0.2**	
Nb	17.3	17.9	**17.6**	**0.4**	
Cr	61.0	60.1	**60.5**	**0.7**	
Light	Area 1	Area 2	Area 3	**Mean**	**StdDev**
Pt	28.0	27.7	27.8	**27.8**	**0.1**
Nb	11.0	11.1	10.6	**10.9**	**0.3**
Cr	61.0	61.2	61.6	**61.3**	**0.3**
Medium-grey	Area 1	Area 2	Area 3	**Mean**	**StdDev**
Pt	22.0	21.7	21.0	**21.6**	**0.5**
Nb	15.8	17.2	18.4	**17.1**	**1.3**
Cr	62.2	61.1	60.6	**61.3**	**0.8**

Table F26. EDX data for nominal $Nb_{20}:Cr_{60}:Pt_{20}$ (at.%) alloy in the as-cast condition, with a dark ~Cr_3Pt phase, Sample 15 (c).

Overall	Area 1	Area 2	**Mean**	**StdDev**		
Pt	20.7	20.1	**20.4**	**0.5**		
Nb	17.0	16.1	**16.6**	**0.7**		
Cr	62.2	63.9	**63.0**	**1.1**		
Dark	Area 1	Area 2	Area 3	Area 4	**Mean**	**StdDev**
Pt	21.2	21.0	20.9	20.8	**21.0**	**0.1**
Nb	9.2	8.3	9.1	9.2	**8.9**	**0.4**
Cr	69.7	70.7	70.1	70.0	**70.1**	**0.4**
Medium-grey	Area 1	Area 2	**Mean**	**StdDev**		
Pt	21.3	21.0	**21.2**	**0.3**		
Nb	17.5	18.1	**17.8**	**0.4**		
Cr	61.2	61.0	**61.1**	**0.1**		

Table F27. EDX data for nominal $Nb_{35}:Cr_{40}:Pt_{25}$ (at.%) alloy in the as-cast condition, with dark ~$NbCr_2$ dendrites, Sample 16 (a)

Light	Area 1	**Mean**	**StdDev**
Pt	29.6	-	-
Nb	32.2	-	-
Cr	38.2	-	-

Overall	Area 1	Area 2	Area 3	Area 4	Area 5	Area 6	**Mean**	**StdDev**
Pt	24.5	24.4	24.6	24.6	24.2	24.8	**24.5**	**0.2**
Nb	37.9	37.4	37.1	37.7	37.2	37.2	**37.4**	**0.3**
Cr	37.5	38.3	38.3	37.7	38.6	38.0	**38.1**	**0.4**

Medium-grey	Area 1	Area 2	Area 3	Area 4	Area 5	Area 6	Area 7	**Mean**	**StdDev**
Pt	28.7	30.1	28.4	27.4	28.5	29.3	29.2	**28.8**	**0.9**
Nb	42.7	41.2	43.1	46.5	43.4	42.7	43.0	**43.2**	**1.6**
Cr	28.6	28.8	28.4	26.1	28.2	27.9	27.8	**28.0**	**0.9**

Dark	Area 1	Area 2	Area 3	Area 4	Area 5	Area 6	Area 7	Area 8	Area 9	**Mean**	**StdDev**
Pt	18.6	18.9	19.0	18.6	18.6	18.9	18.7	18.6	18.7	**18.7**	**0.2**
Nb	36.3	36.8	36.5	35.8	36.2	36.3	36.7	36.7	37.0	**36.5**	**0.3**
Cr	45.1	44.4	44.5	45.6	45.2	44.9	44.7	44.8	44.3	**44.8**	**0.4**

Table F28. EDX data for nominal $Nb_{35}:Cr_{40}:Pt_{25}$ (at.%) alloy in the as-cast condition, with light ~$NbPt_2$ phase, Sample 16 (b)

Overall	Area 1	**Mean**	**StdDev**					
Pt	30.8	-	-					
Nb	31.7	-	-					
Cr	37.5	-	-					
Light	Area 1	Area 2	Area 3	Area 4	Area 5	Area 6	**Mean**	**StdDev**
Pt	37.8	39.0	39.2	39.3	39.2	39.7	**39.0**	**0.6**
Nb	29.5	29.9	29.9	29.8	30.3	29.4	**29.8**	**0.3**
Cr	32.7	31.2	30.9	31.0	30.5	30.9	**31.2**	**0.8**
Medium-grey	Area 1	Area 2	Area 3	Area 4	Area 5	**Mean**	**StdDev**	
Pt	30.7	30.2	29.6	30.6	30.0	**30.2**	**0.4**	
Nb	31.8	32.0	32.5	31.8	32.1	**32.0**	**0.3**	
Cr	37.5	37.8	37.8	37.6	37.9	**37.7**	**0.2**	

Table F29. EDX data for nominal $Nb_{40}:Cr_{25}:Pt_{35}$ (at.%) alloy in the as-cast condition, Sample 17.

Overall	Area 1	Area 2	Area 3	Area 4	Area 5	**Mean**	**StdDev**					
Pt	34.5	34.7	34.1	34.1	34.4	**34.4**	**0.3**					
Nb	36.5	36.8	37.1	36.6	36.9	**36.8**	**0.2**					
Cr	29.0	28.45	28.8	29.3	28.7	**28.9**	**0.3**					
Light	Area 1	Area 2	Area 3	Area 4	Area 5	Area 6	Area 7	Area 8	Area 9	Area 10	**Mean**	**StdDev**
Pt	40.1	40.3	40.7	40.8	35.3	34.5	40.3	36.0	40.7	39.6	**38.8**	**2.5**
Nb	33.3	33.7	33.6	33.3	37.0	36.8	33.8	34.5	32.0	32.6	**34.1**	**1.6**
Cr	26.6	25.9	25.8	25.9	27.8	28.7	25.9	29.5	27.3	27.8	**27.1**	**1.3**
Medium-grey	Area 1	Area 2	Area 3	Area 4	Area 5	Area 6	Area 7	Area 8	Area 9	Area 10	**Mean**	**StdDev**
Pt	32.4	31.8	31.9	31.9	33.1	31.4	31.1	32.2	30.2	33.6	**31.9**	**1.0**
Nb	43.2	40.5	41.5	41.6	42.9	38.7	39.3	42.3	33.8	38.6	**40.2**	**2.8**
Cr	24.4	27.8	26.6	26.5	24.0	29.9	29.6	25.5	36.0	27.8	**27.8**	**3.5**

Table F30. EDX data for nominal $Nb_{57}:Cr_{18}:Pt_{25}$ (at.%) alloy in the as-cast condition, Sample 18.

Medium-grey	Area 1	Area 2	Area 3	Area 4	**Mean**	**StdDev**				
Pt	24.3	24.5	24.0	24.7	**24.4**	**0.3**				
Nb	45.3	46.8	46.8	46.9	**46.5**	**0.8**				
Cr	30.4	28.7	29.2	28.4	**29.2**	**0.9**				
Overall	Area 1	Area 2	Area 3	Area 4	Area 5	Area 6	Area 7	**Mean**	**StdDev**	
Pt	21.3	22.1	23.1	21.4	23.1	23.8	23.2	**22.6**	**1.0**	
Nb	43.5	43.5	43.5	43.4	43.2	42.6	43.5	**43.3**	**0.3**	
Cr	35.3	34.4	33.4	35.2	33.7	33.6	33.4	**34.1**	**0.8**	
Light matrix	Area 1	Area 2	Area 3	Area 4	Area 5	Area 6	Area 7	**Mean**	**StdDev**	
Pt	25.0	-	-	-	-	-	-	**-**	**-**	
Nb	59.0	-	-	-	-	-	-	**-**	**-**	
Cr	16.1	-	-	-	-	-	-	**-**	**-**	
Dark	Area 1	Area 2	Area 3	Area 4	Area 5	Area 6	Area 7	Area 8	**Mean**	**StdDev**
Pt	15.6	16.1	17.6	17.5	16.4	16.9	15.7	15.9	**16.5**	**0.8**
Nb	33.9	33.4	32.9	33.4	34.0	33.5	33.6	33.4	**33.5**	**0.3**
Cr	50.5	50.6	49.4	49.1	49.7	49.6	50.7	50.7	**50.0**	**0.6**

APPENDIX G

Papers published during the course of this investigation:

1. F.M.L. Mulaudzi, L.A. Cornish and M.J. Witcomb, An SEM Study of the Pt-Cr-Nb System, Proceedings of the Microscopy Society of Southern Africa, Volume 38, (2008), p.24.
2. F.M.L Mulaudzi, L.A. Cornish and M.J. Witcomb, An Investigation of Selected As-Cast Pt-Cr-Nb Alloys, Advanced Metals Initiative Conference, 18th–19th November 2008, CD (Printed from CD; page numbers strange and are from printing).

Other Presentations made during the course of this investigation:

1. F.M.L. Mulaudzi, L.A. Cornish and M.J. Witcomb, Constitution of the Pt-Cr-Nb System, Materials Physics Research Institute (MPRI) Seminar, University of the Witwatersrand, 25th February 2008.

AN SEM STUDY OF THE Pt-Cr-Nb SYSTEM

F.M.L. Mulaudzi[1,2], L.A. Cornish[1,2] and M.J. Witcomb[2,3]

[1]School of Chemical and Metallurgical Engineering, University of the Witwatersrand, Johannesburg, South Africa
[2]DST/NRF Centre of Excellence for Strong Materials, University of the Witwatersrand, Johannesburg, South Africa
[3]Electron Microscope Unit, University of the Witwatersrand, Johannesburg, South Africa

Since World War II, Ni-based superalloys (NBSAs) have been operating at high temperature in severe aggressive environmental conditions in power generations and acroplane turbine engines[1]. Despite the development of advanced processing technologies like single crystal technology, air cooling and thermal barrier coatings, these superalloys have nearly reached their temperature capability limit, which is defined by the melting point of Ni[1]. Platinum has a higher melting point, and so Pt-based alloys for high temperature applications are being developed at Mintek, and have microstructures that are analogous to the γ/γ' microstructure of the NBSAs[2]. Currently, the optimum alloy is Pt_{84}:Al_{11}:Ru_2:Cr_3[3]. Niobium (Nb) is a possible addition to increase the alloy's melting point, but only binary phase diagram data are available, and a Pt-Al-Nb study has been made[4], but no Pt-Cr-Nb phase diagram was found in the literature.

Prior to the investigation, it was necessary to check phases existing in the component binaries Cr-Pt, Cr-Nb and Nb-Pt system.

Alloy compositions were selected to include two binary phases by extrapolation from the binary phase diagrams. Samples were made from elements of at least 99.95% purity, and all ingot samples, 2g each, were arc melted in an argon atmosphere, using Ti as an oxygen-getter. The as-cast samples were cut in half with an Accutom® cutting wheel and then prepared metallographically using OPS polishing. Microstructures of the alloys were examined in JEOL JSM-840 and LEO-1525 SEMs equipped with EDX. All imaging was conducted in the backscattered electron (BSE) mode for phase contrast. X-ray diffraction (XRD) spectra were obtained on a Phillips (PW1710) X-ray diffractometer, using a Cu-Kα source. Phases were identified by comparison with the ICDD database.

In the nominal Nb_{15}:Cr_{70}:Pt_{15} alloy, the first phase to form was (Cr) dendrites, then ~$NbCr_2$ and finally ~Cr_3Pt, as shown in Fig 1(a). The microstructure showed two peritectic reactions. The nominal Nb_{40}:Cr_{45}:Pt_{15} alloy was quite brittle with cracks. This alloy comprised dendrites of ~$NbCr_2$, with a sparse eutectic of ~$NbCr_2$ + ~Nb_3Pt, as shown in Fig 1(b). The solidification sequence of nominal Nb_{10}:Cr_{15}:Pt_{15} is shown in Fig 2(a): (Nb) dendrites, a matrix of ~Nb_3Pt and a ~Nb_3Pt + ~$NbCr_2$ eutectic. Nominal Nb_{35}:Cr_{30}:Pt_{35} alloy comprised mainly cored (Pt) dendrites, with interdendritic ~Cr_3Pt and ~$NbCr_2$, as shown in Figure 2(b). These phases were confirmed by XRD and EDX analyses correlated with binary compositions.

Two new eutectic reactions have been discovered: (~$NbCr_2$ + ~Nb_3Pt) and (~Nb_3Pt + ~$NbCr_2$), as well as some peritectic reactions.

The assistance of Mintek, the PDI (Platinum Development Initiative) and DST/ NRF Centre of Excellence in Strong Materials are gratefully acknowledged.

References

1. Sims, C.T. et al. (1987) Wiley-Interscience, USA.
2. Wolff, I.M. and Hill, P.J. Platinum Metals Rev. 44, (4), (2000), pp. 158-166.
3. Süss, R. et al., (2001) Proc. Microsc. Soc. South. Afr. 31, 21.
4. Ndlovu, G.F. et al. (2006) Proc. Microsc. Soc. South. Afr. 36, 11.

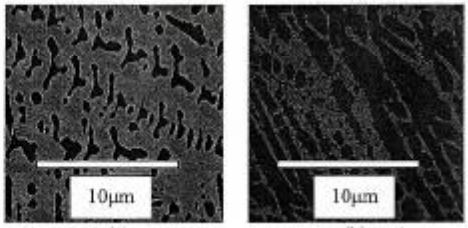

(a) (b)

Figure 1. SEM-BSE images of (a) nominal Nb_{15}:Cr_{70}:Pt_{15}, showing dark dendrites of Cr, medium-grey of ~$NbCr_2$, and light matrix of ~Cr_3Pt; (b) nominal Nb_{40}:Cr_{45}:Pt_{15}, showing dark dendrites of ~$NbCr_2$, with a sparse eutectic of ~$NbCr_2$ (dark) + Nb_3Pt (light).

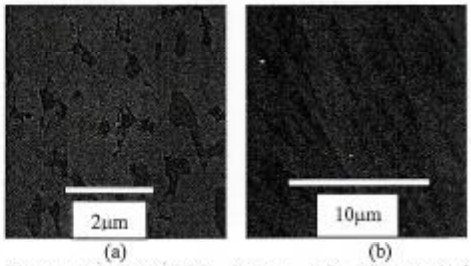

(a) (b)

Figure 2. SEM-BSE images of (a) nominal Nb_{10}:Cr_{15}:Pt_{15}, showing medium-grey dendrites of (Nb), with a light matrix of ~Nb_3Pt and ~Nb_3Pt (light) + ~$NbCr_2$ (dark) eutectic; and (b) nominal Nb_{35}:Cr_{30}:Pt_{35}, showing light (Pt) dendrites, medium-grey ~Cr_3Pt and dark ~$NbCr_2$.

Corresponding author: *marandelam@hotmail.com*